8-7-2018

CLINICAL AND TRANSLATIONAL IMPLICATIONS OF CENTROSOME AMPLIFICATION AND CLUSTERING IN MULTIPLE MALIGNANCIES

Karuna Mittal

CLINICAL AND TRANSLATIONAL IMPLICATIONS OF CENTROSOME AMPLIFICATION AND CLUSTERING IN MULTIPLE MALIGNANCIES

by

KARUNA MITTAL

Under the Direction of Ritu Aneja, PhD

ABSTRACT

Cancer initiation and progression are multistep processes that rely on the generation and accumulation of non-lethal mutations, which deregulate function of tumor suppressor genes and activate oncogenic pathways. Evolving through a landscape of heterogeneous somatic mutations, mutated cells undergo subsequent selection pressures and the one endowed with the greatest fitness advantage survives giving rise to genetically diverse cell populations resulting in intratumor heterogeneity (ITH). Presence of abnormal number of centrosomes is one of the key factors contributing towards ITH. Clustering of amplified centrosomes allows cancer cells to avoid mitotic spindle multipolarity that could otherwise result in cell death either by mitotic catastrophe or a high-grade multipolar division yielding intolerably severe aneuploidy. Thus, centrosome

clustering enables low-grade chromosomal missegregation and their unequal distribution to daughter cells resulting chromosomal instability (CIN), thus contributing to neoplastic transformation. Owing to the presence of genetically different cells in a tumor, monotargeted therapy spares clones lacking therapy-specific targets giving them the opportunity to repopulate the tumor with immunity toward the applied therapy and propensity to recur. Therefore, ITH poses major challenges to both clinicians and drug developers as it precludes detection of low-level clones, prediction of tumor evolution, development of drugs to target specific clones and evaluation of effective, yet non-toxic combinatorial regimens to combat ITH.

I envision that a comprehensive quantitative analysis of centrosome amplification (CA), which is a bona-fide driver of ITH might help better understand clinical behavior and improve therapeutic management of tumors. To this end, my research, presented here, primarily focuses on testing i) the impact of centrosome amplification and centrosome clustering protein (KIFC1) on clinical outcomes in multiple malignancies and ii) the role of tumor hypoxia in inducing centrosome amplification in cancer. Collectively, my findings reveal that CA and KIFC1 are prognostic and predictive in multiple malignancies and that tumor hypoxia plays a crucial role in inducing CA in tumors. This body of work expands our knowledge in causes and clinical implications of CA to help guide treatment decisions and development of precision medicine for multiple malignancies.

INDEX WORDS: Centrosome amplification, Centrosome clustering, Hypoxia, KIFC1, Intratumoral heterogeneity, Cancer

CLINICAL AND TRANSLATIONAL IMPLICATIONS OF CENTROSOME AMPLIFICATION AND CLUSTERING IN MULTIPLE MALIGNANCIES

by

KARUNA MITTAL

A Dissertation Submitted in Partial Fulfillment of the Requirements for the Degree of

Doctor of Philosophy

in the College of Arts and Sciences

Georgia State University

2018

CLINICAL AND TRANSLATIONAL IMPLICATIONS OF CENTROSOME AMPLIFICATION AND CLUSTERING IN MULTIPLE MALIGNANCIES

by

KARUNA MITTAL

Committee Chair: Ritu Aneja

Committee: Deborah J Baro

Zhi-Ren Liu

Emilius Adrianus Maria Janssen

Electronic Version Approved:

Office of Graduate Studies

College of Arts and Sciences

Georgia State University

August 2018

DEDICATION

This dissertation is dedicated to my husband, Nishith, who has been a constant source of support and encouragement during the challenges of graduate school and life. I also want to dedicate this work to my loving mother who has always loved me unconditionally and taught me to work hard for the things that I aspire to achieve.

ACKNOWLEDGEMENTS

I would like to express my sincere gratitude to my advisor, Dr. Ritu Aneja, for the patient guidance, encouragement, advice and opportunities she has provided throughout my time as her student. I also want to thank her and senior research scientist Dr. Padmashree C. G. Rida for their enduring professional and personal guidance and support; my dissertation committee members, Drs. Deborah J Baro, Emilius Adrianus Maria Janssen and Zhi-Ren Liu, and my qualifying committee members, Dr. Andrew Gewirtz, for their constructive feedback and encouragement; and my current and former colleagues in the lab, Nikita, Shristi, Sergey, Shriya, Chakri, Dr. Angela Ogden and Drs. Vaishali Pannu, Shashi Donthamshetty, and Chunhua Yang, for their assistance and friendship. In particular I am thankful to my fellow team mates Da Hoon Choi, Jaspreet Kaur, Ishita Chaudhary, Guanaho Wei and Brian D Melton for the stimulating discussions, for the sleepless nights we were working together before deadlines, and for all the fun we have had in the last four years.

TABLE OF CONTENTS

LIST OF TABLES

LIST OF FIGURES

1 INTRODUCTION

1.1 Centrosome structure and centrosome cycle

The centrosome is the main microtubule (MT)-organizing center in all mammalian cells; it plays important roles in various cellular processes such as cell division, mitotic spindle assembly, polarity, and migration. Structurally, a centrosome is composed of a pair of centrioles (each measure ~200 by 400 nm)[1] arranged orthogonally connected through linker proteins and surrounded by a dynamic collection of ~200 -300 centrosome-associated proteins collectively called as the pericentriolar matrix (PCM)[2, 3]. The mother centriole regulates PCM organization, stabilization, and size[4]. The PCM proteins include cell cycle regulators and proteins that help in organizing and nucleating microtubules thus, helping centrosomes to perform their key role as microtubule organizing centers. With recent advancements in the studies, it has become clear that role of centrosomes extends well beyond just the microtubule organizers. Multiple studies have shown that centrosomes function as coordination centers in eukaryotic cells and with the interaction of multiple cytoplasmic proteins major decisions regarding the cellular processes are made.

Similar to DNA replication, centrosome duplication also occurs only once per cycle (cell cycle control). Another level of regulation is the copy number control where only one centriole, i.e., daughter centriole is produced from the pre-existing mother centriole[4]. Any defect or disturbance in the regulation of these mechanisms can affect the proper execution of various processes that result in the centrosomal abnormalities. Alterations in centrosome number and structure lead to defects in the mitotic spindle organization and consequently in chromosome instability, which is a major source of aneuploidy in cancers.

1.2 How cells generate extra centrosomes?

Centrosome amplification (CA) refers to the presence of supernumerary (numerical amplification) or abnormally large centrosomes (structural amplification),[5, 6] and occurs early in pre-cancerous and pre-invasive lesions and is linked to aggressiveness in several types of cancer. There are several pathways that can lead to the acquisition of extra centrosomes, which are not mutually exclusive. Deregulation of the centrosome duplication cycle leads to the centriole overduplication and formation of supernumerary centrosomes via consecutive rounds of centrosome reproduction or fast concurrent formation of daughter centrioles around the existing centrioles giving rise to numerical amplification. Another cause of numerical amplification is the failure of cytokinesis, owing to which polyploid cells with supernumerary centrosomes are generated. On occasion, numerical amplification also arises from fragmentation of the pericentriolar matrix. Similarly, several factors account for structural defects which include accumulation of excessive PCM around the centrioles (likely due to deregulated expression of genes coding for centrosomal components or altered posttranslational modifications), resulting in centrosomes that appear altered in size.[7] PCM size is regulated by centrioles, free cytoplasmic αβ-tubulin, centrobin, kinases like PLK1 and CHK1, and several coiled-coil proteins like pericentrin and CPAP [8-10]. The mechanisms undergirding structural CA in cancer are still poorly defined, although several stimulators of PCM assembly are overexpressed in cancer (e.g., PLK1 [11] and CHK1 [12]), cancer cells often harbor supernumerary centrioles (which could then recruit excessive PCM), and the PCM expands following DNA damage [13]. Another possible reason for structural aberration can be tight clustering of centrosomes, which thus cannot be individually distinguished. Another possible reason for this can be structural defects in centrioles; this is a completely unexplored area

because the size of normal centriole is very small and requires very sophisticated microscopy techniques especially for tumor samples. [5]

In addition, deregulation of the oncogenes or tumor suppressor genes which regulates expression of centrosome-associated genes have been shown to lead to the formation of supernumerary centrosomes. For, e.g., the expression of an important protein Polo like kinase 4 (PLK4) is regulated by various factors. A transcriptional factor KLF14 transcriptionally represses expression of PLK4 and thus knock out of KLF14 has been shown to result in centrosome amplification via an increase in expression of PLK4[14]. Similarly, p53 which is a tumor suppressor gene also negatively regulates expression of PLK4 and thus induces centrosome amplification indirectly through PLK4[15]. In addition, HPV-16 viral E6 and E7 oncoproteins have been shown to disrupt host cell cycle checkpoints important for oncogenic transformation that results in disruption of normal centriole duplication (increased PLK4 mRNA levels) induces centrosome amplification (CA)[16].

Another important factor which deregulates expression of the several centrosome-associated genes is the tumor microenvironment. Tumor hypoxia is one of the most critical component of tumor microenvironment. Although studies have reported that hypoxia increases levels of CA associated proteins such as Aurora-A/STK15 protein and PLK4 [17-19], the mechanism under grinding this phenomenon is not well understood. Thus, understanding the mechanism by which hypoxia induces CA is the primary goal of the first manuscript in this dissertation (Chapter 2).

Prognostic and predictive role of Centrosome amplification in human cancers

Theodor Boveri postulated a century ago that multiple centrosomes are seen in cancer cells and may lead to tumorigenesis. Since then, centrosomes have been studied in growing list of human

cancers including bladder, blood, bone and soft tissue, brain, breast, cervix, colorectum, head and neck, hepatobiliary tract, kidney, ovary, prostate, and hematological malignancies. From these observations, the question naturally arises whether supernumerary centrosomes are simply innocent bystanders or whether they play a causative role in fueling tumor evolution. Studies have reported that CA occurs in precancerous and preinvasive lesions (including DCIS) , indicating that CA is an early event in tumorigenesis and is involved in the transition from early to advanced stages of carcinogenesis. Furthermore, one landmark study demonstrated that induction of CA could initiate tumor formation and metastasis in flies [5]. Multiple studies have reported that centrosome amplification correlates with high-grade tumors and poor prognosis [16]. In prostate, head and neck and breast cancers, CA is correlated with the lymph node and distant metastasis. Thus, it is becoming increasingly understood that rather than serving as a mere beacon of malignancy, supernumerary centrosomes actually drive malignant transformation. Indeed, several threads of evidence now suggest the association of CA with more aggressive tumors raising the possibility that CA could be an evolutionarily-favored trait that confers advantageous characteristics on the cells that harbor this feature and could promote tumor progression and aggressiveness. In sum, CA is associated with several indices of aggressiveness, like genomic instability, cell migration, and metastasis which may indicate the propensity of a tumor to metastasize, although further study to substantiate this paradigm is required in clinical models with high rates of metastasis. Thus, testing the role of CA in the underlying aggressive disease course in one of the highly metastasized and aggressive cancer i.e, Pancreatic adenocarcinoma is the primary goal of the study described in the second manuscript in this dissertation (Chapter 3).

Furthermore, the role of CA in predicting tumor recurrence has been highlighted in multiple malignancies such as urothelial cancers and head and neck squamous cell carcinoma (HNSCC)

highlighting its potential as a biomarker for advanced disease [26]. In HNSCC it has been observed that tumor margins with higher CA recur more frequently than those with less CA. These findings are interesting as ideally, the tumor margins should be free of malignant cells but if CA is observed in the tumor margins that indicates either presence of malignant or potentially malignant cells harboring CA in these tumor margins. This escape of the premalignant cells from histological detection may be a potential cause of tumor recurrence. Similarly, a high rate of recurrence is observed in the ductal carcinoma in situ and due to the lack of accurate recurrence risk prediction models patients are often under or over treated. Studies have shown that CA is present in the precancerous and preinvasive lesions of the breast. In addition, genes whose deregulation has been previously implicated in induction of CA such as Cyclin-d, Aurora-A, Nek2, and p53 are also deregulated in DCIS. Thus, there is tantalizing possibility that the organellar-level differences may exist between recurrent and nonrecurrent DCIS. To this end evaluating the role of CA to predict the risk of LR after lumpectomy (breast conservation surgery) is the primary goal of the study described in the third manuscript of this dissertation (Chapter 4).

1.3 Drawbacks of current quantitation methods of Centrosome amplification

Although the extent of CA in tumor samples can be readily quantified by using simple immunohistochemical methods that are clinically adaptable and cost-effective, the quantitative techniques currently used to measure CA suffer severe drawbacks. Most of the studies have considered the numerical amplification as a measure of centrosome amplification. Although some recent studies have highlighted the role of structural amplification and quantitated them using either volume of gamma-tubulin spots or centriolar length but were not able to show all this in the human clinical samples. Moreover, the clustered centrosomes have often been misquantified as

structurally amplified centrosomes. Furthermore, none of the studies have made a clear distinction regarding the contribution of structural and numerical amplification towards the progression of the disease in cancer. A rigorous statistical analysis of correlations between clinicopathologic factors (such as tumor grade, stage, outcome) and CA has not been performed yet. Thus, a true systematic quantitation technique which includes both structural and numerical amplification is urgently needed as a foundation for centrosome-based risk assessment in clinical tissue samples. In the study presented in the third manuscript (Chapter 4) of this dissertation, we have presented a novel methodology to quantitate both numerical and structural centrosomal aberrations in tumor samples. Our analytical pipeline allows robust interrogation of the ability of centrosomal overload to predict the risk of LR after lumpectomy.

1.4 Centrosome clustering and chromosomal instability

Presence of extra centrosomes leads to the formation of the multi-polar mitotic spindles and ultimately undergoes the mitotic catastrophe. In cancer cells, excess centrosomes cluster into two polar groups during mitosis, giving rise to pseudo-bipolar spindles which undergoes a transient multipolar stage. This multipolar intermediate favors the formation of merotelic attachment of individual kinetochores to more than one spindle pole. Such inappropriate attachments can cause missegregation of whole chromosomes and/or chromosomal breakage which gives rise to a lagging chromosome which may result in chromosome missegregation and aneuploidy. The quantity of microtubules involved in merotelic attachments dictates the behavior of the merotelically attached chromosome [20]. If the microtubules oriented on the wrong spindle pole are few the chromosome segregation proceeds without apparent impairment whereas if equal number of microtubules are attached to the right and wrong spindle poles, the chromosome lags during anaphase due to strong,

opposite poleward forces, but ultimately it tends to segregate to the right cell as a micronucleus. Thus, inappropriate attachments cause missegregation of whole chromosomes and/or chromosomal breakage which gives rise to a lagging chromosome and these chromosomes becomes trapped in and are either removed from the site or the cleavage furrow regresses resulting in the polyploidy. [21]. Furthermore, even if the lagging chromosome segregates to the right cell as a micronucleus, micronuclear DNA replicates aberrantly and asynchronously with primary nuclear DNA, resulting in rapid accrual of complex, clustered chromosome rearrangements [22-25]. Thus, if it is, equi-merotely it results in "all-at-once," catastrophic mutagenesis, which permits rapid karyotype evolution and if many microtubules are attached to the wrong pole (multi-merotely) [20], results in aneuploidy. Furthermore, clustered supernumerary centrosomes are inherited by progeny cells, leading to a perpetuation of chromosomal instability (CIN) in the cell lineage and can promote aggressive disease features [26].

Whether CIN promotes or inhibits tumorigenesis depends on the type of cell (some being inherently more tolerant of DNA damage and aneuploidy than others), its genetic background (e.g., pre-existing p53 mutations), the specific karyotype that is acquired (e.g., gain vs. loss of an oncogene), and the rate of CIN (with moderate levels tolerated better than extreme levels). It has been presented in multiple studies that CA induction in mice with the suppressed function of p53 leads to tumorigenesis. Single-cell genome sequencing has revealed that major aneuploid rearrangements (which can be caused by CA) occur early in breast tumor evolution, followed by incremental clonal diversification over time [27, 28]. Furthermore, studies have shown that TNBC the most heterogeneous subtype of breast cancer exhibits highest CA among all subtypes and CA is associated with poor overall survival in these patients. Intriguingly, high grade serous ovarian adenocarcinoma shares similar genomic features with triple negative breast cancer (TNBC) as per

reports from Cancer Genome Atlas (TCGA) Network analysis; in particular, the deregulated pathways characterizing HGSOC are very similar to those in TNBC [29]. Specifically, the most common mutations present in both kinds of tumors (HGSOC and TNBC) are of p53 and BRCA1/2. Given that the BRCA1 and BRCA2 tumor suppressor genes directly preserve genomic stability by regulating DNA repair, p53-mediated cell cycle checkpoint control as well as centrosome duplication cycle [30-32]. Mutations in these genes predisposes a cell for the development of CA leading to CIN. Furthermore, HGSOC tumors frequently overexpress cyclin E and Aurora-A, resulting in aberrant activation of the centrosome duplication cycle that induces centrosome amplification (CA), [33-35]. If CA is more extensive in HGSOC, it stands to reason that their cells may rely more staunchly on clustering molecules, such as KIFC1, for survival; thus, clustering molecules may be particularly valuable prognostic biomarkers and predictors of response to declustering drugs in HGSOC patients. Evaluation of KIFC1 as a prognostic biomarker in HGSOC is the goal of the study described in the fourth manuscript in this dissertation (Chapter 5).

1.5 KIFC1 the centrosome clustering protein is a cancer cell-specific target

KIFC1, also known as HSET, is a nonessential kinesin motor protein, that plays a crucial role in centrosome clustering in cancer cells [36, 37]. Knockdown of KIFC1 was shown to induce multipolar spindle defects and cell death in mitotic cancer cell lines containing extra centrosomes like MDA-MB 231[37] whereas it had no effect on cell division in a variety of control cell lines like BJ fibroblasts, which virtually exhibits no CA, mouse NIH-3T3 fibroblast sand human breast MCF-7, which exhibit only low level of CA [37]. Studies have shown that KIFC1 is elevated in several cancer types [38-41], including, breast, ovarian and colon cancer [42]. Thus, in cancer cells, the role of KIFC1 becomes indispensable due to the presence of supernumerary centrosomes.

This differential dependence of cancer cells on KIFC1 for viability makes KIFC1 a cancer-cell selective therapeutic target for "centrosome-rich" cancers, including those of the breast, prostate, bladder, colon, and brain. In addition, it has been shown in multiple studies that KIFC1 is overexpressed in chemoresistant (resistance against tubulin targeted drugs like docetaxel, taxane, and tamoxifen) breast and prostate cancers and that inhibition of KIFC1 have been seen to increase the sensitivity of cancer cells to taxanes. Thus, it is reasonable to suspect that KIFC1 might act as a therapeutic target for the chemoresistant cancers which exhibit high levels of CA. Numerical and structural CA has been reported in CRCS and researchers have reported CA and chromosomal instability in several CRC cell lines suggesting a link between CA and CIN in CRCs. In another study, it was reported that inactivation of p53 in CRC cells HCT116 lead to a 3.5-fold increase in tetraploidization. Loss or mutation of p53 gene is the most frequent genetic lesion in CRCs and is the reason behind resistance to 5-fluorouracil, the first-choice chemotherapy drug for CRC. Given that i) the p53 mutated CRCs exhibit higher levels of CA and ii) the traditional chemotherapies are not effective it becomes reasonable to state that centrosome declustering drugs might serve as the novel therapeutic target in this cancer. Thus, studying the role of KIFC1 as a therapeutic target and the mechanism as in how the expression of KIFC1 is regulated in p53 null/mutant CRCs is the main goal of the study presented in chapter 6 (manuscript 5) of this dissertation.

1.6 Griseofulvin, a novel KIFC1 inhibitor

Griseofulvin (GF) is an antifungal drug that is known to induce centrosome declustering. Multiple studies have shown that GF inhibits proliferation of the tumor cells by inducing multipolarity. The mechanism of action through which GF causes centrosome declustering is not very well understood. Recently it has been shown that GF works with the similar mechanism of action as other tubulin interactive agents where they act by binding a specific site of tubulin to inhibit the

formations of microtubules. The consequent suppression of microtubule dynamics leads to centrosome declustering, multipolar mitosis, and cell death. Inhibition of centrosome clustering by suppressing the kinesin KIFC1 selectively kills cancer cells containing extra centrosomes [37, 43]. Several KIFC1 inhibitors - AZ82 [44], CW069 [45, 46], and PJ34 [47, 48]- have been developed that induce multipolar mitosis, preferentially in cancer cells, in vitro, and in vivo. All these drugs work through different mechanisms and have shown high levels of toxicity in in vitro and in vivo models; therefore, they have not paved their way to clinical trials yet. GF [49], has attracted extensive interest as a potential anticancer agent due to its low toxicity and [50-53] greater efficiency in inhibiting proliferation of tumor cells. Furthermore, it has been shown aneuploid CRC cells display higher sensitivity to GF, delay aster formation and microtubular regrowth and display centrosome declustering. Understanding the mechanisms by which GF acts can pave the way for rational design and synthesis of more effective and cancer cell specific "kinder and gentler" chemotherapy, the secondary goal of the study described in the fifth manuscript in this dissertation (Chapter 6).

1.7 Docetaxel-induced polyploidization underlying drug resistance and disease relapse in cancer

Drug resistance against tubulin targeted drugs like Docetaxel, taxane and tamoxifen is a major issue in cancer therapeutics. Though the use of these drugs prolongs overall and progression-free survival in multiple malignancies their clinical utility is strictly limited due to disease relapse. Several lines of thought exist to explain the disease relapse after a modest increase in overall survival and one of the most intriguing mechanisms illustrated in various studies is the formation of giant multinucleated polyploid (MP) cells after therapeutic intervention with either taxane-based chemotherapy including docetaxel or DNA damaging agents. These polyploid cells can be

a result of DNA over-replication [54], abrogated mitotic checkpoint [55] or failed cytokinesis [56]. It was long assumed that these giant polyploid cells do not survive and die due to "mitotic catastrophe" subsequent to multipolar cell division. But, recent evidence indicated that while most polyploid cells succumb to cell death, a small percentage of them survive and produce viable progeny [57, 58]. The mechanism of generation of viable clones from these polyploid cells is poorly understood. Alos, the knowledge about the characteristics of these polyploid cells which protects them from chemotherapy and imparts aggressive cellular features is also not sufficient to design therapies which can help eliminate these giant cells following docetaxel treatment. Thus, understanding the mechanism of the generation of polyploid cells and their chemoresistance nature is the primary goal of the study presented in the sixth manuscript in the dissertation (Chapter 7).

1.8 References

1. Azimzadeh, J. and W.F. Marshall, *Building the centriole.* Curr Biol, 2010. **20**(18): p. R816-25.
2. Andersen, J.S., et al., *Proteomic characterization of the human centrosome by protein correlation profiling.* Nature, 2003. **426**(6966): p. 570-4.
3. Jakobsen, L., et al., *Novel asymmetrically localizing components of human centrosomes identified by complementary proteomics methods.* EMBO J, 2011. **30**(8): p. 1520-35.
4. Nigg, E.A., *Centrosome duplication: of rules and licenses.* Trends Cell Biol, 2007. **17**(5): p. 215-21.
5. Godinho, S.A. and D. Pellman, *Causes and consequences of centrosome abnormalities in cancer.* Philos Trans R Soc Lond B Biol Sci, 2014. **369**(1650).
6. Ogden, A., P.C. Rida, and R. Aneja, *Heading off with the herd: how cancer cells might maneuver supernumerary centrosomes for directional migration.* Cancer Metastasis Rev, 2013. **32**(1-2): p. 269-87.
7. Nigg, E.A., *Origins and consequences of centrosome aberrations in human cancers.* Int J Cancer, 2006. **119**(12): p. 2717-23.
8. Woodruff, J.B., O. Wueseke, and A.A. Hyman, *Pericentriolar material structure and dynamics.* Philosophical Transactions of the Royal Society B: Biological Sciences, 2014. **369**(1650): p. 20130459.
9. Antonczak, A.K., et al., *Opposing effects of pericentrin and microcephalin on the pericentriolar material regulate CHK1 activation in the DNA damage response.* Oncogene, 2015.

10. Conduit, P.T., et al., *Centrioles regulate centrosome size by controlling the rate of Cnn incorporation into the PCM.* Curr Biol, 2010. **20**(24): p. 2178-86.
11. Degenhardt, Y. and T. Lampkin, *Targeting Polo-like Kinase in Cancer Therapy.* Clinical Cancer Research, 2010. **16**(2): p. 384-389.
12. Zhang, Y. and T. Hunter, *Roles of Chk1 in cell biology and cancer therapy.* International Journal of Cancer, 2014. **134**(5): p. 1013-1023.
13. Mullee, L.I. and C.G. Morrison, *Centrosomes in the DNA damage response-the hub outside the centre.* Chromosome Res, 2015.
14. Fan, G., et al., *Loss of KLF14 triggers centrosome amplification and tumorigenesis.* Nat Commun, 2015. **6**: p. 8450.
15. Li, J., et al., *SAK, a new polo-like kinase, is transcriptionally repressed by p53 and induces apoptosis upon RNAi silencing.* Neoplasia, 2005. **7**(4): p. 312-23.
16. Duensing, S. and K. Münger, *Human papillomaviruses and centrosome duplication errors: modeling the origins of genomic instability.* Oncogene, 2002. **21**: p. 6241.
17. Lukasiewicz, K.B. and W.L. Lingle, *Aurora A, centrosome structure, and the centrosome cycle.* Environ Mol Mutagen, 2009. **50**(8): p. 602-19.
18. Zhou, H., et al., *Tumour amplified kinase STK15/BTAK induces centrosome amplification, aneuploidy and transformation.* Nat Genet, 1998. **20**(2): p. 189-93.
19. Katayama, H., et al., *Interaction and feedback regulation between STK15/BTAK/Aurora-A kinase and protein phosphatase 1 through mitotic cell division cycle.* J Biol Chem, 2001. **276**(49): p. 46219-24.
20. Thompson, S.L. and D.A. Compton, *Chromosome missegregation in human cells arises through specific types of kinetochore–microtubule attachment errors.* Proceedings of the National Academy of Sciences of the United States of America, 2011. **108**(44): p. 17974-17978.
21. Steigemann, P., et al., *Aurora B-Mediated Abscission Checkpoint Protects against Tetraploidization.* Cell. **136**(3): p. 473-484.
22. Zhang, C.Z., M.L. Leibowitz, and D. Pellman, *Chromothripsis and beyond: rapid genome evolution from complex chromosomal rearrangements.* Genes Dev, 2013. **27**(23): p. 2513-30.
23. Holland, A.J. and D.W. Cleveland, *Mechanisms and consequences of localized, complex chromosomal rearrangements in cancer and developmental diseases.* Nature medicine, 2012. **18**(11): p. 1630-1638.
24. Zhang, C.Z., et al., *Chromothripsis from DNA damage in micronuclei.* Nature, 2015. **522**(7555): p. 179-84.
25. Leibowitz, M.L., C.Z. Zhang, and D. Pellman, *Chromothripsis: A New Mechanism for Rapid Karyotype Evolution.* Annu Rev Genet, 2015. **49**: p. 183-211.
26. Funk, L.C., L.M. Zasadil, and B.A. Weaver, *Living in CIN: Mitotic Infidelity and Its Consequences for Tumor Promotion and Suppression.* Developmental Cell, 2016. **39**(6): p. 638-652.
27. Wang, Y., et al., *Clonal evolution in breast cancer revealed by single nucleus genome sequencing.* Nature, 2014. **512**(7513): p. 155-160.
28. Navin, N., et al., *Tumor Evolution Inferred by Single Cell Sequencing.* Nature, 2011. **472**(7341): p. 90-94.
29. *Comprehensive molecular portraits of human breast tumours.* Nature, 2012. **490**(7418): p. 61-70.

30. Scully, R., *Role of BRCA gene dysfunction in breast and ovarian cancer predisposition.* Breast Cancer Res, 2000. **2**(5): p. 324-30.
31. Liu, Y. and M. Kulesz-Martin, *p53 protein at the hub of cellular DNA damage response pathways through sequence-specific and non-sequence-specific DNA binding.* Carcinogenesis, 2001. **22**(6): p. 851-60.
32. Venkitaraman, A.R., *Cancer susceptibility and the functions of BRCA1 and BRCA2.* Cell, 2002. **108**(2): p. 171-82.
33. Pils, D., et al., *Cyclin E1 (CCNE1) as independent positive prognostic factor in advanced stage serous ovarian cancer patients - a study of the OVCAD consortium.* Eur J Cancer, 2014. **50**(1): p. 99-110.
34. Lassus, H., et al., *Aurora-A overexpression and aneuploidy predict poor outcome in serous ovarian carcinoma.* Gynecol Oncol, 2011. **120**(1): p. 11-7.
35. Landen, C.N., Jr., et al., *Overexpression of the centrosomal protein Aurora-A kinase is associated with poor prognosis in epithelial ovarian cancer patients.* Clin Cancer Res, 2007. **13**(14): p. 4098-104.
36. Kleylein-Sohn, J., et al., *Acentrosomal spindle organization renders cancer cells dependent on the kinesin HSET.* J Cell Sci, 2012. **125**(Pt 22): p. 5391-402.
37. Kwon, M., et al., *Mechanisms to suppress multipolar divisions in cancer cells with extra centrosomes.* Genes Dev, 2008. **22**(16): p. 2189-203.
38. Chan, J.Y., *A clinical overview of centrosome amplification in human cancers.* Int J Biol Sci, 2011. **7**(8): p. 1122-44.
39. Grinberg-Rashi, H., et al., *The expression of three genes in primary non-small cell lung cancer is associated with metastatic spread to the brain.* Clin Cancer Res, 2009. **15**(5): p. 1755-61.
40. Pannu, V., et al., *HSET overexpression fuels tumor progression via centrosome clustering-independent mechanisms in breast cancer patients.* Oncotarget, 2015. **6**(8): p. 6076-91.
41. Pawar, S., et al., *KIFCI, a novel putative prognostic biomarker for ovarian adenocarcinomas: delineating protein interaction networks and signaling circuitries.* J Ovarian Res, 2014. **7**: p. 53.
42. Rath, O. and F. Kozielski, *Kinesins and cancer.* Nat Rev Cancer, 2012. **12**(8): p. 527-39.
43. Fielding, A.B., et al., *A critical role of integrin-linked kinase, ch-TOG and TACC3 in centrosome clustering in cancer cells.* Oncogene, 2011. **30**(5): p. 521-34.
44. Wu, J., et al., *Discovery and mechanistic study of a small molecule inhibitor for motor protein KIFC1.* ACS Chem Biol, 2013. **8**(10): p. 2201-8.
45. Bhakta-Guha, D., et al., *Dis-organizing centrosomal clusters: specific cancer therapy for a generic spread?* Curr Med Chem, 2015. **22**(6): p. 685-94.
46. Watts, C.A., et al., *Design, synthesis, and biological evaluation of an allosteric inhibitor of HSET that targets cancer cells with supernumerary centrosomes.* Chem Biol, 2013. **20**(11): p. 1399-410.
47. Antolin, A.A., et al., *Identification of pim kinases as novel targets for PJ34 with confounding effects in PARP biology.* ACS Chem Biol, 2012. **7**(12): p. 1962-7.
48. Castiel, A., et al., *A phenanthrene derived PARP inhibitor is an extra-centrosomes de-clustering agent exclusively eradicating human cancer cells.* BMC Cancer, 2011. **11**: p. 412.

49. Rathinasamy, K., et al., *Griseofulvin stabilizes microtubule dynamics, activates p53 and inhibits the proliferation of MCF-7 cells synergistically with vinblastine.* BMC Cancer, 2010. **10**: p. 213.
50. Ho, Y.S., et al., *Griseofulvin potentiates antitumorigenesis effects of nocodazole through induction of apoptosis and G2/M cell cycle arrest in human colorectal cancer cells.* Int J Cancer, 2001. **91**(3): p. 393-401.
51. Panda, D., et al., *Kinetic suppression of microtubule dynamic instability by griseofulvin: implications for its possible use in the treatment of cancer.* Proc Natl Acad Sci U S A, 2005. **102**(28): p. 9878-83.
52. Rebacz, B., et al., *Identification of griseofulvin as an inhibitor of centrosomal clustering in a phenotype-based screen.* Cancer Res, 2007. **67**(13): p. 6342-50.
53. Singh, P., et al., *Microtubule assembly dynamics: an attractive target for anticancer drugs.* IUBMB Life, 2008. **60**(6): p. 368-75.
54. Nakayama, Y., et al., *Bleomycin-induced over-replication involves sustained inhibition of mitotic entry through the ATM/ATR pathway.* Exp Cell Res, 2009. **315**(15): p. 2515-28.
55. Erenpreisa, J., et al., *Endopolyploidy in irradiated p53-deficient tumour cell lines: persistence of cell division activity in giant cells expressing Aurora-B kinase.* Cell Biol Int, 2008. **32**(9): p. 1044-56.
56. Sagona, A.P. and H. Stenmark, *Cytokinesis and cancer.* FEBS Lett, 2010. **584**(12): p. 2652-61.
57. Coward, J. and A. Harding, *Size Does Matter: Why Polyploid Tumor Cells are Critical Drug Targets in the War on Cancer.* Front Oncol, 2014. **4**: p. 123.
58. Erenpreisa, J. and M.S. Cragg, *Cancer: a matter of life cycle?* Cell Biol Int, 2007. **31**(12): p. 1507-10.

2 AMPLIFIED CENTROSOMES AND MITOTIC INDEX DISPLAY POOR CONCORDANCE BETWEEN PATIENT TUMORS AND CULTURED CANCER CELLS

Parts of this chapter have been published verbatim in ***Scientific Reports 2017 Mar 8;7:43984*** *as* ***"Amplified centrosomes and mitotic index display poor concordance between patient tumors and cultured cancer cells."***

Authors listed on the paper and their contributions:

1. **Karuna Mittal**: First author of the paper- Conceived and designed the study, carried out major experiments of the study, analyzed and interpreted the data, and wrote the manuscript.
2. Da Hoon Choi: Carried out the immunoblot assays
3. Angela Ogden: Performed in silico data analysis
4. Shashi Donthamsetty: Helped with hypoxia experiments
5. Brian D. Melton: Carried out fluorescence imaging for hypoxia treated and control cells
6. Meenakshi. V. Gupta: Provided tissue samples
7. Vaishali Pannu: Helped in designing some experiments
8. Guilherme Cantuaria: Provided tissue samples
9. Sooryanarayana Varambally: Performed in silico data analysis
10. Michelle D. Reid: Provided tissue samples
11. Kristin Jonsdottir: Contributed microarray and associated clinical data
12. Emiel A. M. Janssen: Contributed microarray and associated clinical data
13. Mohammad A. Aleskandarany: Helped in scoring of immunohistochemical tissue staining
14. Ian O. Ellis: Critically revised the manuscript.
15. Emad A. Rakha: Critically revised the manuscript.
16. Padmashree C. G. Rida: Co-corresponding author of the study- Helped in designing the study and critically revised the manuscript
17. Ritu Aneja: Co-corresponding author of the study- Helped in designing the study and critically revised the manuscript

2.1 Abstract

Centrosome amplification (CA) and aberrant mitoses are considered beacons of malignancy. Cancer cell doubling times in patient tumors are longer than in cultures, but differences in CA between tumors and cultured cells are uncharacterized. We compare mitoses and CA in patient tumors, xenografts, and tumor cell lines. We find that mitoses are rare in-patient tumors compared with xenografts and cell lines. Contrastingly, CA is more extensive in-patient tumors and xenografts (~35-50% cells) than cell lines (~5-15%), although CA declines in patient-derived tumor cells over time. Intratumoral hypoxia may explain elevated CA in vivo because exposure of cultured cells to hypoxia or mimicking hypoxia pharmacologically or genetically increases CA, and that HIF-1α induces CA in tumor cells by transcriptionally regulating expression of centrosome associated protein PLK4. HIF1α and hypoxic gene signature expression correlate with CA and centrosomal gene signature expression in breast tumors. These results highlight the importance of utilizing low-passage-number patient-derived cell lines in studying CA to more faithfully recapitulate in vivo cellular phenotypes.

2.2 Introduction

Cancer has always been reckoned as a mass of abnormal cells growing rapidly in a deregulated manner. This basic rationale underlies the inception of chemotherapeutic strategies targeting mitosis and development of antimitotic drugs. Since cancer cells divide at a more rapid rate than normal cells, disruption of mitosis has been perceived as the most effective and selective therapeutic strategy against malignant cells. Although mitosis-targeting drugs, such as inhibitors of Aurora kinases, Polo-like kinases, and Kinesin-spindle protein, have been very successful in preclinical trials, their poor performance in the clinical setting has raised doubts about the relevance of this chemotherapeutic strategy.[1] Multiple studies affirm that the rationale

undergirding the development of mitosis-targeting drugs is flawed as, frequent mitosis is not a hallmark of human cancers, as previously postulated.[1, 2] In contrast with immortalized cell cultures and xenograft models, which are most frequently used to assess the efficacy of antimitotic drugs, human tumors tend to have very low mitotic rates (with the mean mitotic index in many tumor types being <1%).[2] Furthermore, the mean doubling time of a variety of human tumors is >100 days, much higher than that of tumors in pre-clinical models. Although recent cell culture studies have been highly informative, they bear limited conformity with events in vivo. Another important factor affecting the potential relevance of cell culture data is drug bioavailability. The drug concentration in the tumor microenvironment varies significantly in vivo, with drug concentrations rising, peaking, and falling as the drug circulates and then is removed from the body. In a study evaluating single-cell responses to the antimitotic drug paclitaxel in murine xenograft tumors as compared with cell culture, mitotic frequency was found to be lower in tumors than in cell culture.[3] Interestingly, the peak mitotic index in tumors exposed to paclitaxel was lower and the tumor cells survived longer after mitotic arrest, becoming multinucleated rather than dying directly from mitotic arrest, as opposed to cell cultures. Thus, the in vivo tumor microenvironment was found to be far less pro-apoptotic than the environment of cultured cells.

Another cancer cell-specific trait, CA, which refers to the presence of supernumerary or abnormally large centrosomes,[4, 5] occurs early in pre-cancerous and pre-invasive lesions and is linked to aggressiveness in several types of cancer. CA is believed to drive tumor progression by promoting chromosomal instability and the generation of aggressive tumor clones that are more capable of rapid metastasis. However, the presence of more than two centrosomes within a cell may result in the formation of multipolar spindles, leading to “mitotic catastrophe”[4] and eventual cell death. To avoid this, cancer cells cluster supernumerary centrosomes into two polar groups to

allow formation of a “pseudobipolar” mitotic spindle, a phenomenon that leads to their ultimate survival.[4-8] Given that cancer cells rely heavily on centrosome clustering mechanisms for viability, putative centrosome declustering agents have emerged as promising anticancer drugs.[9-11] [12] Most studies of these drugs rely on cancer cell lines and tumor cell line xenograft models, yet it is unknown how faithfully they recapitulate the profound CA often observed in patient tumors or whether there is a potentially superior model.

Herein, we quantified the prevalence of mitoses and CA in patient tumors compared with tumor cell lines and tumor cell line xenografts. We report that CA, but not mitotic index, is found at high levels in patient tumors, suggesting that CA may be a more valuable chemotherapeutic target than mitosis. We also found that CA progressively declines, and mitotic index progressively increases in culture, suggesting differences exist between the in vivo and in vitro microenvironments that have important ramifications for experimental design. Most often, cells cultured in vitro are supplied with copious amounts of oxygen, perhaps to fulfill the metabolic requirement of the voraciously growing log-phase cancer cells. However, in solid tumors, the oxygen concentrations in many regions of the tumor may be severely inadequate resulting in a hypoxic tumor deprived of oxygen.[13] We report here that induction of hypoxia or mimicking hypoxic conditions induces CA in vitro via HIF-1α and that HIF-1α induces CA in tumor cells by transcriptionally regulating expression of centrosome associated protein PLK4. Moreover, HIF-1α expression was found to correlate with CA in breast tumors. Ultimately, our study emphasizes the limitations of traditional cell culture models for studying CA and highlights the importance of low-passage patient-derived cell lines as being more representative of the true clinical scenario.

2.3 Materials and methods

2.3.1 Clinical tissue samples

Formalin-fixed paraffin-embedded slides of breast, pancreatic and bladder cancer tissue were procured from Northside Hospital and Emory University Hospital, in Atlanta. The Institutional Review Board of Northside hospital and Emory University approved all aspects of the study. Fresh tumor samples (samples obtained by partial mastectomy pretreatment) were procured from West Georgia Hospital, Lagrange under approved protocols. Methods were carried out in accordance with approved guidelines and informed consent was obtained from all subjects. Descriptive statistics for patient and clinicopathologic characteristics are provided in Tables 2.3.1-3.

2.3.2 Established tumor cell lines

MDA-MB-231, MIA PaCa-2, T24, CFPAC, CAPAN1, HCT116-p53-/-, HCT116 p53WT, PC3 and DU145 cell lines were obtained from American type cell culture (ATCC) and were grown in standard conditions. Briefly, grown in *Dulbecco's Modified Eagle's medium (DMEM),* RPMI or Hyclones 5A medium as per instructions supplemented with 10% Hyclone fetal bovine serum (FBS) and 1% penicillin/streptomycin. Cells were maintained in humidified 5% CO_2 atmosphere at 37°C. Patient-derived tumor cell lines: Tumor cells were isolated from a TNBC patient tumor (partial mastectomy) obtained from West Georgia hospital. To isolate tumor cells for culture, the tumor tissue was first minced into small pieces and then was digested in a mixture of DMEM/F12 medium containing 2 mg/ml bovine serum albumin, 2 mg/ml collagenase type IV, and 2 mg/ml hyalurodinase at 37°C for 30-40 min with continuous agitation. After the tumor chunks were completely digested, cells were filtered through a 70 μm mesh, centrifuged at 2,000 rpm for 10

minutes, resuspended in fresh DMEM/F12 supplemented with 10% FBS and 1% penicillin, and plated in 10 mm culture dishes in humidified 5% CO_2 atmosphere at 37°C.

2.3.3 Tumor cell line xenografts

All animal experiments were performed in compliance with Institutional Animal Care and Use Committee guidelines. For implantation into nude mice, MBD-MB-231 cells were washed with PBS, digested with trypsin, resuspended in DMEM 1X containing 10% FBS, and pooled. After centrifugation, cells were resuspended in Matrigel (BD Biosciences Discovery Labware, Bedford, MA)-DMEM 1X (1:3) at a concentration of 1×10^6 cells/100 μL, 100 μL of which was subcutaneously implanted into the dorsa of 6-week-old female Bald*/nu* mice (Harlan Sprague-Dawley, Indianapolis, IN). Tumor volumes were monitored constantly for 6 weeks, and after that tumors were excised and fixed in 10% formalin, embedded in paraffin, sectioned at 5 μm, and immunolabeled for centrosomes (γ-tubulin) and mitotically-active cells (Ph3).

2.3.4 Lysate preparation and immunoblotting

Cells were cultured to ~80% confluence and protein lysates were prepared as described previously.[39] Briefly cells were scraped with 250ul of 1x lysis prepared from 10x cell lysis buffer (Cell Signaling). The 1x lysis buffer contained 1 mM b-glycerophosphate, 20 mM Tris–HCl (pH 7.5), 1 mM Na2EDTA, 1 mM Na3VO4, 150 mM NaCl, 1 mM EGTA, 2.5 mM Na4P2O7, 1ug/ml leupeptin, and 1 % Triton. 10% Protease inhibitor was added to prevent degradation of proteins. Cell lysates were fractionated using 10 % SDS-PAGE gel Fresh tissue sections were sonicated and lysates were then prepared using the same lysis buffer. Polyacrylamide gel electrophoresis was used to resolve the proteins, which were transferred onto polyvinylidene fluoride membranes (Millipore). The Pierce ECL chemiluminescence detection kit (Thermo Scientific) was used to visualize the immune-reactive bands. β-actin was used as loading control.

2.3.5 Immunohistofluoresence staining

Formalin-fixed paraffin-embedded tissue slides were deparaffinized followed by serial rehydration in ethanol baths (100%, 95%, 70% and 50%). Antigens were retrieved by heating in a pressure cooker in citrate buffer (pH 6.0) at psi 15 for 30 min. Blocking was performed by incubating the slides with the ultra-vision protein block (Life Sciences) for 30 min. Tissue samples were then incubated overnight with primary mouse antibody against γ-tubulin (Table X) at 1:1000 dilution) at 4°C, followed by washing 3X with PBS. The samples were then incubated with secondary antibody (Alexa-488 anti-mouse) at 1:2000 dilution for 2 h, at 37°C followed by washing 3X with PBS. Finally, coverslips were mounted with Prolong-Gold Antifade Reagent with DAPI (Invitrogen).

2.3.6 Immunohistochemical staining and scoring

Deparaffinization and antigen retrieval were performed as described as for immunohistofluoresence staining. Thereafter, the tissues were immunolabeled using antibody against Ph3 (dilution 1:1000) or HIF-1α (1:1000). Ph3-positive cells were counted in 10 randomly selected fields (~500 cells) to determine the percentage of mitotic cells. Enzymatic antibody detection was performed with the Universal LSAB + Kit/HRP (DAKO, CA, USA). HIF-1α staining intensity was scored as 0=none, 1=low, 2=moderate, or 3=high, and the percentage of positive cells (i.e., with 1+ staining intensity) from 10 randomly selected fields (~500 cells) was determined. The product of the staining intensity and the percent of positive cells (nuclei) constituted the WI.

2.3.7 Immunocytofluorescence staining

Cells were grown on glass coverslips, fixed with ice-cold methanol for 10 min, and then blocked with 2% bovine serum albumin/1XPBS/0.05% Triton X-100 at 37°C for 1 h. Coverslips were

incubated in primary antibodies against γ-tubulin and α-tubulin at 1:2000 dilution for 1 h at 37°C, washed with 2% bovine serum albumin/1XPBS for 10 min at room temperature, and then incubated in 1:2000 Alexa 488- or 555-conjugated secondary antibodies (Invitrogen; Carlsbad, CA). Cells were mounted with Prolong Gold Antifade Reagent with DAPI (Invitrogen).

2.3.8 Microscopy

Images of tissue samples were taken utilizing the Zeiss LSC 700 confocal microscope (Oberkochen, Germany) and were processed with Zen software (Oberkochen, Germany). Magnifications and more details on imaging is provided in individual sections.

2.3.9 Quantitation of centrosome amplification

Numbers and volumes of γ-tubulin foci were used as indicators of numerical and structural centrosome amplification, respectively. Since gamma-tubulin is present in both centrioles and the PCM, above-normal volumes of γ-tubulin foci represent the cumulative structural volume amplification of both PCM and centrioles. Centrosomal volumes were calculated using the 3D measurement module from the Zeiss imaging software. Average centrosomal volumes ranged between 0.22-0.76 μm^3 in normal breast, 0.20-0.56 μm^3 in normal pancreas, and 0.20-0.74 μm^3 in normal bladder tissue. The percentage of cells with >2 centrosomes as quantitated from 10 randomly selected fields (around 500 cells) in tumor areas pre-marked by a pathologist was determined for each tissue type as well as cell lines (Supplementary Figure. 2.7.1). CA was calculated as a percentage by adding the percent cells harboring more than two centrosomes and the percent cells harboring centrosomes with volume larger than 0.76 μm^3, 0.56 μm^3 and 0.74 μm^3 for breast, pancreatic and bladder tissues respectively. A more detailed description of the quantitation process along with a schematic is given in the supplementary materials and Supplementary Figure.1.

2.3.10 Induction of hypoxia and mimicking hypoxic conditions

Hypoxia chamber*:* Cells grown on glass coverslips were either placed in a hypoxic modulated incubator chamber (flushed with 1% O_2 gas mixture at 20 L/min for 7-10 minutes every 3-6 hrs) or a normoxic incubator. After 48 h, cells were trypsinized and lysates were prepared for immunoblotting assays. To pharmacologically induce hypoxia cells were treated with 100µm of Cocl2 for 24 hrs. Further to stabilize HIF-1 α in normoxic conditions cells were treated with 1mM DMOG (SIGMA) for 24 hrs and 5µM MG132 for 5 hrs. Glass coverslips having cells were fixed with ice cold methanol and staining was performed as described in cell staining section

2.3.11 HIF-1α overexpression

HIF-1α was genetically overexpressed by transfecting cells with GFP-tagged degradation resistant HIF -1α. HA-HIF-1α P402A/P564A-pcDNA3 was a generous gift from Dr. Willian Kaelin (Addgene plasmid # 18955).[40] Cells at a confluency of ~70% were transfected using Lipofectamine 2000 according to the manufacturer's instructions.

2.3.12 HIF-1α gene knock out

The gene knockout of HIF-1α was performed using CRISPR/Cas 9 method. Where in, guide RNAs to target the human HIF-1α gene was designed using the (http://tools.genome-engineering.org) source. Two individual sgRNAs were designed to target exon 1 of HIF-1α (sgRNA1, 5'CACCGTTTCTTGTCGTTCGCGCCGC3'; sgRNA2, 5'AAACGCGGCGCGAACGACAAGAAAC 3'). sgRNA-encoding oligonucleotides was cloned into pSpCas9-2A-GFP (PX458) (a generous gift from Feng Zhang (Addgene plasmid # 48138) (using standard procedures www.genome-engineering.org)[41]. Transfection of the MDA-MB 231 and MDA-MB 468 cells was performed as described under the section of HIF-1α OE. As a negative control for the transfection efficiency vector pSpCas9-2A-GFP was used. The

pSpCas9(BB)-2A-GFP plasmid was GFP tagged hence the sgRNA and Cas9 expressing cells were sorted using FACS. The sorted GFP positive cells were expanded and the knockout in these cells was verified by exposing these cells to hypoxia followed by immunoblotting for HIF-1α.

2.3.13 ChIP assay

Briefly, MDA-MB-231 and MDA-MB-468 cells were plated at a density of 2.5 x 106 and were cultured in hypoxic and normoxic conditions for 48 hrs. Following the hypoxic and normoxic treatment the cells were crosslinked with 1% formaldehyde; crosslinking was stopped by the addition of 0.125M glycine. Cells were lysed, and the nuclear fraction will be sonicated to shear the crosslinked DNA into an average of 500 bp of sheared DNA. Sonicated lysates were run on a 1% agarose gel to ensure proper fragment size. The sonicated lysates were pre-cleared with salmon-sperm coated agarose beads for an hour at 4o C, followed by washing and lysates were divided equally. Half of the lysate was Immunoprecipitated (IP) with 5µg of the HIF-1α antibody and another half of lysates was immunoprecipitated with control (IgG) antibody (function as nonspecific binding control) and 1% of the lysate was used as input. IP samples were isolated by Protein A/salmon sperm beads and were washed in increasing salt concentration buffers (low salt, high salt, LiCl and 1X TE buffers) followed by elution of DNA and reversal of crosslinks (overnight with 5M NaCl at 65˚C followed by treatment with proteinase K at 45˚C). IP'd DNA were isolated using phenol: chloroform: isopropanol mix (Invitrogen). Following extraction, qRT-PCR amplification was performed on the immunoprecipitated DNA and the total input DNA. Primers were designed to amplify the region of the PLK4 gene that contained the full promoter activity as well as the HIF-1α -responsive regions. The values obtained in the qPCR were normalized to the total amount of DNA put into the reaction (percent input will be used as internal/ positive control).

2.3.14 PLK4 and VEGF reporter plasmid construction

Genomic DNA will be isolated from the HEK293 (Human Kidney epithelial cells) to serve as template for the PCR amplification of 1Kb promoter of human PLK4 gene containing HREs. After PCR cleanup the Promoter was cloned into the pGL4.51 expression vector (which has a luciferase reporter, cytomegalovirus promoter, and ampicillin resistance gene) (Promega) using standard subcloning procedure. MAX Efficiency DH5α competent E. coli was transformed with the vector using heat shock followed by plating on LB agar with 50 µg/ml ampicillin for selection of transformed clones. The plasmid DNA from individual colonies obtained was purified using a commercial spin column. Sequencing was performed to confirm the clones containing PLK4 insert with the correct promoter sequence cloned in the proper orientation, which was then be used for transfections. Similarly, VEGF reporter plasmid was constructed.

2.3.15 Dual luciferase assay

For PLK4 reporter assays, cells were transfected with 500 ng of PLK4 reporter plasmids with 500 ng pRL-TK plasmids. As a positive control another culture of cells was transfected with VEGF reporter plasmids with the pRL- TK plasmid. Lipofectamine 2000 (Invitrogen) was used as a transfection reagent. For each transfection, plasmids were premixed with the transfection reagent. Twenty-four hours after transfection, the cells were transferred to a hypoxia chamber (1% O2) or maintained in normoxia (20% O2). After 48 hours, the cells were harvested, and a Dual Luciferase reporter assay system (Promega) was used for sequential measurements of firefly and Renilla luciferase activities). Firefly luciferase activity was normalized to the Renilla luciferase activity. Each sample was analyzed in quadruplicates, and each transfection was repeated three times. Quantification of luciferase activities and calculation of relative ratios was carried out using a luminometer (TD-20/20; Turner Designs, Sunnyvale, CA, USA).

2.3.16 Statistical analyses

Unless otherwise stated in the methods and results sections, statistical analyses were performed using two-tailed Student's t-tests. The criterion for statistical significance for all analyses was $p<0.05$. Survival analysis (simple Cox model) was performed using SPSS Statistics version 21(IBM).

2.4 Results

2.4.1 Mitotic index is lower in-patient tumors than tumor cell lines and xenografts

To corroborate the view that tumor cells in patients' bodies are not as mitotically active as cancer cells in vitro, we first compared the mitotic indices of patient tumors and established tumor cell lines from different tissue types, including breast, pancreas and bladder. To this end, we quantitated phosphohistone H3 (Ph3)-positive (i.e., mitotic) cells microscopically in 20 paraffin-embedded patient tumor samples (surgical resection) for each cancer type as well as their representative established tumor cell lines. In addition, breast tumor cell line xenografts were analyzed. Descriptive statistics regarding patient and clinicopathologic characteristics for tumor samples utilized are given in Tables 2.4.1, 2.4.2 and 2.3.3. Mitotic indices were approximately 7-fold, 3-fold, and 8-fold higher in MDA-MB-231 breast cancer cells, MIA PaCa-2 pancreatic cancer cells, and T24 bladder cancer cells compared with patient tumors of the respective cancer types. By contrast, mitotic indices were similar between MDA-MB-231 xenografts and cell cultures (Figure. 2.4.1A, B). These studies suggest that established tumor cell lines, whether in cultures or xenografted in nude mice, display higher mitotic indices than patient tumors**.**

Table 2.4.1 Descriptive statistics for patient and clinicopathologic characteristics in the analysis of centrosome amplification and mitotic index in breast tumors.

Variable	Level	Number	Percentage

Race	AA	4	20
	EA	16	80
Gender	Male	0	0
	Female	20	100
Grade	1	9	45
	2	5	25
	3	6	30
Stage	I	10	50
	II	7	35
	III	1	5
	IV	2	10
ER/PR Expression	ER-/PR-	8	40
	ER-/PR+	1	5
	ER+/PR+	11	55
CA (%)	Low (<10%)	0	0
	Moderate (10-40%)	7	35
	High (>40%)	13	65
Mitotic Index	<1	8	40
	1~6	12	60

ER: Estrogen Receptor; PR: Progesterone Receptor; CA: Centrosome Amplification; AA: African American; EA: European American

Table 2.4.2Descriptive statistics for patient and clinicopathologic characteristics in the analysis of centrosome amplification and mitotic index in bladder tumors.

Variable	Level	Number	Percentage
Race	AA	13	65
	EA	7	35
Grade	1	7	35
	2	0	0
	3	13	65

Status	Invasive	Non-invasive	7	35
		Invasive	13	65
	CA (%)	Low (<10%)	0	0
		Moderate (10-40%)	11	55
		High (>40%)	9	45
Index	Mitotic	<1	18	90
		1-6	2	10

CA: Centrosome Amplification; AA: African American; EA: European American

Table 2.4.3Descriptive statistics for patient and clinicopathologic characteristics in the analysis of centrosome amplification and mitotic index in pancreatic tumors.

Variable	Level	Number	Percentage
Race	AA	9	45
	EA	11	55
Gender	Male	11	55
	Female	9	45
Tumor size (cm)	≤2	3	15
	>2	17	85
Grade	Low	10	50
	High	10	50
PNI	Yes	17	85
	No	3	15
LVI	Yes	15	75
	No	5	25
Stage T	1	2	10
	2	2	10
	3	16	80
Stage N	1	15	75
	0	4	20
	Unknown	1	5
Stage M	Yes	19	95
	No	0	0
	Unknown	1	5

LN Positive	≤5	15	75
	>5	5	25
CA (%)	Low (<10%)	0	0
	Moderate (10-40%)	14	70
	High (>40%)	6	30
Mitotic Index (MI)	<1	5	25
	1-6	9	45
	>6	6	30

CA: Centrosome Amplification; AA: African American; EA: European American; PNI: Peri-Neural Invasion; LVI: Lympho-Vascular Invasion

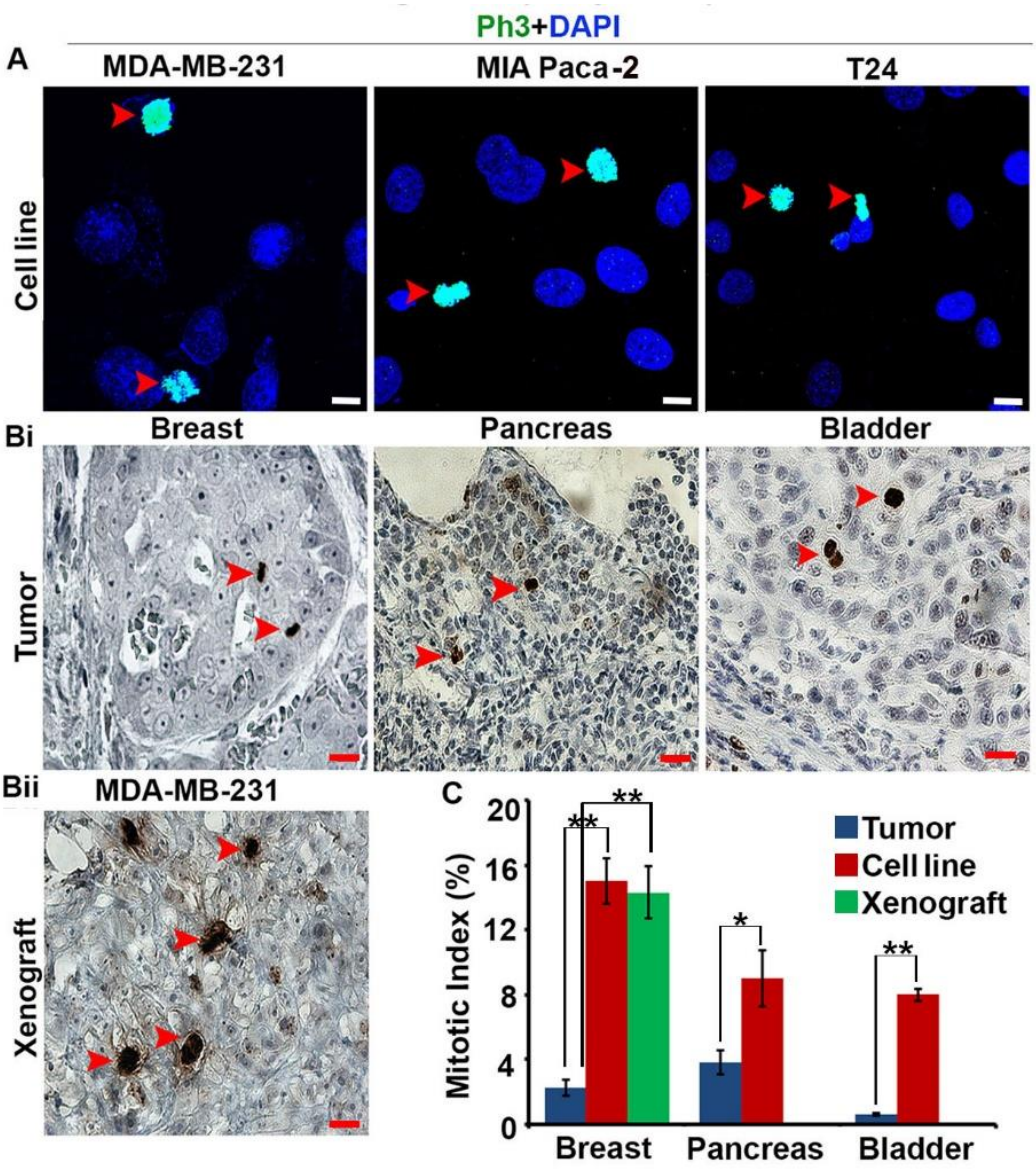

Figure 2.4.1 Human tumors display lower mitotic indices than tumor cell lines and xenografts.

A. Representative immunofluorescent confocal micrographs of tumor cell lines labeled for the mitotic marker phosphohistone H3 (Ph3). Red arrows: Ph3-positive cells. Scale bar (white), 5µm. Bi, Bii. Representative immunohistochemical micrographs of a patient breast tumor and an MDA-MB-231 xenograft labeled for Ph3. Red arrows: Ph3-positive cells. Scale bar (red), 20 µm C. Mitotic indices in patient tumors, tumor cell lines, and MDA-MB-231 xenografts. *$p<0.05$, **$p<0.01$.

2.4.2 CA is higher in-patient tumors and xenografts than tumor cell lines

Having established the low frequency of mitoses in various patient tumor types, we next compared the extent of CA between patient tumor samples and respective tumor cell lines for each cancer type. Breast tumor cell line xenografts were also analyzed. To accomplish this, we microscopically visualized centrosomes in 20 cases for each tissue type along with the specific cell lines. Centrosomes were immunofluorescently stained with anti-gamma tubulin antibody and co-stained with DAPI. Basically, CA can be of two types- numerical and structural. Numerical amplification can arise from several processes but the main mechanism underlying this phenotype is deregulation of the centrosome duplication cycle, which leads to centriole overduplication and formation of supernumerary centrosomes. Another cause of numerical amplification is failure of cytokinesis, owing to which polyploid cells with supernumerary centrosomes are generated. On occasion, numerical amplification arises from fragmentation of the pericentriolar matrix.[14]Similarly several factors account for structural defects which includes accumulation of excessive PCM around the centrioles (likely due to deregulated expression of genes coding for centrosomal components or altered posttranslational modifications), resulting in centrosomes that appear altered in size[15]. Another possible reason for structural aberration can be tight clustering of centrosomes, which thus cannot be individually distinguished. Third possible reason for this can be structural defects in centrioles; this is a completely unexplored area because the size of normal centriole is very small and requires very sophisticated microscopy techniques especially for tumor samples[4].

In light of the numerous challenges mentioned above, we used the volumes of the gamma-tubulin foci as indicators of structural centrosome aberration/amplification. While pancreatic, bladder, and breast tumors exhibited 35%, 36%, and 50% CA, respectively, their corresponding

cultured cell lines exhibited 15%, 10% and 23% CA, respectively (Figure. 2.4.2 A, B). Centrosome clustering was extensive among patient tumors with CA (see inset, Figure. 2.4.2 Ai). Next, we determined whether CA in the MDA-MB-231 cell lines persists following subcutaneous implantation into nude mice. Remarkably, CA in tumor xenografts excised at the end of six weeks was nearly double that of the native MDA-MB-231 cell line, similar to the level of CA found in patient breast tumors (Figure. 2.4.2 B). Taken together, these studies clearly demonstrate a high prevalence of CA in human tumors and MDA-MB-231 xenografts but not in cultured tumor cell lines and suggest that differences between the in vivo tumor microenvironment and culture plate are at least partly responsible for this observation.

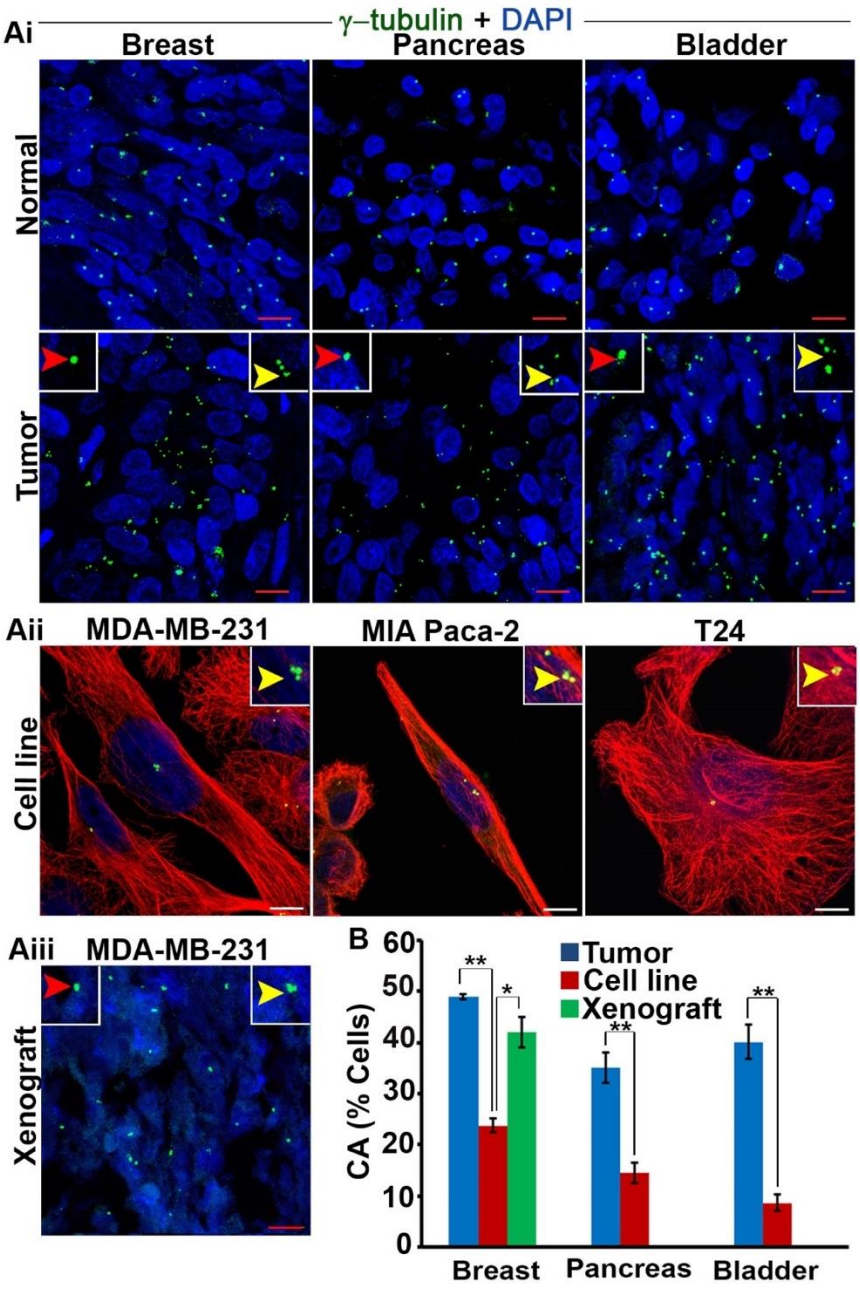

Figure 2.4.2 Human tumors have high centrosome amplification compared to cultured cells.

A) i. Bladder, pancreatic, and breast tumors along with normal adjacent tissue immunostained for centrosomes (γ-tubulin, green) and counterstained with DAPI (blue). Yellow arrows, numerical centrosome amplification; red arrows, structural centrosome amplification. Scale bar (red), 20 µm. Aii. Confocal micrographs of centrosome amplification and clustering in various tumor cell lines. Centrosomes and microtubules were immunolabeled for γ-tubulin (green) and α-tubulin (red), respectively, and DNA was counterstained with DAPI (blue). Scale bar (white) 5 µm. Aiii. Confocal micrographs of centrosome amplification and clustering in MDA-MB-231 xenografts.

Scale bar (red), 20 µm. B. Quantitation of centrosome amplification in human tumors, tumor cell lines, and tumor cell line xenografts. 500 cells were counted in each case. *p<0.05, **p<0.01.

2.4.3 CA and mitotic index in patient-derived tumor cells change differently with passaging

Our observations of the vast disparity in the degree of CA observed in patient tumors and cultured tumor cell lines cast doubt on the clinical relevance of tumor cell lines that are extensively utilized for studying CA. We thus reasoned that patient-derived tumor cell lines at a low passage number may mimic the cellular traits observed in tumor tissues and can emerge as a more useful representative model to conduct in vitro studies. We thus examined the degree of CA in patient-derived tumor cell lines by isolating tumor cells from a triple-negative breast cancer (TNBC) and quantitating CA with passaging. CA in the original tumor sample was ~45% (Figure. 2.4.3 A, Bi). Intriguingly, when tumor cells were dissociated from the tumor mass and cultured, CA progressively declined after passage 2. Passage 3 cells showed a significant 3-fold reduction in CA compared with passage 2 cells (Figure. 3Bi), and by passage 5 the degree of CA fell to ~10%, a level that and was sustained through passage 10 (Figure. 2.4.3A, B). We also observed extensive centrosome clustering in cells from passages 2 and 3 as well as in the original tumor tissue (Figure. 2.4.3A, inset). Taken together, our data underscore the higher concordance of centrosomal traits between low passage number (passage 2-3) patient-derived tumor cells and cells found in patient tumor tissues and xenografts.

In addition, we assessed the change in mitotic index in patient-derived tumor cells with passaging, which differed remarkably from our observations of CA with passaging. The mitotic index did not change significantly until passage 10, at which time it was ~3-fold higher than in the original tumor (Figure. 2.4.3Bii). Taken together, these experiments reveal striking differences in the pace and direction of changes in CA and mitotic index from intratumoral values in patient-

derived tumor cells in culture, suggesting that centrosome homeostasis and mitosis are differentially impacted by differences in the in vivo and in vitro microenvironments.

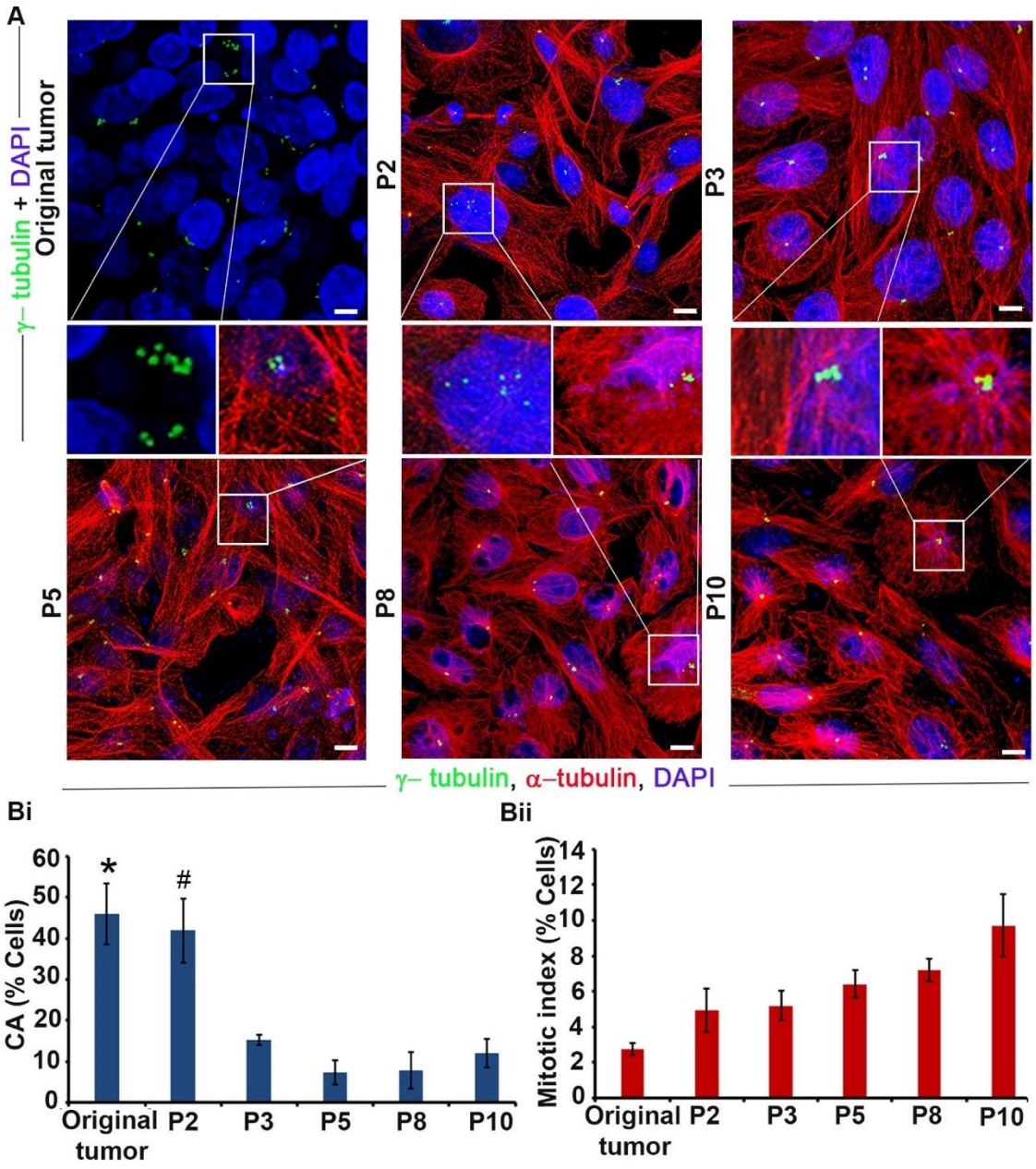

Figure 2.4.3 Centrosome amplification and mitotic index in patient tumors and patient-derived tumor cells with passaging.

A. Confocal micrographs of centrosome amplification and mitotic figures in the original patient tumor and cells isolated from the tumor and cultured through passage 10 (P10). Insets: centrosome amplification and clustering. Scale bar, 5 μm. Bi. Quantitation of centrosome amplification at

various passage numbers compared with the original tumor. * and # indicate that CA is significantly higher in the original tumor and P2, respectively, when compared with P3, P5, P8 and P10 ($p<0.05$). Bii. Mitotic index at various passage numbers compared with the original tumor.

2.4.4 Hypoxia enhances CA via HIF-1α in cultured cells

Given that a hypoxic microenvironment is one of the major potential differences between tumor cells in vitro and in vivo, we rationally hypothesized that hypoxia could underlie the divergence in CA observed in vivo, both in patient tumors and MDA-MB-231 xenografts (which have been shown to be hypoxic[16]), and established tumor cell lines grown in vitro, where oxygen is abundant. To test this hypothesis, we exposed MDA-MB-231 and MDA-MB-468 breast cancer cells to hypoxia for 48 h using a hypoxic chamber flushed with a 1% O_2 gas mixture. The presence of hypoxia was confirmed by upregulation of HIF-1α (Figure. 2.4.4B). As shown in Figure. 2.4.4, cells grown in hypoxic conditions for 48 h showed numerical CA, with both clustered and dispersed centrosomes, as well as structural CA, with enlarged γ-tubulin foci (representing individual centrosomes with excessive γ-tubulin accumulation named as PCM accumulation see representative images in Figure. 2.4.4A). Following hypoxia, upregulation of proteins whose overexpression drives CA (Cyclin E, Aurora A, and PLK4) and centrosome structural proteins (pericentrin and γ-tubulin) was observed (Figure. 4B, with additional data and description provided in Supplementary Figure. 2.4.4C), along with a significant ~1.5-fold increase in CA (Figure. 2.4.4C). Moreover, the average centrosomal volume in cells grown under hypoxic conditions was nearly double the volume in cells grown under normoxic conditions (Figure. 2.4.4D). These results suggest that the presence of hypoxia in patients' tumors could explain, at least in part, the vast differences in CA observed in vivo and in vitro.

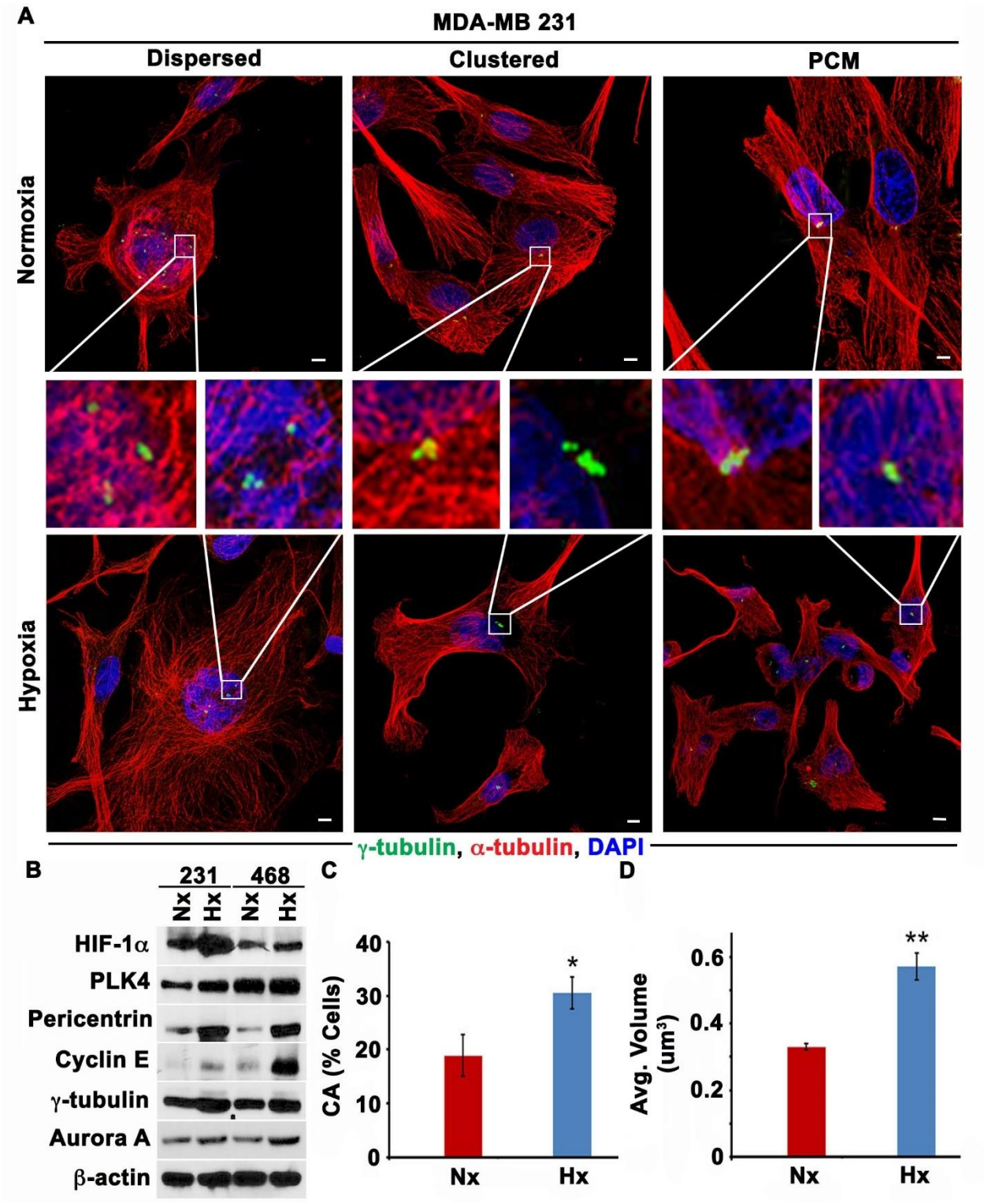

Figure 2.4.4 Hypoxia enhances centrosome amplification.
A. Confocal micrographs of centrosome amplification in MDA-MB-231 cells after 48 h of hypoxia (Hx) or normoxia (Nx). Both numerical centrosome amplification (with centrosomes dispersed or clustered) and structural centrosome amplification ("PCM," indicating abnormally large individual

γ-tubulin foci) were observed. Scale bar, 5 μm. B. Immunoblots of the hypoxia marker HIF1-α, proteins whose overexpression drives centrosome amplification (PLK4, Cyclin E, and Aurora A), and centrosome structural proteins (pericentrin and γ-tubulin) in MDA-MB-231 cells exposed to 24 and 48 h of hypoxia (Hx). C. Quantitation of centrosome amplification in MDA-MB-231 48 h after hypoxia. Scale bar, 5 μm. D. Average centrosomal volumes in normoxic (Hx) and hypoxic (Hx) MDA-MB-231 cells. *$p<0.05$, **$p<0.001$.

2.4.5 Mimicking hypoxia through pharmacologic and genetic methods enhances centrosome amplification

To bolster the findings of our hypoxia chamber experiments, we also mimicked hypoxic conditions in normoxia using pharmacologic and genetic methods in MDA-MB-231 and MDA-MB-468 cells. Hypoxia upregulates transcription factor hypoxia inducible factor 1 which undergoes proteasomal degradation in normoxic conditions. [17-19] So, to stabilize HIF-1α in normoxic conditions we treated the cells with $CoCl_2$, a HIF-1α-stabilizer,[20] which resulted in a ~1.5 fold increase in the CA compared with untreated cells (Fig 2.3.5A, E and Supplementary Figure. 2.7.2A[1]), similar to what we found in the hypoxia chamber experiments. To further characterize the observed centrosomal abnormalities, we co-immunolabeled γ-tubulin and centrin-2 (a centriolar marker) and performed the quantitation as described in Supplementary Figure. 2.7.3A-C. We found that γ-tubulin foci invariably overlapped with centrin-2 foci in both $CoCl_2$-treated and untreated cells, suggesting that the supernumerary γ-tubulin foci observed represent bona fide centrosomes and not mere fragments of pericentriolar material. Moreover, we failed to observe supernumerary centrin-2 foci in enlarged γ-tubulin foci, suggesting that the enlarged γ-tubulin foci represent structurally augmented centrosomes and not supernumerary centrosomes so tightly clustered as to be indistinguishable. The increased CA in $CoCl_2$-treated cells was substantiated by protein immunoblotting, which revealed increases in centrosome structural proteins as well as proteins whose overexpression drives centrosome amplification compared with untreated cells (Figure.

[1] All supplemental data, tables, and figures appear in Appendix A for this chapter

2.4.5B, with additional data and original blots provided in Supplementary Figure. 2.7.4). We next treated the cells with dimethyloxalylglycine (DMOG), which stabilizes HIF-1α in normoxic conditions[21], and MG132, which inhibits 26S proteasomal degradation of HIF-1α[22]. Treatment with either DMOG or MG132 treatment increased CA nearly ~1.5-fold (data shown in Supplementary Figure. 2.7.6C), in alignment with our other observations. We confirmed the increase in CA by protein immunoblotting (Supplementary Figure. 2.7.6B).

Next to confirm that the increase in CA under hypoxia was due to HIF-1α we overexpressed HIF-1α by transfecting cells cultured under normoxic conditions with GFP-tagged degradation-resistant HIF-1α. Transfected cells showed higher CA (~28%) under normoxic conditions than vector controls (~21%) (Supplementary Figure. 6A) and increase in CA was further confirmed with protein immunoblotting (Figure. 2.4.5C). We also knocked-out HIF-1α gene using CRISPR/CAS9 method (details in methods) and exposed these transfected cells to hypoxic conditions and found that levels of centrosomal proteins and proteins whose overexpression drives CA were lower than in vector controls (Figure. 2.4.4D and original blots shown in Supplementary Figure.2.7.5). In addition, cells transfected with vector control showed higher CA (~21%) (representative images Supplementary Figure. 2.7.6A) than HIF-1α knocked out cells, indicating that hypoxia induces CA via HIF-1α. Collectively, these experiments substantiate the paradigm that hypoxic conditions in the tumor microenvironment may account for differences in CA observed between patient tumors/ tumor cell line xenografts and established tumor cell lines.

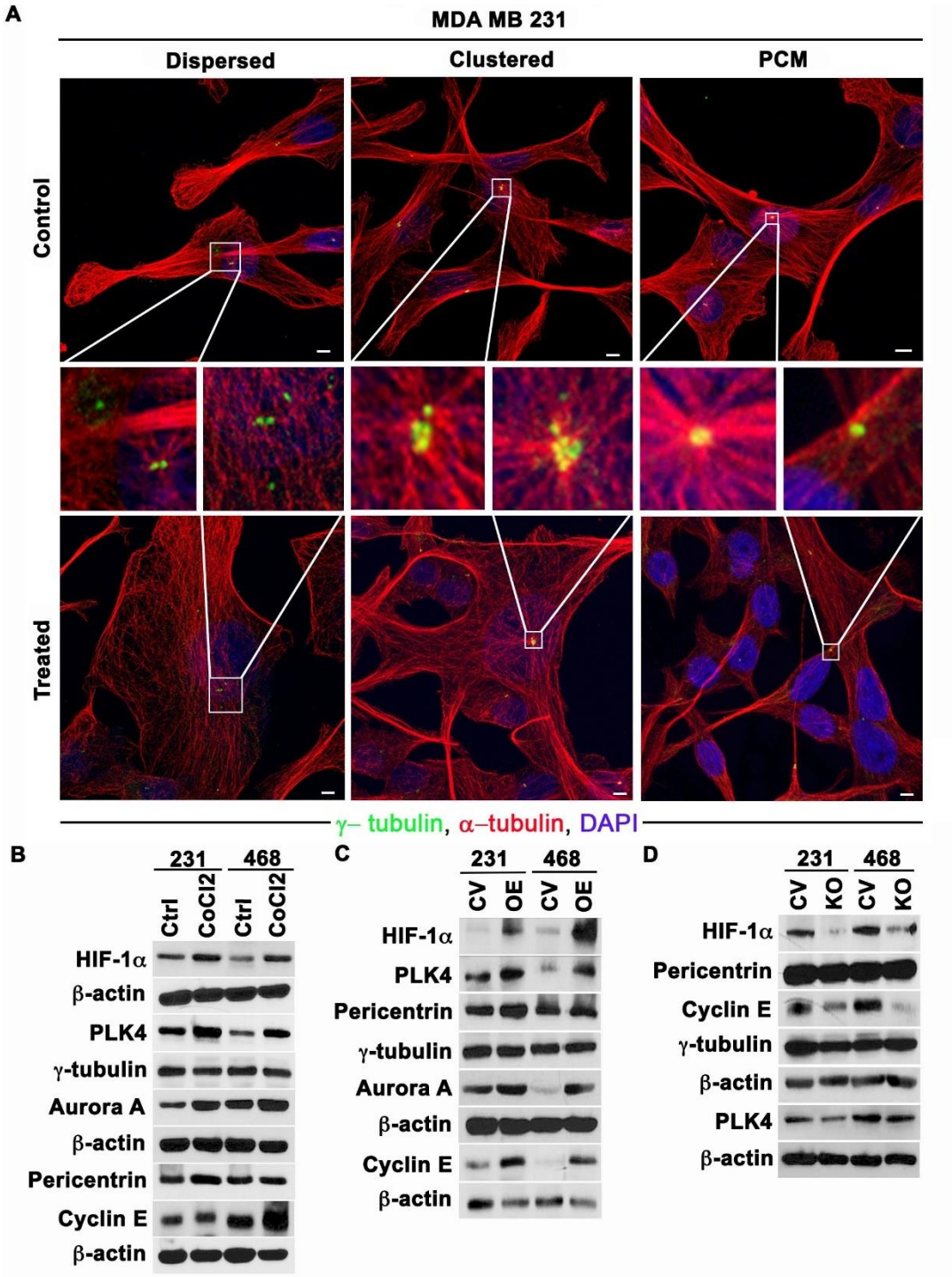

E

	Number of Cells Counted	Dispersed	Clustered	PCM	Number of Cells with Abnormal Centrosomes	% of CA
231 Control	200	5	28	8	41	20.5
231 Treated	200	2	40	19	61	30.5
468 Control	200	3	12	3	18	9
468 Treated	200	1	20	6	27	13.5

Figure 2.4.5 Mimicking hypoxia through pharmacologic and genetic methods enhances centrosome amplification.
A. Confocal micrographs of centrosome amplification (numerical, including dispersed and clustered configurations, and structural) in MDA-MB-231 cells in control conditions (top panel) and after 24 h $CoCl_2$ treatment (bottom panel). Scale bar, 5 μm. B. Immunoblots of HIF-1α and centrosomal proteins in control and $CoCl_2$-treated MDA-MB-231 and MDA-MB-468 cells. C. Immunoblots of HIF1α and centrosomal proteins in MDA-MB-231 and MDA-MB-468 transfected with empty vector or degradation-resistant HIF-1α. D. Immunoblots of HIF-1α and centrosomal proteins in MDA-MB-231 and MDA-MB-468 transfected with Cas9-sgRNA (HIF-1α) construct or control vector (pSpCas9-2A-GFP). E. Quantitation of numerical (including dispersed and clustered configurations) and structural ("PCM") centrosome amplification per microscopic examination for Cocl2 treated and untreated MDA-MB-231 and MDA-MB-468 cells.

2.4.6 Hypoxia is associated with CA in breast tumors

We next examined the relationship between HIF-1α levels and CA in breast cancer samples. To this end, we first immunohistochemically labeled 24 breast cancer and uninvolved adjacent normal tissue samples (samples obtained by partial mastectomy pretreatment) for HIF-1α and calculated weighted indices (WIs) for nuclear HIF-1α. Adjacent serial sections from the same tumors were also immunofluorescently labeled for γ-tubulin (Figure. 2.4.6A, B). CA was calculated as described in the Supplementary Figure. 2.7.1. Descriptive statistics of patient and clinicopathological characteristics, CA levels, and biomarker WIs are given in Table 2.4.4. HIF-1α WI was higher in the tumor areas when compared with adjacent normal tissue. In addition, a strong positive correlation between nuclear HIF-1α WI and CA was found in breast tumor samples (Spearman's rho p=0.722, **p<0.001).**

In addition, we found that higher nuclear HIF-1α was associated with worse overall survival (p=0.041; HR=1.03). We also compared the expression levels of HIF-1α and centrosome structural proteins (γ-tubulin and pericentrin) in fresh frozen clinical samples and uninvolved adjacent tissue from a pair of patients, one with TNBC and the other with non-TNBC.

Immunoblots showed higher expression of HIF1- α and centrosomal proteins in both tumor types in comparison with their normal adjacent tissues (Figure. 2.4.6). Finally, using public microarray datasets, we investigated whether centrosomal gene expression is enriched in breast tumors characterized by a hypoxic gene expression signature. We found that breast tumors with high expression of hypoxia-associated genes exhibited higher expression of centrosomal genes than breast tumors with low expression of hypoxia-associated genes regardless of mitotic index (which could otherwise confound analyses given that centrosomal genes are upregulated in mitosis) (Supplementary Figure. 2.7.7 and Supplementary Tables 2.7.1-5). Furthermore, a score based on the top 10 overexpressed centrosomal genes in breast tumors characterized by high levels of hypoxia-associated genes predicted worse distant metastasis-free survival in 94 node-negative breast cancer patients in multivariable analysis adjusting for various possible confounders (HR=3.39, p=0.011), whereas a hypoxia score previously shown to have prognostic ability in multiple cancers[23, 24] was non-significant in this full model (see Supplementary text and Supplementary Figure. 2.7.7 for more details). Together with our in vitro findings, these clinical data analyses support the hypothesis that hypoxia/HIF-1α drive CA in patient breast tumors and contribute to poor outcomes, such as distant metastasis**.**

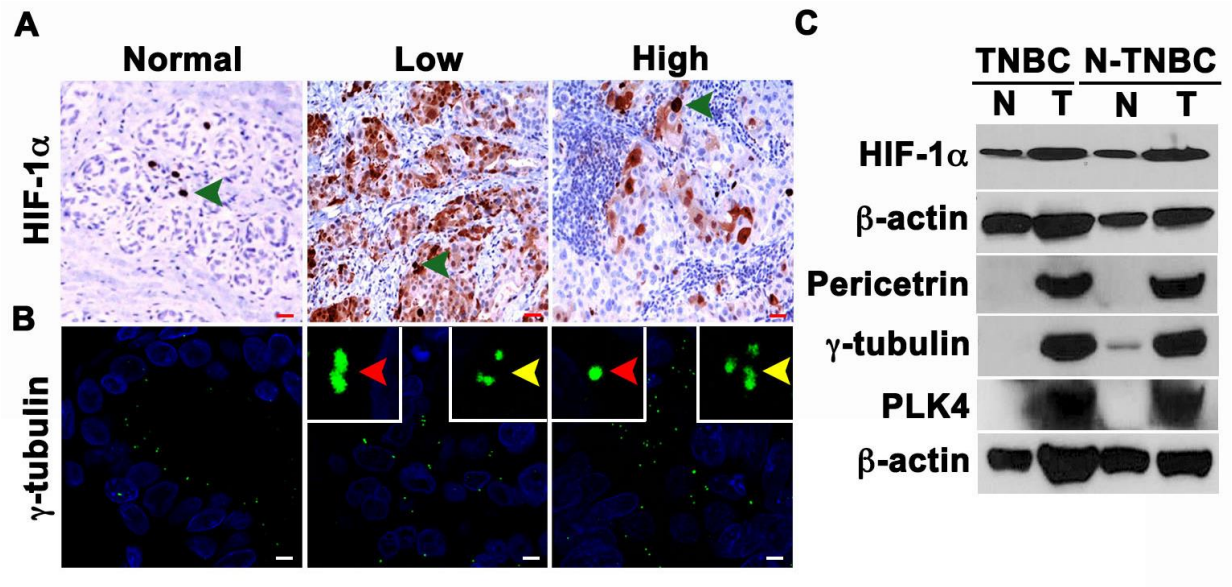

Figure 2.4.6 Higher HIF-1α expression is associated with higher CA.
A. Representative immunohistochemical micrographs of human breast tumors stained for HIF-1α. Green arrows indicate HIF-1α-positive cells. Scale bar (red), 20 μm. B. Breast tumors along with normal adjacent tissue were immunostained for γ-tubulin (green), and DAPI-stained (blue) to visualize centrosomes, and DNA. C. Immunoblots showing the levels of hypoxia and centrosomal markers in patient tumor samples (T) and their adjacent normal (N) tissues.

Table 2.4.4 Descriptive statistics for patient and clinicopathologic characteristics in the analysis of centrosome amplification and HIF-1α in breast tumors.

Variable	Level	Number	Percentage
Race	EA	14	58%
	AA	10	42%
Grade	1	1	4%
	2	3	13%
	3	20	83%
Stage	I	10	42%
	II	8	33%
	III	2	8%
	IV	1	4%
	N/A	2	8%

ER/PR/HER2 Expression	ER-/PR-/HER2-	4	2	100%
CA%	Low (<10%)	6	5	21%
	Moderate (10%-40%)		1	67%
	High (>40%)		3	13%

2.4.7 Hypoxia induces CA via HIF-1α in multiple cancer cells

Furthermore, we wanted to explore if the association of hypoxia with CA was true for all cancers (prostate, pancreatic and colorectal) or was specific for the breast cancer cells. Therefore, we mimicked hypoxic conditions in normoxia using pharmacologic and genetic methods in prostate cancer (PC3 and DU145), pancreatic cancer (CFPAC and CAPAN1) and colorectal cancer (HCT116 p53-/- and HCT116 p53WT) cells. We observed that the stabilization HIF-1α in normoxic conditions resulted in an increase in the CA in all cells compared with untreated cells (Fig 2.4.7) and increase in CA was further confirmed with immunoblotting. Next, we overexpressed HIF-1α by transfecting cells cultured under normoxic conditions with GFP-tagged degradation-resistant HIF-1α. All the transfected cells showed higher CA under normoxic conditions than the corresponding vector controls (Figure. 2.4.7 and 2.4.8B) and increase in CA was further confirmed with protein immunoblotting (Figure. 2.4.8A). Collectively, these experiments substantiate the paradigm that hypoxic conditions in the tumor microenvironment may enhance the CA observed in the tumor cells.

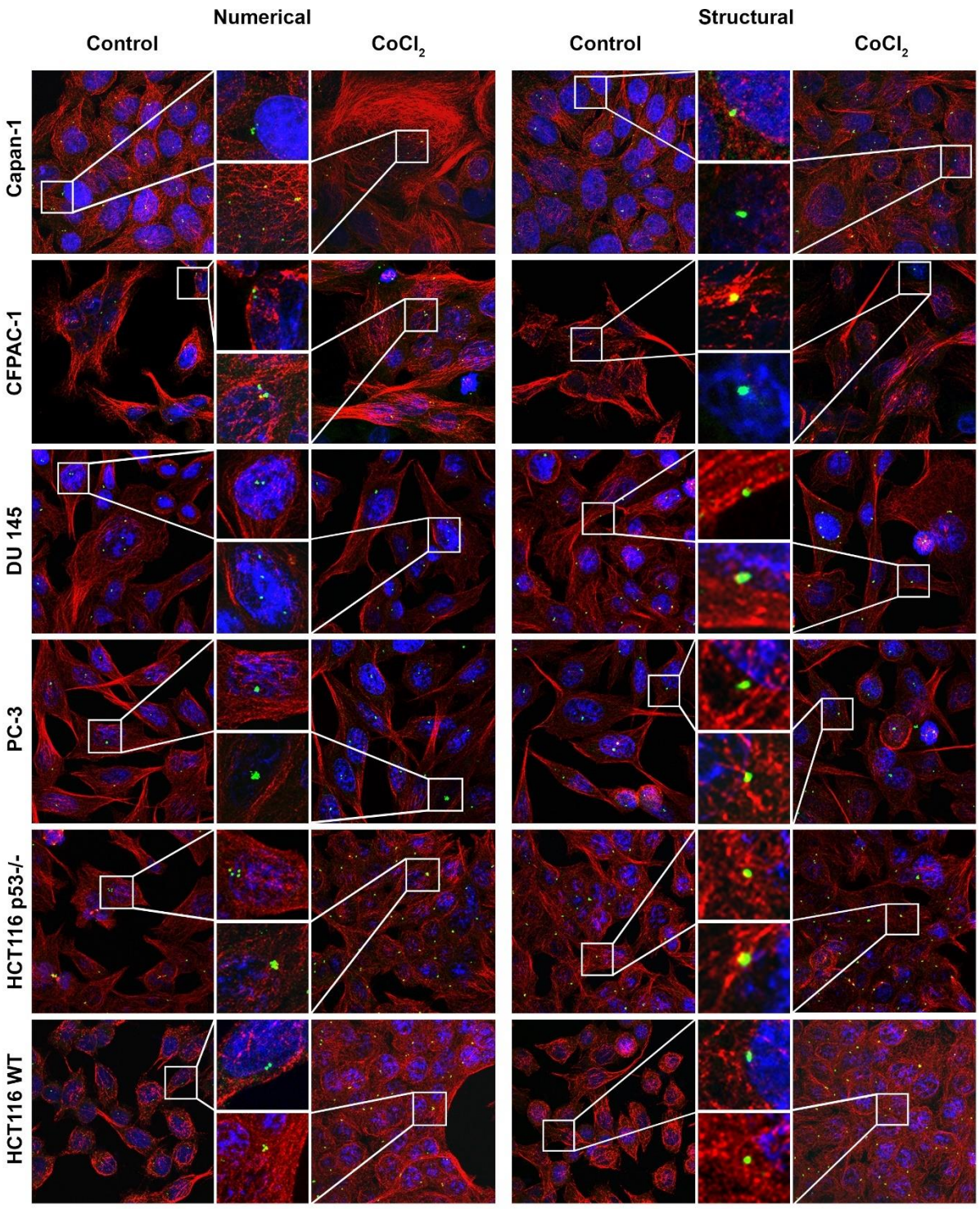

Figure 2.4.7 Mimicking hypoxia through pharmacologic and genetic methods enhances centrosome amplification-representative confocal micrographs.

Confocal micrographs of centrosome amplification (numerical and structural) in CAPAN-1, CFPAC, DU145, PC3, HCT116 p53-/- and HCT116 WT cells in control conditions and after 24 h $CoCl_2$ treatment. Scale bar, 5 μm.

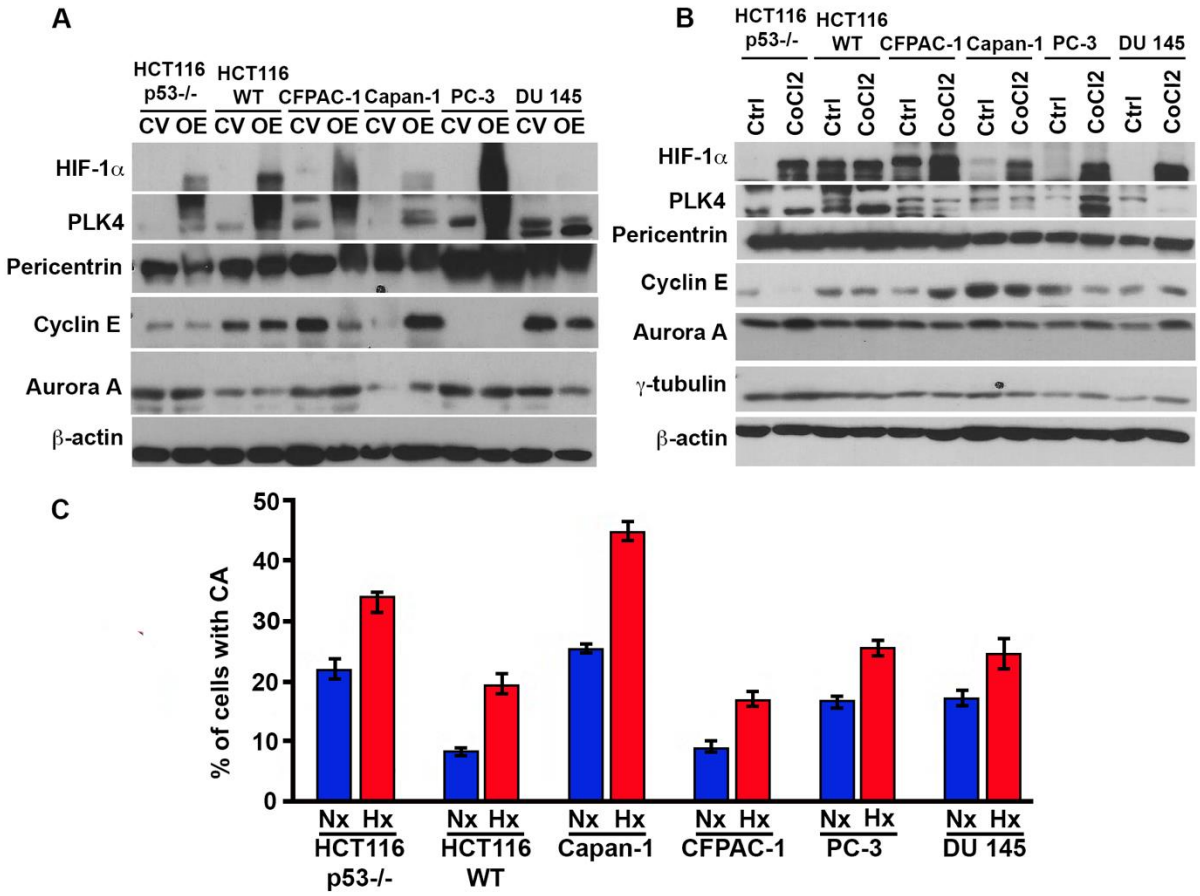

Figure 2.4.8 Mimicking hypoxia through pharmacologic and genetic methods enhances centrosome amplification- Immunoblots of HIF1α and centrosomal proteins and quantitation of CA

A)Immunoblots of HIF1α and centrosomal proteins in CAPAN-1, CFPAC, DU145, PC3, HCT116 p53-/- and HCT116 WT cells transfected with empty vector or degradation-resistant HIF-1α. B) Immunoblots of HIF-1α and centrosomal proteins in control and $CoCl_2$-treated CAPAN-1, CFPAC, DU145, PC3, HCT116 p53-/- and HCT116 WT cells. C) Bar graph representing the quantitation of numerical (including dispersed and clustered configurations) and structural ("PCM") centrosome amplification per microscopic examination for Cocl2 treated and untreated CAPAN-1, CFPAC, DU145, PC3, HCT116 p53-/- and HCT116 WT cells.

2.4.8 HIF-1α induces CA in tumor cells via transcriptionally regulating expression of PLK4

Given that the expression of centrosome-associated protein PLK4 increased with stabilization of HIF-1α and that the literature evidence support the hypoxia-mediated overexpression of PLK4, we suspected that HIF-1α might transcriptionally regulate expression of PLK4. To this end, first, we performed ChIP assay to confirm if the HIF1α binds to HIF-1α-responsive elements (HREs) that are present in the promoter region of PLK4 genes to regulate their transcription. Our results from Chip indicated HIF-1α interaction, with the HRE motif from genomic DNA of MDA-MB 231 and MDA-MB-468 cells under hypoxic conditions, was significantly ($p=0.04$) higher when compared with the cells cultured under normoxic conditions (Figure 2.4.9 A-D).

Next, we performed luciferase reporter assay to confirm the role of the HIF-1α in transcriptional regulation of PLK4. One representative cell line from each cancer type was co-transfected with Plk4 reporter plasmid and pRL- TK plasmid. As a positive control, another culture of cells was transfected with VEGF reporter plasmid AND pRL- TK plasmid. The transfected cells were exposed to hypoxia or normoxia and after 48hrs the relative firefly luciferase activity was measured (normalized to Renilla luciferase activity). Our results indicated that RLU activity for the cells cultured under hypoxia for both PLK4 and VEGF reporters was significantly higher ($p<0.05$) when compared to the cells cultured under normoxic conditions (Figure 2.4.9 E and F). There was ~ 3-fold increase in relative luciferase activity of all the cell lines for both Plk4 plasmid and VEGF. Thus, the results clearly suggest that HIF-1α transcriptionally regulate expression of Plk4.

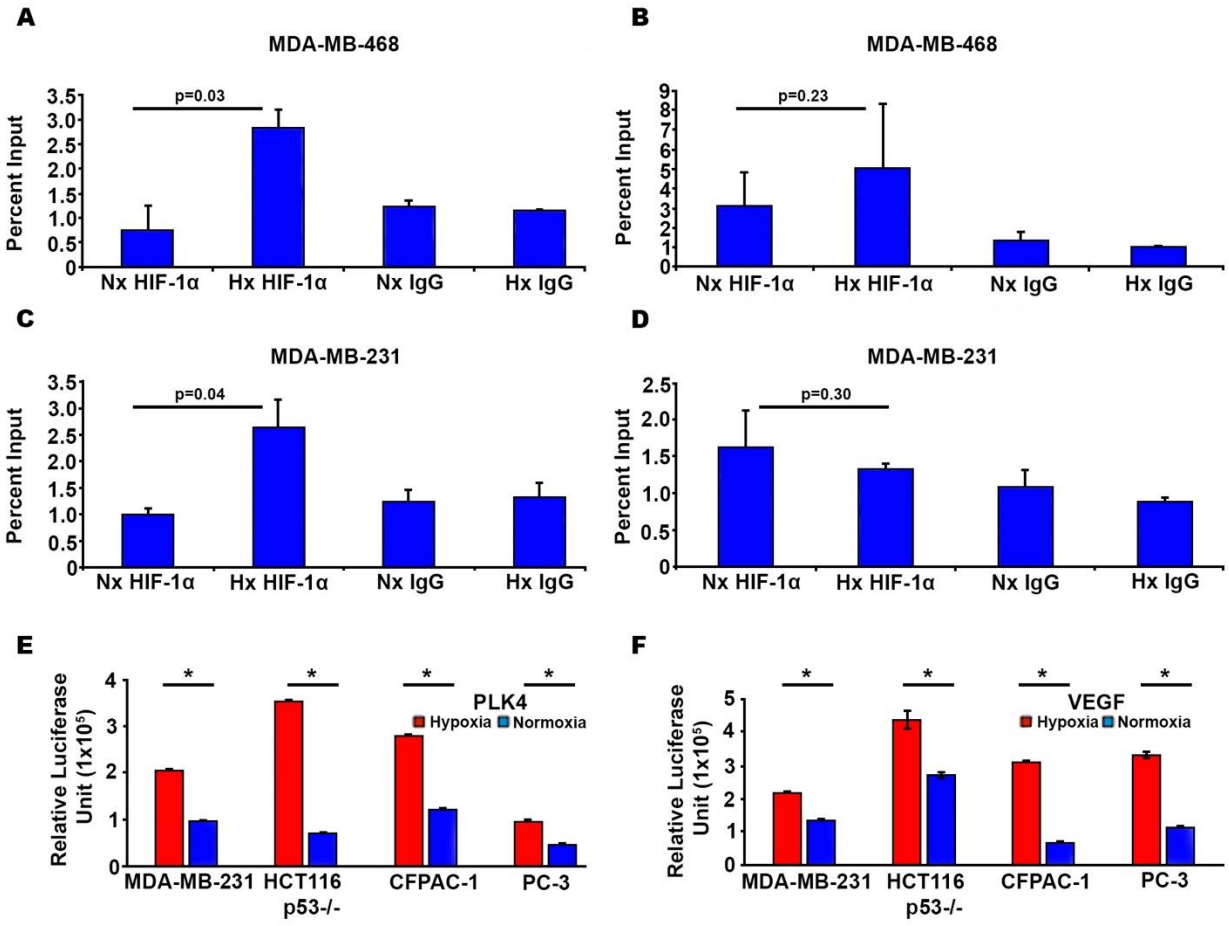

Figure 2.4.9 HIF-1α transcriptionally regulates expression of PLK4.
A) Bar graphs representing the binding of HIF-1α at the PLK4 promoter in MDA-MB-468 cells. B) Bar graphs representing the binding of HIF-1α at the GAPDH promoter in MDA-MB-468 cells. C) Bar graphs representing the binding of HIF-1α at the PLK4 promoter in MDA-MB-231 cells. D) Bar graphs representing the binding of HIF-1α at the PLK4 promoter in MDA-MB-231 cells. E) Bar graph representing the relative luciferase activity at PLK4 promoter in normoxic and hypoxic conditions for MDA-MB-231, HCT116 p53-/-, CFPAC and PC3 cells. F) Bar graph representing the relative luciferase activity at VEGF promoter in normoxic and hypoxic conditions for MDA-MB-231, HCT116 p53-/-, CFPAC and PC3 cells. * represents $p < 0.05$.

2.5 Discussion

While mitosis-targeting drugs have shown remarkable success in immortalized cell lines and tumor xenografts, they have failed to deliver their efficacy in human trials. Our current study provides a rigorous, systematic analysis of the relationship between a universal prognostic factor (mitotic

index) and a well-known cancer-cell specific trait and a potential prognosticator (CA) in a spectrum of model systems ranging from cultured cells, preclinical tumor xenografts, patient-derived primary cultures and patient tumors. Our data reconfirm that rapid cell division is not as predominant a trait of human tumors as it is of immortalized cell lines and tumor cell line xenografts. Since preclinical drug development experiments with antimitotic drugs are most often performed using immortalized cell lines or xenograft models, a large fraction of cells in these systems are vulnerable to antimitotic therapy. Therefore, it is not surprising that in human tumors where the fraction of the mitotically active cells is very low, only a small, insignificant fraction of cells are vulnerable to antimitotic drugs. In addition, many studies have shown that the median doubling times for many human tumors are on the order of months or even years, versus only hours or days for immortalized cell lines and tumor xenografts.[1, 25] The rapid doubling rate of tumors in preclinical models also explain why antimitotic agents prove very effective in these models but fail to show much efficacy against patient tumors. Thus, the lack of response of patient tumors to antimitotic drugs is due to the relative rarity of mitoses and slow doubling rate as highlighted by our study.

While human cancers including colon, breast, bladder, prostate, gliomas, and pancreas show profound CA,[26] we found immortalized cell lines are characterized by a much milder extent of this cell biological trait. The poor concordance between the extent of CA in tumors and cells in vitro can thus restrict the utility of cultured cells for studying CA mechanisms in vitro as well as for exploring the potential and promise of CA as a therapeutic target or prognostic biomarker. We reason that cancer cells seeking to adapt to and thrive in the tumor microenvironments encounter diverse selection pressures during tumor progression, such as

varying levels of oxygen. CA drives chromosomal instability[27] and thereby generates karyotypic diversity, a trait that is highly desirable for tumors seeking a survival advantage; beyond a certain point however, chromosome instability itself may become a selection pressure that jeopardizes the viability of cancer cells, which may not be able to maintain a chromosomal composition necessary for optimal cell growth. It is likely that in continuous cultures, the diminution of CA is due to cells having achieved a karyotypic composition wherein the persistence of amplified centrosomes could potentially have deleterious effects. When such a state is attained, CA may itself serve as a selection pressure, thus explaining the attenuation in the extent of amplification in cultured cells compared to human tumors.

Based on our findings, it seems possible that CA could be a superior target to mitosis, an infrequent event in patient tumors, since a third to half of cells in patient tumors exhibit CA (Figure. 2). Immortalized cell lines, on the other hand, display a much lower degree of CA. This discordance can in part be explained by the presence of hypoxia in the microenvironment of the tumor, which is usually absent in vitro. In addition, cells are usually cultured in vitro with excessive glucose and growth factors compared with the tumor microenvironment, which helps cultured cells to grow rapidly and thus be more sensitive to antimitotic drugs. Cancer cells dwell within a complex milieu of normal cells, blood vessels, endogenous small molecules, and secreted factors, which together comprise the tumor microenvironment. Hypoxia is one of the hallmarks of the tumor microenvironment, which is critically essential for cancer initiation, progression, metastasis, and drug resistance.[28, 29] Indeed a major detriment of using cell lines is that the vital interaction of tumor cells with their microenvironment is inherently omitted. Thus, when cancer cells are grown in culture dishes in a two-dimensional plane, the oxygen levels between cells stay relatively

equal, which is an improbable setting within a growing three-dimensional tumor in a patient's body. Moreover, the artificial, non-physiological environment in which cells in laboratory cultures are sustained fails to recapitulate the complex three-dimensional cellular interactions that exist in vivo. Another major inadequacy of cell culture is its inability to model the effects of physiologic responses to a tumor, such as the immune response and angiogenesis, two factors known to strongly influence tumor development.[30] Altogether, our study underscores the remarkable disparity in CA and mitosis between patient tumors and model systems, which must be carefully considered when designing experiments to study these phenomena.

Reports indicate that hypoxia, which is known to induce overexpression of HIF1-α, increases Aurora A/STK15 protein levels, which has been well documented to induce CA.[31-33] Our study demonstrates that cells grown under hypoxic conditions exhibit higher CA, Aurora A and PLK4 levels compared with cells grown under normoxic conditions. Although it is possible that hypoxia may favor the proliferation or survival of cancer cells with extra centrosomes and therefore favor the maintenance of CA in the population, our results support the notion that hypoxia induces CA perhaps via promoting overexpression of proteins such as PLK4. Our findings clearly suggest that HIF-1α directly regulates expression of PLK4 and increase in PLK4 levels in response to hypoxia results in higher CA in various cancer cells. Based on our studies, we speculate that hypoxia enhances the metastatic potential of cancer cells by inducing CA through upregulation of proteins such as Aurora A, PLK4, and Cyclin E, although a more comprehensive study is needed to investigate this tantalizing research question. Many studies have demonstrated that hypoxia is associated with an increased capacity for metastasis.[34, 35] We[36] and others[8, 37] have shown

that supernumerary centrosomes confer cytoskeletal advantages on the cells that harbor them; this could increase directional migration and invasiveness and thus enhance metastatic potential.

While these preclinical models (both established tumor cell lines and tumor cell line xenografts) are far from ideal, they have been widely used given that the rapid doubling times in such models permit a fast-tracked drug-development timeline. Nonetheless, this perceived advantage rather puts us at a loss when the doubling time itself is in the spotlight and the drug's activity relies on the preponderance of the mitotic population, which hinges on doubling rate. The brisk doubling times of the preclinical models explain why drugs targeting mitosis proved active in these models but were ineffective against patient tumors.[1, 2, 25] Our study highlights the importance of low-passage patient-derived cell line systems as being most representative of the clinical scenario and thus constituting an invaluable experimental model that could better guide drug development and clinical trial design.

Centrosome amplification is now well established as a hallmark of cancer. However, the presence of more than two centrosomes within a cell can be problematic as it may lead to formation of multipolar spindles leading to "mitotic catastrophe"[4] and cell death. To avoid multipolar spindle formation and subsequent mitotic catastrophe, cancer cells cluster supernumerary centrosomes into two polar groups to allow formation of a "pseudobipolar" mitotic spindle and produce viable daughter cells.[6, 38] Since our study clearly demonstrates that human tumors display a high frequency of CA, inhibition of centrosome clustering could have afflicted tumor cells to succumb to mitotic catastrophe and be eliminated. Given that cells with CA are suspected to have metastatic potential, antagonizing centrosome clustering could prove to be a strategy to suppress metastasis. Recently, many drugs have been shown to have centrosome declustering,

including griseofulvin, noscapine and several of its derivatives (e.g., bromonoscapine and reduced bromonoscapine), the PARP inhibitor PJ-34, and HSET inhibitors like AZ82 and CW069.[9-12] To discern meaningful activity of these drugs before they are tested in clinical trials as potential centrosome declustering dugs, it is imperative that we consider the shortcomings of our existent cell line models and rather develop robust and relevant preclinical models that mimic cellular traits observed in patient tumors. Our study clearly shows that established tumor cell lines exhibit lower CA than patient tumors and thus may be inferior model systems for testing centrosome targeted drugs than early-passage patient-derived tumor cell lines, which exhibit similar CA to patient tumors.

Undoubtedly the incongruity in CA between patient tumors and established tumor cell lines depreciates the importance of centrosomes as viable attractive targets and rather overstates mitosis as a target, perhaps resulting in the drug development process being blindsided. Our findings thus underscore the critical need to cautiously identify models that resemble patient tumors more closely in those characteristics/traits that are being targeted and are thus more clinically relevant. This is the first report to substantiate the previously unrecognized discordance associated with mitotic frequency and the extent of CA between various model systems. Our study emphasizes the limitations of in vitro cultures perhaps owing to genomic convergence upon continuous passaging and highlights the importance of low-passage patient-derived cell line system as most representative of the clinical scenario and thus a good preclinical model to study the therapeutic potential of centrosome targeting drugs compared to conventional continuous cell lines. Our study also underscores the significance of CA as a superior chemotherapeutic target and delineates the molecular mechanism whereby HIF-1α strongly upregulates PLK4 expression and drives rampant CA in these tumors. Therefore, our findings indicate that HIF-1α-mediated upregulation of PLK4 tumors drives its distinct tumor biology and establishes a causative link between two biological

phenomena – hypoxia and CA – that co-occur in many solid tumors. Based upon our findings, we suggest that low-passage patient-derived tumor cells and tumor xenografts could serve as good preclinical models for testing these drugs since the degree of CA found in these models closely resembles that in patient tumors. Taken together, our results suggest that CA could prove to be a better therapeutic target than mitosis owing to its higher incidence in human tumors, which perhaps occurs in low oxygen hypoxic tumor environment.

2.6 References

1. Komlodi-Pasztor, E., et al., *Mitosis is not a key target of microtubule agents in patient tumors.* Nat Rev Clin Oncol, 2011. **8**(4): p. 244-50.
2. Komlodi-Pasztor, E., D.L. Sackett, and A.T. Fojo, *Inhibitors targeting mitosis: tales of how great drugs against a promising target were brought down by a flawed rationale.* Clin Cancer Res, 2012. **18**(1): p. 51-63.
3. Orth, J.D., et al., *Analysis of mitosis and antimitotic drug responses in tumors by in vivo microscopy and single-cell pharmacodynamics.* Cancer Res, 2011. **71**(13): p. 4608-16.
4. Godinho, S.A. and D. Pellman, *Causes and consequences of centrosome abnormalities in cancer.* Philos Trans R Soc Lond B Biol Sci, 2014. **369**(1650).
5. Ogden, A., P.C. Rida, and R. Aneja, *Heading off with the herd: how cancer cells might maneuver supernumerary centrosomes for directional migration.* Cancer Metastasis Rev, 2013. **32**(1-2): p. 269-87.
6. Ganem, N.J., S.A. Godinho, and D. Pellman, *A mechanism linking extra centrosomes to chromosomal instability.* Nature, 2009. **460**(7252): p. 278-82.
7. Godinho, S.A., M. Kwon, and D. Pellman, *Centrosomes and cancer: how cancer cells divide with too many centrosomes.* Cancer Metastasis Rev, 2009. **28**(1-2): p. 85-98.
8. Kwon, M., et al., *Mechanisms to suppress multipolar divisions in cancer cells with extra centrosomes.* Genes Dev, 2008. **22**(16): p. 2189-203.
9. Castiel, A., et al., *A phenanthrene derived PARP inhibitor is an extra-centrosomes de-clustering agent exclusively eradicating human cancer cells.* BMC Cancer, 2011. **11**: p. 412.
10. Raab, M.S., et al., *GF-15, a novel inhibitor of centrosomal clustering, suppresses tumor cell growth in vitro and in vivo.* Cancer Res, 2012. **72**(20): p. 5374-85.
11. Watts, C.A., et al., *Design, synthesis, and biological evaluation of an allosteric inhibitor of HSET that targets cancer cells with supernumerary centrosomes.* Chem Biol, 2013. **20**(11): p. 1399-410.
12. Wu, J., et al., *Discovery and mechanistic study of a small molecule inhibitor for motor protein KIFC1.* ACS Chem Biol, 2013. **8**(10): p. 2201-8.
13. Vaupel, P. and L. Harrison, *Tumor hypoxia: causative factors, compensatory mechanisms, and cellular response.* Oncologist, 2004. **9 Suppl 5**: p. 4-9.
14. Chan, J.Y., *A clinical overview of centrosome amplification in human cancers.* Int J Biol Sci, 2011. **7**(8): p. 1122-44.

15. Nigg, E.A., *Origins and consequences of centrosome aberrations in human cancers.* Int J Cancer, 2006. **119**(12): p. 2717-23.
16. Semenza, G.L., *The hypoxic tumor microenvironment: A driving force for breast cancer progression.* Biochim Biophys Acta, 2016. **1863**(3): p. 382-91.
17. Generali, D., et al., *Hypoxia-inducible factor-1alpha expression predicts a poor response to primary chemoendocrine therapy and disease-free survival in primary human breast cancer.* Clin Cancer Res, 2006. **12**(15): p. 4562-8.
18. Bao, B., et al., *The biological kinship of hypoxia with CSC and EMT and their relationship with deregulated expression of miRNAs and tumor aggressiveness.* Biochim Biophys Acta, 2012. **1826**(2): p. 272-96.
19. Liu, Z.J., G.L. Semenza, and H.F. Zhang, *Hypoxia-inducible factor 1 and breast cancer metastasis.* J Zhejiang Univ Sci B, 2015. **16**(1): p. 32-43.
20. Yuan, Y., et al., *Cobalt inhibits the interaction between hypoxia-inducible factor-alpha and von Hippel-Lindau protein by direct binding to hypoxia-inducible factor-alpha.* J Biol Chem, 2003. **278**(18): p. 15911-6.
21. Botusan, I.R., et al., *Stabilization of HIF-1alpha is critical to improve wound healing in diabetic mice.* Proc Natl Acad Sci U S A, 2008. **105**(49): p. 19426-31.
22. Kaluz, S., M. Kaluzova, and E.J. Stanbridge, *Proteasomal inhibition attenuates transcriptional activity of hypoxia-inducible factor 1 (HIF-1) via specific effect on the HIF-1alpha C-terminal activation domain.* Mol Cell Biol, 2006. **26**(15): p. 5895-907.
23. Eustace, A., et al., *A 26-gene hypoxia signature predicts benefit from hypoxia-modifying therapy in laryngeal cancer but not bladder cancer.* Clin Cancer Res, 2013. **19**(17): p. 4879-88.
24. Buffa, F.M., et al., *Large meta-analysis of multiple cancers reveals a common, compact and highly prognostic hypoxia metagene.* Br J Cancer, 2010. **102**(2): p. 428-35.
25. Ogden, A., et al., *Interphase microtubules: chief casualties in the war on cancer?* Drug Discov Today, 2014. **19**(7): p. 824-9.
26. Mittal, K., et al., *Amplified centrosomes may underlie aggressive disease course in pancreatic ductal adenocarcinoma.* Cell Cycle, 2015: p. 0.
27. Cosenza, M.R. and A. Kramer, *Centrosome amplification, chromosomal instability and cancer: mechanistic, clinical and therapeutic issues.* Chromosome Res, 2016. **24**(1): p. 105-26.
28. Baak, J.P., et al., *Multivariate prognostic evaluation of the mitotic activity index and fibrotic focus in node-negative invasive breast cancers.* Eur J Cancer, 2005. **41**(14): p. 2093-101.
29. Cheng, G.M. and K.K. To, *Adverse Cell Culture Conditions Mimicking the Tumor Microenvironment Upregulate ABCG2 to Mediate Multidrug Resistance and a More Malignant Phenotype.* ISRN Oncol, 2012. **2012**: p. 746025.
30. Thomas, S., et al., *CD24 is an effector of HIF-1-driven primary tumor growth and metastasis.* Cancer Res, 2012. **72**(21): p. 5600-12.
31. Lukasiewicz, K.B. and W.L. Lingle, *Aurora A, centrosome structure, and the centrosome cycle.* Environ Mol Mutagen, 2009. **50**(8): p. 602-19.
32. Zhou, H., et al., *Tumour amplified kinase STK15/BTAK induces centrosome amplification, aneuploidy and transformation.* Nat Genet, 1998. **20**(2): p. 189-93.

33. Katayama, H., et al., *Interaction and feedback regulation between STK15/BTAK/Aurora-A kinase and protein phosphatase 1 through mitotic cell division cycle.* J Biol Chem, 2001. **276**(49): p. 46219-24.
34. Le, Q.T., N.C. Denko, and A.J. Giaccia, *Hypoxic gene expression and metastasis.* Cancer Metastasis Rev, 2004. **23**(3-4): p. 293-310.
35. Subarsky, P. and R.P. Hill, *The hypoxic tumour microenvironment and metastatic progression.* Clin Exp Metastasis, 2003. **20**(3): p. 237-50.
36. Pannu, V., et al., *Rampant centrosome amplification underlies more aggressive disease course of triple negative breast cancers.* Oncotarget, 2015. **6**(12): p. 10487-97.
37. Godinho, S.A., et al., *Oncogene-like induction of cellular invasion from centrosome amplification.* Nature, 2014. **510**(7503): p. 167-71.
38. Marthiens, V., M. Piel, and R. Basto, *Never tear us apart--the importance of centrosome clustering.* J Cell Sci, 2012. **125**(Pt 14): p. 3281-92.
39. Mittal, K., et al., *A centrosome clustering protein, KIFC1, predicts aggressive disease course in serous ovarian adenocarcinomas.* J Ovarian Res, 2016. **9**: p. 17.
40. Yan, Q., et al., *The hypoxia-inducible factor 2alpha N-terminal and C-terminal transactivation domains cooperate to promote renal tumorigenesis in vivo.* Mol Cell Biol, 2007. **27**(6): p. 2092-102.
41. Ran, F.A., et al., *Genome engineering using the CRISPR-Cas9 system.* Nat Protoc, 2013. **8**(11): p. 2281-308.

3 AMPLIFIED CENTROSOMES MAY UNDERLIE AGGRESSIVE DISEASE COURSE IN PANCREATIC DUCTAL ADENOCARCINOMA

Parts of this chapter have been published verbatim in ***Cell Cycle 2015 June; 14(17): 2798-809***

*as "**Amplified centrosomes may underlie aggressive disease course in pancreatic ductal adenocarcinoma.**"*

Authors listed on the paper and their contributions:

1. Karuna Mittal: Conceived and designed the study, carried out major experiments (staining, imaging, western blots, migration and invasion assays), analyzed and interpreted the data, and wrote the manuscript.
2. Angela Ogden: Performed in silico data analysis and critically revised the manuscript.
3. Michelle D. Reid: Provided tissue samples.
4. Sooryanarayana Varambally: Performed in silico data analysis.
5. Padmashree C. G. Rida: Helped in designing the study and critically revised the manuscript.
6. Ritu Aneja: Co-corresponding author of the study- Helped in designing the study and critically revised the manuscript.

3.1 Abstract

Centrosome amplification (CA), the presence of centrosomes that are abnormally numerous or enlarged, is a well-established driver of tumor initiation and progression associated with poor prognosis across a diversity of malignancies. Pancreatic ductal adenocarcinoma (PDAC) carries one of the most dismal prognoses of all cancer types, and a majority of these tumors are characterized by numerical and structural centrosomal aberrations; therefore, CA may underlie the nearly unsurpassed aggressiveness of this disease. In this study, we sought to determine whether CA was associated with worse clinical outcomes, poor prognostic indicators, markers of epithelial-mesenchymal transition (EMT), and ethnic health disparity in PDAC. We also evaluated whether CA could precipitate more aggressive phenotypes in a panel of cultured pancreatic cancer cell lines. Using publicly-available datasets, we examined the association between the expression of genes whose dysregulation drives CA and overall survival and the expression of EMT markers in PDAC patients. We found that increased expression of these CA-related genes was associated with worse overall survival and increased EMT marker expression. Quantitative analysis of centrosomal profiles in pancreatic cancer cell lines and tissue sections uncovered that pancreatic cell lines exhibited different levels of CA, and markers of CA were associated with the expression of EMT markers. We induced CA in pancreatic cancer cells and found that CA empowered the cells with enhanced invasive and migratory capabilities. In addition, we discovered that PDACs from African American (AA) patients exhibited a greater extent of both numerical and structural CA than PDACs from European American (EA) patients. Taken together, these findings suggest that CA may fuel a more aggressive disease course in PDAC patients. Given the prevalence of CA among pancreatic tumors,

especially ones from AA patients, future studies should test their susceptibility to centrosome declustering drugs, which could offer urgently needed targeted therapy with potentially low toxicity.

3.2 Introduction

Pancreatic cancer is the fourth most fatal cancer in the United States, although it constitutes only 2.7% of new cancer cases [1]. Greater than 90% of all pancreatic neoplasms derive from ductal cells, and ~85% of these are invasive PDACs [2]. Over the past 30 years, improvements in survival for PDAC patients have paled in comparison with improvements for patients suffering from other cancers. This unsettling trend is expected to continue in the near future, and it is projected that by 2030 pancreatic cancer will depose colorectal cancer to become the second-leading cause of cancer-related death in the United States [3, 4]. A leading cause for the exceptionally high mortality of PDAC is its general lack of clinically useful prognostic markers and therapeutic targets, which contrasts with many other malignancies (such as breast and lung), in which much greater strides in precision medicine have been made. Surgical resection is the only treatment to date that appreciably extends survival in PDAC, with a median survival of ~18 months for patients who undergo complete resection compared with only ~6 months for patients with unresectable tumors [5]. Gemcitabine is the standard of care for patients with advanced disease, although it improves survival only by about one month [6]. Therefore, it is critical to identify prognostic and predictive indicators and clinically actionable drivers of disease aggressiveness in PDAC. Such an approach has achieved breakthroughs for other highly aggressive, treatment-refractory cancers, such as melanoma [4], by enabling risk stratification of patients and the administration of targeted therapies. A deluge of gene expression and proteomic studies has implicated ~10% of the exome in pancreatic cancer [7], but the size and complexity of these data

have so far thwarted their integration into an actionable portrait of the disease. Indeed, at present there is only one FDA-approved biomarker for pancreatic cancer, carbohydrate antigen 19-9; however, it has low prognostic value before surgery or chemotherapy, so its utility is mostly limited to post-treatment monitoring of disease progression [8]. Furthermore, only one FDA-approved targeted therapy is available for PDAC, erlotinib (in combination with gemcitabine), although it improves survival by less than 2 weeks and, thus, is rarely prescribed [4]. Consequently, there is a critical need for improved prognostic biomarkers and therapeutic targets for PDAC.

Biomarkers and drug targets are generally sought at "omics" levels of late, but a seemingly overlooked pool of candidates is comprised of organelles. These structures constitute the output of the cell's own integration of the staggeringly complex molecular signaling events within it, so organelles represent particularly comprehensive and clinically significant biomarkers and drug targets. Investigation of organelle-level variations among PDACs of differing aggressiveness represents entirely uncharted territory. The centrosome has emerged as a central driver of tumor aggressiveness across cancer types. CA (the presence of excessively numerous or voluminous centrosomes) can initiate tumorigenesis, engenders chromosomal instability, and precipitates invasive tumor behavior [9-11]. In order for cancer cells to avail themselves of the advantages of CA, however, they must prevent spindle multipolarity during mitosis, lest they succumb to fatal mitotic catastrophe. As a result, cancer cells deftly cluster supernumerary centrosomes into two diametrically opposed groups in order to achieve pseudo-bipolar spindle geometry and survive. The extent of CA correlates positively with aggressiveness across the entire spectrum of cancer types [12]. Consequently, it is rational to suspect that CA is involved in PDAC, which is nearly unrivaled in its aggressive behavior among malignancies. Furthermore, a small study focused on centrosome abnormalities in PDAC revealed a striking difference in the profiles of centrosomes,

both in terms of their number and size, as compared with normal pancreas [13]. Another study observed that centrosome abnormalities (defined as supernumerary or structurally aberrant centrosomes) detected by pericentrin immunofluorescence staining were correlated with nuclear abnormalities (namely, bi- or multinucleation or the presence of giant nuclei) in a panel of pancreatic cancer cell lines [14]. These studies lend credence to our rationale that CA may underlie the more aggressive disease course experienced by PDAC patients and may hold promise as a prognostic and therapeutic target in PDAC.

To address the above-specified line of inquiry, we investigated the association between CA and disease aggressiveness in PDAC using publicly available microarray data, with genes whose dysregulation is known to drive CA serving as surrogates for amplified centrosomes. Intriguingly, we found that high expression levels of these genes were significantly associated with worse overall survival and increased expression of EMT markers. In addition, we performed a comprehensive quantitative analysis to ascertain whether structural and numerical CA are associated with clinicopathologic features of PDACs or the ethnicity of PDAC patients. We discovered that moderately differentiated PDACs exhibited the most extensive CA compared with well- and poorly differentiated PDACs, although among well-differentiated PDACs CA was significantly associated with duodenal invasion. CA was not associated with other clinicopathologic features. Intriguingly, AA PDACs were found to have significantly higher numerical and structural CA compared with EA PDACs. Finally, to determine whether CA is causally implicated in pancreatic tumorigenesis, we induced CA in cultured pancreatic cancer cell lines. We found that supernumerary centrosomes enhanced cell migration and invasion and upregulated the expression of EMT markers. Collectively, these observations insinuate that CA may be involved in PDAC aggressiveness.

3.3 Materials and Methods

3.3.1 Public microarray data analysis

Robust Multi-array Average-normalized expression levels of genes whose dysregulation is known to drive CA (including *AURKA*, *CCNA2*, *CCND1*, *CCNE2*, *CDK1*, *CEP63*, *CEP152*, *E2F1*, *E2F2*, *E2F3*, *LMO4*, *MDM2*, *MYCN*, *NDR1*, *NEK2*, *PIM1*, *PIN1*, *PLK4*, *RAD6*, *and STIL*) from the primary PDACs of 42 patients were obtained from GEO series GSE28735. Cutoff Finder [17] was used to determine optimal cut-points in individual gene expression levels to stratify patients into two groups based on overall survival using the log-rank test. The same data were used to obtain Pearson's correlation coefficients between genes whose dysregulation drives CA (*AURKA*, *CDK1*, *STIL*, *PIM1*, *PLK4*, and *NEK2*) and EMT markers (*PLAUR* and *MMP3*), which were validated using gene expression data from 39 PDACs from GEO series GSE15471. SPSS software (IBM) was used for the analyses, with $P<0.05$ indicating statistical significance.

3.3.2 Clinical tissue samples

Formalin-fixed paraffin-embedded slides of PDAC and normal pancreatic tissue were procured from Emory hospital. The Emory University Institutional Review Board approved all aspects of the study.

3.3.3 Immunofluorescence staining, imaging, and scoring of clinical specimens

For immunofluorescence staining all tissue slides were deparaffinized by baking at 67°C for 2 h followed by 3 xylene washes. Slides were then rehydrated by passing them through a series of ethanol baths (100%, 95%, 70%, and 50%). Antigen retrieval was performed by incubating slides in citrate buffer (pH 6.0) in a pressure cooker at 15 psi for 3 min. Tissue samples were then incubated overnight with primary mouse antibody against γ-tubulin (1:1000 dilution) at 4°C. The

samples were then washed with 3X phosphate-buffered saline (PBS) before incubating them in secondary antibody (Alexa-488 anti-mouse) at 37°C for 2 h. Samples were washed with 3X PBS and then mounted with Prolong-Gold antifade reagent that contained DAPI (Invitrogen). Tissue samples were imaged using the Zeiss LSC 700 confocal microscope (Oberkochen, Germany), and images were processed with Zen software (Oberkochen, Germany). The percentage of cells with CA was quantitated from 10 randomly selected fields, with ~500 cells counted for each sample.

3.3.4 Immunohostochemistry, scoring, and WI calculation for clinical specimens

Deparaffinization and antigen retrieval were performed as described for immunofluorescence staining. Thereafter, the tissues were immunolabeled using Plk4 and MMP2 antibodies. Enzymatic antibody detection was performed with the Universal LSAB + Kit/HRP (DAKO, CA, USA). The staining intensity was scored as 0=none, 1=low, 2=moderate, or 3=high, and the percentage of cells from 10 randomly selected fields (~500 cells) was determined. The product of the staining intensity and the percent of positive cells constituted the WI. Pearson's correlation coefficients between WIs were sought using SPSS.

3.3.5 Cell culture

MIA PaCa-2, Capan-1, CFPAC-1, and HPAF-II cell lines were grown in Dulbecco's Modified Eagle's medium supplemented with 10% Hyclone fetal bovine serum and 1% penicillin/streptomycin. All cell lines were maintained in humidified 5% CO_2 atmosphere at 37°C.

3.3.6 Cell lysate preparation, immunobloting, immunofluorescence staining, and confocal microscopy

Protein lysates were prepared, and immunoblotting was performed as described earlier [51]. Polyacrylamide gel electrophoresis was used to resolve the proteins, which were transferred onto polyvinylidene fluoride membranes (Millipore). The Pierce ECL chemiluminescence detection kit

(Thermo Scientific) was used to visualize the immune-reactive bands. β-actin was used as loading control. For immunofluorescence staining, cells were grown on glass coverslips and fixed with ice-cold methanol for 10 min. Blocking was done by incubating with 2% bovine serum albumin/1XPBS/0.05% Triton X-100 at 37°C for 1 h. Coverslips were incubated in primary antibodies against γ-tubulin and α-tubulin at 1:2000 dilution for 1 h at 37°C. The cells were washed with 2% bovine serum albumin/1XPBS for 10 min at room temperature before incubating with a 1:2000 dilution of Alexa 488- or 555-conjugated secondary antibodies (Invitrogen; Carlsbad, CA). Cells were mounted with ProLong Gold Antifade Reagent with DAPI (Invitrogen). Antibodies against γ-tubulin and α-tubulin were from Sigma (St. Louis, MO); antibodies against Aurora A and β-actin were from Cell Signaling (St. Louis, MO,USA); antibodies against centrin-2 were from Santa Cruz Biotechnology (Santa Cruz, CA); and antibodies against Plk4 and MMP2 were from Abcam (Cambridge, MA, USA). Horseradish peroxidase-conjugated secondary antibodies were from Santa Cruz Biotechnology (Santa Cruz, CA).

3.3.7 Cell migration assay

Monolayers of the aphidicolin-treated and control CFPAC-1 cells were scratched with a 200 µl pipette tip after serum starving for 8 h. Using a 20X objective, images were taken every hour using the Zeiss Axio Observer. Image J was used to define the edges of the wound and to measure wound area, and the percent change in the wound area was calculated based on the closure of wound over time.

3.3.8 Boyden chamber assay

Control and aphidicolin-treated CFPAC-1 cells were collected after 48 h and resuspended in media at 5 x 10^4cells/ml. Transmigration assay was carried out in a Boyden chamber system. The upper wells of the chamber were loaded with 200 µl of cell suspension, and 500 µl media

containing 20% FBS was added in lower chambers as a chemoattractant. Chambers were incubated for 12 h at 37°C and 5% CO_2. Cells that migrated to the bottom surface of the filter were fixed with 70% methanol, stained with crystal violet, and counted under a microscope in 10 randomly selected fields using a 20X objective.

3.3.9 Statistical Methods

Unless otherwise stated in the methods and results, statistical analyses were performed using Student's t-test, and the criterion for statistical significance was $P<0.05$.

3.4 Results

3.4.1 Increased expression of genes that drive CA is associated with worse overall survival in PDAC

Previous studies have reported an association between CA and chromosomal instability in PDAC [15, 16]. Furthermore, liver metastases exhibited a greater extent of CA than the primary tumors in an orthotopic implantation model of PDAC [16]. However, the association of CA with a more aggressive disease course in PDAC patients has not been explored. As there are currently no publicly available datasets with information on CA per se, we instead analyzed expression levels of genes whose deregulation is known to drive CA (including *AURKA, CCNA2, CCND1, CCNE2, CDK1, CEP63, CEP152, E2F1, E2F2, E2F3, LMO4, MDM2, MYCN, NDR1, NEK2, PIM1, PIN1, PLK4, RAD6, and STIL*). Specifically, we tested the associations between Robust Multi-array Average-normalized expression levels of these genes in primary PDACs from 42 patients and overall survival using Gene Expression Omnibus (GEO) series GSE28735. Survival over time was estimated using the Kaplan-Meier method. Cutoff Finder, which applies the log-rank test to determine an optimal cut-point based on significance [17], was used to stratify patients

into low- and high-risk groups. High expression levels of nine genes (specifically, *AURKA*, *CCNA2*, *CCNE2*, *CDK1*, *CEP152*, *NEK2*, *PIM1*, *PLK4*, and *STIL*) were found to be associated with worse overall survival with $P<0.1$ Associations with five genes, namely *CDK1*, *NEK2*, *PIM1*, *PLK4*, and *STIL*, were significant ($P<0.05$), as depicted in Kaplan-Meier plots in **Figure 3.4.1** Consequently, CA may be associated with worse overall survival in PDAC. We found that genes whose dysregulation drives CA and clustering are upregulated in PDACs (n=36) relative to normal pancreatic tissue (n=12) using the GEO series GSE16515 (**Supplemental Figure 3.7.1**[2]). We further found that expression levels of *AURKA*, *CDK1*, *STIL*, *PIM1*, *PLK4*, and *NEK2* in PDACs mostly correlate with the expression of the EMT markers *PLAUR* and *MMP3* using GEO series GSE28735 (**Table 3.4.1**), which we validated using GEO series GSE15471 (**Table 3.4.2**). These results suggest that CA may be associated with increased metastatic potential of PDACs and poor survival prospects for PDAC patients.

[2] All supplemental data, tables, and figures appear in Appendix B for this chapter

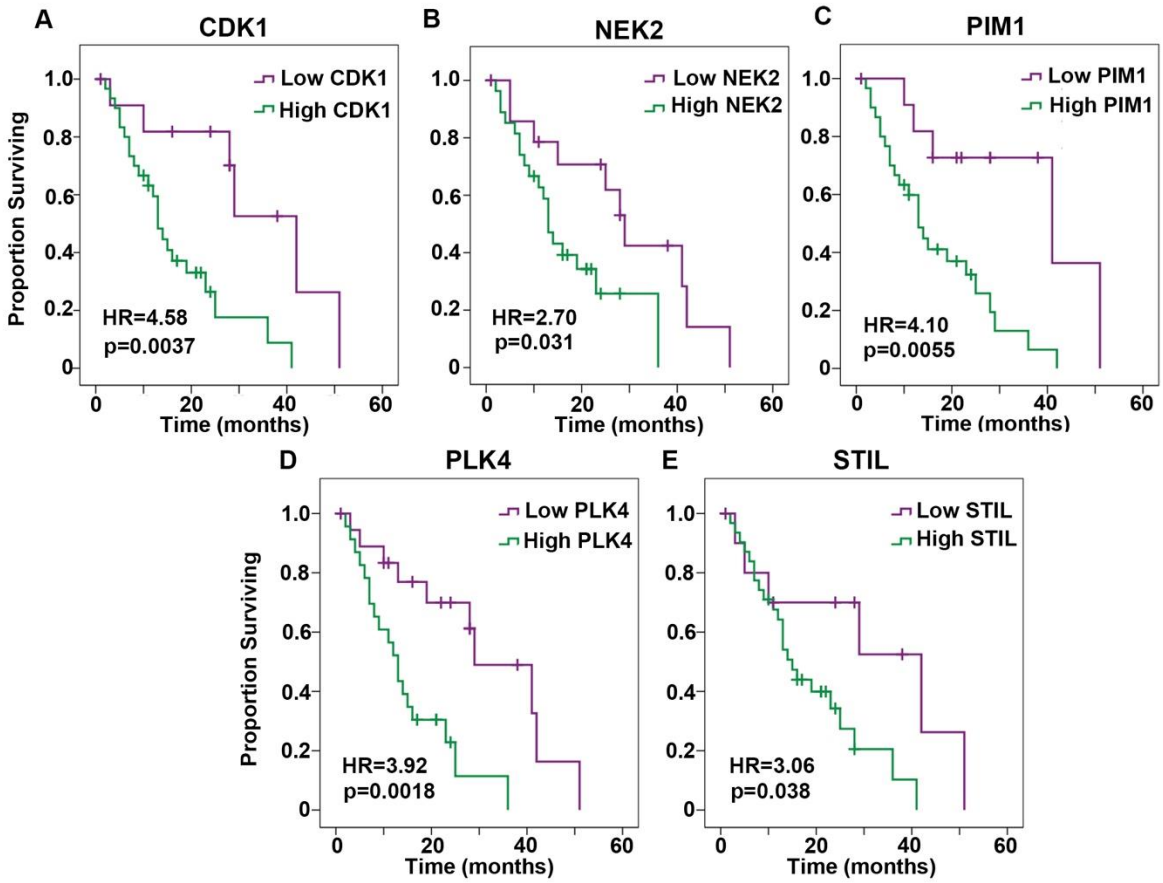

Figure 3.4.1 Kaplan-Meier plots of overall survival based on low or high expression of genes whose dysregulation drives CA in pancreatic ductal adenocarcinomas.
Expression was categorized as low or high based on whether the value was below or above the following cut-points in normalized expression levels, given in parentheses here after each gene: **A.** *CDK1* (2.97), **B.** *NEK2* (3.79), **C.** *PIM1* (5.70), **D.** *PLK4* (3.47), and **E.** *STIL* (3.06). HR=Hazard Ratio

Table 3.4.1 Correlation between the expression of CA associated gene and EMT markers in GEO series GSE28735.
Genes whose dysregulation drives centrosome amplification (*AURKA, CDK1, STIL, PIM1, PLK4,* and *NEK2*), that contribute to centrosome structure (*CETN2*), or that indicate epithelial-mesenchymal transition (*PLAUR* and *MMP3*). Normalized gene expression levels from breast tumors in GEO series GSE28735 were used for the statistical analysis.

		AURKA	*CDK1*	*STIL*	*PIM1*	*PLK4*	*NEK2*	*CETN2*
PLAUR	Pearson Correlation	0.311	0.395	0.305	0.539	0.237	0.359	0.403
	Sig. (2-tailed)	0.037	0.007	0.042	0.000	0.117	0.015	0.006
	N	45	45	45	45	45	45	45
MMP3	Pearson Correlation	0.142	0.271	0.506	-0.058	0.248	0.376	0.514
	Sig. (2-tailed)	0.353	0.072	0.000	0.705	0.100	0.011	0.000
	N	45	45	45	45	45	45	45

Table 3.4.2 Correlation between the expression of CA associated gene and EMT markers in GEO series GSE15471
Genes whose dysregulation drives centrosome amplification (AURKA, CDK1, STIL, PIM1, PLK4, and NEK2), that contribute to centrosome structure (CETN2), or that indicate epithelial-mesenchymal transition (PLAUR and MMP3

		AURKA	*CDK1*	*STIL*	*PIM1*	*PLK4*	*NEK2*	*CETN2*
PLAUR	Pearson Correlation	0.567	0.590	0.578	0.436	0.578	0.454	0.414
	Sig.(2-tailed)	0.000	0.000	0.000	0.005	0.000	0.004	0.009
	N	39	39	39	39	39	39	39
MMP3	Pearson Correlation	0.388	0.429	0.256	0.003	0.450	0.472	0.019
	Sig. (2-tailed)	0.015	0.006	0.116	0.985	0.004	0.002	0.909
	N	39	39	39	39	39	39	39

We next sought correlations between protein levels of an EMT marker (MMP2) and CA driver (Plk4) in PDAC samples. To this end, we first immunohistochemically stained 54 PDACs and uninvolved adjacent normal tissue for Plk4 and MMP2 and calculated weighted indices (WIs). The

staining intensity was scored as 0=none, 1=low, 2=moderate, or 3=high, and the percentage of positive cells (i.e., with 1+ staining intensity) from 10 randomly selected fields (~500 cells) was determined. The product of the staining intensity and the percent of positive cells constituted the WI. Descriptive statistics regarding patient and clinicopathological characteristics and biomarker WIs are given in **Table 3.4.3.** Both Plk4 and MMP2 proteins were overexpressed in PDACs **(Figure 3.4.2).** In addition, a strong positive Pearson's correlation was found between these markers in PDACs (r=0.460, P<0.001).

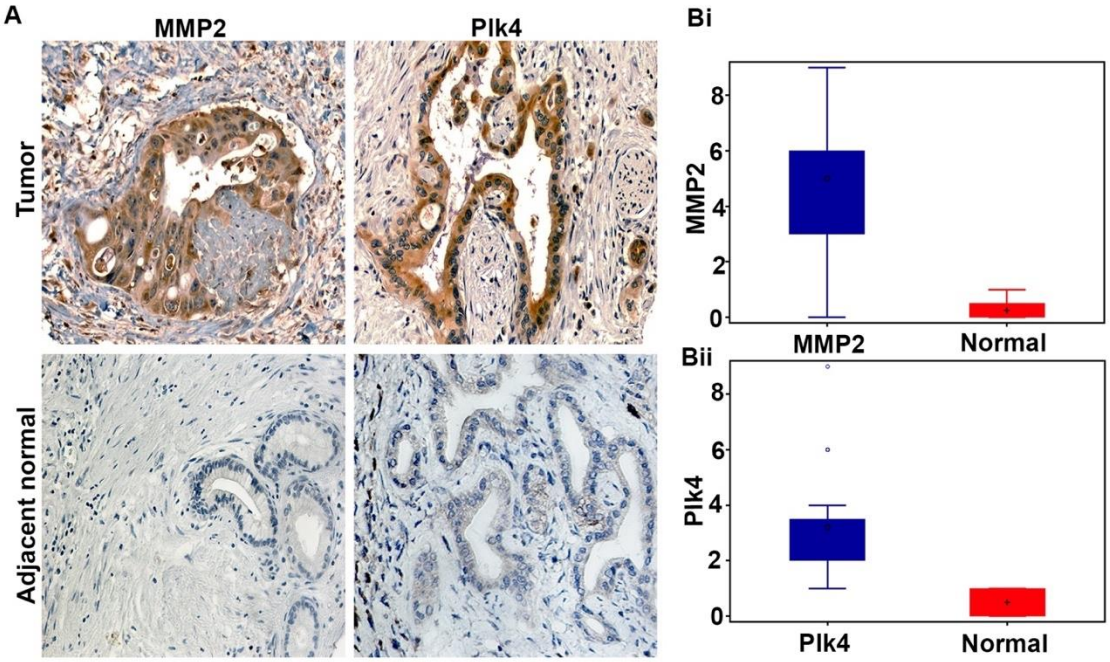

Figure 3.4.2 Pancreatic ductal adenocarcinomas exhibit higher expression of Plk4 and MMP2.
A. Representative micrographs showing immunohistochemical staining for Plk4 (a protein whose overexpression drives centrosome amplification) and MMP2 (an epithelial-mesenchymal transition marker) in uninvolved adjacent normal and tumor tissue from grade-matched PDAC patients. Bi. Box-and-whisker plot depicting the MMP2 weighted index in PDACs and normal pancreas. Bii. Box-and-whisker plot depicting the Plk4 weighted index in PDACs and normal pancreas.

Table 3.4.3Descriptive statistics for PDAC patient and clinicopathologic characteristics in the analysis of MMP2 and Plk4 levels in tumors and matched normal tissue.

Variable	Level	Number	Percentage
Race	AA	23	42.6
	CA	31	57.4
Tumor Size (cm)	<=2	8	14.8
	>2	46	85.2
Tumor Size	Median	3	
	Mean	3.55	
	Maximum	12	
	Minimum	0.25	
	St.dev	1.99	
Grade	1	10	18.5
	2	31	57.4
	3	13	24.07
MMP2 WI	Median	6	
	Mean	4.20	
	Maximum	9	
	Minimum	0	
	St.dev	3.07	
Plk4 WI	Median	2	
	Mean	2.11	
	Maximum	9	
	Minimum	0	
	St.dev	2.17	
MMP2 WI	Low (<2)	13	24.1
	Moderate (2-6)	34	63.0
	High (>6)	7	13.0
Plk4 WI	Low (<2)	25	46.3
	Moderate (2-6)	27	50.0
	High (>6)	2	3.7
PNI	Yes	43	79.6
	No	10	18.5
LVI	Yes	26	48.1
	No	28	51.9
Age at diagnosis	Median	64	
	Mean	62.05	
	Maximum	84	
	Minimum	35	
	St.dev	9.88	
Duodenum Invasion	Yes	20	37.0
	No	34	63.0
Soft tissue involvement	Yes	37	68.5
	No	17	31.5

3.4.2 Amplified centrosomes enhance the motility and invasiveness of pancreatic cancer cells

Having confirmed an association between a protein whose overexpression drives CA and a marker of EMT, we were interested in exploring how CA may transform non-invasive pancreatic tumors into aggressive ones that metastasize. Thus, we examined whether CA can enhance the motility and invasiveness of pancreatic cancer cells. To this end, we first screened three well-established pancreatic cancer cell lines (namely, MIA PaCa-2, CFPAC-1, and HPAFII) by immunostaining centrosomes (γ-tubulin, green) and microtubules (α-tubulin, red) and counterstaining nuclei with 4′,6-diamidino-2-phenylindole (DAPI) (blue) (**Figure 3.4.3A**). We found that HPAFII cells exhibited the greatest extent of numerical CA (~20% of cells), followed by MIA PaCA-2 (~15% of cells) and CFPAC-1 (~10% of cells) (**Figure 3B**). We also evaluated the expression of centrosome-related proteins in these cell lines using immunoblotting methods. We found that the cell lines with high CA expressed elevated levels of centrosome structural proteins (centrin-2 and γ-tubulin) and proteins whose dysregulation is known to drive CA (Aurora A and Plk4) (**Figure 3.4.3C**). We next asked if aberrations in centrosome number translate into aberrations in mitotic spindle geometry. We found that all three cell lines exhibited a significantly lower proportion of cells with multipolar spindles in comparison with the proportion of cells with supernumerary centrosomes (**Figure 3.4.3B**). This discordance corroborates the hypothesis that cancer cells deal with supernumerary centrosomes by clustering them to form pseudobipolar spindles. Taken together, our data suggest that cultured pancreatic cancer cells are characterized by CA, which they are generally successful in managing by executing centrosome clustering.

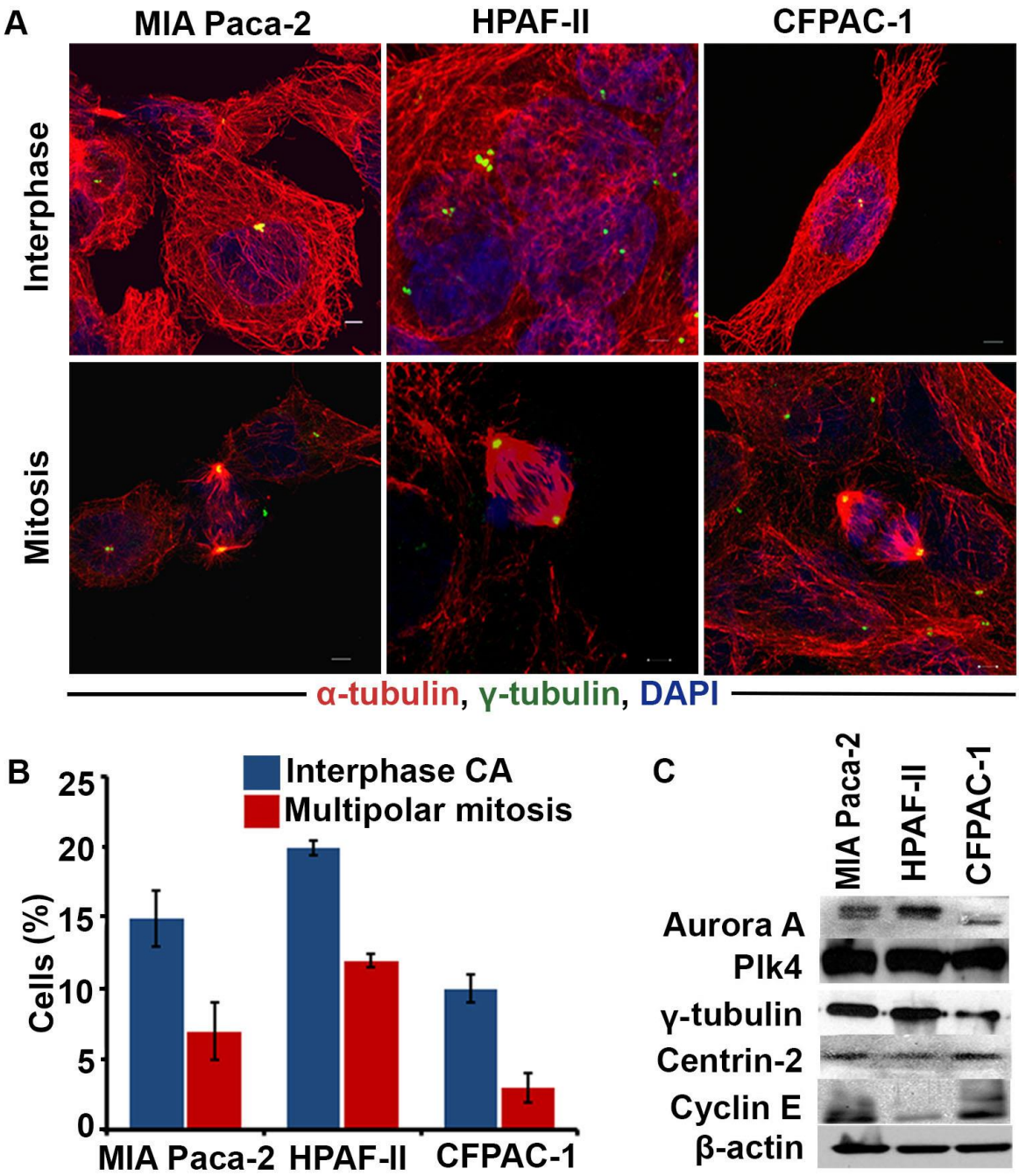

Figure 3.4.3 Pancreatic cancer cells with high levels of centrosome amplification (CA) express high levels of centrosome structural proteins and proteins whose dysregulation drives CA.

A. Immunofluorescence micrographs showing MIA PaCa-2, HIFA-II, and CFPAC-1 cells in interphase and mitosis stained for γ-tubulin (green), α-tubulin (red), and nuclei (blue). B. Bar graph representing the percentage of cells with CA in MIA PaCa-2, CFPAC-1, and HPFA-II cells. C. Immunoblots depicting the levels of centrosome structural proteins (γ-tubulin and centrin-2)

and proteins whose dysregulations drives CA (Aurora A, Plk4, and Cyclin E) in MIA PaCa-2, HPFA-II, and CFPAC-1 cells.

Next, we were curious to learn whether inducing CA via pharmacological means would enhance the motility of pancreatic cancer cells with lower levels of CA. To this end, we induced CA in CFPAC-1 pancreatic cancer cells (~10% of which have CA, the lowest level in the lines we surveyed) by treating them with 25 μm aphidicolin for 48 h. Aphidicolin arrests cells in G1/S phase by inhibiting DNA polymerase [18, 19]. After treatment ~22% of cells exhibited amplified centrosomes. We then performed a wound-healing assay, which revealed that pharmacological induction of CA stimulated migration, as the wound was filled in about half the time taken by control cells (**Figure 3.4.4A** and **Bi**). Thereafter, we examined the invasive capabilities of cells with supernumerary centrosomes by performing a classical Boyden chamber assay. We observed that 80% of the CFPAC-1 cells in which CA was induced invaded the Matrigel in 12 h in contrast with only 53% of control cells (that is, CFPAC-1 cells not treated with aphidicolin) (**Figure 3.4.4Bii and C**). We confirmed that CA was induced in aphidicolin-treated cells by immunoblotting for centrin-2 and Plk4 levels (**Figure 3.4.4D**). In addition, we noted that cells treated with aphidicolin expressed higher levels of N-cadherin (**Figure 3.4.4D**), suggesting that these cells may have attained a more mesenchymal phenotype. In summary, our findings that CA upregulates N-cadherin levels, invasive capacity, and wound-healing imply that CA may contribute to epithelial-mesenchymal transition in pancreatic cancer cells.

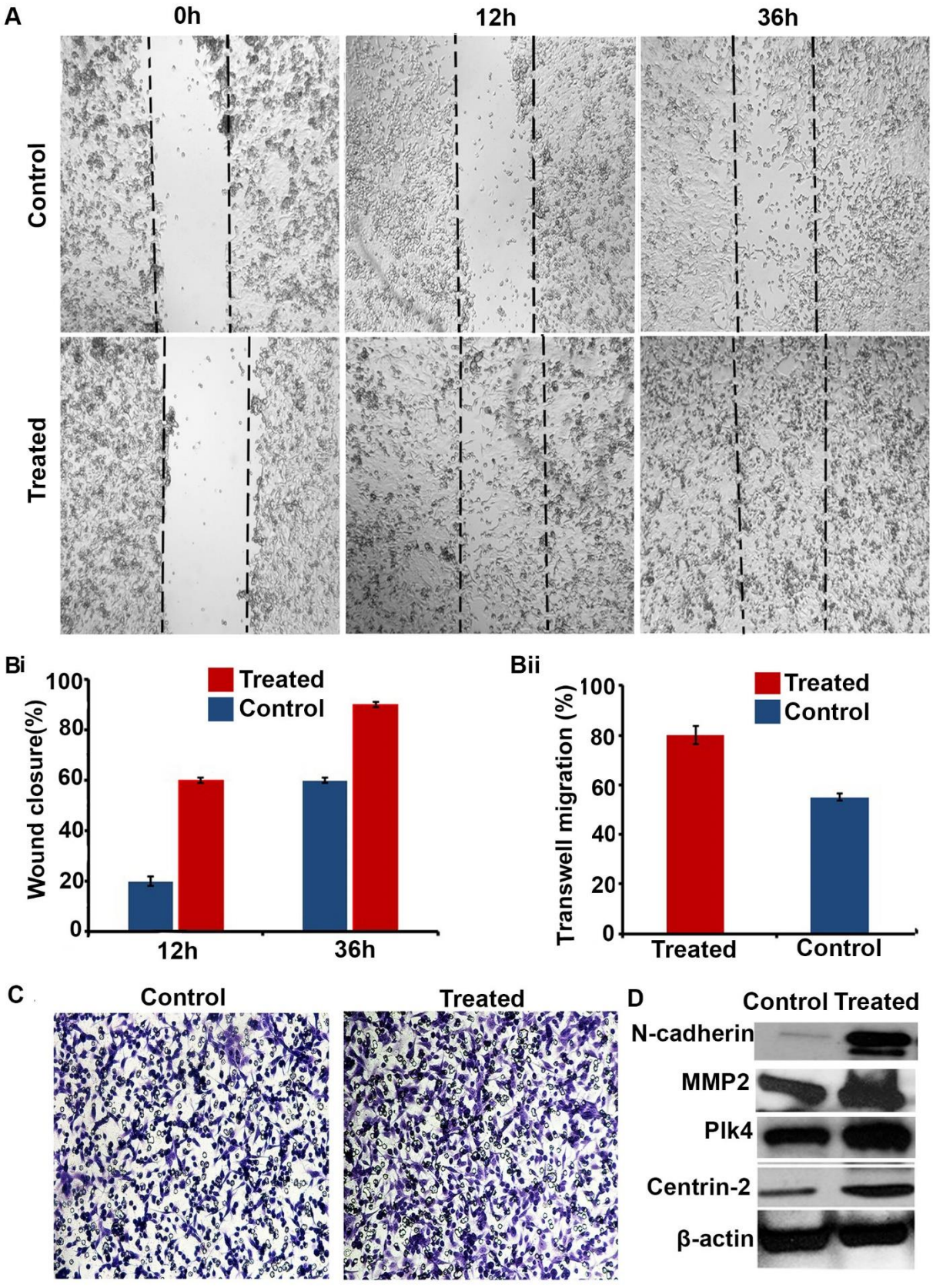
A
0h
12h
36h
Control
Treated
Bi
Wound closure(%)
Treated
Control
12h
36h
Bii
Transwell migration (%)
Treated
Control
C
Control
Treated
D
Control Treated
N-cadherin
MMP2
Plk4
Centrin-2
β-actin

Figure 3.4.4 Cells with centrosome amplification (CA) migrate more rapidly in a wound-healing assay.
A. Bright-field micrographs showing the wound-healing capacity of CFPAC-1 control (untreated) and aphidicolin-treated cells at 0, 12, and 36 h. Bi. Bar graphs representing the percent of aphidicolin-treated and control (untreated) CFPAC-1 cells in the wound. Bii. Bar graphs representing the percent of aphidicolin-treated and control CFPAC-1 cells that invaded the Boyden chamber. C. Brightfield micrographs showing the invasion capacity of CFPAC-1 control and aphidicolin-treated cells after 24 h. D. Immunoblots of centrosome structural proteins (centrin-2), a protein whose dysregulation drives CA (Plk4), and epithelial-mesenchymal transition markers (N-cadherin and MMP2) in CFPAC-1 control and aphidicolin-treated cells.

3.4.3 Amplified centrosomes distinguish AA PDACs from EA PDACs

A previous study of 13 PDACs uncovered that a greater proportion of PDAC cells have CA, both numerical and structural, than normal pancreas [20]. However, the association of CA with poor prognostic indicators in pancreatic cancer is unknown. To address this, we examined the centrosomal profiles of 64 PDACs and sought associations with clinicopathologic parameters including age, sex, ethnicity, tumor size, grade/extent of differentiation, stage, lymphovascular and perineural invasion, lymph node metastasis, and surgical margin status. Descriptive statistics regarding patient and clinicopathologic characteristics are given in **Table 3.4.4.** Formalin-fixed tissue sections from the PDACs were immunostained for centrosomes (γ-tubulin) and nuclei were counterstained with DAPI (**Figure 3.4.5A**). Centrosome number and volume were quantitated in tumor areas pre-marked by a gastrointestinal pathologist using confocal microscopy. Tumor cells with more than two centrosomes or centrosomes greater than 0.56 μm^3 in volume were regarded as having numerical or structural CA, respectively. The volume of 0.56 μm^3 was used as a cut-point because that was the maximum centrosome volume found in normal pancreatic cells using the 3D volume measurement module from the Zeiss imaging software. The percentage of cells exhibiting centrosomal aberrations was quantitated from 10 randomly selected fields (approximately 500 cells) for each sample. The mean volume of the γ-tubulin spots observed in pancreatic cancer tissues was 1.75 μm^3, which was ~9 times greater than the mean volume in

normal pancreatic cells. Pancreatic tumors also exhibited extensive numerical CA, with ~25-40% of cells bearing extra centrosomes, unlike normal pancreatic tissue, in which only ~5% of cells had extra centrosomes. When we compared the extent of CA between tumors of different levels of differentiation, we found that moderately differentiated tumors exhibited the highest CA when compared with well- and poorly differentiated tumors (**Figure 3.4.5B**); however, the results were not statistically significant, perhaps due to the paucity of well-differentiated tumors in our dataset (n=6), as PDACs are most often moderately to poorly differentiated. While CA was associated with duodenal invasion in well-differentiated PDACs (r=0.772, p=0.042), it was not associated with tumor size, stage, perineural or lymphovascular invasion, or number of positive lymph nodes in PDACs of any degree of differentiation. In summary, CA clearly differentiates PDACs from adjacent normal tissue and is associated with duodenal invasion in well-differentiated PDACs.

Table 3.4.4 Descriptive statistics for PDAC patient and clinicopathologic characteristics in the analysis of centrosome amplification in tumors and matched normal tissue.

Variable	Level	Number	Percentage
Race	AA	30	46.88
	CA	34	53.13
Centrosomal amplification	Low (<10%)	14	21.88
	Moderate (10 ~40%)	38	59.38
	High (40%<)	12	15.63
Tumor Differentiation	Well	6	9.38
	Moderate	40	62.50
	Poor	14	21.88
Tumor	<=2	10	14.49
	>2	54	78.26
Tumor in size (cm)	Median	3.1	-
	Mean	3.60	-
	Maximum	12	-
	Minimum	1	-
	St.Dev	1.9	-
Age at diagnosis	Median	66	-
	Mean	64.4307692	-
	Maximum	87	-
	Minimum	35	-
	St.Dev	10.8147788	-
	Median	36.33	-

% Centrosome amplification	Mean	36.19	-
	Maximum	72.22	-
	Minimum	1.40	-
	St.Dev	18.00	-
Duodenum Invasion	Yes	32	50
	No	32	50
Soft tissue involvement	Yes	50	50
	No	14	21.875
PNI	Yes	55	85.9375
	No	10	15.625
LVI	Yes	26	40.625
	No	38	59.375

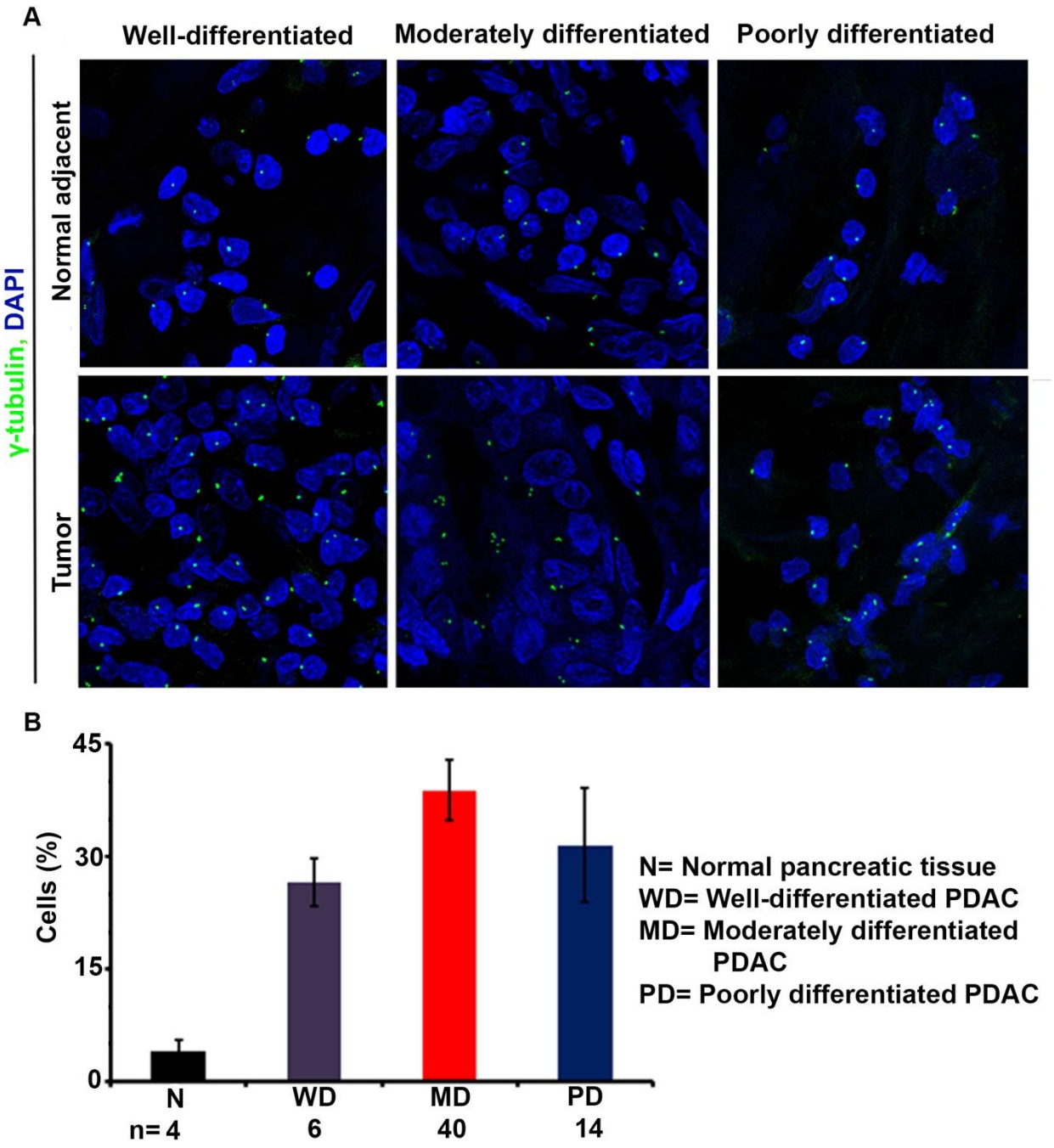

Figure 3.4.5Centrosome amplification (CA) in PDACs and normal pancreatic tissue.
A. Representative confocal micrographs depicting centrosomal profiles in well-, moderately, and poorly differentiated PDACs and adjacent normal pancreatic tissue. Centrosomes were immunostained (γ-tubulin, green) and nuclei were counterstained with DAPI (blue). B. Bar graph representation of the percentage of cells showing CA in well-, moderately, and poorly differentiated PDACs and normal pancreatic tissue samples. ~500 cells were counted in each case.

Finally, because AA ethnicity is a risk factor for the development of PDAC [21], we were interested in determining whether centrosomal profiles from AA patients differed from those of EA patients. Interestingly, when we immunostained moderately differentiated pancreatic tumor samples from AA and EA PDAC patients (n=20 for each group) (**Figure 3.4.6A**) and compared their centrosomal profiles, we found that numerical and structural CA in AA tumors were significantly higher than in EA tumors (**Figure 3.4.6B** and **C**, respectively).

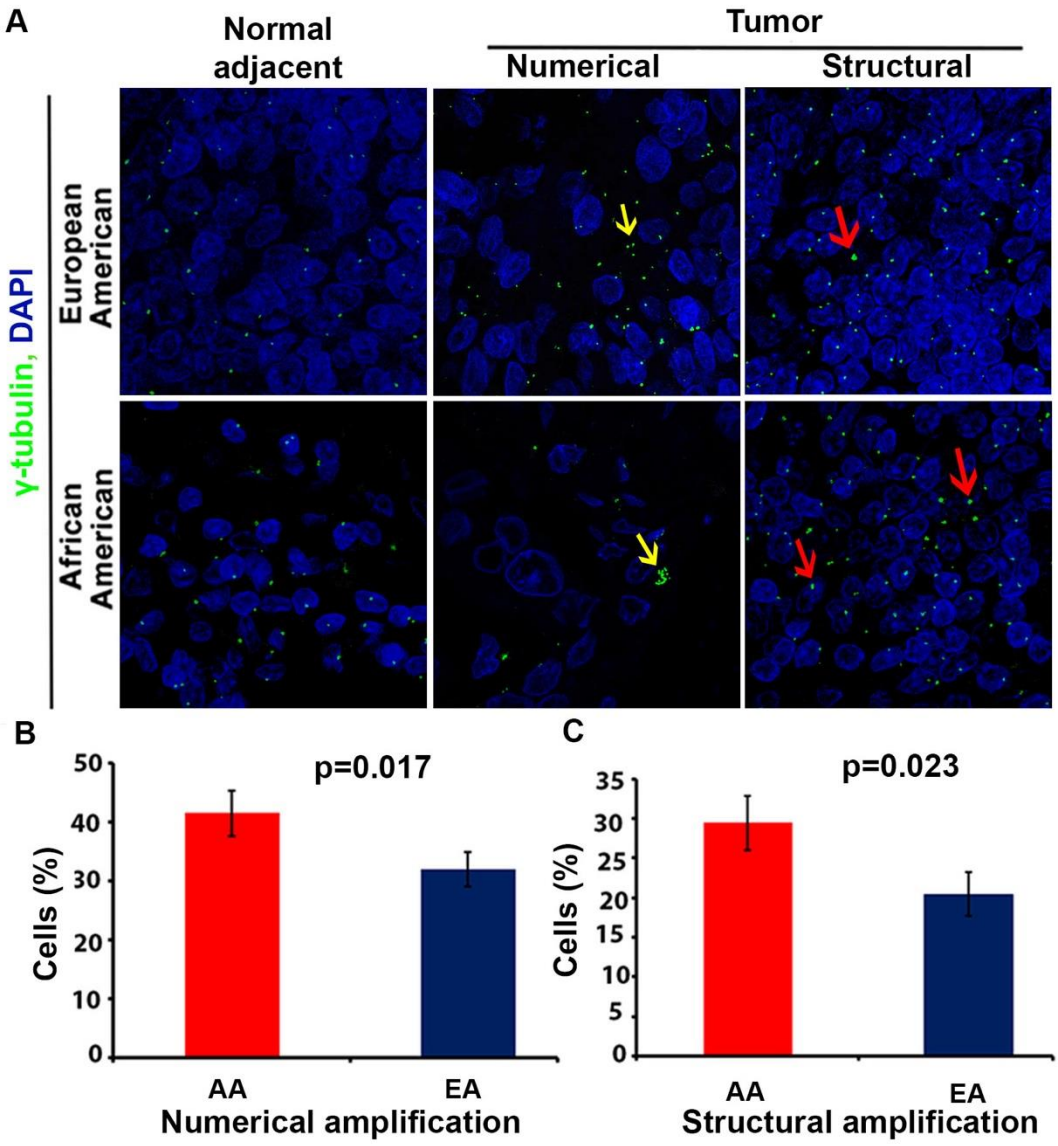

Figure 3.4.6 Centrosome amplification (CA) in PDACs and normal pancreas specimens from AA and EA patients.

A. Representative confocal micrographs depicting centrosomal profiles in grade-matched AA and EA PDACs and adjacent normal tissues. Centrosomes were immunostained for γ-tubulin (green) and nuclei were counterstained with DAPI (blue). B. Bar graphs representing the percent of cells showing numerical CA in AA and EA tissue samples. C. Bar graphs representing the percent of cells showing structural CA in AA and EA PDAC tissue samples. ~500 cells were counted in each case.

3.5 Discussion

Five-year survival rates in PDAC hover around 5% notwithstanding about a half century of research into the etiology of its aggressive nature and potential therapeutic interventions [22]. Out of this burgeoning body of research has emerged an appreciation of the remarkably complex mutational landscape of PDACs, their extensive intratumor heterogeneity due to chromosomal instability, and their extraordinary propensity to metastasize [22, 23], although this knowledge has not translated into considerable improvements in patient outcomes. Chromosomal instability appears to be an early event in the development of PDAC [24], which no doubt contributes to its exceptional aggressiveness. Efforts to identify sources of genetic dysfunction in this cancer type have mostly focused on individual genes or gene signatures without much consideration for potential organelle-level abnormalities. However, CA is a well-established mediator of chromosomal instability [25], and the extent of CA correlates with chromosomal instability in pancreatic cancer cells [26]. Furthermore, CA has been causally implicated in chromosomal instability, as induction of CA in BJ fibroblasts and RPE1 cells via treatment with cytochalasin D (a cytokinesis inhibitor) significantly increases the rate of chromosome missegregation [10]. It has been found that the vast majority of PDACs exhibit CA [15], suggesting that CA is a hallmark of these tumors. Therefore, it seems likely that in PDAC CA is at least partly responsible for intratumor heterogeneity, which is associated with adverse outcomes, and it is rational to suspect that CA is associated with worse clinicopathology and survival rates in PDAC. Our study is the first to demonstrate that high expression levels of genes whose dysregulation drives CA are

associated with worse overall survival in this cancer type, although CA itself was not significantly associated with worse clinicopathology aside from an association with duodenal invasion in well-differentiated tumors.

In addition to being characterized by genomic complexity and chromosomal instability, PDAC is also typified by a high propensity to metastasize. At diagnosis 80% of patients have advanced tumors, almost two-thirds of which have metastasized distantly [27]. Moreover, among patients who receive a potentially curative resection, ~70-80% will experience a local or distant recurrence regardless of whether chemotherapy is administered [28]. CA is a primary suspect in conferral of metastatic abilities to tumors, as induction of CA via overexpression of Plk4 or treatment with dihydrocytochalasin B (a cytokinesis inhibitor) has been demonstrated to prompt invasiveness in MCF10A breast epithelial cells and non-transformed keratinocytes [11]. Specifically, CA precipitates the formation of matrix protein-degrading invasive protrusions and antagonizes intercellular adhesion via augmented microtubule nucleation and Rac1 activation. Nonetheless, it was previously unknown whether CA contributes to invasiveness or enhanced migratory capacity in PDAC. In the present study, we discovered that induction of CA via treatment with aphidicolin enhanced pancreatic cancer cell invasion and migration, suggesting that CA may promote metastasis in PDAC, which is congruent with our finding that CA was associated with duodenal invasion in well-differentiated PDACs. Furthermore, we found that induction of CA upregulated N-cadherin expression, consistent with EMT. The expression of genes whose dysregulation drives CA mostly correlated with the expression of the *PLAUR* and *MMP3* genes, and the extent of CA correlated with expression of the MMP2 protein. Furthermore, induction of CA upregulated MMP3 and N-cadherin protein levels. *PLAUR* encodes the urokinase-type plasminogen activator receptor (uPAR), which promotes pancreatic cancer cell migration and

invasion *in vitro* and hepatic metastases and retroperitoneal invasion *in vivo* [29], and amplification of the *PLAUR* gene is associated with decreased survival in PDAC [30]. The ligand of uPAR, urokinase, cleaves plasminogen to plasmin, which then cleaves pro-MMPs to active MMPs that, together with plasmin, degrade the extracellular matrix to facilitate invasion of tumor cells [31]. The MMP3 protein has been demonstrated to stimulate pancreatic cancer cell invasion [31], and, similar to the uPAR and N-cadherin proteins, both MMP2 and MMP3 are considered to be EMT effector proteins [32, 33]. Based on our findings, it appears that CA may encourage EMT, which is further substantiated by our finding that induction of CA enhances migration and invasion of pancreatic cancer cells. These findings corroborate the hypothesis that amplified centrosomes compel metastatic dissemination in PDAC [34].

Previous studies have shown that cancer cells manage the excessive centrosomal load by forming juxtanuclear supercentrosomal clusters, which they maintain all through interphase and then disperse transiently in prophase, followed soon by tight reclustering [35]. Centrosome declustering drugs, such as the non-toxic antifungal griseofulvin and antitussive noscapine, disaggregate the centrosomal clusters, forcing the mitotic spindle to assume a persistently high-grade multipolar configuration that is incompatible with cell survival [36]. A previous study discovered that the CFPAC-1 cell line exhibits considerable centrosome clustering, with more than half of mitoses in cells with CA assuming a pseudobipolar configuration [37], similar to our findings. Together, these suggest that pancreatic cancer cells tend to cluster their supernumerary centrosomes. As a corollary, it seems that centrosome declustering drugs could prove advantageous in PDAC, an intriguing hypothesis that merits testing.

We discovered that AA PDACs exhibited more extensive numerical and structural CA compared with EA PDACs. The age-adjusted incidence of PDAC is ~30% higher among AA than

EA [38], and AA race is an established risk factor for PDAC [21]. Various socioeconomic and lifestyle factors that may contribute to the development of PDAC are more common in the AA population [21], as are certain K-Ras mutations and possibly strong HER2 expression [39]. Intriguingly, it has been demonstrated that K-Ras^{G12D} induces CA in mammary epithelial cells [40] and head and neck papilloma cells [41]. One study found that this mutation is more prevalent among AA than EA (47% vs. 34%), although the difference did not reach statistical significance [39], perhaps due to the relatively small sample size. K-Ras^{G12V}, on the other hand, was significantly more prevalent among AAs in this study, but we are unaware of any data regarding the impact of this mutation on CA. What might be considered indirect evidence that K-Ras^{G12V} promotes CA is the recent finding by Hu and colleagues that this mutation increases the frequency of multipolar anaphases and apoptosis following treatment of ED-1 murine lung cancer cells with seliciclib, a cyclin-dependent kinase inhibitor [42]. CA renders cancer cells vulnerable to multipolar mitosis [36], so cells undergoing multipolar anaphase might have supernumerary centrosomes, although this was not directly tested in that study. The relationship between ethnicity and mutations in genes whose dysregulation is known to drive CA that are common in PDAC (e.g., *TP53* [43, 44], *SMAD4* [41], *CDKN2A* [45], *CHEK2* [46], depicted in **Supplemental Figure 3.7.2**) merits investigation. One study found that a greater proportion of AA PDACs displayed strong HER2 expression than EA PDACs [39], and HER2 overexpression is associated with CA in breast cancer [47, 48]; thus, HER2 overexpression may contribute to the greater extent of CA we uncovered in AA PDACs. More research is needed to confirm the CA-promoting role of ethnicity-associated gene amplifications and mutations in PDAC, although it is tempting to speculate that they underlie the differences in centrosome profiles we observed between AAs and EAs. The diversity of factors that may confer increased PDAC risk that are associated with AA ethnicity are

depicted in **Supplemental Figure 3.7.3**. Although CA is a well-defined risk factor for cancer aggressiveness [36], the literature reports that AAs with PDAC do not experience worse overall survival in multivariate analyses accounting for a variety of factors, such as treatment received and socioeconomic status, as detailed by a recent review of nine relevant studies [49]. This discrepancy cannot be resolved based on existing data and deserves further exploration. Regardless, it stands to reason that AA ethnicity might predict therapeutic response to declustering drugs, and clinical trials testing these drugs clearly should consider ethnicity in their assessment of drug efficacy.

In summary, our microarray analysis suggests that higher levels of certain genes whose dysregulation promotes CA are associated with worse overall survival, although further study is needed to confirm that CA itself is indeed associated with worse clinical outcomes. In line with these *in silico* results, we found that induction of CA in PDAC cell lines resulted in more aggressive cellular behavior, such as increased motility and invasiveness. For the most part, however, we did not find that CA was associated with worse clinicopatholgic features in PDACs aside from lymphovascular invasion in well-differentiated tumors. A larger sample size is needed to confirm these immunohistochemical findings, which seem generally to conflict with us *in silico* and *in vitro* findings. It is possible that the relationship between CA and clinicopathologic features is complex, and some weighted combination of the numerical and structural CA values would be more strongly associated with clinicopathologic features like the extent of differentiation, tumor size, and lymph node positivity. Furthermore, we did not consider subtypes in this study, but it is possible that CA is a prognostic factor only within certain subtypes. Gene expression studies have shown that PDACs can be divided into three subgroups: classical, quasimesenchymal, and exocrine-like [50]. It would be intriguing to evaluate whether quasimesenchymal tumors evince the most extensive CA because this subtype is defined by the expression of genes that promote a

mesenchymal phenotype, which we found was promoted by induction of CA. Interestingly, the quasimesenchymal subtype is associated with the poorest overall survival after resection [50]. In future studies, it will be important to test whether PDACs are susceptible to centrosome declustering drugs and to identify whether certain subtypes of this cancer have more profound centrosome abnormalities and thus might be more susceptible to these drugs. Ultimately, our study establishes CA, a long-standing cancer cell-selective trait, as a quantifiable cell biological property in PDAC that undoubtedly merits further investigation.

3.6 References

1. Siegel, R., D. Naishadham, and A. Jemal, *Cancer statistics, 2013.* CA: A Cancer Journal for Clinicians, 2013. **63**(1): p. 11-30.
2. Klimstra, D.S. and N.V. Adsay, *CHAPTER 35 - Tumors of the Pancreas and Ampulla of Vater*, in *Surgical Pathology of the GI Tract, Liver, Biliary Tract, and Pancreas (Second Edition)*, R.D.O.R. Goldblum, Editor. 2009, W.B. Saunders: Philadelphia. p. 909-960.
3. Rahib, L., et al., *Projecting cancer incidence and deaths to 2030: the unexpected burden of thyroid, liver, and pancreas cancers in the United States.* Cancer Res, 2014. **74**(11): p. 2913-21.
4. Garrido-Laguna, I. and M. Hidalgo, *Pancreatic cancer: from state-of-the-art treatments to promising novel therapies.* Nat Rev Clin Oncol, 2015. **advance online publication**.
5. Bachmann, J., et al., *Pancreatic resection for pancreatic cancer.* HPB : The Official Journal of the International Hepato Pancreato Biliary Association, 2006. **8**(5): p. 346-351.
6. Thota, R., J.M. Pauff, and J.D. Berlin, *Treatment of metastatic pancreatic adenocarcinoma: a review.* Oncology (Williston Park), 2014. **28**(1): p. 70-4.
7. Harsha, H.C., et al., *A compendium of potential biomarkers of pancreatic cancer.* PLoS Med, 2009. **6**(4): p. e1000046.
8. Fong, Z.V. and J.M. Winter, *Biomarkers in pancreatic cancer: diagnostic, prognostic, and predictive.* Cancer J, 2012. **18**(6): p. 530-8.
9. Basto, R., et al., *Centrosome amplification can initiate tumorigenesis in flies.* Cell, 2008. **133**(6): p. 1032-42.
10. Ganem, N.J., S.A. Godinho, and D. Pellman, *A mechanism linking extra centrosomes to chromosomal instability.* Nature, 2009. **460**(7252): p. 278-82.
11. Godinho, S.A., et al., *Oncogene-like induction of cellular invasion from centrosome amplification.* Nature, 2014. **510**(7503): p. 167-71.
12. Chan, J.Y., *A clinical overview of centrosome amplification in human cancers.* Int J Biol Sci, 2011. **7**(8): p. 1122-44.
13. Sato, N., et al., *Centrosome abnormalities in pancreatic ductal carcinoma.* Clin Cancer Res, 1999. **5**(5): p. 963-70.

14. Zhu, J., et al., *AURKA amplification, chromosome instability, and centrosome abnormality in human pancreatic carcinoma cells.* Cancer Gene Cytogenet, 2005. **159**(1): p. 10-7.
15. Sato, N., et al., *Centrosome abnormalities in pancreatic ductal carcinoma.* Clinical cancer research: an official journal of the American Association for Cancer Research, 1999. **5**(5): p. 963-70.
16. Shono, M., et al., *Stepwise Progression of Centrosome Defects Associated with Local Tumor Growth and Metastatic Process of Human Pancreatic Carcinoma Cells Transplanted Orthotopically into Nude Mice.* Lab Invest, 0000. **81**(7): p. 945-952.
17. Budczies, J., et al., *Cutoff Finder: a comprehensive and straightforward Web application enabling rapid biomarker cutoff optimization.* PLoS One, 2012. **7**(12): p. e51862.
18. Pedrali-Noy, G., et al., *Synchronization of HeLa cell cultures by inhibition of DNA polymerase alpha with aphidicolin.* Nucleic Acids Res, 1980. **8**(2): p. 377-87.
19. Ichikawa, A., et al., *Aphidicolin: a specific inhibitor of DNA synthesis in synchronous mastocytoma P-815 cells.* Jpn J Pharmacol, 1980. **30**(3): p. 301-8.
20. Sato, N., et al., *Centrosome Abnormalities in Pancreatic Ductal Carcinoma.* Clinical Cancer Research, 1999. **5**(5): p. 963-970.
21. Yeo, T.P., *Demographics, epidemiology, and inheritance of pancreatic ductal adenocarcinoma.* Semin Oncol, 2015. **42**(1): p. 8-18.
22. Waddell, N., et al., *Whole genomes redefine the mutational landscape of pancreatic cancer.* Nature, 2015. **518**(7540): p. 495-501.
23. Samuel, N. and T.J. Hudson, *The molecular and cellular heterogeneity of pancreatic ductal adenocarcinoma.* Nat Rev Gastroenterol Hepatol, 2012. **9**(2): p. 77-87.
24. Moskovitz, A.H., et al., *Chromosomal instability in pancreatic ductal cells from patients with chronic pancreatitis and pancreatic adenocarcinoma.* Genes Chromosomes Cancer, 2003. **37**(2): p. 201-6.
25. Ganem, N.J., S.A. Godinho, and D. Pellman, *A Mechanism Linking Extra Centrosomes to Chromosomal Instability.* Nature, 2009. **460**(7252): p. 278-282.
26. Sato, N., et al., *Correlation between centrosome abnormalities and chromosomal instability in human pancreatic cancer cells.* Cancer Genet Cytogenet, 2001. **126**(1): p. 13-9.
27. Werner, J., et al., *Advanced-stage pancreatic cancer: therapy options.* Nat Rev Clin Oncol, 2013. **10**(6): p. 323-333.
28. Neoptolemos, J.P., et al., *A randomized trial of chemoradiotherapy and chemotherapy after resection of pancreatic cancer.* N Engl J Med, 2004. **350**(12): p. 1200-10.
29. Bauer, T.W., et al., *Targeting of Urokinase Plasminogen Activator Receptor in Human Pancreatic Carcinoma Cells Inhibits c-Met– and Insulin-like Growth Factor-I Receptor–Mediated Migration and Invasion and Orthotopic Tumor Growth in Mice.* Cancer Research, 2005. **65**(17): p. 7775-7781.
30. Hildenbrand, R., et al., *Amplification of the urokinase-type plasminogen activator receptor (uPAR) gene in ductal pancreatic carcinomas identifies a clinically high-risk group.* Am J Pathol, 2009. **174**(6): p. 2246-53.
31. Mehner, C., et al., *Tumor cell-derived MMP3 orchestrates Rac1b and tissue alterations that promote pancreatic adenocarcinoma.* Mol Cancer Res, 2014. **12**(10): p. 1430-9.
32. Tsai, J.H. and J. Yang, *Epithelial-mesenchymal plasticity in carcinoma metastasis.* Genes Dev, 2013. **27**(20): p. 2192-206.

33. Lee, J.M., et al., *The epithelial-mesenchymal transition: new insights in signaling, development, and disease.* J Cell Biol, 2006. **172**(7): p. 973-81.
34. Ogden, A., P.C. Rida, and R. Aneja, *Heading off with the herd: how cancer cells might maneuver supernumerary centrosomes for directional migration.* Cancer Metastasis Rev, 2013. **32**(1-2): p. 269-87.
35. Pannu, V., et al., *Centrosome-declustering drugs mediate a two-pronged attack on interphase and mitosis in supercentrosomal cancer cells.* Cell Death Dis, 2014. **5**: p. e1538.
36. Ogden, A., P.C. Rida, and R. Aneja, *Let's huddle to prevent a muddle: centrosome declustering as an attractive anticancer strategy.* Cell Death Differ, 2012. **19**(8): p. 1255-67.
37. Kwon, M., et al., *Mechanisms to suppress multipolar divisions in cancer cells with extra centrosomes.* Genes Dev, 2008. **22**(16): p. 2189-203.
38. Howlader N, N.A., Krapcho M, Garshell J, Miller D, Altekruse SF, Kosary CL, Yu M, Ruhl J, Tatalovich Z, Mariotto A, Lewis DR, Chen HS, Feuer EJ, Cronin KA (eds). , *SEER Cancer Statistics Review, 1975-2012,*
39. Pernick, N.L., et al., *Clinicopathologic analysis of pancreatic adenocarcinoma in African Americans and Caucasians.* Pancreas, 2003. **26**(1): p. 28-32.
40. Zeng, X., et al., *The Ras oncogene signals centrosome amplification in mammary epithelial cells through cyclin D1/Cdk4 and Nek2.* Oncogene, 2010. **29**(36): p. 5103-12.
41. Bornstein, S., et al., *Smad4 loss in mice causes spontaneous head and neck cancer with increased genomic instability and inflammation.* J Clin Invest, 2009. **119**(11): p. 3408-19.
42. Hu, S., et al., *CDK2 Inhibition Causes Anaphase Catastrophe in Lung Cancer through the Centrosomal Protein CP110.* Cancer Res, 2015.
43. Tarapore, P. and K. Fukasawa, *Loss of p53 and centrosome hyperamplification.* Oncogene, 2002. **21**(40): p. 6234-40.
44. Fukasawa, K., *P53, cyclin-dependent kinase and abnormal amplification of centrosomes.* Biochim Biophys Acta, 2008. **1786**(1): p. 15-23.
45. McDermott, K.M., et al., *p16(INK4a) Prevents Centrosome Dysfunction and Genomic Instability in Primary Cells.* PLoS Biology, 2006. **4**(3): p. e51.
46. Yang, H.W., et al., *Alternative Splicing of CHEK2 and Codeletion with NF2 Promote Chromosomal Instability in Meningioma.* Neoplasia (New York, N.Y.), 2012. **14**(1): p. 20-28.
47. Guo, H.-q., et al., *Analysis of the cellular centrosome in fine-needle aspirations of the breast.* Breast cancer research : BCR, 2007. **9**(4): p. R48-R48.
48. Montagna, C., et al., *Centrosome abnormalities, recurring deletions of chromosome 4, and genomic amplification of HER2/neu define mouse mammary gland adenocarcinomas induced by mutant HER2/neu.* Oncogene, 2002. **21**(6): p. 890-8.
49. Khawja, S.N., et al., *Pancreatic cancer disparities in african americans.* Pancreas, 2015. **44**(4): p. 522-7.
50. Collisson, E.A., et al., *Subtypes of pancreatic ductal adenocarcinoma and their differing responses to therapy.* Nat Med, 2011. **17**(4): p. 500-503.
51. Pannu, V., et al., *HSET overexpression fuels tumor progression via centrosome clustering-independent mechanisms in breast cancer patients.* Oncotarget, 2015. **6**(8): p. 6076-91.

4 A QUANTITATIVE CENTROSOMAL AMPLIFICATION SCORE (CAS) PREDICTS LOCAL RECURRENCE IN DUCTAL CARCINOMA IN SITU

This study is not published yet. People who contributed to this study are listed below with their contributions:

1. Karuna Mittal: Conceived and designed the study, carried out major experiments (staining, imaging and analysis of the discovery cohort), analyzed and interpreted the data, and wrote the manuscript.
2. Guanhao Wei: Performed the statistical analysis.
3. Jaspreet Kaur: Performed staining and imaging for validation cohort.
4. Michael Shawky Toss: Provided all the tissue samples and associated clinical data helped in calculating the VNPI index for the samples.
5. Da Hoon Choi: Performed image analysis for the validation cohort.
6. Remus. M. Osan: Guided in the statistical analysis and building of the mathematical model and equation for CAS score.
7. Emad A. Rakha: Provided all the tissue samples and provided feedback and suggestions on data presentation.
8. Emiel A. M. Janssen: Contributed tissue samples, associated clinical data and scientific guidance on the study design.
9. Padmashree C. G. Rida: Co-corresponding author on the study -helped in designing the study and critically revised the manuscript.
10. Ritu Aneja: Co-corresponding author of the study- helped in designing the study and critically revised the manuscript.

4.1 ABSTRACT

About 60-80% of ductal carcinoma in situ (DCIS) cases are high-grade (HG) DCIS with an elevated risk of local recurrence (LR) even after a lumpectomy. Due to the lack of accurate recurrence risk prediction model's patients are often under or over treated. Current prognostic models such as Oncotype DX and VNPI lack consistency and are limited to a specific subset of patients. Here in this study, we show that the extent of centrosome amplification (CA) in a DCIS lesion can predict the risk of LR after lumpectomy. By evaluating the severity and frequency of CA in two different cohorts (n=133 and n=207 respectively) we have developed a quantitative Centrosomal Amplification Score (CAS) for each tumor sample. Our results show that the DCIS patients with recurrence exhibited higher CAS and higher CAS was associated with the risk of developing ipsilateral breast event (HR=7.58 for DC and HR=5.8 for VC, $p<0.0001$) which stayed significant (HR=8.5, $p<0.0001$) after taking in account the other confounding factors like age, tumor size, comedo necrosis and radiotherapy. For the high and low CAS groups, the 5-year risks of recurrence were 87.5% and 12.5% respectively ($p<0.001$). Mixed DCIS cases exhibited higher CAS when compared with pure DCIS suggesting presence of the CA as early as in premalignant condition which became significantly higher in the invasive lesions confirming the role of CA in tumor progression. Thus, our data shows that CAS quantifies the risk of recurrence in DCIS with the highest concordance and provides a new tool to help tailor the treatment according to individuals risk of recurrence in DCIS patients.

4.2 Introduction

About 25% of breast cancers (BCs) are DCIS, a pre-invasive form of BC wherein malignant cells are confined to the lumen of a mammary duct with no evidence of invasion beyond the epithelial basement membrane into the adjacent breast stroma. While approximately 60,000 cases of DCIS are diagnosed in the United States each year, 20%-53% of women with untreated DCIS will progress to invasive BC over the course of ≥10 years[1]. Since the progressive potential of a DCIS lesion cannot be reliably determined, surgery (lumpectomy) and radiation is the common course of treatment, with the addition of hormonal therapy in some cases[2]. Unfortunately, despite a lumpectomy, ~35% of DCIS patients present with a local recurrence (LR)[3]. The major challenges in improving the clinical maintenance of the DCIS patients reside in the tailoring of treatment according to individual risks of recurrence to avoid the undertreatment of cases with high risk of recurrence and overtreatment of patients with low risk. Therefore, accurate prognostic markers are required which can improve the recurrence risk stratification for DCIS patients.

Current recurrence predictors such as Van Nuys index[4] and DCIS nomogram[5] (from Memorial Sloan Kettering) based on commonly used histopathological parameters such as histologic grade, tumor margins, and age lack consistency and reproducibility in LR risk prediction[6, 7]. In addition, these tools fail to integrate the molecular predictors, underestimating the heterogeneity of DCIS lesions. Furthermore, the individual prognostic markers have not been successful in predicting risk as they are limited to a specific cohort of patients, lacks external validation and fail to incorporate the histological parameters. Although studies have shown that commercially available and expensive gene-expression based assay Oncotype DX DCIS score has some value in predicting recurrence but the key drawbacks of this score are its limited applicability to a set of patients (ECOG 5194 study) and the poor stratification of high and intermediate- risk patients thus

leaving the actual prognostic value of this tool questionable[8]. Therefore, a pressing clinical need for prognostic indices that incorporate clinical, histopathological and molecular biomarkers taking into account the heterogeneous nature of DCIS lesions persists.

Studies have shown that extensive genetic and phenotypic intratumoral heterogeneity (ITH) is present in DCIS lesions and greater the ITH present in a pre-invasive lesion, the greater is the likelihood of LR and invasive BC[9]. Chromosomal instability (CIN) is well-recognized as a driver of ITH and amplified centrosomes underlie erroneous mitoses and fuel CIN[10, 11]. While normal cells have one centrosome prior to S-phase and two centrosomes after S-phase, cancer cells display centrosome amplification[12] (CA) - an abnormal increase in the number and/or volume of centrosomes. Studies have shown that CA correlates with increased tumor grade, size, metastasis, and/or recurrence in multiple malignancies[13]. Moreover, studies have shown that within DCIS precancerous and preinvasive lesions (including DCIS), indicating that CA is an early event in tumorigenesis[14, 15]. Studies have reported that CA increases with the grade in DCIS and have higher expression of Aurora-A and Nek2 kinases which play key role in centrosome cycle. Also, multiple studies have highlighted the role of genes associated with centrosomes including cyclin-d, cyclin-E, and genes regulating centrosome cycle such as p53, p21 to predict the risk of recurrence in DCIS[16].

Given the evidence supporting i) the presence of CA in DCIS and ii) that many of the signaling pathways whose deregulation has been previously implicated in the induction of CA are deregulated in DCIS it is reasonable to postulate that the organellar-level differences may exist between recurrent and nonrecurrent DCIS. In this study, we present a novel methodology to

quantitate both numerical and structural centrosomal aberrations in tumor samples. Our analytical pipeline allows robust interrogation of the ability of centrosomal overload to predict the risk of LR after lumpectomy. The algorithm developed quantitates the frequency/prevalence and severity of CA (numerical and structural) in clinical samples, and computes a score called the centrosome amplification score (CAS). In this study, we observed that CAS is significantly different for recurrence and no recurrence DCIS patients and that higher CAS was associated with poorer RFS in both discovery and validation cohort. CAS score was able to stratify the patients in high risk and low-risk groups of recurrence with highest concordance (76%; 87.5% of patients with recurrence were in high CAS group) among that reported for all other available recurrence predictive tools. Furthermore, when we incorporated the clinical and histological parameters which are commonly used in the clinics the concordance of CAS increased to 82% thus giving us a tool which incorporates the contribution of clinical, histopathological and molecular biomarkers all in one score and can help tailor the treatment according to the risk of recurrence for DCIS patients. In addition, we observed that the mixed DCIS exhibited higher CAS when compared to the pure DCIS that confirming role of CA in tumor progression.

4.3 Materials and Methods

4.3.1 Clinical tissue sample

Formalin-fixed paraffin embedded DCIS tissue sections (**ICART5 cohort)** were procured from the Nottingham City Hospital DCIS series. Patients were diagnosed between year 1987 to 2012. Samples used in the discovery cohort (n=133) were restricted to pure DCIS cases treated with breast conserving, rather than complete mastectomy, surgery (BCS). Whereas for the validation cohort (n=120) pure DCIS cases treated with either lumpectomy or masectomy were included. DCIS lesions without involvement of invasive component were confirmed by three

independent pathologists. The mixed DCIS (n=87) cohort consisted of tissue sections from patients which were presented with coexisting pure DCIS and invasive lesions. The samples were accompanied by data pertaining to their clinicopathologic variables such as age, Nottingham grade, TNM stage, Ki67 Index, menopausal status, and information about, treatment (adjuvant and radiotherapy), overall survival, progression-free survival, recurrence-free survival (RFS) and date of initial diagnosis, date of surgery, and patient status at last contact. The Institutional Review Board of Nottingham City Hospital approved all aspects of the study. Methods were carried out in "accordance" with approved guidelines stipulated in MTAs and DUAs between Nottingham City Hospital, Nottingham, UK and Georgia State University. Informed consent was obtained from all subjects.

4.3.2 Immunofluorescence imaging of clinical samples

Centrosomes in formalin fixed paraffin-embedded DCIS tissues were immunofluorescently stained for γ-tubulin (red) and nuclei (with DAPI). Images of tissue samples were acquired with Zeiss LSM 700 confocal microscope (using 63x oil emersion lens with numerical aperture of 1.4 and 1.5x optical zoom). All imaging parameters were fixed across all samples. Some imaging parameters that require special attention include fluorophore saturation, detector saturation, offset, and sampling. For optimal results, laser power is adjusted to the minimum level wherein fluorophore emission is saturated. For detector saturation, the gain (master) is adjusted such that the detector registers the target fluorophores in each channel within full range of detector settings (8-bit, 12-bit, 16-bit) to prevent over and under saturation that can result in inaccurate data. The offset was adjusted to minimize the background present in the sample. Given the fact that fine structural details cannot be compromised, we used 1.5X digital zoom setting that results in a

sampling size of 0.07 um/pixel, which is the maximum level of detail a detector can detect. The premarked (by pathologist) DCIS/tumor areas were imaged to obtain at least 10 regions of interest (ROIs) each containing 20-30 nuclei and associated centrosomes.

4.3.3 Scoring of clinical samples

Next, raw 3D image data was processed using IMARIS Biplane 8.2 3D volume rendering software to determine volume of each centrosome within each ROI. "Volume rendering" refers to transforming a 2D image stack for 3D visualization and subsequent analysis. To exclude non-specific signals, a common background subtraction was applied to all images. This parameter is determined by first measuring the average diameter of ~100 centrosomes in 10 ROIs, and then using this measurement as the background subtraction threshold. Automatic detection based on this measurement helped us to eliminate user bias by providing the same level of background subtraction to all samples. Surfacing of target objects (centrosomes) helped us to correct point spread function and to define contours of centrosomes. Next, we applied splitting function where any clustered centrosomes mistakenly detected as single bodies were split by the software into individual centrosomes. Finally, data from all optical sections was ordered to enable volume measurement for each centrosome. The final data of volumes of all centrosomes was then compared to a maximum intensity projection image and centrosomes for each cell are quantified based on proximity to their associated nuclei. The number and volume of all centrosomes associated with each nucleus in the tumor area was recorded.

4.3.4 Analysis

Centrosomes in breast tissues (normal, DCIS or tumor) were categorized into individually distinguishable centrosomes (iCTRs) and megacentrosomes (mCTRs). iCTRs are defined as centrosomes that stain positive for γ-tubulin, with centrosomes numbers and boundaries clearly

distinguishable and volumes that lie within the range of centrosome volumes found in normal breast tissue stained for γ-tubulin. mCTRs are centrosomes in a neoplastic region that stain positive for γ-tubulin and whose volume is greater than the upper limit of the centrosome volume range found in corresponding normal tissue immunostained for γ-tubulin. mCTRs are the centrosomes with aberrantly large volumes. Volume range for a normal centrosome in breast tissue was determined by analyzing volumes of both adjacent uninvolved tissue from cancer patients and normal tissue for disease-free individuals for each cancer type.

4.3.5 Determination of normal volume of centrosomes

To determine the normal range of volume, we analyzed volume of 500 centrosomes for each sample in adjacent uninvolved tissue from cancer patients (n=40) and in normal tissues (n=40) from reduction mammoplasties. We evaluated the volume of centrosomes as described in analysis section. Interestingly we observed that the mean centrosome volume for the adjacent uninvolved tissue sections was higher when compared to the normal tissues from reduction mammoplasty. Thus, chose the smallest and largest values for iCTR volume of normal tissues as "normal centrosome volume range" for breast tissue. Mean volumes of centrosomes in normal breast epithelial cells ranged from 0.02-0.74 μm3. All centrosomes in each ROI are thus categorized as iCTRs or mCTRs.

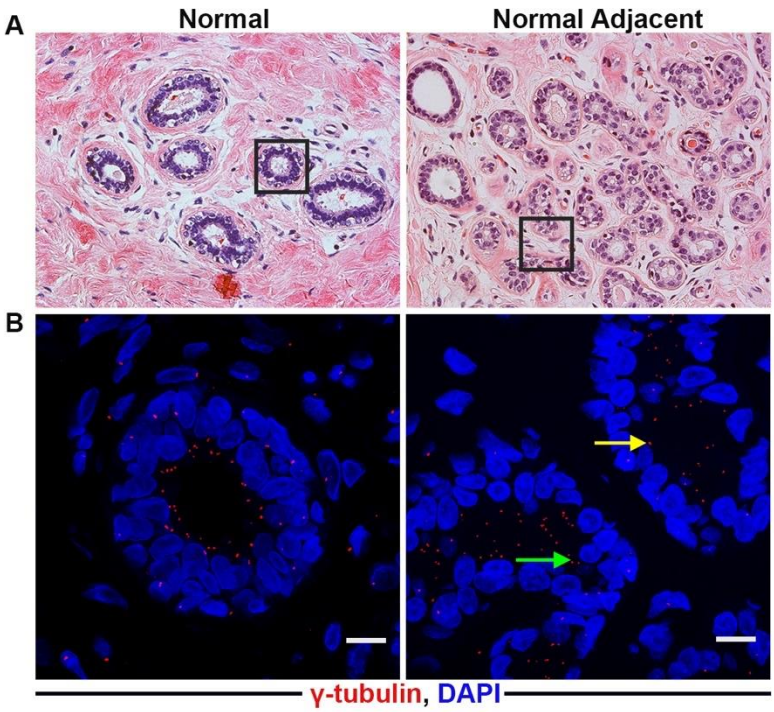

Figure 4.3.1 Representative immunographs of normal and normal adjacent breast tissue sections for centrosomes.
Representative H&E images of the ducts of the DCIS recurrence and no recurrence cases. (Images were captured at 20x magnification). (B) Confocal micrographs showing numerical and structural CA in recurrence and no recurrence DCIS tissue sections.

4.3.6 Algorithm-based analytics

A cumulative Centrosome Amplification Score (CAS) was computed for each sample on the basis of the formula: CAStotal =CASi + CASm, where CASi and CASm are scores that describe numerical and structural CA phenotypes, respectively, in the sample.

Equation 1 for CASi represents how an aggregate value reflecting both frequency and severity of numerical CA is derived for the sample:

$$CASi = Average\left(\frac{N_i - R_{th}}{R}\right) * \frac{percentage(N_i > R_{th})}{scaling\ factor\ \beta_i}$$

$$= \left(\frac{\sum_{i=1,N_i>2}^{N}(N_i - 2)}{\sum_{i=1}^{N} I(N_i > 2)} * \frac{1}{R}\right) * \frac{p_i}{\beta_i}$$

where: R_{th} is the threshold for number of centrosomes, which is 2 here. pi is the percentage of cells with >2 iCTRs; ßi is a scaling factor that may be used to ensure that both CASi and CASm are given equal weight in the formula for CAStotal; R is the range for normal distribution from 0 to 2, which is 2 here; Ni is the number of iCTRs in a cell that contains more than 2 iCTRs; N is the total number of cells analyzed in the sample; i in Ni is used to indicate taking the average over cells with numerical CA.

The "severity" component of CASi, (i.e., $Average\ \left(\frac{N_i - R_{th}}{R}\right)$ quantifies how "severe" the numerical CA is [i.e., the extent to which the numerical CA exceeds the baseline value of 2 in cells that carry three or more iCTRs (i.e., Ni >2)]. Therefore, cancer cells with 1 and 2 iCTRs do not contribute to this component. Since cells with larger numbers of iCTRs represent a more severe numerical CA, a linear measurement was implemented to provide a measure of the number of iCTRs (above the baseline value of 2) in a given cell by computing the score (Ni - 2) for each cell. Finally, an average of all these scores is determined. The "frequency" component of the CASi score (i.e., pi/ßi) provides the scaled frequency of numerical CA in the sample. CASi scaling factor β_i value we used here is 0.1 for breast tissue. Equation II for CASm represents how an aggregate value reflecting both frequency and severity of structural centrosome amplification, is derived for the sample:

$$CASm = Average\left(\frac{V_{im} - V_{th}}{\sigma_{V_{im}}}\right) * \frac{percentage(V_{im} > V_{th})}{scaling\ factor\ \beta_m}$$

$$= \frac{\sum_{i=1}^{N}\sum_{m=1}^{N_i}(V_{im} - 0.735) * I((V_{im} > 0.735)}{\sigma_{V_{im}}} * \frac{p_m}{\beta_m}$$

where: pm is the percentage of cells with mCTRs; $V_{im}$is the volume of a megacentrosome associated with a cell nucleus of m_{th} centrosome in i_{th} nucleus; where a megacentrosome is defined as a centrosome whose volume exceeds the V_{th} critical for that tissue; V_{th} critical for a given tissue is the maximum volume of a normal centrosome in that tissue which was 0.735 for breast tissue; ßm is a scaling factor used to ensure that both CASi and CASm are given equal weight in the formula for CAStotal. value of ßm used here is 0. 148.. $\sigma_{V\,im}$ is the standard deviation of centrosomes?

For each mCTR (centrosome whose volume exceeds the upper limit of the normal centrosome volume range for that tissue), a z-score is computed based on the formula below, reflecting the extent to which the volume of that mCTR exceeds the maximal normal value (i.e., the value for $V_{im} - V_{th}$critical is computed) relative to the baseline (achieved by dividing by the $\sigma_{V\,im}$ the standard deviation):

$$\mathrm{z} = \frac{V_{im} - V_{th}}{\sigma_{V\,im}}$$

Next, this value is multiplied by the number of mCTRs per nucleus. Finally, all these values are averaged in order to obtain the severity score. The frequency component of CASm has essentially the same overall mathematical formula as the corresponding term in the CASi component. In the present form of the algorithm, the components CASi and CASm, contribute equally to the total CAS score and are thus given equal weight.

4.3.7 Statistical Analysis

The test of group mean differences shown in Box-Whisker Plots is based on nonparametric Wilcoxon Rank Sum Tests and Kruskal-Wallis Tests depending on the number of groups.

Recurrence free survival was used as the endpoint for the survival analysis. Log-rank test of equality over strata was applied to test the differences among the Kaplan Meier survival curves. Cutoff points selected for all CAS scores in discovery set were kept same for validation cohort as well. To estimate the effect of related variables on Hazard Ratios(HRs) together with 95% confidence intervals, we used univariate or multivariate cox proportional hazard regression model. Statistical analysis was performed using SAS software 9.4 (SAS Institute Inc., Cary, NC). Statistical significance we claimed was based on $p< 0.05$ for each test we conducted.

4.4 Results

4.4.1 Traditional histopathological parameters fail to predict recurrence in DCIS patients from the discovery set

In our discovery dataset, there were 133 (ICART5 cohort) patient samples with sufficient tissue for CA analysis. Out of these 133 samples 32 patients presented with ipsilateral recurrence. Patient cohort details are shown in Table 1. The median age of the 133 patients in the discovery group was 58, and the median follow up was 24 months. Comedo necrosis was present in 111 and no necrosis in 22 patients. Out of 133 patients, 118 were nuclear grade 3, 10 were nuclear grade 2, and 5 were nuclear grade 1. 3% of patients had close excision margins (1mm or less). Out of 133 patients, 55 received patients received radiotherapy, and none of the patients were treated with adjuvant chemo or hormonal therapy. Tumor high grade, the presence of comedo necrosis and radiotherapy were three clinicopathological parameters which showed significant proportional differences within the recurrence group and who remained recurrence-free (Table 4.4.1) in the subgroups. However, when we performed univariate Cox regression analysis none of these parameters showed any significant association with RFS (Table 4.4.2). Thus, indicating the limited role of the histopathological parameters in predicting recurrence in this dataset.

Table 4.4.1 Descriptive statistics of clinicopathological characteristics for DCIS patients (ICART5 cohort) based on the recurrence status in the discovery cohort.

Baseline Characteristics	Recurrence Free	Recurrence	p value
Patient Age			
Age>58, n (%)	51 (50.00)	15 (46.88)	0.7577
Age<=58, n(%)	51 (50.00)	17 (53.13)	
Tumor Size			
Size>16, n(%)	50 (49.02)	17 (53.13)	0.6853
Size<=16, n(%)	52 (50.98)	15 (46.88)	
Grade, n(%)			
High	94 (92.16)	25 (78.13)	0.0281
Mid and Low	8 (7.84)	7 (21.88)	
Comedo Necrosis, n(%)			
No	12 (11.76)	11 (34.38)	0.0031
Yes	90 (88.24)	21 (65.63)	
Radiotherapy, n(%)			
No	55 (53.92)	24 (75.00)	0.0344
Yes	47 (46.08)	8 (25.00)	
Receptor Status, n(%)			
ER/PR Negative	4 (3.92)	2 (6.25)	0.6344
ER/PR Positive	17 (16.67)	9 (28.13)	
HER2-Negative	17 (16.67)	5 (15.63)	
HER2-Positive	5 (4.90)	1 (3.13)	
TNBC	9 (8.82)	1 (3.13)	
Other	50 (49.02)	14 (43.75)	

4.4.2 Recurrent DCIS exhibits higher CAS compared to non-recurrent DCIS

First, we immunofluorescently stained (details in materials and methods section) formalin fixed paraffin embedded resection samples from DCIS patients (n=133) for centrosomes using an antibody against γ-tubulin, and co-stained with DAPI for nuclei. As described in the materials and methods section employing confocal microscopy we imaged the immune-stained slides and

processed the raw 3D image data using IMARIS Biplane 8.2 3D volume rendering software. Next, we calculated the centrosome number and volume in ~250 cells of each sample and finally, with the help of mathematical equation, we integrated the numerical (CASi) and structural (CASm) aberrations to generate a composite CAS total value for each sample. We observed that the DCIS cases with recurrence (mean score 1.3055) exhibited significantly higher CASi when compared with the no recurrence samples (mean score 0.73196) (p=0.0002; Figure.4.4.1C) (Note: values indicated in the boxplots are based on Wilcoxon's rank test). As mentioned in materials and method section CASi is a combination of the severity and frequency of CA. When we looked at them separately, DCIS cases with recurrence showed higher severity (p=0.09 Figure.4.4.2A) and significantly higher frequency (p=0.0001 Figure.4.4.2B). Furthermore, when we looked at the structural amplification the value of CASm was significantly higher (p=0.0280, Figure.4.4.1D) in recurrence (mean score 1.09586) cases when compared with the no recurrence (mean score 0.80612) cases. Not only this further when CASm was broken in the severity and frequency we found that DCIS cases with recurrence exhibited significantly higher severity (p=0.0070, Figure.4.4.2C) and frequency (p=0.0468, Figure.4.4.2D) for structural amplification. Lastly, when we combined the CASi and CASm to generate the CAS total values as mentioned in materials and methods section, we observed that the CAS total was significantly higher in the recurrence (mean score 2.4050) group when compared with the no-recurrence group (mean score 1.5381). Thus, collectively our data suggests that a significant difference in centrosomal aberrations exist between the recurrence and recurrence-free DCIS samples.

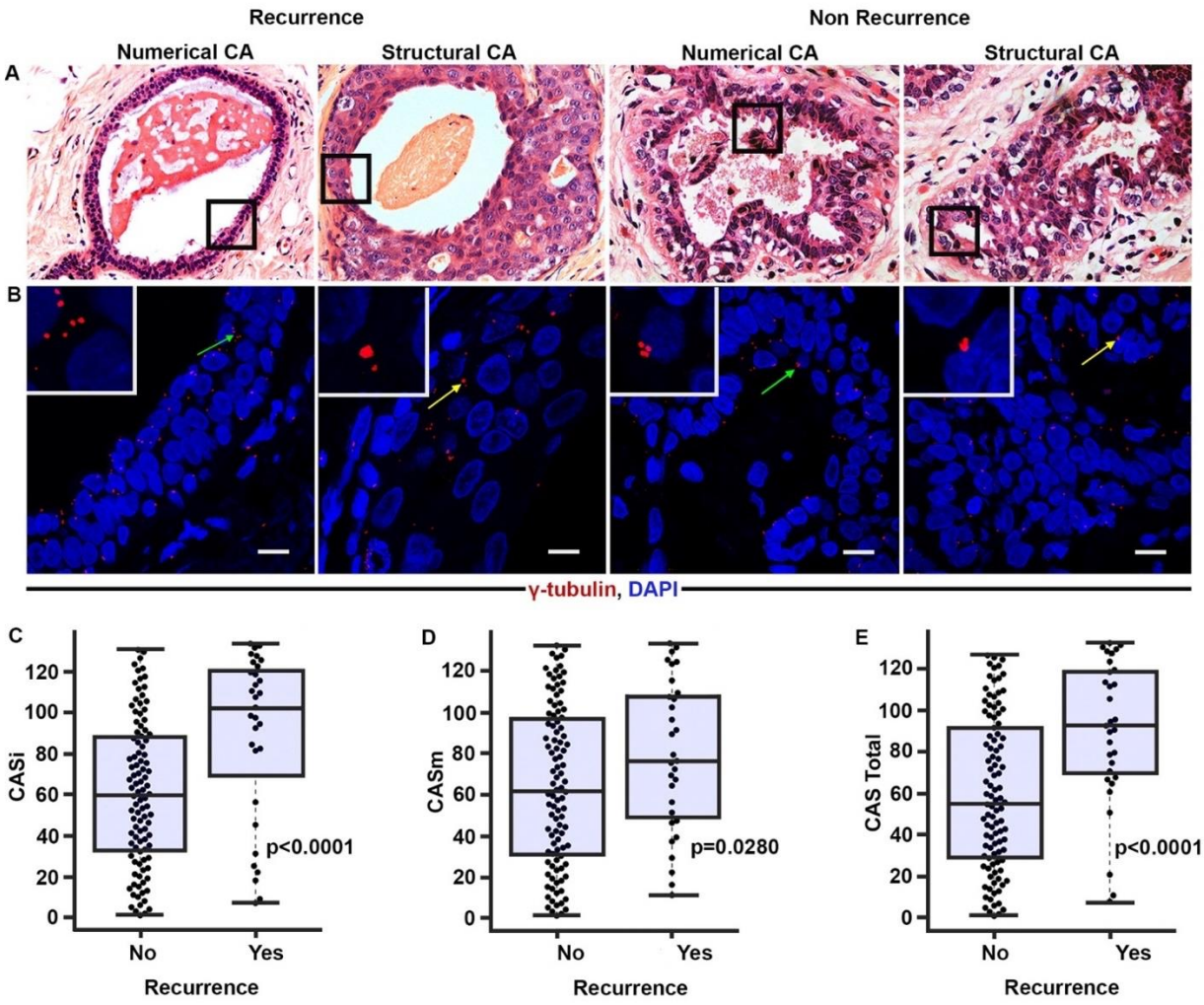

Figure 4.4.1 DCIS with ipsilateral recurrence exhibit higher CAS.
(A) Representative H&E images of the ducts of the DCIS recurrence and no recurrence cases. (Images were captured at 20x magnification). (B) Confocal micrographs showing numerical and structural CA in recurrence and no recurrence DCIS tissue sections. DCIS tissue sections were immunostained for centrosomes (γ-tubulin, red) and counterstained with DAPI (blue). Scale bar (white), 20μm. (C) Representative Beeswarm Box plots for the pure DCIS (n=133) cases with recurrence (n=32) and no-recurrence (101) for CASi. (D) Representative Beeswarm Box plots for the pure DCIS (n=133) cases with recurrence (n=32) and no-recurrence (101) for CASm, (E) Representative Beeswarm Box plots for the pure DCIS (n=133) cases with recurrence (n=32) and no-recurrence (101) for CAStotal. $p<0.05$ was considered statistically significant.

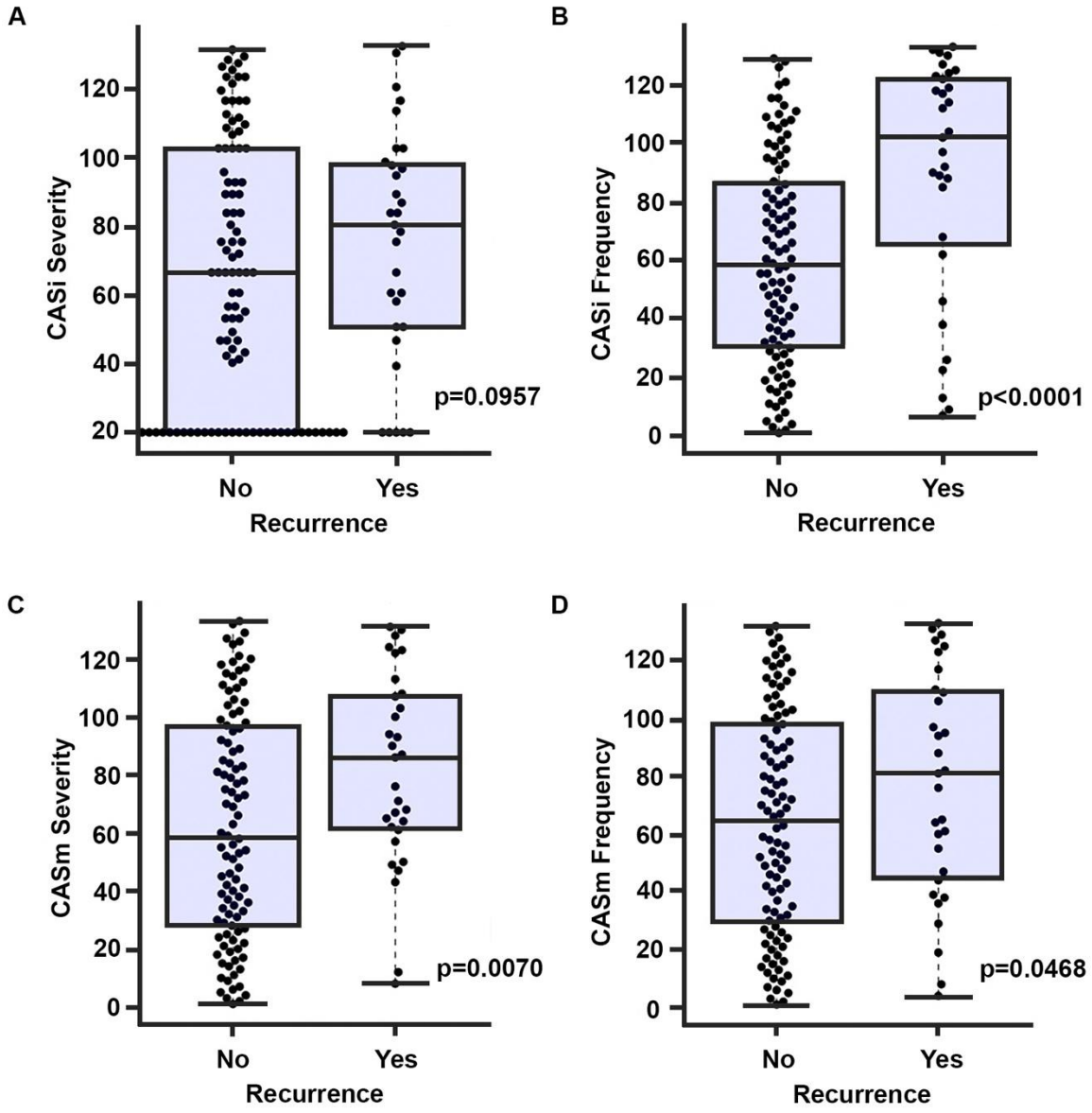

Figure 4.4.2 DCIS with ipsilateral recurrence exhibit higher CAS
Representative Beeswarn Box plots for the pure DCIS (n=133) cases with recurrence (n=32) and no-recurrence (101) for different CAS values. A) CASi severity distribution, B) CASi frequency distribution, C) CASm severity distribution, D) CASm frequency distribution. $p<0.05$ was considered significant**.**

Next, we co-immunolabelled 15 DCIS samples with the centrosomes and centrioles respectively with γ-tubulin and centrin-2 and performed the quantitation as described above. We found that γ-tubulin foci invariably overlapped with centrin-2 foci in all the samples confirming that the

structural amplified centrosomes represent enlarged γ-tubulin foci are bona fide centrosomes and not just fragments of the pericentriolar material. In addition, we observed that there were no supernumerary centrin-2 foci were present, suggesting that the enlarged γ-tubulin foci represent structurally augmented centrosomes and not supernumerary centrosomes so tightly clustered as to be indistinguishable (Fig 4.4.3).

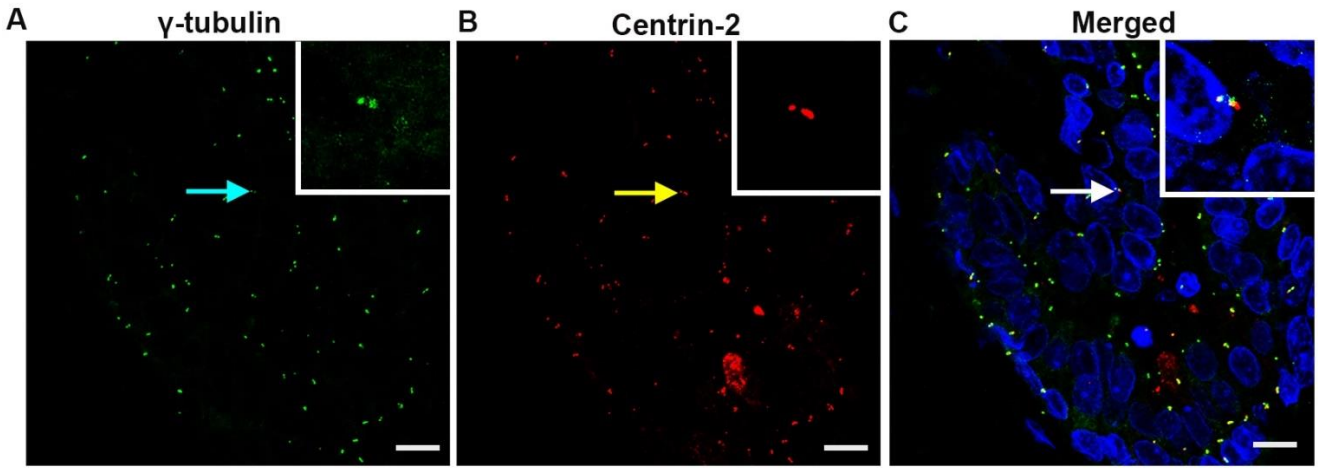

Figure 4.4.3 Representative immunographs DCIS tissue sections immunolabeled for centrin-2 (red) and γ-tubulin (green) and DAPI (blue) in split form.

4.4.3 CAS can stratify high- grade DCIS patients into subgroups with the high and low risk of recurrence

Further, when we stratified all the patients into low- and high-CAS groups (threshold used was the one that minimized log-rank p-value) (Figure. 4.4.4), we observed that high-CASi (threshold=0.09) DCIS patients were associated with poorer RFS ($p<0.001$, HR=4.802; for CASisi $p=0.0879$, HR=2.77, threshold= 1.09; for CASifi $p<0.0001$, HR=4.766, threshold= 0.08) when compared with the low CASi group. Similarly, we observed that high CASm (threshold=0.0877) group was associated with poorer RFS ($p=0.0243$, HR=2.396; for CASmsi $p=0.0055$, HR=5.409, threshold=.3133, CASmfi $p=0.069$, HR=2.446, threshold=0.171) when compared with the low

CASm group. Total CAS (threshold= 1.435) value was able to stratify the high-risk and low-risk DCIS patients with highest significance and Hazard ratio ($p<0.001$, HR= 7.185) (Fig4.4.4 and 4.4.5). Interestingly, we observed that 93% of the cases with recurrence were in high CAS group. This association with CAS stayed significant ($p<0.001$, HR=8.51) even after accounting for the confounding factors like comedo necrosis, tumor grade, tumor size, age and the radiotherapy status of the patient's Table 4.4.2. As shown in Table 4.4.2 none of the clinicopathological parameters showed any significant association with the recurrence except the CAS in both univariate and multivariate analysis.

Furthermore, we performed the concordance analysis using SAS PROC PHREG procedures. This procedure is based on the Harrell's concordance index. Herein higher the C-statistics values, the better the model can discriminate between patients who will present recurrence and patients who do not. The results from this statistical test indicated that for any patient who has poorer/lower RFS it would have a probability of 72.6% to be in CAS total high group.

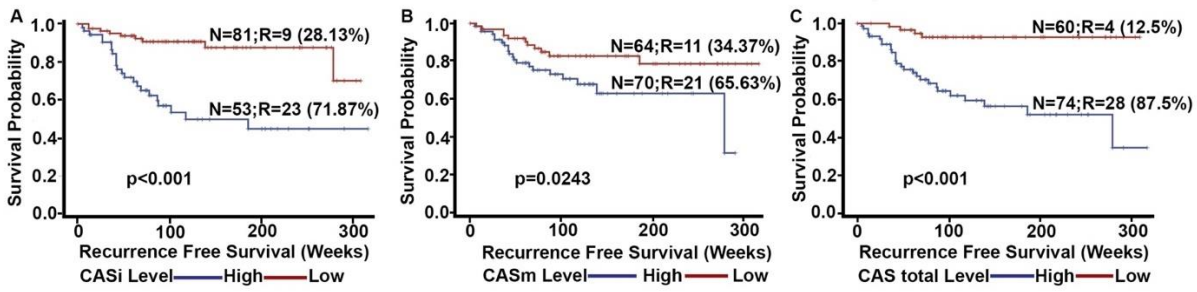

Figure 4.4.4 Higher CAS is associated with poorer RFS in DCIS patients
Kaplan Meier survival curves representing the RFS in DCIS patients: (A) CASi high and low groups, (B) CASm high and low groups, (C) CASt high and low groups. N is the total number of patients in each group and R represents the number of patients who showed recurrence. % calculated represents percentage/proportion of the recurrence patients out of the total number of

recurrence patients in both groups. p<0.05 is considered significant.

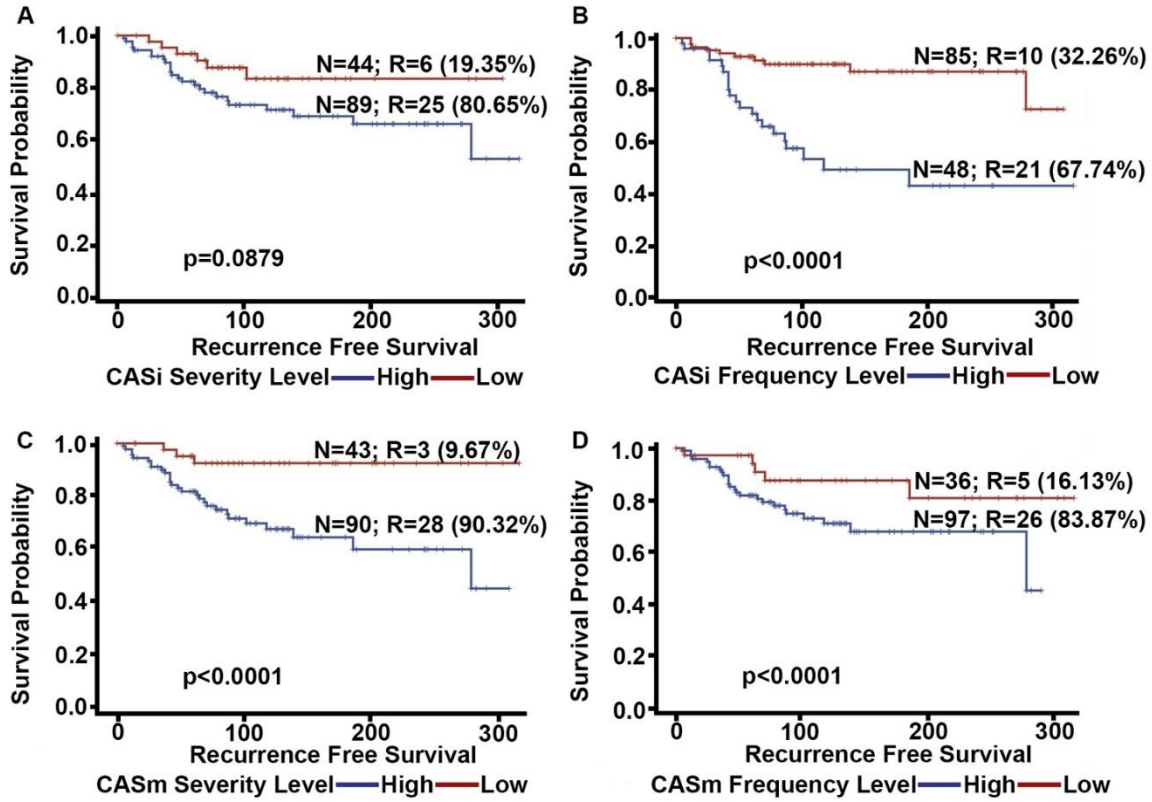

Figure 4.4.5 Higher CAS is associated with poor RFS in DCIS patients

Kaplan Meier survival curves representing the RFS in DCIS patients: (A) CASi high and low groups based on the severity component, (B) CASi high and low groups based on the frequency component, (C) CASm high and low groups based on the severity component, (D) CASm high and low groups based on the frequency component. N is the total number of patients in each group and R represents the number of patients who showed recurrence. % calculated represents percentage/proportion of the recurrence patients out of the total number of recurrence patients in both groups. p<0.05 is considered significant**.**

Table 4.4.2 Univariate and Multivariate Cox proportional regression analysis for the risk of recurrence in DCIS patients treated with lumpectomy comparing the influence of common clinicopathological variables along with the CAS total model.

Variables		Univariate Analysis				Multivariate Analysis			
		Pr > ChiSq	Hazard Ratio	95% Hazard Ratio Confidence Limits		Pr > Chi Sq	Hazard Ratio	95% Hazard Ratio Confidence Limits	
CAS total	CASt High vs low	0.001	7.58	2.893	24.164	<.0001	8.361	2.893	24.164
Age	Age High vs low	0.8532	0.935	0.459	1.904	0.6345	0.837	0.402	1.742
Tumor size	Tumor size High vs low	0.3032	1.466	0.708	3.306	0.4269	1.354	0.641	2.858
Grade	Grade High vs low	0.0921	0.317	0.134	0.752	0.0927	0.440	0.169	1.146

Comedo Necrosis	Comedo present vs absent	0.0603	2.441	1.149	5.185	0.0714	2.106	0.937	4.733
Radiotherapy	Radiotherapy No	0.1405	1.959	0.870	4.414	0.3472	1.530	.630	.714

4.4.4 CAS can stratify the DCIS patients in recurrence and recurrence-free group with higher significance than the Van Nuys Prognostic Index (VNPI)

VNPI is based on clinical and histopathological markers like tumor size, margin width, pathologic classification (based on nuclear grade and presence/absence of comedo necrosis) and age of the patients. This index has been used in clinics to decide the treatment strategy for the patients presented with DCIS. Therefore, to test the performance of this test in our cohort we calculated VNPI based on the scoring methods described in the literature. Briefly, each of the factors is assigned a score between 1-3, and the sum total of values for the four parameters is taken as final score further stratify the patients in high, low and intermediate risk groups of the recurrence. Herein, we used the binary cutoff score of ≥8. Next, we performed univariate and Kaplan Meier Survival analysis to compare the performance of the VNPI index in the discovery cohort (n=100 as VNPI index was available only for 100 patients out of total 133) (Fig 4.4.6A and B). We observed that there was no significant association of higher VNPI with the poor RFS and that VNPI was not able to stratify the patients in the high and low-risk for recurrence. In contrast, CAS for the same patients was able to stratify the patients in high and low risk group and was able to predict recurrence with higher significance and HRs (CAS- 8.8 vs. VNPI 0.959) (Table 4.4.3). Moreover, when we performed multivariate analysis taking in account the other confounding factors like tumor size, presence of comedo necrosis, age and radiotherapy along with VNPI, CAS presented highest association with RFS with HR=10.41. These findings suggest that the CAS

model is better than the traditional VNPI index in predicting the recurrence in DCIS patients.

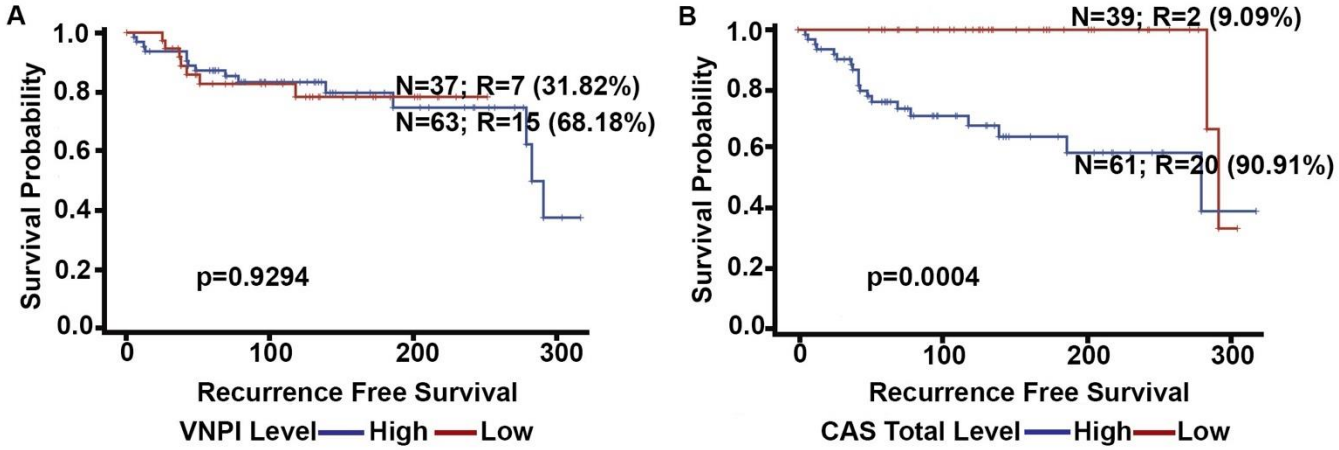

Figure 4.4.6 Kaplan Meier survival curves representing the RFS in DCIS patients based on the VNPI and CAS.
N is the total number of patients in each group and R represents the number of patients who showed recurrence. % calculated represents percentage/proportion of the recurrence patients out of the total number of recurrence patients in both groups. $p<0.05$ is considered significant.

Table 4.4.3 Univariate analysis for the risk of recurrence in DCIS patients treated with lumpectomy comparing the performance of VNPI and CAS models.

Variables		Univariate Analysis			
		p-value	Hazard Ratio	95% Hazard Ratio Confidence Limits	
CAS total	High vs low	0.0034	8.847	2.0671	37.93
VNPI	High vs low	0.9291	0.959	0.377	2.436

4.4.5 CAS combined with age, tumor size and comedo necrosis is a superior model for prediction of recurrence in DCIS patients

To further test the clinical significance of CAS score, we evaluated the associations of CAS with the clinicopathological parameters used traditionally in clinical practice. In line with the understanding that CA is associated with the more aggressive phenotype of the disease, we observed that the CAS association with the recurrence risk (RR) in these subgroup analyses was similar to that of the overall group of patients. Herein, in the recurrence rate forest plot (Fig 4.4.7) it is shown that the high age group (red boxes) which is regardless of CAS is at high risk of

recurrence (0.44) compared to that for overall patients (0.33). When we further stratified this group in high and low CAS groups we observed that the recurrence rates for the high CAS group (green boxes- RR-0.73) and low (blue boxes-RR- 0.10) (Fig 4.4.7) suggesting that CAS was further able to stratify high and low age group in high and low-risk groups as with better RR. Similar trends were observed for the tumor size, tumor grade, radiotherapy and comedo necrosis.

Thus, collectively these findings suggested that CAS compliments the traditional histopathological parameters and is able to further stratify the patients in high and low-risk group of recurrence with better RR. Next, to analyze if the compounded effect of CAS plus other parameters is able to further stratify the patients' estimated recurrence rate with more significant RFS difference among hazard ratios we constructed a multivariate logistic regression model using CASi, CASm, Age(High/Low), Comedo Necrosis(presence/absence), and Size(Large/Small) to estimate whether recurrence will happen or not. Here we defined odds as ratio of Recurrence against Recurrence free and computed the log odds value using following mathematical equation.

Log(Odds)=-3.1807+1.6072*CASi+0.7823*CASm-0.4757*I(age=High)

+0.9535*I(Comedo=present) +0.3230*I(Size=Large)

Here based on log(odds) value we classified patients in recurrence and recurrence free groups. Wherein if log odds is positive, then we classify that case into recurrence group, and if it is negative, it falls in into recurrence free group. When we compared our prediction result with true final recurrence status, we observed 83.02% concordance rate. This multivariate model greatly improves prediction accuracy compared with the model using CAS as predictor only, which has 74.47% of concordance. Thus, collectively these findings suggest that the CAS compliments the traditional histopathological parameters and if combined with these clinical parameters is a superior model.

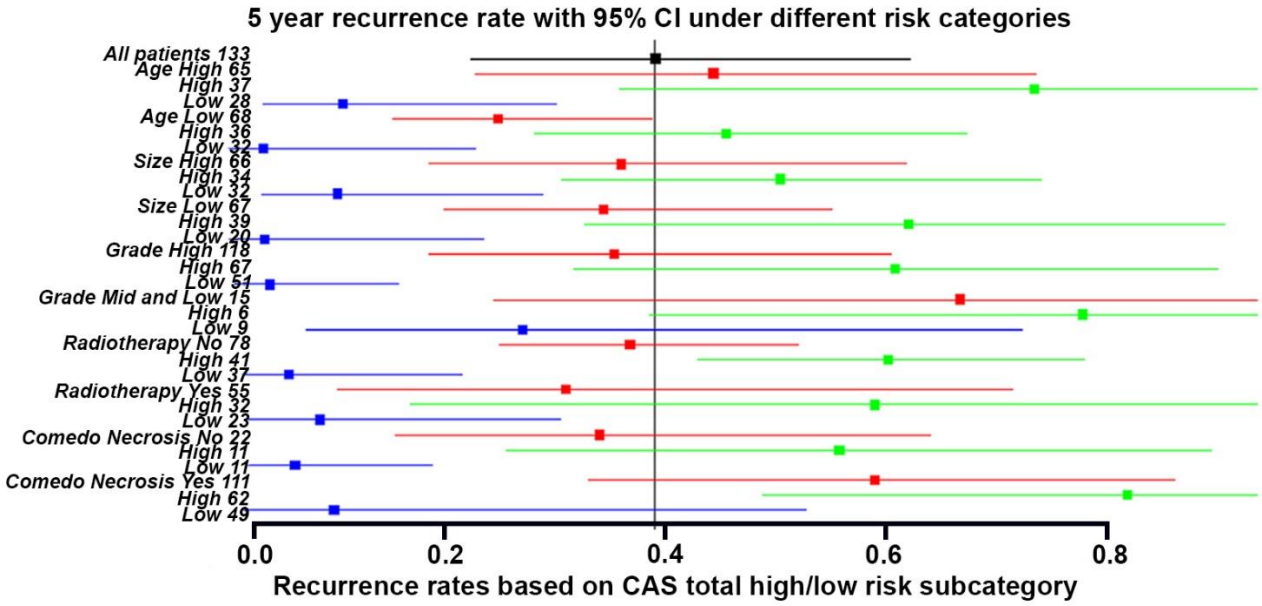

Figure 4.4.7 Recurrence rate for the clinically relevant parameters based on CAS total
Forest plot representing the estimates of the 5- year recurrence rate (with 95% confidence interval) according to the CAS high and low risk subgroups for the clinical and pathological parameters. Black box represents overall recurrence rate in patients (.39) Red box represents the recurrence rate presented for the specific clinical parameter regardless of CAS. Green box represents the recurrence rate in the high CAS group and blue represents recurrence rate in CAS low group in every specific subgroup.

4.4.6 Recurrent DCIS cases exhibit higher CAS compared to the non-recurrence cases, and high CAS is associated with worse RFS, in the validation cohort

Next, to confirm the legitimacy of the prediction of CAS and the CAS plus score (CP) model we tested its performance on an exclusively different cohort of DCIS patients. Our validation cohort consisted of 120 patient samples out of which 27 patients presented with ipsilateral recurrence. Patient cohort details are shown in Table 4. The median age of the 120 patients in the discovery group was 56, and the median follow up was 19 months. Relative to the discovery cohort patients were equally distributed in subgroups based on Comedo necrosis and grades. Where Comedo necrosis was present in 67 and no necrosis in 53. Out of 120 Patients, 60 were nuclear grade high, 37 were grade median and 23 were low grade. 1.7% of patients had close excision margins

(1mm or less). Only 14 patients were treated with the radiotherapy out of 120. In this cohort, the clinicopathological parameters like tumor size, presence of the comedo necrosis and no radiotherapy were three clinicopathological parameters which showed significant proportional differences within the recurrence group as well as when compared with the patients who remained recurrence-free and they were also associated with the RFS.

Employing the same methodology as mentioned for discovery cohort we immunofluorescently stained 120 formalin fixed paraffin embedded resection samples from DCIS patients to visualize centrosomes and calculated the CAS scores. Similar to the discovery cohort we observed that regardless of grade DCIS cases with recurrence exhibited significantly higher CAS total when compared with the no recurrence samples ($p<0.0001$) (Figure.4.4.8B). Further we observed similar trends for the other CAS values as we observed in discovery cohort where significant higher CAS values were noted between the ranked mean score values of CASi ($p<0.0001$) and CASm ($p<0.0001$) including the severity (CASi- $p=0.0046$, CASm-$p=0.0037$) and frequency (CASi- $p<0.0001$, CASm-$p<0.0001$) for recurrence group when compared with the no recurrence group (Figure 4.4.8 and 4.4.9).

Table 4.4.4 Descriptive statistics of clinicopathological characteristics for DCIS patients (ICART5 cohort) based on the recurrence status in the validation cohort.

Baseline Characteristics	Recurrence Free	Recurrence	p value
Patient Age			
Age>58, n(%)	47 (50.54)	8 (29.63)	0.0549
Age<=58, n(%)	46 (49.46)	19 (70.37)	
Tumor Size			
Size>16, n(%)	38 (40.86)	20 (74.07)	0.0024
Size<=16, n(%)	55 (59.14)	7 (25.93)	
Grade, n(%)			
High	46 (49.46)	14 (51.85)	0.8270
Mid and Low	47 (50.54)	13 (48.15)	
Comedo Necrosis, n(%)			
Absent	58 (62.37)	9 (34.62)	0.0117
Present	35 (37.63)	17 (65.38)	
Radiotherapy, n(%)			
No	81 (87.10)	25 (92.59)	0.4336
Yes	12 (12.90)	2 (7.41)	

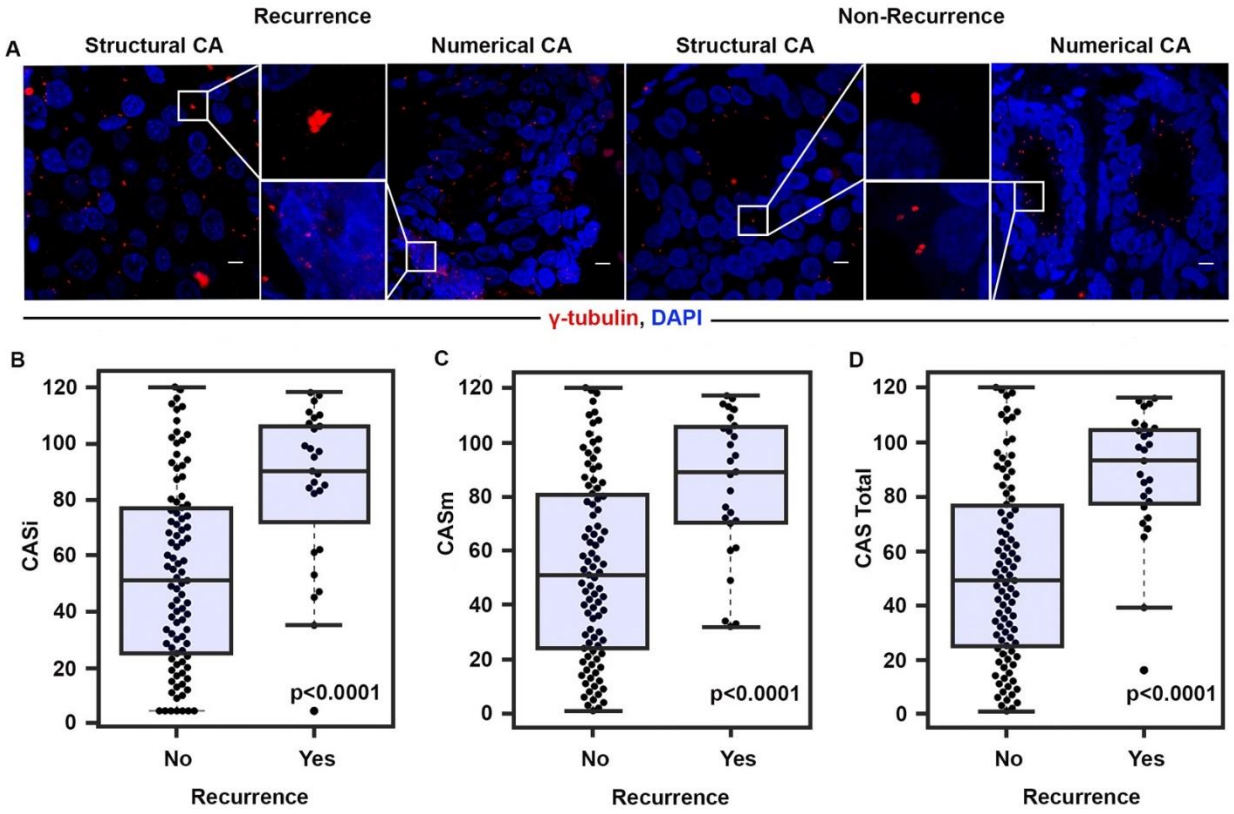

Figure 4.4.8 DCIS with ipsilateral recurrence exhibit higher CAS in validation cohort
(A) Confocal micrographs showing numerical and structural CA in recurrence and no recurrence DCIS tissue sections. DCIS tissue sections were immunostained for centrosomes (γ-tubulin, red) and counterstained with DAPI (blue). Scale bar (white), 20μm. (B) Representative Box-whisker plots for the pure DCIS (n=120) cases with recurrence (n=27) and no-recurrence 93) for CASi. (C) Representative Box-whisker plots for the pure DCIS (n=120) cases with recurrence (n=27) and no-recurrence 93) for CASm. (D) Representative Box-whisker plots for the pure DCIS (n=120) cases with recurrence (n=27) and no-recurrence 93) for CAS total. $p<0.05$ was considered statistically significant.

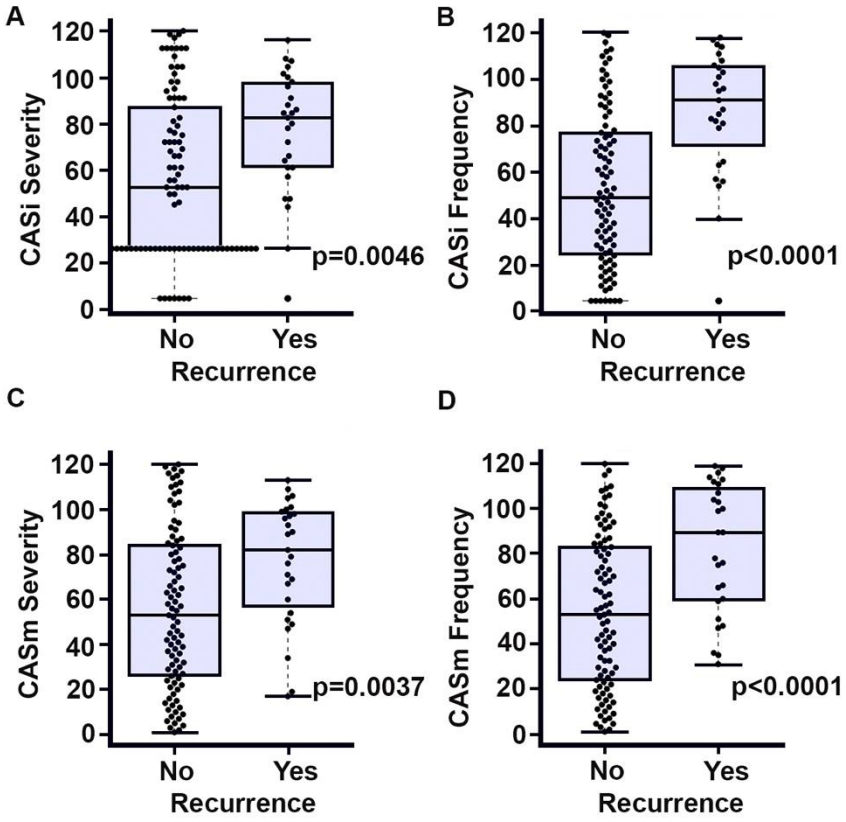

Figure 4.4.9 DCIS with ipsilateral recurrence exhibit higher CAS
Representative Box-whisker plots for the Grade matched (grade 3) pure DCIS (n=127) cases with recurrence (n=30) and no-recurrence (93) for different CAS values. A) CASi distribution, B) CASi severity distribution, C) CASi frequency distribution, D) CASm distribution, E) CASm severity distribution, F) CASm frequency distribution. $p<0.05$ was considered significant.

Furthermore, in line with the findings in discovery cohort, when we looked at the RFS based on the predefined CAS cutoffs for discovery cohort, we observed that CAS values were able to stratify patients in high and low risk of recurrence with great significance. As shown in the Fig 8A high 74% of the recurrence patients fall into high CASi group whereas only 23% of the no recurrence patients fall in this group. 92% of patients from the recurrence-free group are classified in the low CASm group. Similarly, for CAS total significantly higher proportion of recurrence-free patients i.e. 73% falls in the low CAS group whereas the significantly higher proportion of recurrence group, i.e. 66.96% of recurrence falls in the high CAS total group. Though lower than the discovery

cohort the hazard ratios of CAS total (p<0.001, HR=4.127) on the validation cohort are still higher than the other clinicopathological parameters (Table 4.4.5). This association stays significant even after controlling the other confounding factors like age, tumor size, grade, comedo necrosis and radiotherapy. Thus, the results collectively indicate that the CAS can significantly predict recurrence in DCIS patients from two different cohorts.

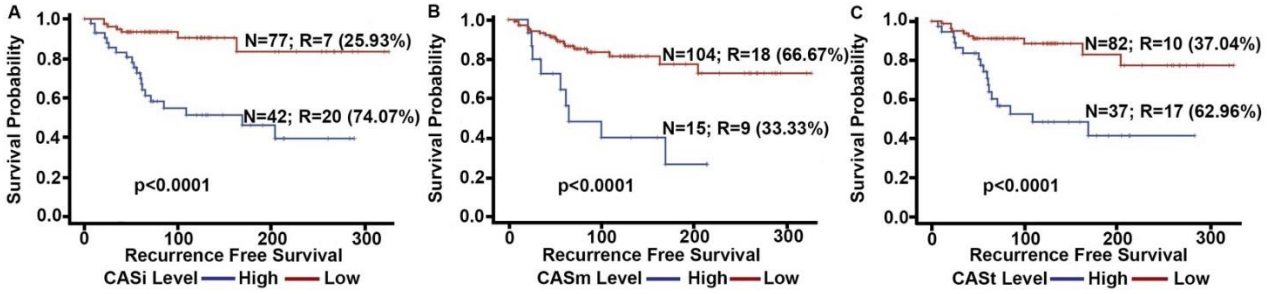

Figure 4.4.10 Higher CAS is associated with poor RFS in DCIS patients
Kaplan Meier survival curves representing the RFS in DCIS patients form validation cohort (A) CASi high and low groups, (B) CASm high and low groups, (C) CASt high and low groups. N is the total number of patients in each group and R represents the number of patients who showed recurrence. % calculated represents percentage/proportion of the recurrence patients out of the total number of recurrence patients in both groups. p<0.05 is considered significant.

Table 4.4.5 Univariate and Multivariable Cox proportional regression analysis for the risk of recurrence in DCIS patients treated with lumpectomy comparing the influence of common clinicopathological variables along with the CAStotal model for validation cohort.

Variables		Univariate Analysis				Multivariate Analysis			
		p-value	Hazard Ratio	95% Hazard Ratio Confidence Limits		p-value	Hazard Ratio	95% Hazard Ratio Confidence Limits	
CAS total	CASt High vs low	<0.001	4.127	1.870	9.111	<.0048	3.391	1.451	7.926
Age	Age High vs low	0.1289	0.523	0.227	1.207	0.0632	0.392	0.402	1.503
Tumor size	Tumor size High vs low	0.0264	1.38	0.134	3.298	0.0172	2.743	1.197	6.284
Grade	Grade High vs low	0.9364	0.969	0.446	2.107	0.8893	1.072	0.4	2.869
Comedo Necrosis	Comedo present vs absent	0.0144	2.745	1.222	6.165	0.0177	3.073	1.215	7.770
Radiotherapy	Radiotherapy No	0.7828	1.226	0.228	5.216	0.7509	1.279	0.280	5.845

4.4.7 Higher CAS is observed in the mixed DCIS cases when compared with the Pure DCIS

In our mixed DCIS cohort, there were 87 patient samples with sufficient tissue for CA analysis. Out of these 87 samples 10 patients presented with ipsilateral recurrence. Patient cohort details are shown in Table 4.4.6. The median age of the 87 patients in the mixed group was 55 and the median follow up was 27.7 months. Comedo necrosis was present in 57 and no necrosis in 30. Out of 87 patients, 32 were nuclear grade 3, 39 were grade 2, and 16 were grade 1. Given the presence of an invasive component in the mixed DCIS cohort the 40 patients were treated with adjuvant chemotherapy and 59 were treated with radiotherapy following surgery Table 4.4.6. We stained the mixed DCIS cases (n=87) for centrosomes using the same methodology as mentioned for discovery and validation cohorts. We observed that the mixed DCIS samples exhibited significantly higher CASi ($p=0.0043$), CASm ($p=0.0006$) and CAS total ($p<0.0001$) when compared to the pure DCIS cases (n=133) (Fig 4.4.11). This suggested that CA has a critical role in tumor progression.

Table 4.4.6 Descriptive statistics of clinicopathological characteristics for mixed DCIS patients (ICART5 cohort) based on the recurrence status.

Baseline Characteristics	Recurrence Free	Recurrence	p value
Patient Age			
Age>58, n(%)	26 (33.77)	4 (40.00)	0.6964
Age<=58, n(%)	51 (66.23)	6 (60.00)	
Tumor Size			
Size>16, n(%)	36 (46.75)	4 (40.00)	0.6869
Size<=16, n(%)	41 (53.25)	6 (60.00)	
Grade, n(%)			
High	38 (49.35)	4 (40.00)	0.5777
Mid and Low	39 (50.65)	6 (60.00)	
Comedo Necrosis, n(%)			
No	24 (31.17)	6 (60.00)	0.0711
Yes	53 (68.83)	4 (40.00)	
Lymph Node Metastasis, n(%)			
No	45 (58.44)	6 (60.00)	0.9250
Yes	32 (41.56)	4 (40.00)	
Distant Metastasis, n(%)			
No	61 (79.22)	8 (80.00)	0.9544
Yes	16 (20.78)	2 (20.00)	

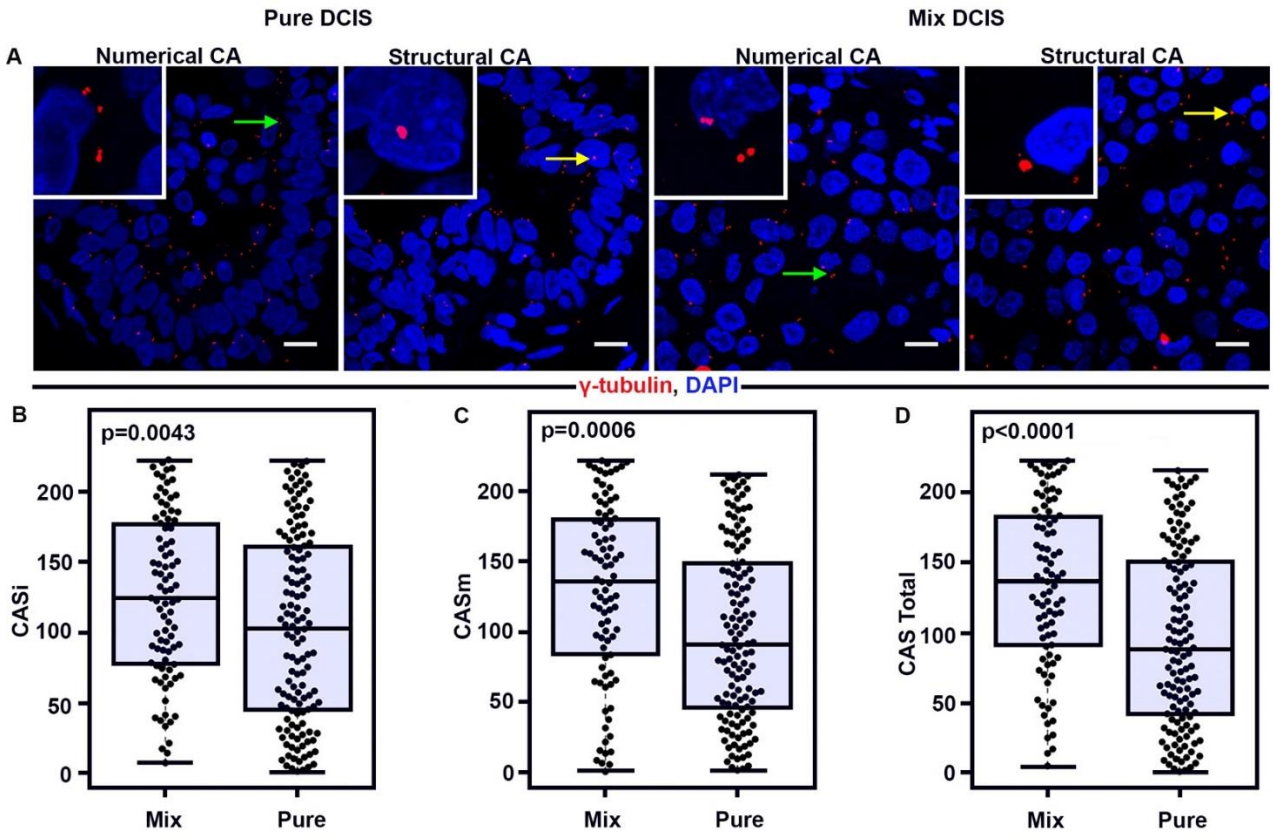

Figure 4.4.11 Mixed DCIS exhibit higher CAS when compared with pure DCIS
Representative Box-whisker plots for the mixed DCIS (n=87) and pure DCIS (n=133) cases. A) CASi distribution, B) CASm distribution, C) CASt distribution. $p<0.05$ was considered significant.

4.5 Discussion

In the current management of DCIS patients, physicians are faced with the issue of whether to recommend adjuvant radiotherapy and/or chemotherapy treatment to their patients in addition to surgery. To aid in this decision, a number of factors are taken into account, including patient age, tumor margins, grade, and size, but the evidence to support these and other potential features as prognostic is variable. In the current study, we developed a novel methodology and algorithm to quantitate both numerical and structural centrosomal aberrations in tumor samples and generated a recurrence prediction score to help in the treatment decision. Our findings indicate that the patients with recurrence exhibit higher CAS total when compared with the recurrence free DCIS

patients. CAS was also associated with poor RFS in DCIS patients and this association was significant even in multivariable models. CAS total presented an HR of 7.5 in a univariate model and 8.5 in a multivariate model. These associations of CAS stayed significant in our validation cohort as well. We further compared the performance of CAS with a known predictive model VNPI. VNPI is based on clinical and histopathological markers like tumor size, margin width and pathologic classification (based on nuclear grade and presence/absence of comedo necrosis)[4, 17, 18] incorporates age as the fourth contributing factor for the prediction. When both CAS and VNPI were factored into multivariable models, only CAS was significantly associated with RFS. This finding suggests that when CAS is accounted for VNPI no longer holds predictive value.

CAS was further able to stratify the DCIS patients into high and low-risk groups of recurrence and was able to predict 5-year risk of local recurrence with higher concordance than what has been proposed by other models, independent of traditional clinical and pathological factors. These findings stayed significant for the validation cohort as well even though our discovery and validation cohort had patients with different clinical and pathological parameters thus indicating the applicability of CAS model is not limited to a specific cohort of patients. Most of the predictive models which have been used in clinics till now have been proven beneficial for specific cohort of patients such as Oncotype DCIS score. This test has limited applicability only to the cases with resection margins of at least 3 mm and low- or intermediate-grade DCIS measuring 2.5 cm or less, or if HG DCIS 1 cm or less in size, as this is the set of patients from ECOG 5194 study upon which the test was initially clinically validated[8]. Thus, the global applicability of this test is limited.

Furthermore, when we further stratified the DCIS patients in the different subgroups based on the traditional clinical and histopathological parameters the recurrence rate (RR) of CAS high

group increased. In high age group regardless of CAS the recurrence rate was 44% (33% in overall patients) When we further stratified this (high age) group in high and low CAS groups we observed that the recurrence rates for the high CAS group increased to 73% suggesting that CAS was further able to stratify high and low age group in high and low-risk group. We observed similar trends for the other clinical and pathological markers such as tumor size and presence of comedo necrosis. Thus, we generated a combined score where we incorporated the prediction rate from these clinical and pathological factors. This new score, i.e., CAS plus score increased the concordance for recurrence prediction from 76.2 for CAS total alone to 82 with CAS plus score. These findings suggest that with the incorporation of these clinical and pathological parameters the recurrence prediction increased with a significant number for CAS.

Another major challenge in the management of DCIS is the determination of the accurate margins. It is now documented that 10-50% of DCIS lumpectomies are followed by a re-surgery because of "close or positive margins"-in which some tumor is still found on postsurgical pathologic review in the margins of the removed breast tissue[19]. The positive margin suggests that some tumor was left behind in the body cavity, and frequently leads to a second surgery. These re-excisions cause considerable morbidity, as well as emotional, and financial burdens on the patients. Here in the current study we observed that high CAS was associated with positive margins and since CAS able to stratify the patients in high and low risk groups of recurrence we suspect that if CAS based risk profiling is done on the core biopsies it could significantly reduce re-surgeries by better predicting who might need a mastectomy to begin with, and for whom re-surgery might not be necessary even in the event of close/positive margins.

CAS, as described earlier, is the linear expression of the extent and the frequency of numerical and structural CA. Centrosome clustering enables chromosomal missegregation

chromosomes and their unequal distribution to daughter cells resulting in chromosomal instability (CIN), thus contributing to neoplastic transformation. Given that CIN engenders karyotypic diversity within tumors, we assert that CAS may perhaps even serve as an indirect measure of ITH in DCIS. Moreover, our findings also indicate higher levels of CAS in the mixed DCIS cases. These findings are in line with the previous findings where we and others observed TNBCs the most aggressive subtype of breast cancer exhibit highest CA among all subtypes[20, 21]. These findings further substantiate the role of CA in tumor progression and given that CA translates to the greater risk of malignant transformation, it may help to determine the patient prognosis. An exciting avenue for future research would be to profile CA in all the stages of tumor progression starting from the atypical hyperplasia to invasive and metastatic disease to evaluate if CA can function as a biomarker for tumor evolution.

4.6 References:

1. Page, D.L., et al., *Intraductal carcinoma of the breast: follow-up after biopsy only.* Cancer, 1982. **49**(4): p. 751-8.
2. Esserman, L. and C. Yau, *Rethinking the Standard for Ductal Carcinoma In Situ Treatment.* JAMA Oncol, 2015. **1**(7): p. 881-3.
3. Freedman, G.M. and B.L. Fowble, *Local recurrence after mastectomy or breast-conserving surgery and radiation.* Oncology (Williston Park), 2000. **14**(11): p. 1561-81; discussion 1581-2, 1582-4.
4. Silverstein, M.J. and M.D. Lagios, *Treatment selection for patients with ductal carcinoma in situ (DCIS) of the breast using the University of Southern California/Van Nuys (USC/VNPI) prognostic index.* Breast J, 2015. **21**(2): p. 127-32.
5. Rudloff, U., et al., *Nomogram for predicting the risk of local recurrence after breast-conserving surgery for ductal carcinoma in situ.* J Clin Oncol, 2010. **28**(23): p. 3762-9.
6. Boland, G.P., et al., *Value of the Van Nuys Prognostic Index in prediction of recurrence of ductal carcinoma in situ after breast-conserving surgery.* Br J Surg, 2003. **90**(4): p. 426-32.
7. Momtahen, S., J. Curtin, and K. Mittal, *Current Chemotherapy and Potential New Targets in Uterine Leiomyosarcoma.* J Clin Med Res, 2016. **8**(3): p. 181-9.
8. Solin, L.J., et al., *A multigene expression assay to predict local recurrence risk for ductal carcinoma in situ of the breast.* J Natl Cancer Inst, 2013. **105**(10): p. 701-10.
9. Yap, T.A., et al., *Intratumor heterogeneity: seeing the wood for the trees.* Sci Transl Med, 2012. **4**(127): p. 127ps10.

10. Godinho, S.A. and D. Pellman, *Causes and consequences of centrosome abnormalities in cancer.* Philos Trans R Soc Lond B Biol Sci, 2014. **369**(1650).

11. McBride, M., P.C. Rida, and R. Aneja, *Turning the headlights on novel cancer biomarkers: Inspection of mechanics underlying intratumor heterogeneity.* Mol Aspects Med, 2015. **45**: p. 3-13.

12. Nigg, E.A., *Centrosome duplication: of rules and licenses.* Trends Cell Biol, 2007. **17**(5): p. 215-21.

13. Chan, J.Y., *A clinical overview of centrosome amplification in human cancers.* Int J Biol Sci, 2011. **7**(8): p. 1122-44.

14. D'Assoro, A.B., W.L. Lingle, and J.L. Salisbury, *Centrosome amplification and the development of cancer.* Oncogene, 2002. **21**(40): p. 6146-53.

15. Fukasawa, K., *Centrosome amplification, chromosome instability and cancer development.* Cancer Lett, 2005. **230**(1): p. 6-19.

16. Hoque, A., et al., *Loss of aurora A/STK15/BTAK overexpression correlates with transition of in situ to invasive ductal carcinoma of the breast.* Cancer Epidemiol Biomarkers Prev, 2003. **12**(12): p. 1518-22.

17. Silverstein, M.J. and C. Buchanan, *Ductal carcinoma in situ: USC/Van Nuys Prognostic Index and the impact of margin status.* Breast, 2003. **12**(6): p. 457-71.

18. Silverstein, M.J., et al., *Developing a prognostic index for ductal carcinoma in situ of the breast. Are we there yet?* Cancer, 1996. **78**(5): p. 1138-40.

19. Pilewskie, M. and M. Morrow, *Margins in breast cancer: How much is enough?* Cancer, 2018. **124**(7): p. 1335-1341.

20. Pannu, V., et al., *Rampant centrosome amplification underlies more aggressive disease course of triple negative breast cancers.* Oncotarget, 2015. **6**(12): p. 10487-97.

21. Denu, R.A., et al., *Centrosome amplification induces high grade features and is prognostic of worse outcomes in breast cancer.* BMC Cancer, 2016. **16**: p. 47.

5 A CENTROSOME CLUSTERING PROTEIN, KIFC1, PREDICTS AGGRESSIVE DISEASE COURSE IN SEROUS OVARIAN ADENOCARCINOMA

Parts of this chapter have been published verbatim in Journal of Ovarian Research 2016; Mar 18;9;17as "A centrosome clustering protein KIFC1, predicts aggressive disease course in serous ovarian adenocarcinomas."

Authors listed on the paper and their contributions:

1. Karuna Mittal: Conceived and designed the study, carried out major experiments of the study (Immunohostochemical and immunofluorescence staining and imaging), analyzed and interpreted the clinical and invitro data, and wrote the manuscript.
2. Da Hoon Choi: Carried out the immunoblot assays
3. Sergey Klimov: Performed clinical in silico data analysis
4. Srikanth Pawar: Performed in silico data analysis for cell lines
5. Ramneet Kaur: Performed clinical in silico data analysis
6. Meenakshi. V. Gupta: Provided tissue samples
7. Anirban Mitra: Provided the cell lines used in the study
8. Ralph Sams: Helped with scoring of immunohistochemical staining
9. Guilherme Cantuaria: Provided tissue samples and scientific guidance
10. Padmashree C. G. Rida: Co-corresponding author of the study- Helped in designing the study and critically revised the manuscript
11. Ritu Aneja: Co-corresponding author of the study- Helped in designing the study and critically revised the manuscript

5.1 Abstract

Amplified centrosomes are widely recognized as a hallmark of cancer. Although supernumerary centrosomes would be expected to compromise cell viability by yielding multipolar spindles that results in death-inducing aneuploidy, cancer cells suppress multipolarity by clustering their extra centrosomes. Thus, cancer cells, with the aid of clustering mechanisms, maintain pseudobipolar spindle phenotypes that are associated with low-grade aneuploidy, an edge to their survival. KIFC1, a nonessential minus end-directed motor of the kinesin-14 family, is a centrosome clustering molecule, essential for viability of extra centrosome-bearing cancer cells. Given that ovarian cancers robustly display amplified centrosomes, we examined the overexpression of KIFC1 in human ovarian tumors. We found that in clinical epithelial ovarian cancer (EOC) samples, an expression level of KIFC1 was significantly higher when compared to normal tissues. KIFC1 expression also increased with tumor grade. Our *In silico* analyses showed that higher KIFC1 expression was associated with poor overall survival (OS) in serous ovarian adenocarcinoma (SOC) patients suggesting that an aggressive disease course in ovarian adenocarcinoma patients can be attributed to high KIFC1 levels. Also, gene expression levels of KIFC1 in high-grade serous ovarian carcinoma (HGSOC) highly correlated with expression of genes driving centrosome amplification (CA), as examined in publically-available databases. The pathway analysis results indicated that the genes overexpressed in KIFC1 high group were associated with processes like regulation of the cell cycle and cell proliferation. In addition, when we performed gene set enrichment analysis (GSEA) for identifying the gene ontologies associated to KIFC1 high group, we found that the first 100 genes enriched in KIFC1 high group were from centrosome components, mitotic cell cycle, and microtubule-based processes. Results from *in vitro* experiments on well-established *in vitro* models of HGSOC (OVSAHO, KURAMOCHI),

OVCAR3 and SKOV3) revealed that they display robust centrosome amplification and expression levels of KIFC1 was directly associated (inversely correlated) to the status of multipolar mitosis. This association of KIFC1 and centrosome amplification with HGSOC might be able to explain the increased aggressiveness in this disease. These findings compellingly underscore that KIFC1 can be a biomarker that predicts an aggressive disease course in ovarian adenocarcinomas.

5.2 Introduction

Ovarian cancer is the sixth most common cancer affecting women worldwide and is the fifth leading cause of deaths related to gynecological malignancies with less than 40% overall cure rate [1]. The overall mortality of ovarian cancer has remained largely unchanged over the past decades even though there is a great advancement in surgical and therapeutic approaches [2]. The standard treatment for ovarian cancer patients is debulking surgery followed by a platinum- based chemotherapy (cisplatin and carboplatin) [3, 4]. One of the primary causes of the high mortality and poor survival in ovarian cancer is the diagnosis at late stages [5]. Despite years of extensive research, there is still a dearth of reliable biomarkers for early detection, prognosis, and predicting disease aggressiveness. Since ovarian cancer is a heterogeneous disease with different histopathological features and clinical behavior, a better understanding of molecular subtypes and search for clinically-facile prognostic factors that can aid in histological subtyping is imperative. Greater than 90% of malignant ovarian tumors are epithelial ovarian carcinomas (EOC) comprising of various subtypes namely serous, endometrioid, clear cell, transitional cell, squamous cell and mucinous carcinomas [6, 7]. About 70-80% of all cases are serous ovarian cancer (SOC) among which high-grade serous ovarian cancer (HGSOC) is the most prevalent [8]. Intriguingly, HGSOC shares similar genomic features with triple negative breast cancer (TNBC) as per reports from Cancer Genome Atlas (TCGA) Network analysis; in particular, the deregulated pathways

characterizing HGSOC are very similar to those in TNBC [9]. Several independent studies have indicated that HGSOC is associated with very high genomic instability and chromosomal aberrations including intrachromosomal breaks and aneuploidy, which incidentally, also typify and drive intratumoral heterogeneity in TNBC [10, 11].

Specifically, the most common mutations present in both kinds of tumors (HGSOC and TNBC) are of p53 and BRCA1/2. It is well established that BRCA1 and BRCA2 tumor suppressor genes directly preserve genomic stability by regulating DNA repair, p53-mediated cell cycle checkpoint control as well as centrosome duplication cycle [12-14]. These findings establish the causative link between BRCA1 and BRCA2 mutations and extensive chromosomal instability found in HGSOC patients. Furthermore, HGSOC tumors frequently overexpress cyclin E and Aurora-A, resulting in aberrant activation of the centrosome duplication cycle that induces centrosome amplification (CA), and eventually genetic instability fueling ovarian cancer progression [15-17]. CA results in numerous and voluminous centrosomes [18]. Subjectively, the presence of supernumerary centrosomes sets the stage for the formation of multipolar spindles that may succumb to a mitotic catastrophe. However, cancer cells avoid this calamitous fate by clustering their extra centrosomes at the two spindle poles, which allows them to evade cell death but ultimately engenders low-grade aneuploidy and genetic instability [19-21].

KIFC1, a nonessential kinesin motor protein, also known as HSET, plays a critical role in clustering of extra centrosomes in cancer cells. Recently several studies have shown that knockdown of KIFC1 in cancer cell lines containing supernumerary centrosomes causes the excess centrosomes to be scattered by pole-separating forces that induce spindle multipolarity and cell death. However, KIFC1 is not required for bipolar spindle assembly in healthy somatic cells [22, 23]. We recently demonstrated that EOC clinical samples harbor extra centrosomes and display

high levels of centrosome clustering in interphase as well as mitosis. In addition, the study highlighted that the gene expression levels of KIFC1 are higher in EOC when compared to normal ovarian tissues *in silico* and is associated with worse prognosis and survival [24]. To further understand and validate results of our previous study, we herein evaluated KIFC1 expression in clinical samples of ovarian cancer by utilizing immunohistochemical staining. Our results indicated higher KIFC1 expression in EOC tumor samples when compared to normal tissues. Furthermore, KIFC1 expression levels in EOC increased with an increase in tumor grade. To understand better the association of KIFC1 with CA, we examined correlations between expression levels of KIFC1 and genes driving CA. Intriguingly, higher gene expression levels of KIFC1 was significantly correlated to expression of CA-driving genes. When GSEA was performed for the genes enriched in KIFC1-high group, they were also found to be related to centrosome components and microtubule-based processes. We further validated the correlation by doing quantitative analysis of CA and extent of clustering in cell lines derived from SOC patients. Our results indicated that KIFC1 was highly expressed in these *in vitro* models of SOC and was also associated to levels of centrosome clustering (mitotic), enabling cells to bypass mitotic catastrophe.

Taken together our findings underscore that KIFC1 is a potential prognostic biomarker in ovarian adenocarcinomas wherein expression levels of KIFC1 may predict the course of disease aggressiveness. Work is underway in our laboratory to pin point molecular mechanism to explain the association of KIFC1 and CA with ovarian cancer aggressiveness and poor patient outcomes.

5.3 Materials and Methods

5.3.1 Cell Culture

The four ovarian cancer cell lines primarily utilized in this study included OVCAR3, KURAMOCHI, SKOV3, and OVSAHO. The SKOV3 and OVCAR3 cell lines were obtained from

ATCC and KURAMOCHI, and OVSAHO were obtained from JCRB. All the cell lines were cultured according to the instructions given by the company.

5.3.2 Immunohistochemistry and scoring

Formalin-fixed paraffin-embedded tissue microarrays (TMAs) for ovarian cancer were obtained from US, Biomax, Inc. Company provided the ethical statement to confirm that, all the participants provided their written consents and patient privacy and anonymity was maintained. TMAs were deparaffinized in a 60°C oven for 20 minutes and placed in 3 consecutive xylene washes. Rehydration of the slides were carried out by putting them through a series of washes involving different concentrations of ethanol in water - 100%, 95%, 70%, and 50% - for 3 minutes each. The antigen retrieval process was done using a pressure cooker and 0.01M citrate buffer with a pH of 6.1. The slides were heated at a temperature of 120°C for 30 minutes. After cooling in ice for 20 minutes, the slides were first subjected to hydrogen peroxide blocking and then protein blocking (both obtained from ThermoScientific) for 20 minutes and 10 minutes, respectively. Tissues were incubated with anti-KIFC1 antibody (Abcam) for 1 hour, before incubating with MACH2 HRP-conjugated secondary antibody (Biocare Medical) for 30 minutes. Enzymatic antibody detection using Betazoid DAB Chromogen Kit (Biocare Medical) was followed by nuclear staining with Myer's hematoxylin (Dako). The staining intensity was scored as 0=none, 1=low, 2=moderate, or 3=high, and the percentage of KIFC1-positive cells from 10 randomly selected fields (~500 cells) was determined. The product of the staining intensity and the percent of positive cells constituted the WI. Statistical analysis was performed using – Tukey's post hoc test.

5.3.3 Cell staining and imaging

Cells were cultured on coverslips and, after the confluency reached approximately 80%, the cells were fixed with ice-cold methanol for 7 minutes. The cells were blocked with 5%

BSA/0.01% Triton X for 45 minutes at room temperature and then incubated at 37°C with antibodies directed against γ-tubulin and α-tubulin at a dilution of 1:2000 for 30 minutes. The cells underwent quick washes 5 times with 1xPBS before being incubated with Alexa Fluor 488 anti-mouse and Alexa Fluor 555 anti-rabbit at a dilution of 1:2000 at 37°C for 30 minutes. After washing the cells 8 times with 1x PBS briefly, the cells were then incubated with Hoechst 33342 (1:5000 dilution) at room temperature for 10 minutes. The cells were mounted with Prolong-Gold antifade reagent after being washed with 1x PBS 3 times and observed using Zeiss LSM 700 Confocal microscope (Oberkochen, Germany) and the images were processed with ZEN software (Oberkochen, Germany).

5.3.4 Immunoblotting

Cell lysates were prepared from 80% confluent cells by scraping with 250ul of 1x lysis prepared from 10x cell lysis buffer (Cell Signaling). The 1x lysis buffer contained 1mM b-glycerophosphate, 20mM Tris-HCl (pH 7.5), 1mM Na2EDTA, 1mM Na3VO4, 150mM NaCl, 1mM EGTA, 2.5mM Na4P2O7, 1ug/ml leupeptin, and 1% Triton. Cell lysates were fractionated using 10% SDS-PAGE gel. The samples were allowed to run at 70V for 90 minutes. Protein transfer onto polyvinylidene difluoride (PVDF) membrane was done for 2 hours via the wet transfer method at 70V. The membrane was then blocked in 5% non-fat, dry milk in 1x TBST for 1 hour at room temperature and probed with the relevant antibodies at a dilution of 1:1000 overnight at 4°C. Primary antibody incubation was followed by incubation with the corresponding secondary antibody at a dilution of 1: 10,000 for 1 hour at room temperature. SuperSignal West Pico Chemiluminescent Substrate (ThermoScientific) was directly applied to the membrane for the subsequent analysis. Cyclin E and Centrin-2 antobodies were obtained from Santa Cruz Biotech, γ-tubulin from Dako, and KIFC1 and Aurora A antibodies from Abcam.

5.3.5 In silico analysis

One channel microarray data was downloaded from gene expression omnibus (GEO) database for primary ovarian cancer samples GSE 9899 [25]. Data was Mas5.0 normalized and was further taken for processing. Logarithm to the base 2-transformed KIFC1 expression levels from all ovarian cancer samples (n=284) regardless of histotypes were extracted from GEO database. Further analysis were carried only on the serous adenocarcinoma samples (n=200). Overall survival (OS) was calculated as the time interval (in months) from the date of histological diagnosis to date of death from any cause. KIFC1 was categorized into high and low groups based on the optimal overall survival cut - points using the log-rank test.

5.3.6 Public microarray data analysis

Robust Multi-array Average normalized expression levels of KIFC1 and genes which drive CA (*CCNA2, CDK1, NEK2, AURKA, MYCN, CCNE2, STIL, LMO4, PLK4, MDM2, CEP63, E2F1, E2F2, E2F3, CEP152, PIM1, PIN1, CCND1)* from the primary serous ovarian carcinoma of 154 patients were obtained from GEO series GSE 9899 To obtain Pearson's correlation coefficients between genes whose dysregulation drives CA, SAS software (IBM) was used for the analyses, with $p<0.05$ indicating statistical significance.

5.3.7 Gene set enrichment analysis of public microarray data

Publicly available pre-processed gene expression profiles of primary ovarian tumors (n=154 from Tothill dataset [25], GSE9899; Patients were stratified into two groups by KIFC1 score. Patients with KIFC1 expressions below the optimal KIFC1 survival threshold where placed in the low-risk group whereas the above threshold patients where stratified to the high-risk group. GSEA was performed as indicated in studies by Tamayo, et al. (2005, PNAS 102, 15545-15550) and Mootha,

Lindgren, et al. (2003, Nat Genet 34, 267-273). False discovery rate q-values.25 were considered statistically significant.

5.3.8 In silico analysis of KIFC1 gene expression and centrosomal amplification index (CAI) genes in cell lines

One channel microarray data was downloaded from GEO database for four cell lines with GSM ids GSM133614, GSM133609, GSM887467 and GSM887488 namely, Ovcar-5, SKOV3, OVSAHO, and OVCAR3 respectively. Data was Mas5.0 normalized and was further taken for processing. Logarithm to the base 2 transformed KIFC1 and expression levels from ovarian cell lines were extracted from the GEO database. PLK4, Aur-A, Aur B, Cyclin E, Centrin, γ-tubulin and pericentrin genes expression values were added to make centrosomal amplification index.

5.3.9 Statistical analysis

Statistical analyses were performed using two-tailed Student's t-tests, Anova and Tukey's post hoc tests. The criterion for statistical significance for all analyses was $p<0.05$. Standard errors were calculated using the general Excel formula where we divided the standard deviation by the square root of the number of samples. Kaplan-Meier analysis and Cox regression were performed using SPSS (IBM). Optimal cut-points were identified with the stratification which gave the largest log-rank χ^2 value.

5.4 Results

5.4.1 KIFC1 is overexpressed in Epithelial Ovarian adenocarcinoma (EOC) clinical samples

We first examined whether KIFC1 is upregulated in human ovarian cancers by analyzing KIFC1 overexpression in EOC clinical samples. To this end, we immunostained paraffin-embedded formalin-fixed tissue microarrays of EOC (n=120) and normal ovarian epithelial tissue (n=13) for

KIFC1. The staining intensity was scored as 0=none, 1=low, 2=moderate, or 3=high, and percentage of positive cells (i.e., with 1+ staining intensity) from randomly selected fields (~500 cells) was determined [18]. The product of the staining intensity and the percent of positive cells constituted the Weighted Index (WI). Descriptive statistics regarding patient and clinicopathological characteristics is given in **Table 5.41A, B**. In consonance with our previously published study [24], our immunohistochemical analysis showed overexpression of KIFC1 in EOC tissues with negligible expression in normal ovarian epithelial tissue **(Figure 5.4.1A)**. We found that the number of positively-stained nuclei per field in high-grade ovarian cancers **(Figure 5.4.1A)** was significantly higher compared to low-grade ones. We then compared the nuclear KIFC1 WI values for normal and tumor samples and also across grades for tumor samples. Interestingly, we observed that nuclear KIFC1 WI was significantly higher in EOC tissues when compared to normal tissues ($p<0.01$). Also, the nuclear KIFC1 WI increased with increasing tumor grade **(Figure 5.4.1Bii)** ($p<0.05$). Among subtypes, we noticed that the number of positively-stained nuclei per field in high-grade serous ovarian cancers **(Supplementary Figure. 5.7.1A[3])** was significantly higher compared to low-grade serous ovarian cancers ($p<0.05$). Collectively, these observations indicate robust KIFC1 overexpression in human ovarian adenocarcinoma and strong association of KIFC1 expression levels with clinical progression of the disease. These data suggest that KIFC1 might play an active role in driving the progression of tumors into more malignant and aggressive forms.

[3] [3] All supplemental data, tables, and figures appear in Appendix C for this chapter

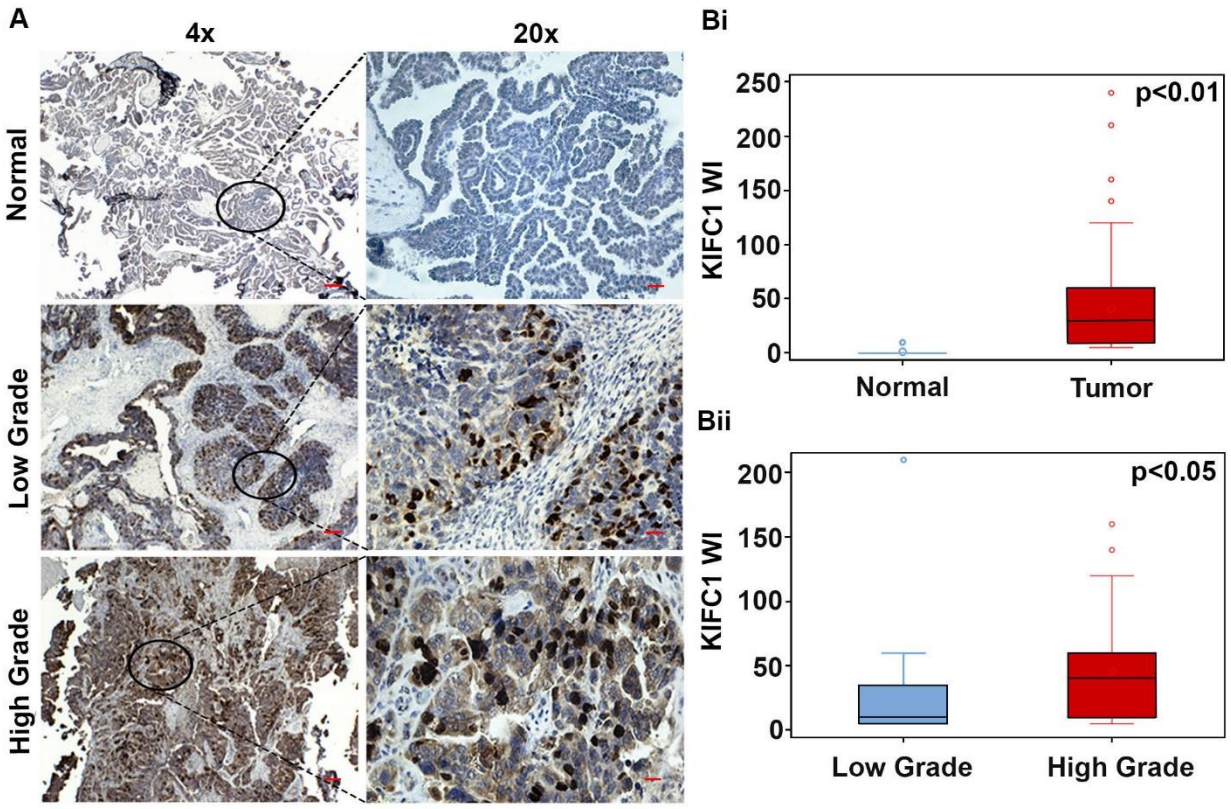

Figure 5.4.1High grade epithelial ovarian carcinomas exhibit higher expression of KIFC1 than low-grade adenocarcinomas and uninvolved, adjacent normal tissues.
A. Low magnification (4x) and their corresponding higher magnification (20x) images depicting KIFC1 expression in normal, low-grade and high-grade EOC tissues. The tissues were stained for KIFC1 (brown) and nuclei (blue). Scale bar (red) 20 µm. Bi. Box-whisker plot depicting the weighted index (WI) of KIFC1 expression in normal and tumor tissue. Bii. Box-whisker plot representing the WI for KIFC1 expression in low and high-grade EOC samples.

Table 5.4.1 A: Descriptive statistics for patient and clinicopathologic characteristics in the analysis of KIFC1 levels in tumors and matched normal tissue.

Variable	Level	Number	Percentage
Age	20-40	23	19.2
	41-60	81	67.5
	61<	16	13.3
Grade	1	32	26.7
	2	36	30
	3	46	38.3
	Unknown	6	5
Stage	I	69	57.5
	II	31	25.8
	III	12	10
	IV	3	2.5
	Unknown	5	4.2
Primary Tumor (T)	T1	72	60
	T2	31	25.8
	T3	12	10
	Unknown	5	4.2
Regional Lymph Nodes(N)	N0	103	85.8
	N1	12	10
	Unknown	5	4.2
Distant Metastasis	Yes	3	2.5
	No	112	93.3
	Unknown	5	4.2
Tissue Type	Malignant	115	95.8
	Metastasis	5	4.2

Table 5.4.1 B: Descriptive statistics for Pathological diagnosis in the analysis of KIFC1 levels in tumors and matched normal tissue.

Variable	Level	Number	Percentage
Pathological Diagnosis	Adenocarcinoma	2	1.7
	Serous Adenocarcinoma	6	5
	Serous Papillary Adenocarcinoma	3	2.5
	Endometrioid Adenocarcinoma	10	8.3
	Metastatic Adenocarcinoma	4	3.3
	Metastatic Mucinous Adenocarcinoma	1	0.8
	Mucinous Adenocarcinoma	11	9.2
	Clear Cell Carcinoma	4	3.3
	Serous Papillary Carcinoma	32	26.7
	Serous Papillary Cystadenocarcinoma	47	39.2

SD= standard deviation;

5.4.2 Enhanced KIFC1 gene expression is associated with poor survival in HGSOC patients

Having established a significant correlation between KIFC1 expression and tumor differentiation, we next wanted to determine if there is any association between KIFC1 gene expression and clinical outcomes (overall survival (OS)) for ovarian cancer patients. To this end, we examined single channel microarray data from GEO (GSE9899) [25] to compare the expression levels of KIFC1 among different subtypes. Interestingly, we found that the gene expression levels of KIFC1 were significantly higher in serous ovarian adenocarcinoma (n=154) when compared to all other subtypes (Borderline serous adenocarcinoma, n=18 and Peritoneal serous adenocarcinoma, n=22)

(Figure 5.4.2A). Further, we examined grade-wise trends in KIFC1 expression in serous ovarian adenocarcinoma. We observed a significant increase in KIFC1 expression levels with increasing grade **(Figure 5.4.2B)**. OS was calculated as the time interval (in months) from the date of histological diagnosis to date of death from any cause. We then carried out a survival analysis wherein patients were stratified into high- and low-KIFC1 expressing subgroups using the optimal KIFC1 expression cut-point (based on the log-rank test). Irrespective of the histological subtypes (n = 284), those with higher KIFC1 expression had shorter OS ($p<0.067$) than patients with lower KIFC1 **(Supplementary Figure 5.7.2A**). To investigate in-depth, we performed a similar survival analysis by stratifying serous ovarian adenocarcinoma patients (n= 201) on the basis of site (primary, n= 154 and metastatic, n= 47) of sample collection. Univariate regression revealed high KIFC1 gene expression correlated significantly (HR= 2.14, $p=0.024$) with poor OS in primary tumors only **(Figure 5.4.2C)** but not in metastatic ones (data not shown). This association stayed significant (HR=2.6, $p=0.006$) during multivariate analysis when potentially confounding factors like grade and tumor stage were added **(Supplementary Figure 5.7.2B)**. In sum, enhanced gene expression levels of KIFC1 in primary tumors is strongly associated with poor clinical outcome.

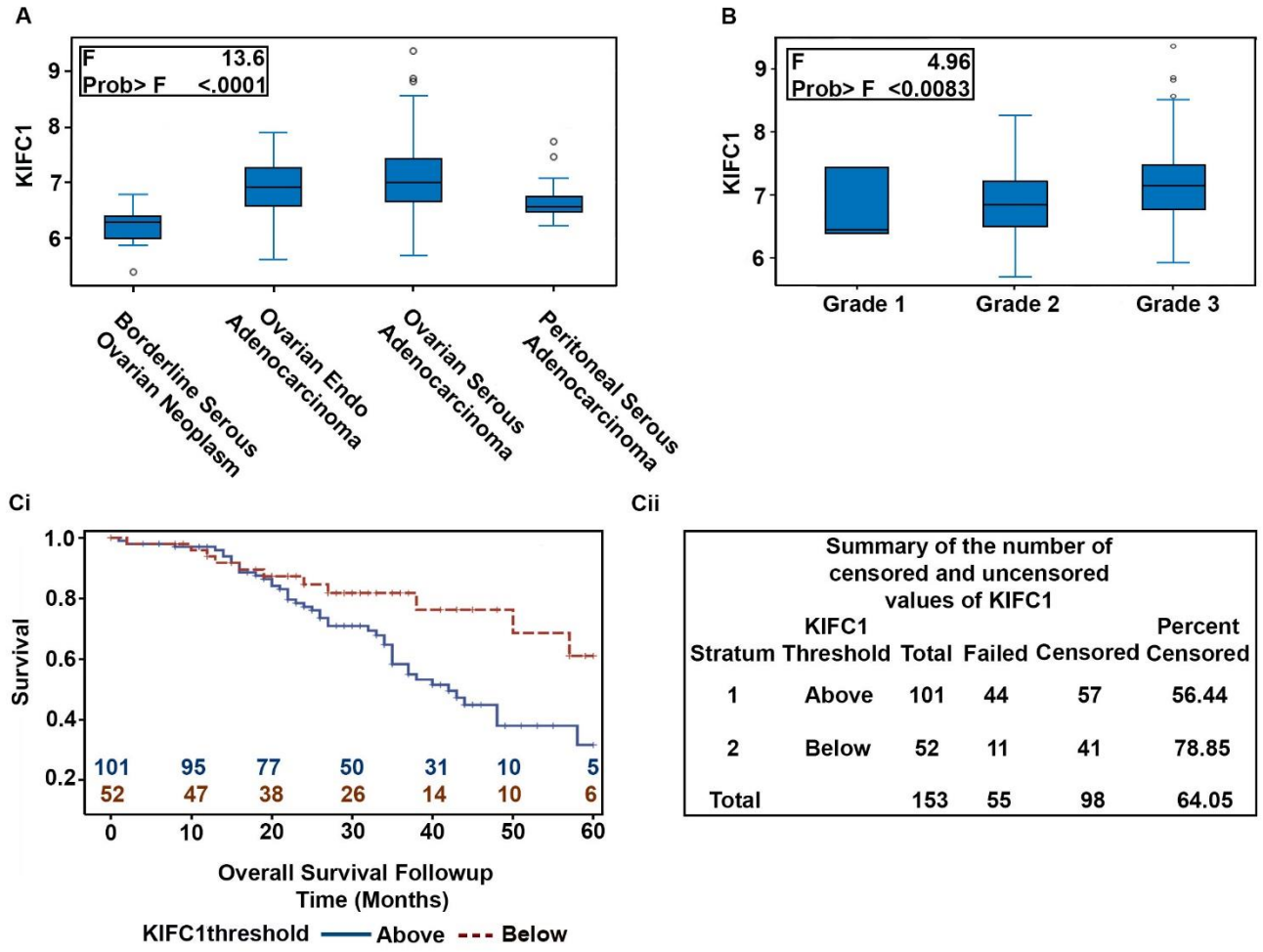

Figure 5.4.2 KIFC1 is highly expressed in High grade serous ovarian adenocarcinoma and is associated with poor overall survival.

A. Box-whisker graphs depicting the expression levels of KIFC1 among different subtypes of ovarian cancer. B. Box- whisker graphs depicting the expression levels of KIFC1 in serous ovarian adenocarcinoma in different tumor grades. Ci. Kaplan-Meier plots showing overall survival of HGSOC patients based on low or high expression of KIFC1 gene. Cii. Summary of the number of censored and uncensored values for the Kaplan-Meier survival analysis.

Table 5.4.2. Descriptive statistics and clinicopathologic characteristics for patients included in in silico analysis of KIFC1 expression and overall survival.

VARIABLE	LEVEL	NUMBER	PERCENTAGE
Age (Range)	20-29	1	0.5
	30-39	4	1.9
	40-49	23	11.1
	50-59	84	40.4
	60-69	54	26
	70-79	40	19.2
	80-89	1	0.5
	Unknown	1	0.5
Cancer Site	Primary	154	74
	Metastasis	50	24
	Unknown	4	1.9
FIGO Stage	I	9	4.3
	II	9	4.3
	III	126	60.6
	IV	10	4.8
	Unknown	54	26
Grade	1	6	2.9
	2	80	38.5
	3	120	57.7
	Unknown	2	1
Survival Status	Alive	109	52.4
	Dead	98	47.1
	Unknown	1	0.5
Recurrence	Recurrence	154	74
	No Recurrence	53	25.5
	Unknown	1	0.5

5.4.3 KIFC1 gene expression correlates with expression of genes related to centrosomal amplification in serous ovarian cancer

Next, we sought to examine the correlation of KIFC1 and genes driving CA. We analyzed expression levels of genes including *CCNA2, CDK1, NEK2, AURKA, MYCN, CCNE2, STIL, LMO4, PLK4, MDM2, CEP63, E2F1, E2F2, E2F3, CEP152, PIM1, PIN1 AND CCND1*, whose deregulation is known to drive ca [18, 26-28]. Specifically, we tested the associations between robust multi-array average-normalized expression levels of these genes in primary soc from 154 patients using gene expression omnibus (GEO) series GSE9899. Higher expression of KIFC1 was significantly correlated with high expression OF *CCNA2, CDK1, NEK2, AURKA, E2F2, MYCN, STIL, CCNE2, E2F3, LMO4, PLK4, PIN1 AND E2F3* (Table. 5.4.3). These results suggest that

KIFC1 upregulation and enhanced centrosome clustering in the serous ovarian adenocarcinomas may enable tumor cells to manage their increased centrosomal load, avert mitotic catastrophe and promote survival.

Next, we identified the biological processes which are deregulated in the KIFC1 high risk group. To this end, we probed the publicly-available microarray dataset (GSE9899) and stratified the 154 serous ovarian adenocarcinoma patients from the dataset into KIFC1-high and KIFC1-low groups. We then identified the gene ontologies of significantly overexpressed genes associated with the KIFC1-high group utilizing the panther classification system. When pathway analysis was performed we found that majority of the genes overexpressed were associated to cellular processes like cell communication, cell cycling, cytokinesis and cell proliferation (Figure 5.4.3ai, ii). We then validated these results by performing the gene set enrichment analysis (26). We found that KIFC1 high group was significantly (FDR <0.25 and es $p<0.05$) enriched in centrosome and cell cycle gene sets (Figure 5.4.3bi, ii and Supplementary Figure 5.7.3a) (see supplementary table 5.7.1, 2 and 3 for these and all other enriched gene ontologies). The results from GSEA showed that the top 100 gene sets enriched in KIFC1 high group were among the ones which plays key roles in, driving ca (*NEK2, PLK1, CCNA2*), clustering centrosomes (*PRC1*), microtubule spindle (*KIF11, NUSAP1, NUMA1*) etc. Altogether our data shows that the KIFC1-high group had a preponderance of genes representing all four important mitotic kinases –namely polo-like kinases (PLK1), aurora kinases (*AURKA, AURK B*), cyclin dependent kinases (*CDK1*) and nima related kinases (*NEK1, NEK2*). The coordination of progression through mitosis is mainly orchestrated by protein phosphorylation ensured by these kinases. Thus, it is reasonable to speculate that overexpression of these kinases results in deregulation of the cell cycle resulting in abnormal mitosis that generates cells with aberrant centrosomes and abnormal chromosomal content.

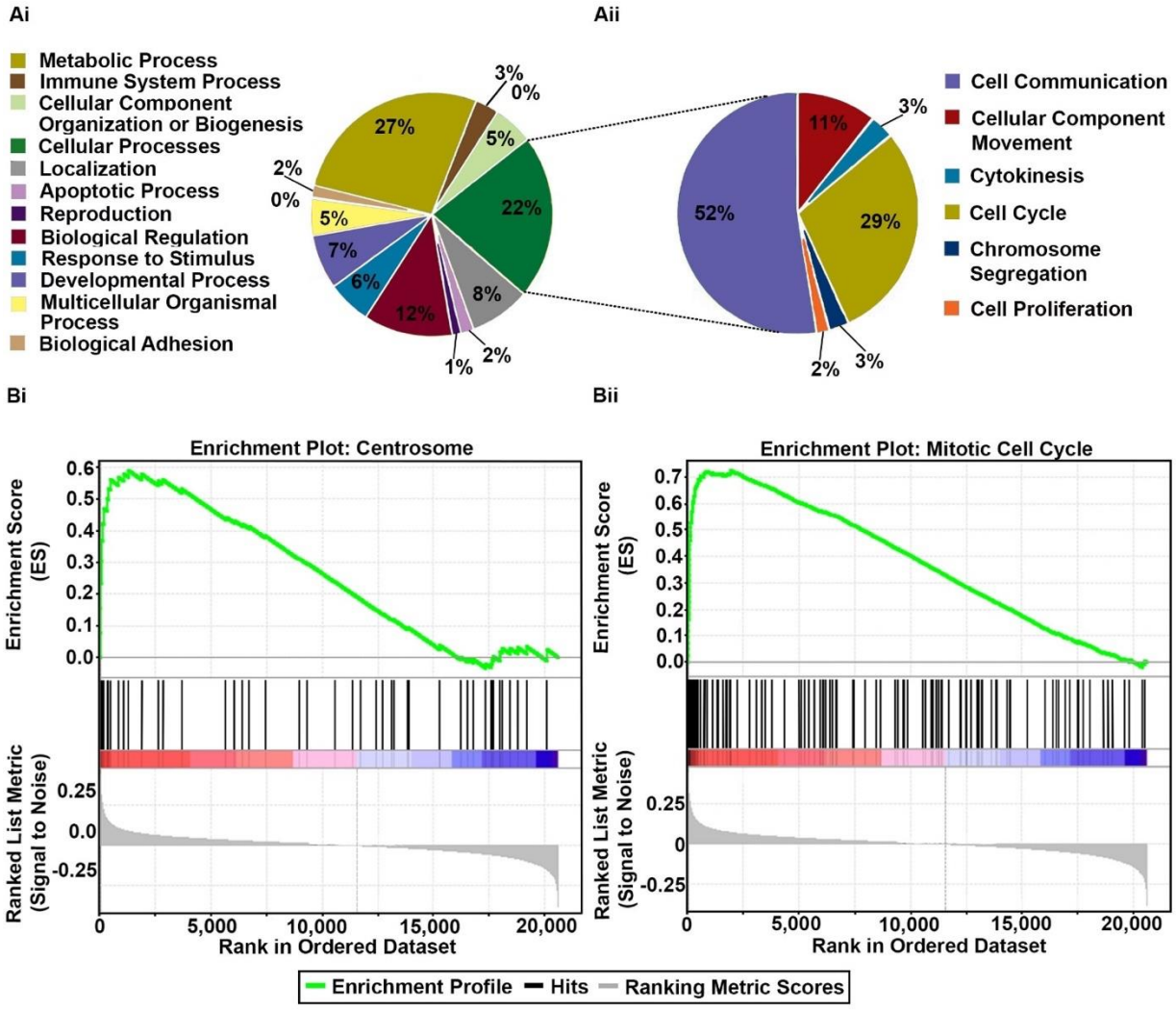

Figure 5.4.3 Gene set enrichment analyses for biological processes associated to KIFC1 high group.

Ai. Biological processes enriched in KIFC1 high group. Aii. Cell cycle processes enriched in KIFC1-high group. Bi Enrichment plots of centrosome-related genes. Bii. Enrichment plot of genes associated with cell cycle progression, with red indicating correlation with the KIFC1-high group and blue the KIFC1-low group.

Table 5.4. 3. Correlation between KIFC1 expression and expression of genes whose dysregulation drives centrosome amplification.

GENE	PEARSON CORRELATION	P-VALUE
CCNA2	0.62527	<.0001
NEK2	0.60066	<.0001
E2F1	0.54218	<.0001
CDK1	0.52124	<.0001
E2F2	0.51764	<.0001
AURKA	0.46987	<.0001
STIL	0.397	<.0001
CCNE2	0.36387	<.0001
LMO4	0.36306	<.0001
PLK4	0.34292	<.0001
MYCN	0.31914	<.0001
E2F3	0.31548	<.0001
MDM2	0.24766	0.002
PIN1	0.23016	0.0041
CEP152	0.18128	0.0245
PIM1	0.17826	0.027

5.4.4 HGSOC cell lines show higher incidence and severity of centrosome amplification

Having confirmed the association between upregulation of KIFC1 gene and CA genes in HGSOC, we wanted to investigate the CA profile in well-established *in vitro* cell lines that mimic HGSOC. To this end, we first screened four well-established cancer cell lines (namely, KURAMOCHI, OVCAR3, OVSAHO and SKOV3 by immunostaining centrosomes (γ-tubulin, green) and microtubules (α-tubulin, red) and counterstaining nuclei with DAPI (blue) **Figure 5.4.4A**. Employing confocal microscopy we imaged 10 areas of interest (at least 500 cells were counted per cell type). Cells with abnormal number (more than two) of gamma tubulin spots were considered as cells with amplified centrosomes. We found that KURAMOCHI exhibited the highest percentage of cells with amplified centrosomes (~38%) followed by OVSAHO (~24%), OVCAR3 (~15%) and SKOV3 (~9%) (**Figure 5.4.4B)**. In a recent molecular profiling study by Domcke et al., KURAMOCHI and OVSAHO were selected as the representative cell lines for HGSOC [29]. Thus, our findings here parallel previous studies that recognize CA as a biomarker of aggressive tumors. Furthermore, we validated our results by evaluating the expression levels of centrosome-related proteins by performing immunoblotting assays. We found that the cell lines with high CA (KURAMOCHI and OVSAHO) expressed higher levels of centrosome structural proteins (densitometry values for centrin-2 relative to loading control β actin (KURAMOCHI - 0.291445, OVSAHO - 0.432561) and proteins whose dysregulation is known to drive CA (for Cyclin-E and Aurora A, KURAMOCHI- 0.194213 and 0.256828, OVSAHO- 0.428814, 1.664283 respectively) (**Figure 5.4.4C)**. Our next step was to investigate if aberrations in centrosome numbers among the different cell lines had any bearing on the mitotic spindle geometry. Interestingly, we found that the percentage of multipolar mitotic cells in three cell lines (OVSAHO, SKOV3 and OVCAR3) was lower (by~2-fold) in comparison with the proportion of

cells with supernumerary centrosomes (**Figure 5.4.4B)**. This difference in the proportion of cells with CA and multipolar spindles clearly supports the hypothesis that ovarian cancer cells cluster supernumerary centrosomes to form pseudobipolar poles. But as the results here indicate that KURAMOCHI showed significantly more multipolar mitoses when compared to the other ovarian cancer cell lines we tested, we evaluated if there existed variability in the level of clustering molecules that help cancer cells to deal with supernumerary centrosomes by corralling them to form pseudobipolar spindles [24]. To this end, we performed immunoblotting to evaluate expression level of centrosome clustering protein KIFC1 in cell lysates obtained from the ovarian adenocarcinoma cells (KURAMOCHI, OVCAR3, OVSAHO and SKOV3). We found that all the three cell lines with pronounced centrosomal clustering expressed higher levels of KIFC1 (SKOV3- 0.342396, OVCAR3- 0.204796 and OVSAHO- 0.452534) whereas negligible KIFCI expression was noted in KURAMOCHI (0.145452). It is noteworthy to mention that a recent report shows that KURAMOCHI is the only cell line that did not induce tumorigenesis *in vivo* [11]. This finding resonates with our notion that centrosome clustering is essential for the viability of cancer cells with extra centrosomes and therefore determines their tumorigenicity.

The *in vitro* findings were validated *in silico* by probing publically-available microarray dataset using Gene set. We interrogated publically-available microarray dataset of ovarian cancer cell lines (GSM133614, GSM133609, GSM887467 and GSM887488). We calculated a cumulative gene expression-based centrosome amplification index (CAI) by adding log-transformed, normalized gene expression for both structural centrosomal proteins (CETN2 (centrin-2), TUBG1 (γ-tubulin), PCNT2 (pericentrin)), and genes implicated in centrosome amplification (PLK4 (polo-like kinase 4) and CCNE1 (cyclin E) genes) (**Supplementary Figure 5.7.4 Ai)**. The analysis showed that CAI genes are expressed in all cell lines but is highest in

OVSAHO. In addition, we evaluated gene expression levels of KIFC1 and found that the gene expression levels of KIFC1 was higher in cancer cell lines in comparison to normal ovarian surface epithelial cells (**Supplementary Figure 5.7.4 Aii)**. Taken together, our results indicated that CA and KIFC1 levels are associated with HGSOC cell lines.

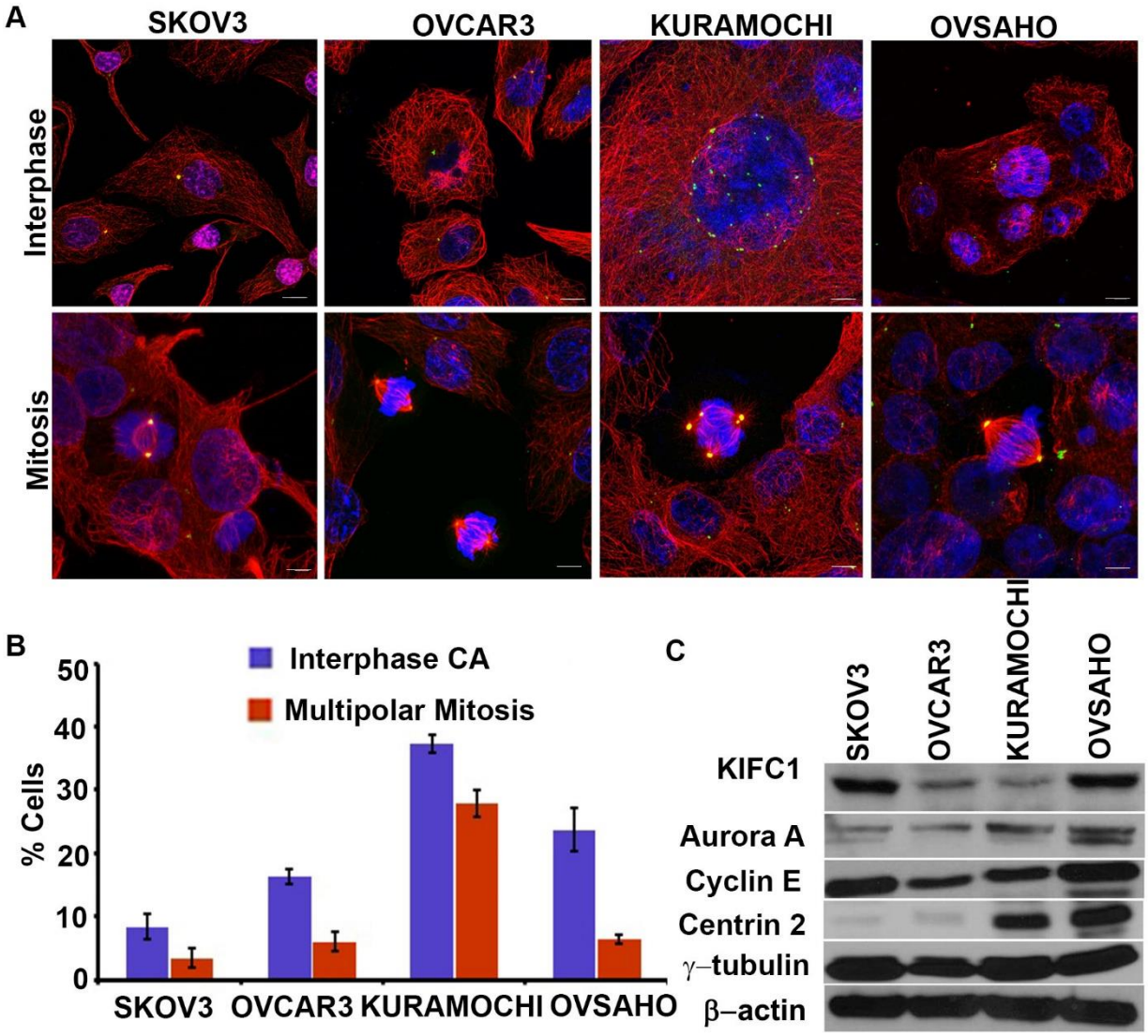

Figure 5.4.4 HGSOC cell lines show higher incidence and severity of Centrosome amplification.

A. Confocal microscopic images showing the presence of centrosome amplification and clustering in ovarian cancer cell lines. Centrosomes and microtubules were visualized by immunostaining for γ-tubulin (green) and α-tubulin, respectively, and DNA was stained using DAPI (blue). Scale bar (white) 5 µm. B. Bar graphical representation of percent cells showing centrosome amplification and multipolar mitosis in human ovarian cancer cell lines. 500 cells were counted in

each case. C. Immunoblots showing the levels of KIFC1 and centrosomal markers in ovarian cancer cells lines (KURAMOCHI, OVCAR3, OVSAHO, and SKOV3).

5.5 Discussion

Ovarian cancer in the advanced stage remains the deadliest gynecologic malignancy. One of the major causes of the low five-year survival is the diagnosis at later stages after it has already metastasized beyond the pelvis [30]. While extensive literature contains information on the different kinds of biomarkers for ovarian cancer, risk predictive or prognostic markers that are utilized in clinical settings are few and far between. Generally, most researchers focus on single prognostic markers which may be insufficient for complete prognostic information, and also most of them have very low clinical utility. A combination of multiple factors needs to be considered simultaneously to more accurately predict a patient's prognosis. Presence of heterogeneity in ovarian cancer is another key factor to be considered in prognosis as many ovarian cancer studies have failed to take into account differences in the histological subtype which clearly pose prognostic and therapeutic challenges [30, 31]. Essentially, these unique attributes and challenges can be addressed by personalizing treatments based upon the unique biomarker profiles of individual patients. Thus, a comprehensive understanding of risk predictive or prognostic factors with regard to histological subtype is imperative to devise relevant treatment strategies specific for the particular group of patients or tumor subtypes.

Chromosomal instability (CIN) is the main cause of complex genomic alterations in tumorigenesis. Since CA engenders CIN, the role of CA driven karyotypic diversity is well studied in several malignancies including pancreatic ductal adenocarcinoma, TNBC and colon cancer [18, 20]. Several studies have highlighted the presence of supernumerary centrosomes in ovarian cancer suggesting that CA is a hallmark of ovarian cancer [32-34]. Recently, we also demonstrated the

presence of amplified centrosomes in EOC [24]. Supernumerary centrosomes in cancer cells tend to cluster to manage the centrosomal load and thus escape from the perils of mitotic catastrophe. KIFC1 is well studied for its role in clustering supernumerary centrosomes [22, 23]. In our previous study, we emphasized the role of KIFC1 in tumor progression of EOC at the gene expression level [24]. In the present study we have validated those findings by immunostaining ovarian cancer tissue samples for KIFC1. Our findings show that KIFC1 expression increases with the grade in EOC. Among the various subtypes that comprise EOC, we found that KIFC1 expression was highest among high-grade SOC samples. This helped us to focus our study on HGSOC, which is a more prevalent and aggressive form of ovarian cancer. This strong relationship of KIFC1 with HGSOC suggests that KIFC1 may be directly involved in tumor development and in driving aggressiveness by allowing the cancer/poorly differentiated cells to escape mitotic catastrophe and thrive. Moreover, data from our GSEA analysis showed that *BIRC5* gene, which codes for the protein Survivin, that performs dual roles in promoting cell proliferation and preventing apoptosis [35, 36], was among the first 20 enriched genes in KIFC1-high group. Thus, KIFC1 overexpression not only protects cancer cells from undergoing mitotic catastrope but also endows them with low-grade aneuploidy, as a form of genomic instability, and high levels of survival signaling that together facilitate tumor evolution and disease progression. This finding was bolstered by results obtained from *in silico* analysis wherein we found that primary tumors with higher gene expression of KIFC1 were associated with poor survival; by contrast, while samples collected from the metastatic sites showed similar expression levels of KIFC1 as in primary sites, high KIFC1 expression in metastatic sites was not significantly correlated to poor survival. This differential effect of high KIFC1 expression strongly suggests that elevated KIFC1 in primary sites perhaps helps tumor cells present in the primary sites to acquire karyotypic

diversity (through CIN), which is more likely to lead to successful metastasis and poor survival. It is possible that once metastasis commences, high KIFC1 levels in the metastatic clones provides little further survival advantage for the cancer cells; alternatively, once metastasis occurs, the survival difference between KIFC1-high and KIFC1-low patients is no longer so marked. Further studies are required to gain more insights into these intriguing issues.

Given the direct association of CA with KIFC1 in the present study, we examined the association of KIFC1 with CA-associated genes. Our in silico analysis indicated that in primary SOC samples KIFC1 expression was positively correlated to the expression of genes which drive CA. CCNA2, NEK2, and AURKA were among the top 10 genes which were highly correlated to KIFC1 expression. Role of NEK2, CCNA2, and AURKA as potential targets in ovarian cancer has been recently highlighted by a detailed systematic bioinformatic study [37]. Besides, this enrichment analysis showed that the KIFC1-high group was enriched in genes implicated in cell cycle regulatory processes, especially genes participating in G2-M transition and the spindle assembly checkpoint (MAD2, BUB1). Several studies in past have reported MAD1 and MAD2 overexpression in different malignancies, and association of this overexpression with aneuploidy and poor overall survival [38-40]. Thus, our findings from the GSEA and Pathway analysis suggests that KIFC1 overexpression drives overexpression of genes that control mitotic checkpoints (Supplementary Table 5.7.2), which by generating aneuploidy, accelerate tumor progression and evolution of more aggressive phenotypes.

In line with these *in silico* findings, we found that cell line derived from HGSOC displayed robust CA, and the proteins which are known to drive CA were also highly expressed. Some recent studies on molecular profiling of ovarian cell lines have demonstrated that OVSAHO represents most of the characteristics (*KRAS*, *p53* and *BRCA1* and 2 mutations) of HGSOC [29] and is

considered to be most aggressive cell line among all. From our study, we found that OVSAHO cells expressed the highest levels of KIFC1 and in spite of presence of interphase supernumerary centrosomes it showed significantly low level of multipolar mitosis. These findings clearly indicate that strong association of CA and clustering with KIFC1 overexpression, which leads to CIN, could be the underlying cause of aggressiveness in these cells. Testing effects of centrosome declustering drugs on these cells could prove to be advantageous.

In conclusion, our results indicate that HGSOC overexpresses KIFC1, which is associated with poor overall survival suggesting a causative link between KIFC1 and tumor aggressiveness. These findings highlight KIFC1 as a potential biomarker to predict disease aggressiveness KIFC1 may also serve as a cancer-selective therapeutic target for high-grade serous ovarian adenocarcinoma patients.

5.6 References

1. Siegel, R., et al., *Cancer statistics, 2014.* CA Cancer J Clin, 2014. **64**(1): p. 9-29.
2. Bast, R.C., Jr., B. Hennessy, and G.B. Mills, *The biology of ovarian cancer: new opportunities for translation.* Nat Rev Cancer, 2009. **9**(6): p. 415-28.
3. Schmid, B.C. and M.K. Oehler, *New perspectives in ovarian cancer treatment.* Maturitas, 2014. **77**(2): p. 128-36.
4. Yap, T.A., C.P. Carden, and S.B. Kaye, *Beyond chemotherapy: targeted therapies in ovarian cancer.* Nat Rev Cancer, 2009. **9**(3): p. 167-81.
5. Vaughan, S., et al., *Rethinking ovarian cancer: recommendations for improving outcomes.* Nat Rev Cancer, 2011. **11**(10): p. 719-25.
6. Auersperg, N., et al., *The biology of ovarian cancer.* Semin Oncol, 1998. **25**(3): p. 281-304.
7. Auersperg, N., *The origin of ovarian carcinomas: a unifying hypothesis.* Int J Gynecol Pathol, 2011. **30**(1): p. 12-21.
8. *Integrated genomic analyses of ovarian carcinoma.* Nature, 2011. **474**(7353): p. 609-15.
9. *Comprehensive molecular portraits of human breast tumours.* Nature, 2012. **490**(7418): p. 61-70.
10. Fleury, H., et al., *Novel high-grade serous epithelial ovarian cancer cell lines that reflect the molecular diversity of both the sporadic and hereditary disease.* Genes Cancer, 2015. **6**(9-10): p. 378-98.
11. Mitra, A.K., et al., *In vivo tumor growth of high-grade serous ovarian cancer cell lines.* Gynecol Oncol, 2015. **138**(2): p. 372-7.

12. Scully, R., *Role of BRCA gene dysfunction in breast and ovarian cancer predisposition.* Breast Cancer Res, 2000. **2**(5): p. 324-30.
13. Liu, Y. and M. Kulesz-Martin, *p53 protein at the hub of cellular DNA damage response pathways through sequence-specific and non-sequence-specific DNA binding.* Carcinogenesis, 2001. **22**(6): p. 851-60.
14. Venkitaraman, A.R., *Cancer susceptibility and the functions of BRCA1 and BRCA2.* Cell, 2002. **108**(2): p. 171-82.
15. Pils, D., et al., *Cyclin E1 (CCNE1) as independent positive prognostic factor in advanced stage serous ovarian cancer patients - a study of the OVCAD consortium.* Eur J Cancer, 2014. **50**(1): p. 99-110.
16. Lassus, H., et al., *Aurora-A overexpression and aneuploidy predict poor outcome in serous ovarian carcinoma.* Gynecol Oncol, 2011. **120**(1): p. 11-7.
17. Landen, C.N., Jr., et al., *Overexpression of the centrosomal protein Aurora-A kinase is associated with poor prognosis in epithelial ovarian cancer patients.* Clin Cancer Res, 2007. **13**(14): p. 4098-104.
18. Mittal, K., et al., *Amplified centrosomes may underlie aggressive disease course in pancreatic ductal adenocarcinoma.* Cell Cycle, 2015. **14**(17): p. 2798-809.
19. Godinho, S.A., et al., *Oncogene-like induction of cellular invasion from centrosome amplification.* Nature, 2014. **510**(7503): p. 167-71.
20. Pannu, V., et al., *Rampant centrosome amplification underlies more aggressive disease course of triple negative breast cancers.* Oncotarget, 2015. **6**(12): p. 10487-97.
21. Basto, R., et al., *Centrosome amplification can initiate tumorigenesis in flies.* Cell, 2008. **133**(6): p. 1032-42.
22. Pannu, V., et al., *HSET overexpression fuels tumor progression via centrosome clustering-independent mechanisms in breast cancer patients.* Oncotarget, 2015. **6**(8): p. 6076-91.
23. Li, Y., et al., *KIFC1 is a novel potential therapeutic target for breast cancer.* Cancer Biol Ther, 2015. **16**(9): p. 1316-22.
24. Pawar, S., et al., *KIFCI, a novel putative prognostic biomarker for ovarian adenocarcinomas: delineating protein interaction networks and signaling circuitries.* J Ovarian Res, 2014. **7**: p. 53.
25. Tothill, R.W., et al., *Novel molecular subtypes of serous and endometrioid ovarian cancer linked to clinical outcome.* Clin Cancer Res, 2008. **14**(16): p. 5198-208.
26. Leontovich, A.A., et al., *Inhibition of Cdk2 activity decreases Aurora-A kinase centrosomal localization and prevents centrosome amplification in breast cancer cells.* Oncol Rep, 2013. **29**(5): p. 1785-8.
27. Montanez-Wiscovich, M.E., et al., *Aberrant expression of LMO4 induces centrosome amplification and mitotic spindle abnormalities in breast cancer cells.* J Pathol, 2010. **222**(3): p. 271-81.
28. Marina, M. and H.I. Saavedra, *Nek2 and Plk4: prognostic markers, drivers of breast tumorigenesis and drug resistance.* Front Biosci (Landmark Ed), 2014. **19**: p. 352-65.
29. Domcke, S., R. Sinha, and D.A. Levine, *Evaluating cell lines as tumour models by comparison of genomic profiles.* 2013. **4**: p. 2126.
30. Agarwal, R. and S.B. Kaye, *Prognostic factors in ovarian cancer: how close are we to a complete picture?* Ann Oncol, 2005. **16**(1): p. 4-6.

31. Davidson, B. and C.G. Trope, *Ovarian cancer: diagnostic, biological and prognostic aspects.* Womens Health (Lond Engl), 2014. **10**(5): p. 519-33.
32. Hsu, L.C., et al., *Centrosome abnormalities in ovarian cancer.* Int J Cancer, 2005. **113**(5): p. 746-51.
33. Bayani, J., et al., *Distinct patterns of structural and numerical chromosomal instability characterize sporadic ovarian cancer.* Neoplasia, 2008. **10**(10): p. 1057-65.
34. Zhang, Y., et al., *Overexpression of WDR62 is associated with centrosome amplification in human ovarian cancer.* J Ovarian Res, 2013. **6**(1): p. 55.
35. Or, Y.Y., et al., *Survivin depletion inhibits tumor growth and enhances chemosensitivity in hepatocellular carcinoma.* Mol Med Rep, 2014. **10**(4): p. 2025-30.
36. Plewka, D., et al., *Survivin in ovary tumors.* Ginekol Pol, 2015. **86**(7): p. 525-30.
37. Ye, Q., L. Lei, and A.X. Aili, *Identification of potential targets for ovarian cancer treatment by systematic bioinformatics analysis.* Eur J Gynaecol Oncol, 2015. **36**(3): p. 283-9.
38. Alizadeh, A.A., et al., *Distinct types of diffuse large B-cell lymphoma identified by gene expression profiling.* Nature, 2000. **403**(6769): p. 503-11.
39. Baker, D.J., et al., *BubR1 insufficiency causes early onset of aging-associated phenotypes and infertility in mice.* Nat Genet, 2004. **36**(7): p. 744-9.
40. Bharadwaj, R. and H. Yu, *The spindle checkpoint, aneuploidy, and cancer.* Oncogene, 2004. **23**(11): p. 2016-27.

6 KIFC1 AS A NOVEL THERAPEUTIC TARGET FOR P53 MUTANT COLORECTAL CANCER

This study is not published yet. People who contributed to this study are listed below with their contributions:

1. Karuna Mittal: Conceived and designed the study, carried out major experiments (immunohistochemical and immunofluorescence staining, imaging, transfection and the declustering experiments), analyzed and interpreted the data, and wrote the manuscript.
2. Guanhao Wei: Performed the statistical analysis.
3. Jaspreet Kaur: Performed immunoblot assays.
4. Remus. M. Osan: Guided in the statistical analysis.
5. Padmashree C. G. Rida: -Helped in designing the study and critically revised the manuscript.
6. Ritu Aneja: Co-corresponding author of the study- Helped in designing the study and critically revised the manuscript.

6.1 Abstract

Loss or mutation of p53 gene is the most frequent genetic lesion in late-stage colon cancers. The optimal management of p53 mutant colorectal cancer (CRC) remains a significant therapeutic challenge owing to its resistance to 5-fluorouracil, the first-choice chemotherapy drug for CRC. Thus, the search for novel therapeutic targets for the treatment of p53 mutant CRC is highly warranted. We report here that p53 negatively regulates expression of KIFC1 (a centrosome clustering protein), which can serve as a potential therapeutic target for p53 mutant CRCs. To test this hypothesis, we first immunohistochemically stained 203 CRC tissue samples for p53, KIFC1, and FOXM1 and calculated their weighted indices (WIs) for nuclear staining. Further, we quantitated the protein levels of KIFC1 and FOXM1 by immunoblotting. For determining the mechanistic relationship of KIFC1 and p53, overexpression (OE) of p53 and ChiP assays were performed. Finally, inhibited KIFC1 by pharmacological and genetic methods to elucidate the role of the KIFC1 inhibition on the vitality of p53-/- CRC cells. Our results indicated that p53-/- and p53 mutant CRC [p53 null n=82, p53mutant n=40, and WT n=81] exhibited significantly ($p<0.001$) higher expression of KIFC1 and FOXM1 when compared with the p53 WT CRC tissue samples and was associated with worse overall survival (HR=4.249, p=<0.001)). p53-/- cells showed increased expression of KIFC1 and FOXM1. OE of p53 in p53-/- cells decreased the expression of FOXM1 and KIFC1 indicating the negative regulation of KIFC1 via FOXM1 which was further strengthened by ChiP assay (FOXM1 interaction with KIFC1 promoter was significantly higher $p=0.037$ in p53-/- cells when compared with p53 WT cells). Inhibition of KIFC1 using shRNA, CW069 (a known KIFC1 inhibitor) and griseofulvin (a known centrosome declustering drug), led to increased multipolarity followed by cell death only in p53-/- CRC cells. Collectively our results indicate that p53 negatively regulates expression of KIFC1 via FOXM1

and contributes to poor outcomes in p53 mutant CRCs. Thus, KIFC1 may serve as a potential therapeutic target for p53 mutant CRCs.

6.2 Introduction

Colorectal cancer (CRC) is one of the leading causes of cancer morbidity and mortality in the United States. Studies indicate that the multistep progression from normal intestinal epithelial tissue to metastatic neoplasm in CRC results from impairment of multiple regulatory mechanisms involving major signaling pathways that regulate important cellular functions [1, 2]. Inactivation of tumor suppressor genes such as those encoding adenomatous polyposis coli (*APC*) [3, 4] and *p53* [5]; and oncogenic activation of *KRAS* and *BRAF* have been shown to be crucial for the pathogenesis of CRC [6]. The mutations in p53 or its loss of function mainly occur at the transition from adenoma to cancer, and the frequency of alterations in the gene increases with the corresponding progression of the lesion [7]. p53 is a stress-inducible transcription factor, which regulates a large number of diverse downstream genes to exert regulative function in multiple signaling processes [8]. p53 mutation occurs in approximately 40%-50% of sporadic CRC, and the status of p53 mutation is closely related to the progression and outcome of sporadic CRC [8, 9].

Studies have shown that CRC cells carrying p53 mutation often develop resistance to the apoptotic effects of 5-fluorouracil (5-FU is the first-line adjuvant therapeutic agents used CRC therapy) [10], both in vitro [11, 12] and in vivo [13-18]. Resistance to chemotherapy represents the major obstacle for the improvement of survival of nearly 50% of CRC patients and the current therapies to target mutant p53 are not effective as different mutations affect p53 function differently and different agents may be required to target different mutations. Thus, identification of molecules or pathways that can be targeted in p53 mutant CRC might help in improving the patient outcome.

Studies have shown that p53, has been linked to the regulation of centrosome duplication and centrosome amplification (CA) is a consequence of mutation of p53 [19-21] in multiple cancers. In cancer cells, excess centrosomes cluster into two polar groups during mitosis, giving rise to pseudo-bipolar spindles. Merotelic attachment of individual kinetochores to more than one spindle pole is a frequent occurrence. Such inappropriate attachments can cause CIN in the resulting two, three, or more daughter cells via missegregation of whole chromosomes and/or the separation of parts of chromosomes via the stress placed on chromosomes by microtubule attachments and their misguided forces, rendering the chromosomes unstable and liable to break [22]. Further, clustered supernumerous centrosomes are inherited by progeny cells, leading to a perpetuation of CIN in progeny cells. Numerical and structural CA has been reported in CRCS and researchers have reported CA and chromosomal instability in several CRC cell lines suggesting a link between CA and CIN in CRCs. In another study, it was reported that inactivation of p53 in CRC cells HCT116 lead to a 3.5-fold increase in tetraploidization. Also, p53 is involved in centrosome clustering and thus preventing cells to undergo mitotic catastrophe. Therefore, loss of p53 leads to both induction of CA and generation of CIN in CRCs.

KIFC1, also known as HSET, is a nonessential kinesin motor protein, that plays a crucial role in centrosome clustering in cancer cells [23, 24]. Knockdown of KIFC1 was shown to induce multipolar spindle defects and cell death in mitotic cancer cell lines containing extra centrosomes [24] whereas it had no effect on cell division in a variety of diploid control cell lines [24]. In cancer cells, the role of KIFC1 becomes indispensable due to the presence of supernumerary centrosomes. This differential dependence of cancer cells on KIFC1 for viability makes KIFC1 a cancer-cell selective therapeutic target. We and others have shown that KIFC1 is elevated in several cancer types [25-28], including colon cancer. To further understand the regulation and expression of

KIFC1 in CRCS herein this study we evaluated KIFC1 expression in clinical samples of p53 mutant, WT and null CRCs and observed higher expression of KIFC1 with p53 mutation/loss and was associated with poor overall survival in patients. Furthermore, to understand better the association KIFC1 and p53 mutation/loss we performed invitro assays to disseminate role of upstream molecules of KIFC1 in indirect regulation through p53. We observed the FOXM1 member of the Forkhead Box (Fox) family of transcription factors positively regulates expression of KIFC1 in p53 null CRC cells. Studies have also shown that p53 negatively regulates expression of FOXM1[29]. Thus, collectively suggesting that p53 negatively regulates expression of KIFC1 in CRCs via FOXM1. Furthermore, we showed that suppression of KIFC1 via pharmacological (CW069 known inhibitor) genetic (siRNA) induces multipolarity in p53-/- CRC cells resulting in increased cell death. Lastly, we presented that CRC cells with p53 mutation show higher sensitivity to griseofulvin (GF), and treatment with GF causes extensive multipolarity followed by mitotic catastrophe in these cells suggesting GF might be triggering centrosome declustering by inhibiting KIFC1. Collectively our study shows that KIFC1 can serve as a novel therapeutic target in p53 null/mutant CRCs.

6.3 Material and Methods

6.3.1 Clinical samples

203 formalin-fixed paraffin-embedded (FFPE) CRC resection samples (full-face sections) with information on all clinicopathologic parameters and clinical outcomes were obtained from Emory University Hospital, Atlanta, USA. All aspects of the study including protocols, sample procurement, and study design were approved by IRBs of Emory University Hospital.

6.3.2 Cell culture

All the cell lines used in the study were obtained from American Type Culture Collection (ATCC). The colon cell lines utilized in this study included HCT 116 wild type (WT) and HCT 116 p53 null. were grown in McCoy's 5A media supplemented with 10% Hyclone Fetal Bovine serum and 1% penicillin/streptomycin. All cell lines were maintained in humidified 5% CO_2 atmosphere at 37^0 C.

6.3.3 Lysate preparation and immunoblotting

Whole cell protein lysates were prepared from ~80% confluent cells with 250ul of 1x RIPA cell lysis buffer (Cell Signaling). The 1x lysis buffer contained 1 mM b-glycerophosphate, 20 mM Tris–HCl (pH 7.5), 1 mM Na2EDTA, 1 mM Na3VO4, 150 mM NaCl, 1 mM EGTA, 2.5 mM Na4P2O7, 1 ug/ml leupeptin, and 1% Triton. Lysis buffer was supplemented with 10% protease inhibitor to prevent protein degradation. Equal amounts of protein (30ug) was loaded and fractionated using 10% SDS-PAGE gel. Pierce ECL kit (Thermo-Scientific) was used for detection of immune-reactive bands corresponding to the respective primary antibody. β-actin was used as loading control.

6.3.4 Immunofluorescence staining, imaging, and scoring of clinical specimens

Formalin-fixed paraffin-embedded tissue slides were deparaffinized in xylene (three changes) followed by serial rehydration in ethanol baths (100%, 95%, 70% and 50%). Antigen retrieval was done by heating slides in a pressure cooker in citrate buffer (pH 8.5) at psi 15 for 30 min. Blocking was performed by incubating the slides with the 100mM glycine for 30 min. Tissue samples were then incubated with primary mouse antibody against γ -tubulin at 1:1000 dilution at room temperature for 1 h, followed by washing 3X with PBS. The samples were then incubated with

secondary antibody (Alexa-555 anti-mouse) at 1:2000 dilution for 2 h, at 37 °C followed by washing 3X with PBS. Next, the tissue samples were incubated with Hoechst 33342 (1:5000) at room temperature for 10 minutes. Finally, coverslips were mounted with Prolong-Gold Antifade Reagent with DAPI (Invitrogen). Tissue samples were imaged using the LSM 700 Confocal microscope (Oberkochen, Germany) and the images were processed using the Zen software (Oberkochen, Germany). The percentage of cells with CA was quantitated from 10 randomly selected fields, with ~ 200 cells counted for each sample.

6.3.5 Immunohistochemistry and scoring

Samples were processed in the same way till antigen retrieval as mentioned above in Immunofluorescence section. Following antigen retrieval, slides were cooled down by keeping them in ice for 20 minutes. Slides were subjected to two blocks- firstly with hydrogen peroxide block for 20 minutes to quench endogenous peroxidase activity, secondly with protein block for 10 minutes. Slides were incubated with primary antibodies for p53 (Santa Cruz) and KIFC1 (Abcam) for 1 hour. MACH2 HRP-conjugated secondary antibody was applied for 30 minutes followed by chromogen visualization by DAB (Biocare Medical). Finally, slides were counterstained with Myer's hematoxylin (Dako), dehydrated with serial washes in ethanol followed by xylene and mounted. A relative intensity score was represented as 0 = none, 1 = low, 2 = moderate, or 3 = high. The product of intensity and frequency was measured as a weighted index (WI) for both the nucleus and cytoplasm.

6.3.6 Immunocytofluorescence staining

Cells were cultured on coverslips and, after the confluency reached approximately 80 %, cells were fixed with ice-cold methanol for 7 min. The cells were blocked with 5 % BSA/0.01 % Triton X for 45 min at room temperature and then incubated at 37 °C with antibodies directed against γ-

tubulin and α-tubulin at a dilution of 1:2000 for 30 min. Cells were washed 5 times with 1x PBS, followed by incubation with anti-rabbit Alexa Fluor 488 and anti-mouse Alexa Fluor 555 at 37^0 C for 30 minutes. Next, cells were washed briefly for 8 times with 1x PBS, followed by staining with Hoechst 33342 used at a dilution of 1:5000 for 10 minutes at room temperature. Finally, cells were washed with 1x PBS for 3minutes and, mounted with Prolong Gold antifade reagent. Immunofluorescence imaging was carried out using the Zeiss LSM 700 confocal microscope (Oberkochen, Germany) and images were analyzed using the Zen software (Oberkochen, Germany).

6.3.7 p53 overexpression and KIFC1 knockdown

HCT 116 WT and null cells were grown to 70% confluency and transfected using Lipofactamine 2000 according to manufacturer's instructions. KIFC1 gene knockdown in HCT116 null cell was achieved using KIFC1 siRNA (Origene). The non-targeting universal scrambled siRNA was used as the negative control in both the cell lies. 24 hours post transfection, whole cell protein lysates were prepared for immunoblot assay. HCT 116 null cells were grown to 70% confluency and transfected using Lipofactamine 2000 according to manufacturer's instructions. For this, 6 ul of lipofectamine was added to 4ug of p53 overexpression vector and the mixture was slowly added to the cells. GFP tagged p53 vector was a generous gift from Dr. Tylor Jacks (Addgene plasmid #12091). 24 hours post transfection, whole cell protein lysates were prepared for immunoblot assay.

6.4 Results

6.4.1 p53-mutant CRCs show poorer overall survival (OS) compared to p53-wild-type CRCs

203 formalin-fixed paraffin-embedded FFPE) CRC resection samples (full-face sections) were stained immunohistochemically (IHC) for p53 **(Figure. 6.4.1A)** and were scored by two independent pathologists without prior knowledge of the patients' pathologic/outcome data. Samples wherein <80% but >1% of cells stained positive for p53 were considered p53 wild type (WT) (n=81), those wherein ≥80% of cells stained positive for p53 were considered p53-mutant (M) (n=40), and those where in <1% cells were stained for p53 were considered as p53-null (N) (n=81). Multiple studies have provided evidence where p53 IHC staining can be used as a surrogate for the mutational analysis in the diagnostic workup of the various carcinomas. Kaplan-Meier survival analysis suggested that p53-null CRC patients have the worse prognosis than p53-mutant and p53-WT. Also, p53 mutant CRCs were associated with worse OS than p53 WT CRCs. (HR=4.249, p=<0.001) **(Figure. 6.4.1B)**. These findings were supported by our in silico findings GSE41258) where the p53-mutant (n=93) CRC was associated with poorer OS (HR=1.46, P=<0.05) **(Figure. 6.4.1C)** than p53-WT CRCs.

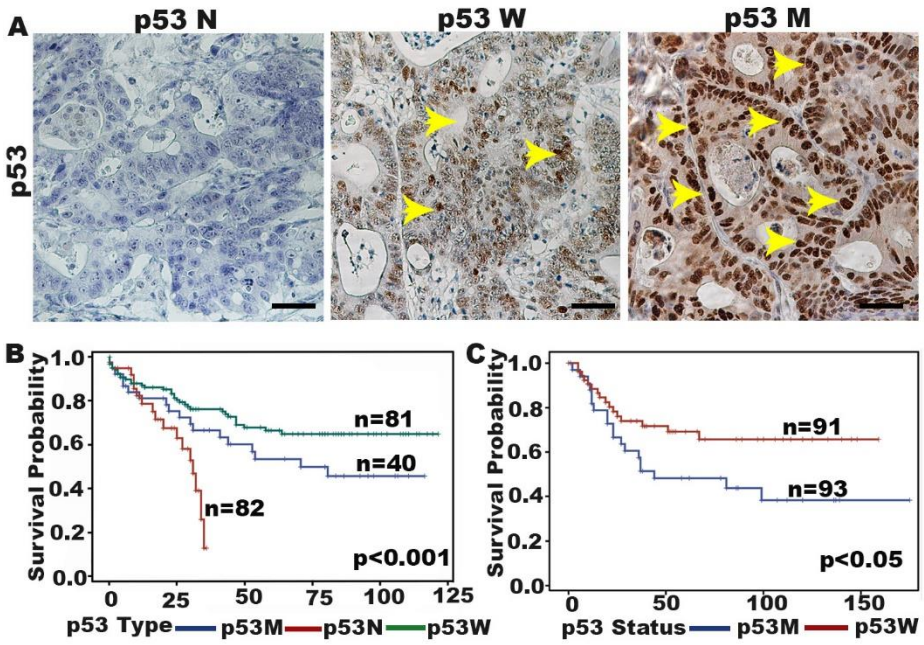

Figure 6.4.1 p53-mutant CRCs show poorer overall survival (OS) compared to p53-wild-type CRCs
A) Representative micrographs of p53 IHC staining in CRC tissue samples. (B) Kaplan-Meier plots of OS based on p53 status in clinical tissue samples. (C) Kaplan-Meier plots of OS based on p53 status in in silico data.

6.4.2 p53-mutant CRCs exhibit higher centrosome amplification than p53-WT CRCs

Studies have shown that p53 mutations in various tumor types are associated with CA. To study this we visualized amplified centrosomes in 40 CRC samples (n=20 p53-WT and n=20 p53-mutant) employing multicolor confocal immunofluorescence microscopy. Centrosomes were labeled by anti-γ-tubulin (green) antibody, and centrosomal aberrations were determined by quantifying percentage of cells bearing abnormal numbers of γ-tubulin foci (more than two). We found that the number of cells/500 cells harboring extra centrosomes was higher in p53-mutant CRCs when compared with to p53-WT CRCs (p=0.086) **(Figure. 6.4.2.1 A, B)**. In line with this, we observed that p53-null colon cancer cell line (HCT116 p53-null CRC cells) exhibited notably higher CA (~40%) as compared to p53-WT (~10%) cells **(Figure. 6.4.2. A, B)**. Furthermore, protein levels of proteins associated with CA were also elevated in p53-null cells when compared

with the p53-WT CRC cells **(Figure. 6.4.3 C)**. Thus, these findings indicate that p53null/mutant CRCs exhibit higher CA when compared to the WT CRCs.

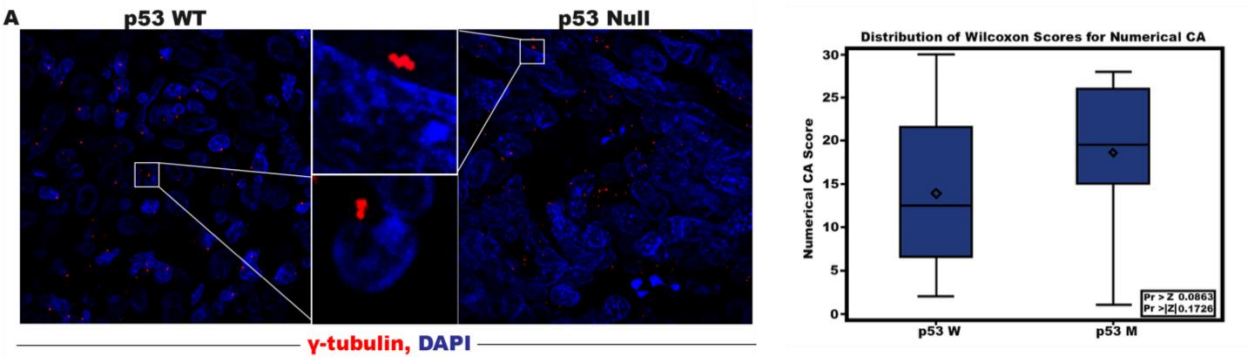

Figure 6.4.2 p53-mutant CRCs exhibit higher centrosome amplification than p53-WT CRCs

(A) Representative confocal images showing the presence of CA in p53-mutant and WT CRC tissue. (B) Box whisker graph representing the distribution of % numerical CA in p53-WT and p53-mutant CRC tissue sections

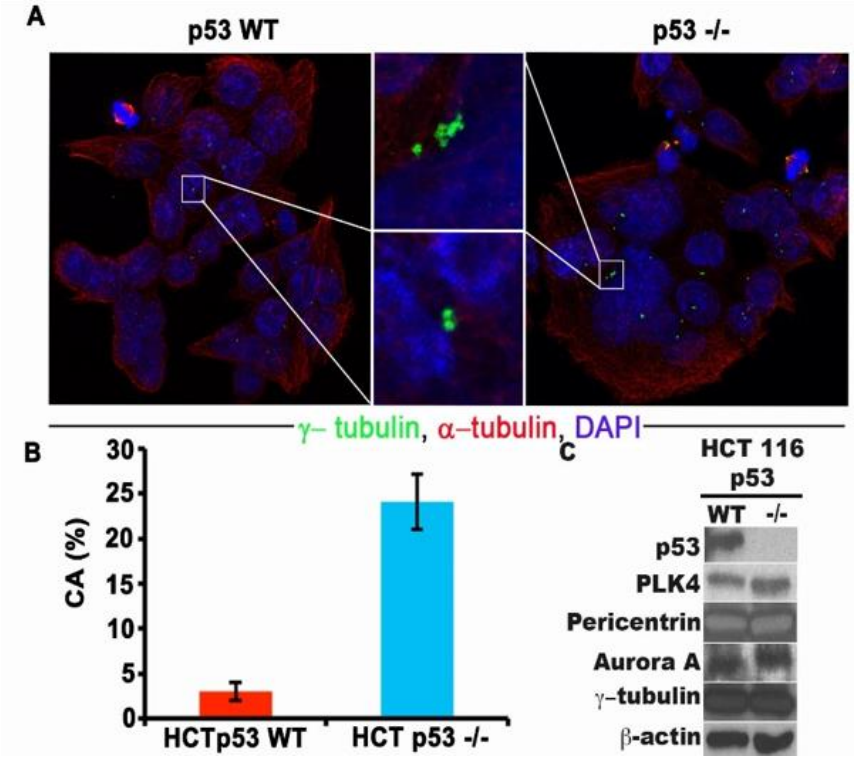

Figure 6.4.3 HCT 116 p53-/- CRC cells exhibit higher centrosome amplification than WT cells

(A) Confocal micrograph showing the presence of CA in HCT-116 p53-null CRC cells and HCT-116 p53-WT cells. Scale bar, 5 µm. (B) Degree of CA in p53-null and p53-WT CRC cells.

(C) Immunoblots showing expression of the CA associated proteins in p53-null and p53-WT CRC cells.

6.4.3 p53-mutant CRCs exhibit higher expression of the centrosome clustering kinesin, KIFC1

In cancer cells that harbor supernumerary centrosomes, KIFC1 is required for proper spindle assembly [23], where it promotes centrosome clustering and suppresses multipolar spindle formation and cell death [24]. Thus, given the association of high CA with p53-mutant status in CRCs, we suspected that KIFC1 levels may perhaps be elevated in these samples in order to cope with the increased centrosomal load. Therefore, serial sections from the 203 CRC tissue samples that were stained for p53 (see 6.3.1.) were stained for KIFC1. Scoring was performed for both the intensity of staining (0 = none,1 = low, 2 = moderate, 3 = high) and the percentage of cells with any positivity (i.e., staining of 1+). KIFC1 WIs were calculated as the product of the nuclear staining intensity and percentage of positive cells. P53-null (p53-/-, n=82) and p53-mutant CRC (n=40) exhibited significantly ($p<0.001$) higher expression of KIFC1 when compared with the p53-WT CRC (n=81) tissue samples **(Figure. 6.4.4 A, B)**. Similarly, we observed that the p53-null CRC cells exhibited higher expression of KIFC1 (immunoblotting) when compared with the p53-WT CRC cells **(Figure. 6.4.4 C)**.

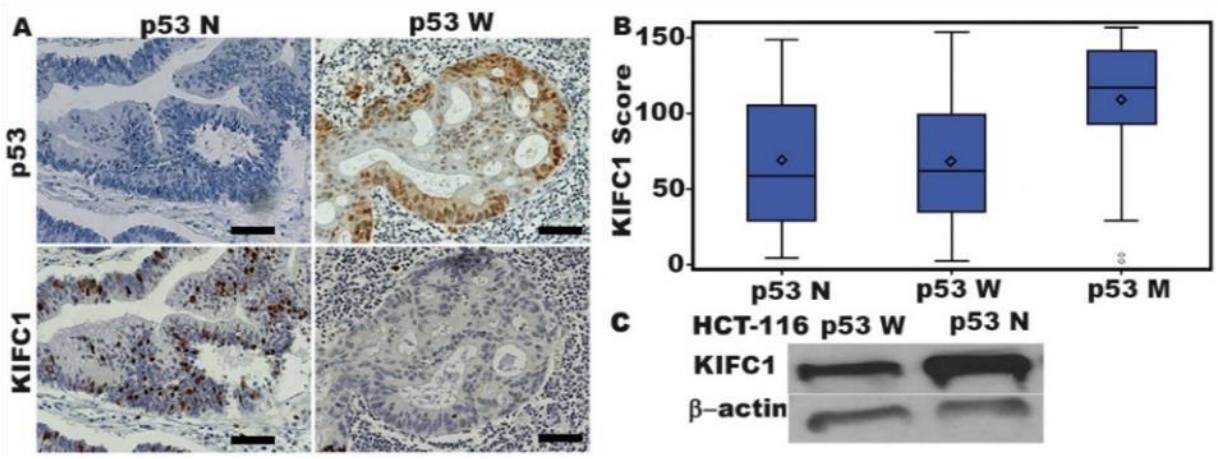

Figure 6.4.4 p53-mutant CRCs exhibit higher expression of the centrosome clustering kinesin, KIFC1

A) Representative micrographs of p53 and KIFC1 IHC staining in p53 null/ mutant and p53-WT CRC tissue samples. B) Box whisker graph representing the KIFC1 expression in p53-null, p53-mutant and p53-WT CRC tissue samples. C) Immunoblots showing expression of KIFC1 in p53-null and p53-WT CRC cells.

6.4.4 FOXM1 expression is correlated with KIFC1 and is higher in p53-mutant when compared with the WT

Serial sections from 203 CRC tissue samples used in Section 6.3.1 were IHC- stained for FOXM1 and WIs for nuclear staining was calculated. We observed that expression of FOXM1 was significantly higher in p53-mutant and p53-null group when compared with the p53-WT CRCs **(Figure 6.4.5)**. In addition, expression of FOXM1 was strongly correlated with KIFC1 expression ($r=1.3$, $p=<0.05$). We also observed that p53-null CRC cells expressed higher levels of FOXM1 when compared with p53-WT CRCs.

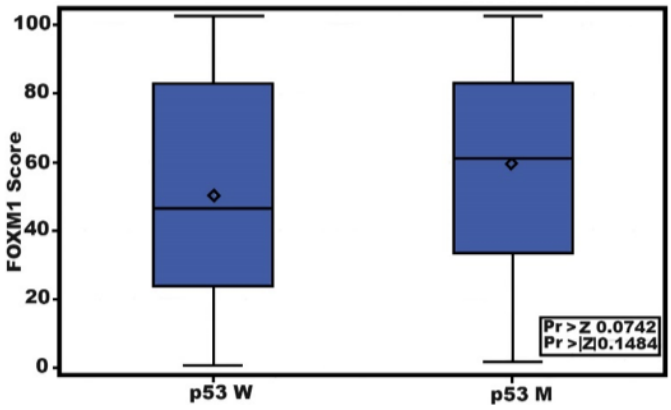

Figure 6.4.5 Box whisker graph representing the FOXM1 expression in p53-mutant and p53-WT CRC tissue samples.

6.4.5 FOXM1 and KIFC1 expression was decreased by p53 overexpression (OE) in p53-null cells and FOXM1 binds to the promoter of KIFC1 with higher binding affinity

Next, we transiently transfected the pEGFP-P53 construct into HCT116 p53-null CRC cells. Given a transfection efficiency of ~70%, we observed that FOXM1 and KIFC1 expression decreased in HCT 116 p53-null CRC cells with OE of p53, when compared with the control vector **(Figure. 6.4.6A)**. Literature has reported that KIFC1 promoter has binding sites for FOXM1. In line with this, our *in silico* analysis using publily-available TRANSFAC dataset showed that KIFC1 promoter regions contain two FOXM1 binding motif sites suggesting that KIFC1 is a potential target gene of FOXM1 (data not shown). Additionally, our ChIP results indicated a significantly higher ($p=0.037$) binding of FOXM1 to the KIFC1 promoter in p53-null CRC cells when compared with the p53-WT CRC cells **(Figure. 6.4.6B)**. Thus, collectively indicating that p53 negatively regulates expression of KIFC1 via FOXM1.

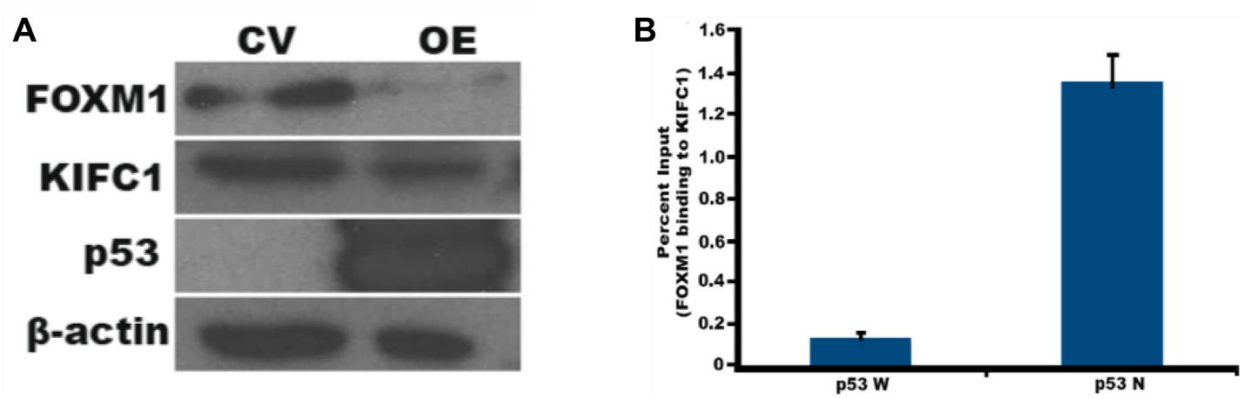

Figure 6.4.6 FOXM1 regulates expression of KIFC1 in p53-/- CRC cells
A) Immunoblots showing decreased expression of KIFC1 and FOXM1 after overexpression of p53 in HCT116 p53-null cells. **B)** Bar graph representing FOXM1 interaction with KIFC1 promoter in HCT 116 p53-null and p53-WT CRC cells.

6.4.6 Inhibition of KIFC1 using siRNA led to increased multipolarity only in p53-/- colon cancer cells

Given that KIFC1 was significantly upregulated in p53-mutant and p53-null CRC cells, we were prompted to examine the effects of depletion of cellular pools of KIFC1 in CRC cells. We performed transient siRNA transfections using pools of KIFC1 siRNA duplexes in p53-null and p53-WT CRC cells. KIFC1 depletion induced centrosome declustering and significant spindle multipolarity **(Figure. 6.4.7A)** in p53-null HCT116 cells. p53-WT HCT 116 cells, however, maintained bipolarity upon KIFC1 RNAi **(Figure. 6.4.7B)**, indicating that KIFC1 is a potential cancer-selective therapeutic target for p53-null/mutant CRC.

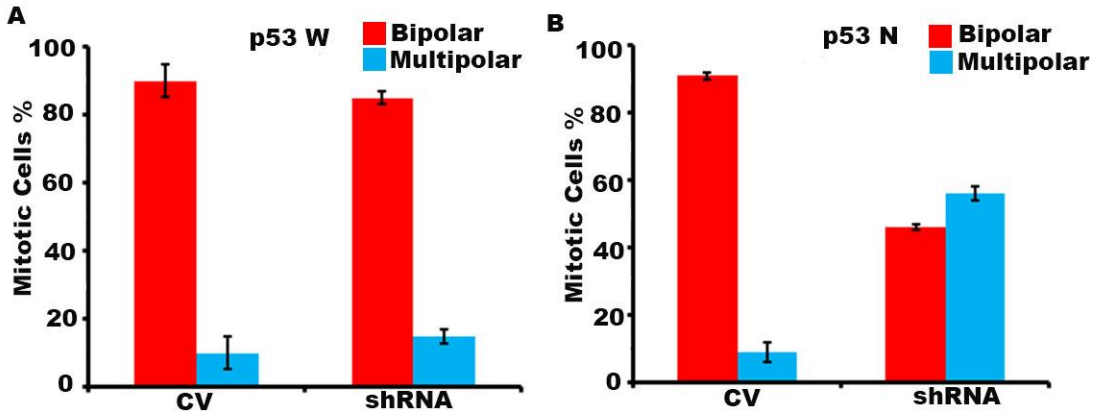

Figure 6.4.7 Bar graph representing % bipolar and multipolar cells in KIFC1 KD and CV (A) p53-WT (B) p53-null CRC cells.

6.4.7 Griseofulvin induces multipolarity and downregulates expression of KIFC1

Griseofulvin (GF) is an antifungal drug which has recently been shown to inhibit proliferation of various types of cancer cells and to inhibit tumor growth in nude mice. Studies have shown that Griseofulvin inhibits microtubule dynamics, which leads to spindle tension causing centrosome declustering, multipolar mitosis and cell death. Thus, we suspected that Griseofulvin might be leading to centrosome declustering via inhibition of KIFC1 activity in p53-mutant CRCs. To this end, we tested efficacy of Griseofulvin in CRC cells. We observed that Griseofulvin induced extensive centrosome declustering and mutlipolarity (~85% of mitotic cells were multipolar) in p53-null CRC cells when compared with the p53-WT CRC cells (~30% of mitotic cells were multipolar). Furthermore, the extent of multipolarity and cell death induced by Griseofulvin was far superior to that of a known KIFC1 inhibitor CW069 **(Figure. 6.4.8A-C)**. Further, we performed intensive in silico modeling and observed that Griseofulvin (similar to CW069) docks onto a pocket within the motor-domain that houses the ATP-binding site of KIFC1 (Loop-5) with similar (-0.24 for CW069 and 0.25 for Griseofulvin) mean ligand efficiency. The predictive free energy (ΔG) for this binding is -6.0 Kcal/mole **(Figure. 6.4.8A, C)**.

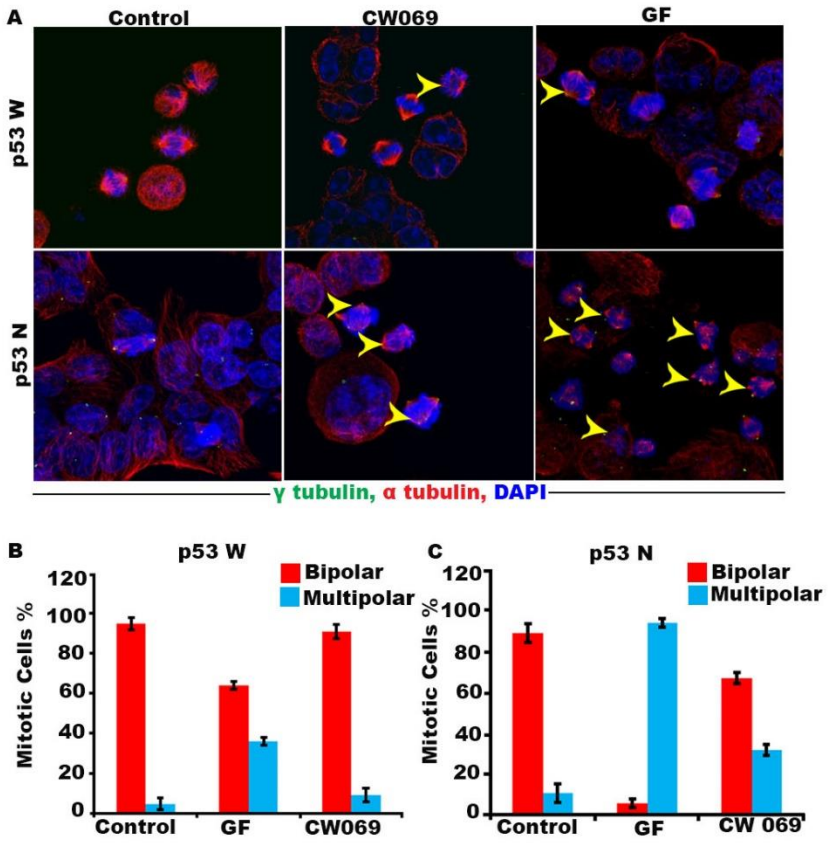

Figure 6.4.8 Griseofulvin induces multipolarity and downregulates expression of KIFC1
A) Confocal micrographs showing rampant multipolarity after treatment with CW069 and Griseofulvin (GF). B) Bar graphs representing % bipolar and multipolar cells in CW069- and GF-treated in p53-WT and p53-null CRC cells.

6.4.8 Griseofulvin inhibits the ATPase activity of KIFC1

Since KIFC1 is a kinesin-like microtubule motor protein, it contains a conserved motor domain that catalyzes ATP hydrolysis and generates a minus end-directed mechanical force along the microtubule. We, therefore, asked if Griseofulvin can inhibit the ATPase activity of KIFC1 in vitro. Employing the Kinesin ATPase ELIPA assay kit (Cytoskeleton Inc.) containing a kinesin heavy chain motor domain protein (KIF5B) (as a positive control) and microtubules as a substrate for kinesin activity, our results indicated that Griseofulvin inhibits KIFC1's ATPase activity to a similar degree as CWO69 **(Figure. 6.4.9B)**. Thus, Griseofulvin inhibits the motor activity of KIFC1 and induces centrosome declustering.

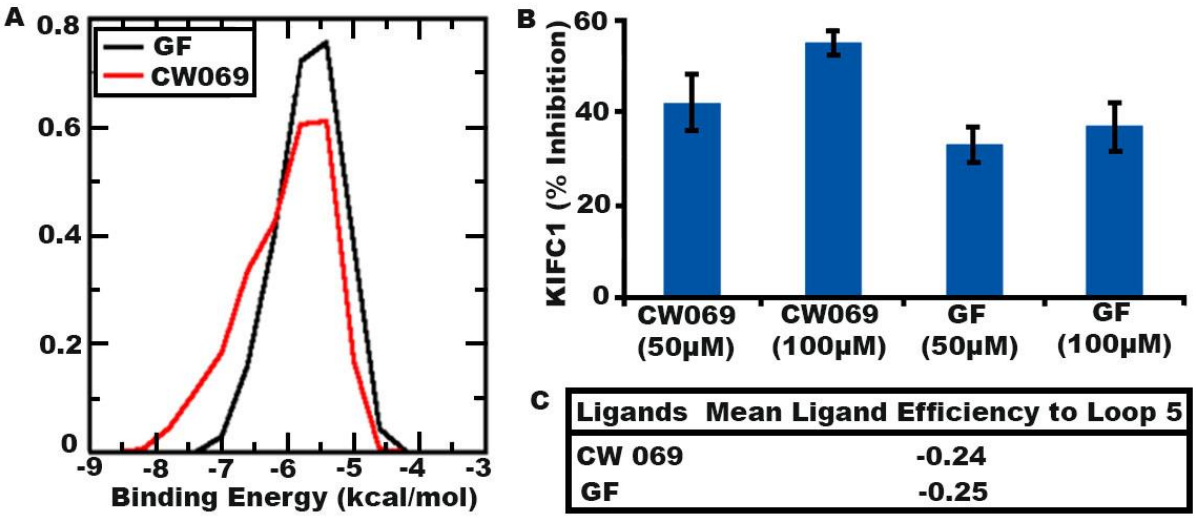

C

Ligands	Mean Ligand Efficiency to Loop 5
CW 069	-0.24
GF	-0.25

Figure 6.4.9 Griseofulvin inhibits the ATPase activity of KIFC1
A) Distribution of binding energies of GF and CW069 from docking simulation. (B) Bar graph representing percentage inhibition of KIFC1 activity by GF and CW069 at 50 and 100µm. (C) Binding efficiency values of the CW069 and GF at loop 5 on KIFC1.

6.5 Discussion

In this study we showed that the expression of KIFC1 is significantly higher in p53 mutant/null CRCS when compared to the p53 WT CRCs and is associated with poor overall survival. Further, we evaluated the role of upstream regulators of KIFC1 to understand better the association KIFC1 and p53 mutation/loss. We observed the FOXM1 member of the Forkhead Box (Fox) family of transcription factors positively regulates expression of KIFC1 in p53 null CRC cells. Studies have also shown that p53 negatively regulates expression of FOXM1[29]. Thus, collectively suggesting that p53 negatively regulates expression of KIFC1 in CRCs via FOXM1. Moreover, we showed that inhibition of KIFC1 via pharmacological (CW069 known inhibitor) and genetic (siRNA) methods induced multipolarity specifically in p53-/- CRC cells resulting in increased cell death. Finally, we observed that HCT116 p53-/- CRC cells were significantly higher sensitivity to GF when compared that of HCT116 p53WT CRC cells, and treatment with GF induced extensive

multipolarity followed by the mitotic catastrophe in the p53 null CRC cells. This suggests that GF might be triggering centrosome declustering by inhibiting KIFC1.

In conclusion, our results indicate that p53 null/mutant CRCs overexpresses KIFC1 which is associated with poor overall survival suggesting a causative link between KIFC1 and tumor aggressiveness. Taken together our findings underscore that KIFC1 is a potential cancer selective therapeutic target for p533 null/mutant CRCs.

6.6 References

1. Fearon, E.R., *Molecular genetics of colorectal cancer.* Ann N Y Acad Sci, 1995. **768**: . 101-10.
2. Fearon, E.R., *Molecular genetics of colorectal cancer.* Annu Rev Pathol, 2011. **6**: p. 479-507.
3. Giardiello, F.M., et al., *APC gene mutations and extraintestinal phenotype of familial adenomatous polyposis.* Gut, 1997. **40**(4): p. 521-5.
4. Segditsas, S. and I. Tomlinson, *Colorectal cancer and genetic alterations in the Wnt pathway.* Oncogene, 2006. **25**(57): p. 7531-7.
5. Fearon, E.R. and P.A. Jones, *Progressing toward a molecular description of colorectal cancer development.* FASEB J, 1992. **6**(10): p. 2783-90.
6. De Roock, W., et al., *KRAS, BRAF, PIK3CA, and PTEN mutations: implications for targeted therapies in metastatic colorectal cancer.* Lancet Oncol, 2011. **12**(6): p. 594-603.
7. Worthley, D.L., et al., *Colorectal carcinogenesis: road maps to cancer.* World J Gastroenterol, 2007. **13**(28): p. 3784-91.
8. Li, X.L., et al., *P53 mutations in colorectal cancer - molecular pathogenesis and pharmacological reactivation.* World J Gastroenterol, 2015. **21**(1): p. 84-93.
9. Takayama, T., et al., *Colorectal cancer: genetics of development and metastasis.* J Gastroenterol, 2006. **41**(3): p. 185-92.
10. Wang, T., et al., *Inhibition of transient receptor potential channel 5 reverses 5-Fluorouracil resistance in human colorectal cancer cells.* J Biol Chem, 2015. **290**(1): p. 448-56.
11. Bunz, F., et al., *Disruption of p53 in human cancer cells alters the responses to therapeutic agents.* J Clin Invest, 1999. **104**(3): p. 263-9.
12. Boyer, J., et al., *Characterization of p53 wild-type and null isogenic colorectal cancer cell lines resistant to 5-fluorouracil, oxaliplatin, and irinotecan.* Clin Cancer Res, 2004. **10**(6): p. 2158-67.
13. Luna-Perez, P., et al., *p53 protein overexpression and response to induction chemoradiation therapy in patients with locally advanced rectal adenocarcinoma.* Ann Surg Oncol, 1998. **5**(3): p. 203-8.
14. Russo, A., et al., *The TP53 colorectal cancer international collaborative study on the prognostic and predictive significance of p53 mutation: influence of tumor site, type of mutation, and adjuvant treatment.* J Clin Oncol, 2005. **23**(30): p. 7518-28.

15. Spitz, F.R., et al., *p53 immunohistochemical staining predicts residual disease after chemoradiation in patients with high-risk rectal cancer.* Clin Cancer Res, 1997. **3**(10): p. 1685-90.
16. Iacopetta, B., *TP53 mutation in colorectal cancer.* Hum Mutat, 2003. **21**(3): p. 271-6.
17. Xu, J., et al., *Unequal prognostic potentials of p53 gain-of-function mutations in human cancers associate with drug-metabolizing activity.* Cell Death Dis, 2014. **5**: p. e1108.
18. Benhattar, J., et al., *p53 mutations as a possible predictor of response to chemotherapy in metastatic colorectal carcinomas.* Int J Cancer, 1996. **69**(3): p. 190-2.
19. Fukasawa, K., *P53, cyclin-dependent kinase and abnormal amplification of centrosomes.* Biochim Biophys Acta, 2008. **1786**(1): p. 15-23.
20. Fukasawa, K., et al., *Abnormal centrosome amplification in the absence of p53.* Science, 1996. **271**(5256): p. 1744-7.
21. Tarapore, P. and K. Fukasawa, *Loss of p53 and centrosome hyperamplification.* Oncogene, 2002. **21**(40): p. 6234-40.
22. Gregan, J., et al., *Merotelic kinetochore attachment: causes and effects.* Trends Cell Biol, 2011. **21**(6): p. 374-81.
23. Kleylein-Sohn, J., et al., *Acentrosomal spindle organization renders cancer cells dependent on the kinesin HSET.* J Cell Sci, 2012. **125**(Pt 22): p. 5391-402.
24. Kwon, M., et al., *Mechanisms to suppress multipolar divisions in cancer cells with extra centrosomes.* Genes Dev, 2008. **22**(16): p. 2189-203.
25. Chan, J.Y., *A clinical overview of centrosome amplification in human cancers.* Int J Biol Sci, 2011. **7**(8): p. 1122-44.
26. Grinberg-Rashi, H., et al., *The expression of three genes in primary non-small cell lung cancer is associated with metastatic spread to the brain.* Clin Cancer Res, 2009. **15**(5): p. 1755-61.
27. Pannu, V., et al., *HSET overexpression fuels tumor progression via centrosome clustering-independent mechanisms in breast cancer patients.* Oncotarget, 2015. **6**(8): p. 6076-91.
28. Pawar, S., et al., *KIFCI, a novel putative prognostic biomarker for ovarian adenocarcinomas: delineating protein interaction networks and signaling circuitries.* J Ovarian Res, 2014. **7**: p. 53.
29. Barsotti, A.M. and C. Prives, *Pro-proliferative FoxM1 is a target of p53-mediated repression.* Oncogene, 2009. **28**(48): p. 4295-305.

7 MULTINUCLEATED POLYPLOIDY DRIVES RESISTANCE TO DOCETAXEL CHEMOTHERAPY IN PROSTATE CANCER

Parts of this chapter have been published verbatim in ***British Journal of Cancer 2017; Apr 25; 116(9:1186-1194 as "Multinucleated polyploidy drives resistance to Docetaxel chemotherapy in prostate cancer."***

Authors listed on the paper and their contributions:

1. Karuna Mittal: Conceived and designed the study, carried out major experiments of the study (drug treatment, immunofluorescence staining and imaging, MTT assay), analyzed and interpreted the clinical and invitro data, and wrote the manuscript.
2. Shashi Donthamsetty: Performed flow cytometry experiments.
3. Ramneet Kaur: Critically revised the manuscript.
4. Chunhua Yang: Performed invivo experiments.
5. Meenakshi. V. Gupta: Provided scientific guidance.
6. Michelle.D. Reid: Provided scientific guidance.
7. Da Hoon Choi: Carried out the immunoblot assays.
8. Padmashree C. G. Rida: Helped in designing the study and critically revised the manuscript
9. Ritu Aneja: Co-corresponding author of the study- Helped in designing the study and critically revised the manuscript.

7.1 Abstract

Docetaxel is the only FDA-approved first-line treatment for castration resistant prostate cancer (CRPC) patients. Docetaxel treatment inevitably leads to tumor recurrence after an initial therapeutic response with generation of multinucleated polyploid (MP) cells. Here we investigated role of MP cells in clinical relapse of CRPC. Herein, prostate cancer (PC-3) cells were treated with docetaxel (5 nM) for 3 days followed by a wash-out and samples were collected at close intervals over 35 days post drug-washout. The tumorigenic potential of the giant MP cells was studied by implanting MP cells subcutaneously as tumor xenografts in nude mice. Docetaxel-induced polyploid cells undergo mitotic slippage and eventually spawn mononucleated cells via asymmetric cell division or neosis. Both MP and cells derived from polyploid cells (CDPCs) had increased survival signals, were positive for CD44 and were resistant to docetaxel chemotherapy. While MP cells were tumorigenic in nude mice, these cells took a significantly longer time to form tumors compared to parent PC-3 cells. Generation of MP cells upon docetaxel therapy is an adaptive response of apoptosis-reluctant cells. These giant cells ultimately contribute to the generation of mononucleated aneuploid cells via neosis and may play a fundamental role precipitating clinical relapse and chemoresistance in CRPC.

7.2 Introduction

Despite significant advances in research, diagnosis, and clinical practice, prostate cancer still remains the second most commonly diagnosed cancer and the sixth most common cause of cancer-related death among men worldwide [1]. Androgen-deprivation remains the mainstay of the first line treatment for both primary and metastatic prostate cancer. Initially majority of the patients respond well to this treatment but eventually the tumor progresses to castration-resistant prostate cancer (CRPC) which is the major cause of mortality [2]. Docetaxel was approved by the

European Medicine Agency and the US Food and Drug Administration in 2004 for the first-line treatment of patients with CRPC and is now the only standard of care in this setting [3, 4]. While this clinical regimen prolongs overall survival in CRPC patients, the cancer unfortunately recurs (clinical relapse) inevitably after an initial illusionary therapeutic response. Currently, there is a lack of mechanistic knowledge underlying this tumor cell "replenishment" after docetaxel treatment which inevitably leads to tumor recurrence and translates to only a modest increase in overall survival. The present study explores this therapy-relapse paradox that inescapably results in tumor recurrence shortly after a therapy response.

The formation of giant multinucleated polyploid (MP) cells after therapeutic intervention with either taxane-based chemotherapy including docetaxel or DNA damaging agents has been well described. Studies have reported that some tumor microenvironmental factors including hypoxia are also responsible for the generation of MP cells. Studies have also shown that hypoxia-mimicking $CoCl_2$ treatment induces formation of polyploid cells that contributes to expansion of a cell subpopulation with stem cell characteristics [5, 6]. These polyploid cells can be a result of DNA over-replication [7], abrogated mitotic checkpoint [8] or failed cytokinesis [9]. It was long assumed that these giant polyploid cells do not survive and die due to "mitotic catastrophe" subsequent to multipolar cell division. But, recent evidence indicated that while most polyploid cells succumb to cell death, a small percentage of them survive and produce viable progeny [10, 11]. A study also found that colon cancer cells treated with DNA damaging agent cisplatin generated giant polyploid cells, a subset of which were able to engender viable clones via asymmetric cell division; furthermore, this phenomenon was recapitulated in an in vivo xenograft model of colon cancer treated with cisplatin [12]. Another study revealed that when PC-3 cells were treated with docetaxel, it led to growth arrest and

formation of multinucleated cells and the generation of docetaxel-resistant progeny [13]. A very recent study has reported the cabazitaxel, a second line chemotherapy in CRPC treatment, also leads to chemoresistance by inducing severe multinucleation in prostate cancer cells [14]. Altogether, these data suggest that polyploid cells that were once presumed to be either destined for terminal growth arrest or cell death may actually represent a "transition state" for generation of viable clones.

The current study aimed to analyze the long-term effects of post docetaxel exposure on prostate cancer cells. Our study shows that most of the prostate cancer cells exposed to docetaxel undergo cell death following mitotic arrest. However, a small percentage of the cells "slip out" of mitosis to form giant MP cells. Most of these MP cells succumbed to cell death, but a small fraction survived for several weeks, eventually giving rise to small mononucleated cells via an asymmetric cell division process called neosis. We further show that these MP cells have tumorigenic potential in nude mice and that both MP cells and cells derived from multinucleated polyploid cells (CDPC) are chemoresistant and were positive for cancer stem cell marker CD44. In conclusion, the formation of MP cells after docetaxel treatment suggests an escape process that is involved in tumor relapse and chemoresistance following an initial illusionary therapeutic response.

7.3 Material and Methods

7.3.1 Cell culture and treatment schedule

PC-3 and DU145 cells were obtained from American Type Cell Culture (ATCC) and were grown in RPMI medium supplemented with 10% fetal bovine serum (FBS) and 1% penicillin/streptomycin. Cells were maintained in humidified 5% CO_2. All experiments were performed using 5nM of docetaxel unless stated otherwise.

7.3.2 Flow cytometry

Cells were harvested at different time intervals, washed twice with ice-cold PBS, and fixed in 70% ethanol for at least 24 h. Cell pellets were then washed with PBS followed by RNase A (2 mg/ml) addition and staining with anti-MPM-2 primary antibody and Alexa-488 conjugated secondary antibody. Propidium iodide (0.1% in 0.6% Triton X-100 in PBS) was added for 45 min in dark followed by analysis on a FACS Canto flow-cytometer (BD Canto) using FlowJo software.

7.3.3 Immunofluorescence

Cells were grown on glass coverslips for immunofluorescence microscopy and were fixed and blocked as described previously [40] . Coverslips were incubated in primary antibodies (1:2000 dilution) against γ-tubulin and α-tubulin at 1:2000 dilution for 1 h at 37°C, washed with 1XPBS for 10 min at room temperature, and then incubated in 1:2000 Alexa 488- or 555-conjugated secondary antibodies (Invitrogen; Carlsbad, CA). Cells were washed 5x with PBS and then mounted with Prolong-Gold antifade reagent that contained DAPI (Invitrogen).

7.3.4 Microscopy

Immunofluorescently stained cells were imaged utilizing the Zeiss LSC 700 confocal microscope (Oberkochen, Germany) and were processed with Zen software (Oberkochen).

7.3.5 Time lapse imaging

Giant MP cells were isolated and plated 12 days after docetaxel removal. Cells were imaged for 7 days using time-lapse microscopy at 40x magnification on Zeiss Axio Observer 5A (Oberkochen, Germany). Differential Interface Contrast Images were captured at multiple points every 2 h for 7 days and were processed with Zen software (Oberkochen, Germany). Magnifications and details related to imaging are provided in individual sections.

7.3.6 Lysate preparation and immunoblotting

Cells were cultured to ~80% confluence and after treatments as mentioned in individual sections protein lysates were prepared as described previously [41]. Polyacrylamide gel electrophoresis was used to resolve the proteins, which were transferred onto polyvinylidene fluoride membranes (Millipore). The immune reactive bands were visualized by using Pierce ECL chemiluminescence detection kit (Thermo Scientific). Primary Antibodies, Phospho-Bcl2 (Thr 56) human, Bcl-XL (54H6), Survivin (71G4B7), Beclin-2 and CD44 (156-3C11) were obtained from Cell Signaling. β-actin (SC47778 from Santa Cruz Biotechnology) was used as loading control. All relative band intensities were quantitated by densitometry and were normalized against β-actin values using ImageJ.

7.3.7 Cell migration assay using Boyden Chambers

A total of 10,000 cells suspended in RPMI medium containing 0.5% FBS were added to the upper well of the Boyden chamber. The lower chamber was filled with RPMI medium containing 10% FBS. After 48 h, cells that had migrated to the bottom surface of the filter were fixed with 70% methanol, stained with crystal violet, and counted under a microscope in ten randomly selected fields at a magnification of 20x.

7.3.8 MTT assay

MTT assay was used to measure metabolic activity suitable for analysis of proliferation rates between PC-3, giant MP, and CDPC. Approximately 10,000 cells of each cell type were seeded into each well of a 96-well microplate. The assay was performed over a six-day period with incubation times at 24 h, 48 h, 72 h, 96 h, 120 h, and 144 h. At the end of each incubation period, 10μl of MTT (Sigma-Aldrich, Germany) at 5mg/ml in PBS was added into each well after removal of the culture medium and incubated for 4 h under the same conditions. After the incubation,

100µl of DMSO was added to dissolve the formazan crystals. Absorbance was measured at 570nm using a 96-well microplate reader.

7.3.9 In Vivo Tumor growth

A total of 50,000 PC-3 cells or giant MP cells (cells that were treated with 5nM docetaxel and harvested one day after drug removal) were subcutaneously injected in the right flank of 6-week old male BALB/c nude mice (Harlan Laboratories, Indianapolis, IN). Tumors were measured every week using a digital Vernier Caliper. The two longest perpendicular axes in the x/y plane of each xenograft tumor were measured to the nearest 0.1 mm. The depth was assumed to be equivalent to the shortest of the perpendicular axes, defined as y. Tumor volume was calculated using the formulae $xy^2/2$ as is standard practice. All animal experiments were performed in compliance with Georgia State University (GSU) Institutional Animal Care and Use Committee (IACUC) guidelines. All animal protocols (including description of experiments and experimenters) were approved by GSU IACUC.

7.3.10 Statistical analyses

Unless otherwise stated in the Methods and Results sections, statistical analyses were performed using two-tailed Student's t-tests. The criterion for statistical significance for all analyses was $p<0.05$.

7.4 Results

7.4.1 Docetaxel induces formation of giant multinucleated polyploid (MP)cells

To corroborate the fact that docetaxel treatment causes mitotic arrest prior to cell death, we examined the cell cycle events post docetaxel treatment. To this end, we treated PC-3 cells with

5nM docetaxel for 72 h and then stained them for MPM-2 antibody (mitotic cell marker) by flow cytometry. As shown in Figure7.4.1A, there was an induction of mitotic arrest 24 h post docetaxel treatment. Using immunofluorescence confocal microscopy, we noticed large number of mitotically-arrested cells (Figure.7.41B) displaying aberrant multipolar spindles 24 h after docetaxel treatment. On the other hand, DMSO treated control cells showed normal bipolar cell division (Figure 7.4.1B). Following this, a disappearance of the M-phase population and an emergence of apoptotic cells (sub-G1 population) was observed at 48 h after docetaxel treatment (Figure 7.4.1D).

We next investigated if docetaxel in addition to causing mitotic arrest and cell death induces other phenotypic changes. At 72 h post-treatment, there was an emergence of G1/G2-interphase cells, which in addition to being much bigger in size were also multinucleated compared to parent PC-3 cells (Figure 7.4.1B). Also, we observed that there was a significant drop in the percentage of MPM-2 positive cells from ~11% at 48 h to 1% at 72 h and a simultaneous increase in MPM-2 negative population from ~26% at 24 h to 42% at 72 h (Figure.7.4.1A, D). Most likely, these large multinucleated cells resulted from a mitotic exit, that is, cells slipping out of mitosis without cell division. Since cells have failed to successfully progress through mitosis to execute cytokinesis, they have twice or more the amount of DNA as compared to parent PC-3 cell in the G1 phase of the cell cycle (Figure.7.41C). We termed these pseudo-G1 like cells as giant multinucleated polyploid (MP) cells. Almost 95% of the surviving cells after 3 days of docetaxel treatment were giant MP cells. Taken together, these observations clearly suggest that, upon docetaxel treatment a small percentage of cells slip out of mitosis resulting in the formation of giant MP cells. The induction of giant MP cells was not limited to PC-3 cells but was also formed in two other cell lines: DU-145 (androgen dependent prostate

cancer cell line) and MDA-MB-231 (triple negative breast cancer cell line) (Supplementary. Figure 7.7.1[4]).

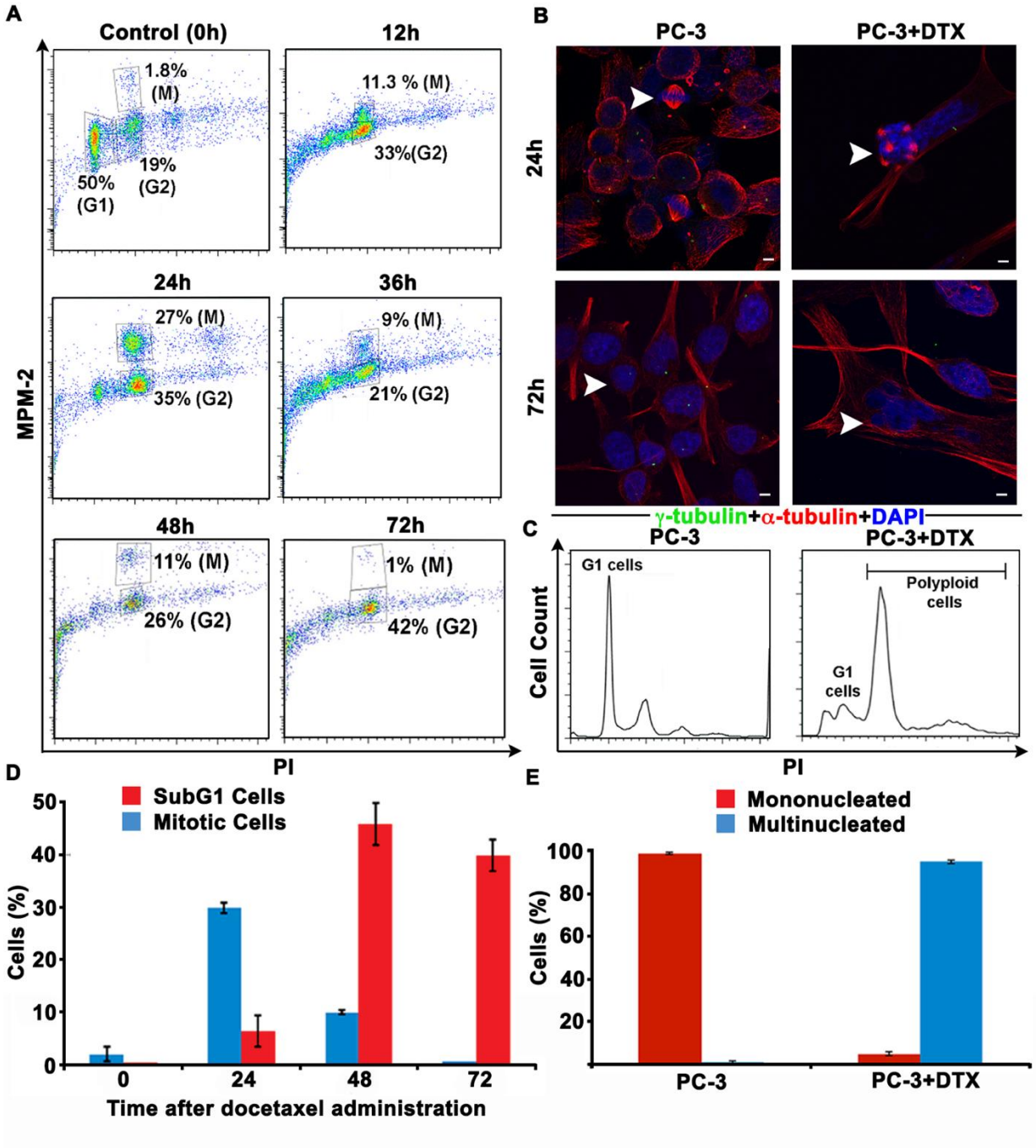

Figure 7.4.1Docetaxel induces formation of giant multinucleated polyploid cells.

[4] All supplemental data, tables, and figures appear in Appendix D for this chapter

A) Cell-cycle histograms of doubly-stained PC-3 cells treated with docetaxel at 5 nM concentration for different time points showing mitotic arrest and slippage at different time points. B) Representative immunofluorescent confocal micrographs of PC-3 cells treated with docetaxel for 24 h and 72 h indicating mitotic arrest and emergence of giant multinucleated polyploid cells respectively. Centrosomes and microtubules were immunolabeled for γ-tubulin (green) and α-tubulin (red), respectively, and DNA was counterstained with DAPI (blue). Scale bar (white) 5 μm. C) Cell-cycle histogram of docetaxel treated PC-3 cells showing emergence of polyploid population. D) Bar-graphs showing the percentage of sub-G1 and mitotic population resulting from 5nM docetaxel treatment. E) Bar-graphs showing the percentage of giant multinucleated polyploid cells 72 h after docetaxel treatment.

7.4.2 Giant MP cells undergo asymmetric cell division via neosis

Having established that docetaxel treatment induces the formation of giant MP cells we next followed the fate of these giant MP cells for the consequent 35 days after docetaxel removal. To accomplish this, we collected cells every 3rd day post drug removal and, employing confocal microscopy we visualized the morphology of PC-3 cells. Microtubules were immunolabeled for α-tubulin (red)and DNA was counterstained with DAPI (blue). For the first 15 days post drug removal we did not observe any remarkable changes in cell morphology. After 15 days in culture we started observing the formation of small mononucleated cells in the vicinity of giant MP cells (Fig 2A). The number of mononucleated cells further increased by day 25 (Figure.7.42A and E). At later time points (day 35) following the removal of docetaxel, sparse colonies of small, tightly-packed, mononucleated cells were observed in the culture dish (Figure.7.42A and E).

We next examined the origin of these mononucleated cells at day 15 after removal of docetaxel. To this end, starting at 12 days after docetaxel removal, we isolated and plated 3 giant MP cells per well by serial dilution and followed them for 7 days using time lapse imaging. We observed asymmetric cell division pattern in giant MP cells through a process known as neosis [15-17]. Small mononucleated daughter cells were seen budding from the giant MP cells from the branches of the giant MP cells (Figure.7.4.2B). To confirm the presence of DNA in the budding cells, we stained the giant MP cell along with the budding cells with Hoechst 33342

and used it in combination with differential interference contrast (DIC) microscopy. Using this method, we were able to detect the presence of DNA in the budding daughter cells (Supplementary Figure. 7.7.2). We named these budding cells as cells derived from multinucleated polyploid cells (CDPC). Furthermore, by using confocal microscopy, we demonstrated that the DNA was transported within the branches of the giant MP cells (Figure.7.4.2C). These results demonstrate that giant MP cells produce daughter cells through a process of budding also known as neosis where the branches of the giant MP cells can serve as vessels for DNA transport.

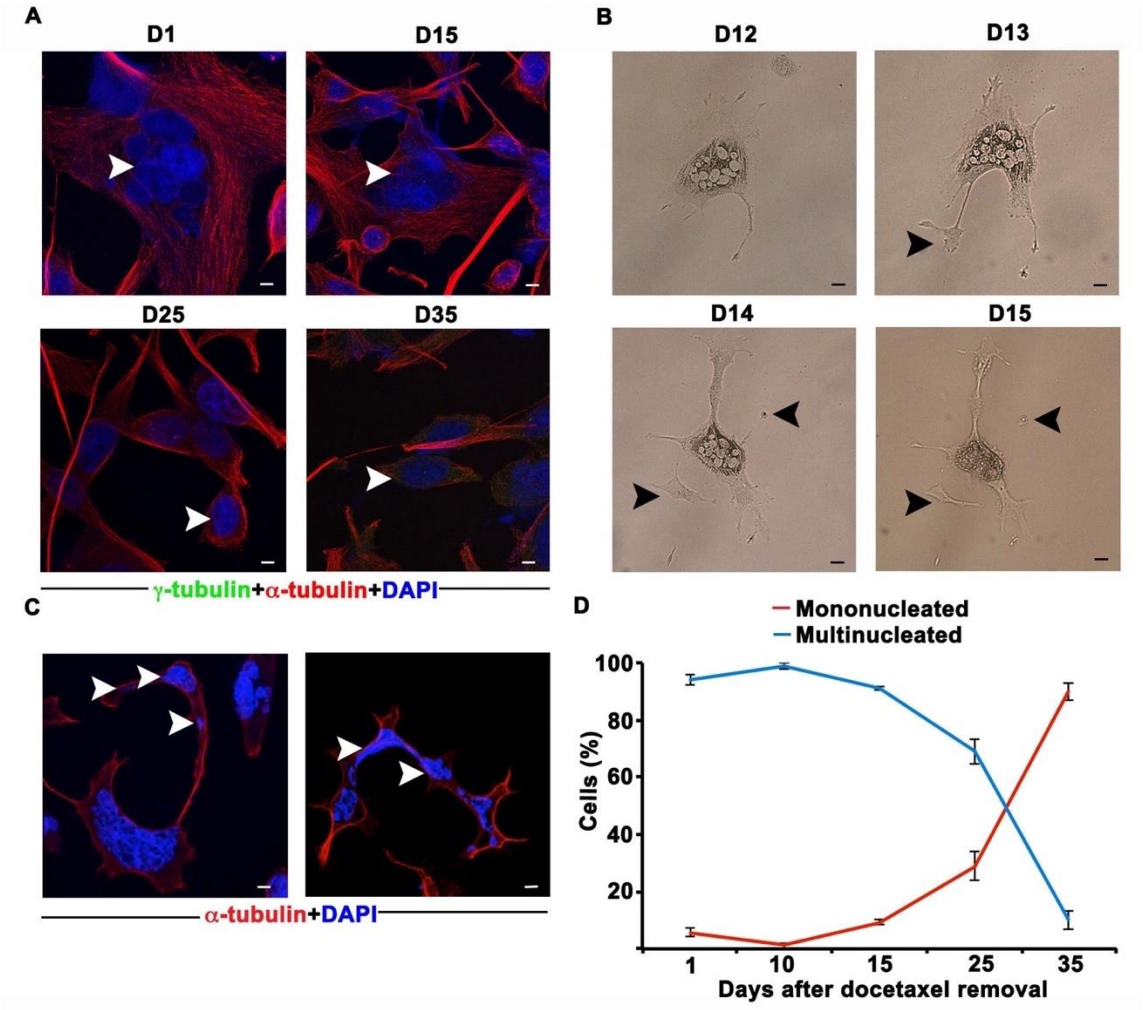

Figure 7.4.2 Giant MP cells undergo asymmetric cell division via neosis.
A) Confocal micrographs of docetaxel treated PC-3 cells. Cells are stained with α-tubulin (red) and DNA (blue) and showed emergence of small mononucleated cells on different days (D) after drug removal. Scale bar (white) 5 µm. B) Time lapse images of giant MP cells generating small-

sized daughter cells via budding (black arrows) over a 7-day period. Scale bar (black) 5 µm. C) Confocal immunographs of cells stained with α-tubulin (red) and DNA (blue) showing transport of DNA from the branches of the giant MP cells (white arrows). D) Line graph representing the total number of small sized nucleated cells and giant MP cells at different days after drug removal.

7.4.3 Giant MP cells and CDPC are chemoresistant

After establishing that giant MP cells can survive and can form small mononucleated cells via neosis, we next determined their response to docetaxel treatment. For this purpose, PC-3, CDPC and giant MP cells were treated with 5nM of docetaxel for 48h. Cell death was estimated by measuring the expression of cleaved caspase-3 and cleaved PARP. Interestingly, we observed increased levels of cleaved caspase-3 staining in PC-3 cells after 48 h of docetaxel treatment (Figure.7.43A). This was further substantiated by increased protein expression of cleaved PARP and cleaved caspase-3 by immunoblotting (Figure.7.43B and Supplementary Table 7.7.1). On the other hand, CDPC and giant MP cells showed lower expression of both cleaved caspase-3 and cleaved PARP after docetaxel exposure, suggesting that these cells were resistant to docetaxel treatment.

Next, we evaluated the sensitivity of PC-3, CDPC and giant MP cells to various concentrations of docetaxel (5nM, 10nM and 20nM) using MTT assay. PC-3 cells exhibited a dose dependent increase in cell death 48 h after docetaxel treatment when compared with, both CDPC and giant MP cells (Figure 7.4.3C). In addition, we assessed the expression of anti-apoptotic and survival proteins in both CDPC and giant MP cells and compared them to the parental cells. The expression of anti-apoptotic proteins like Bcl-2, pBcl-2 and Bcl-XL were much higher in giant MP cells (day 1 to day 25 in figure 3D and Supplementary Table 2) and CDPC (day 35) as compared to parental PC-3 cells (Day0). Similarly, survival protein like survivin and beclin-2 were also higher in giant MP cells and CDPC compared to parent PC-3 cells. Taken together, these results suggested that both giant MP cells and CDPC exhibited a completely

different response to docetaxel treatment as compared to the parental cells owing to the increased expression of anti-apoptotic and survival proteins. We also observed that the giant MP and CDPC cells were positive for CD44 which a cancer stem cell marker is (Supplementary Fig 7.7.3E and Supplementary Table 7.7.4).

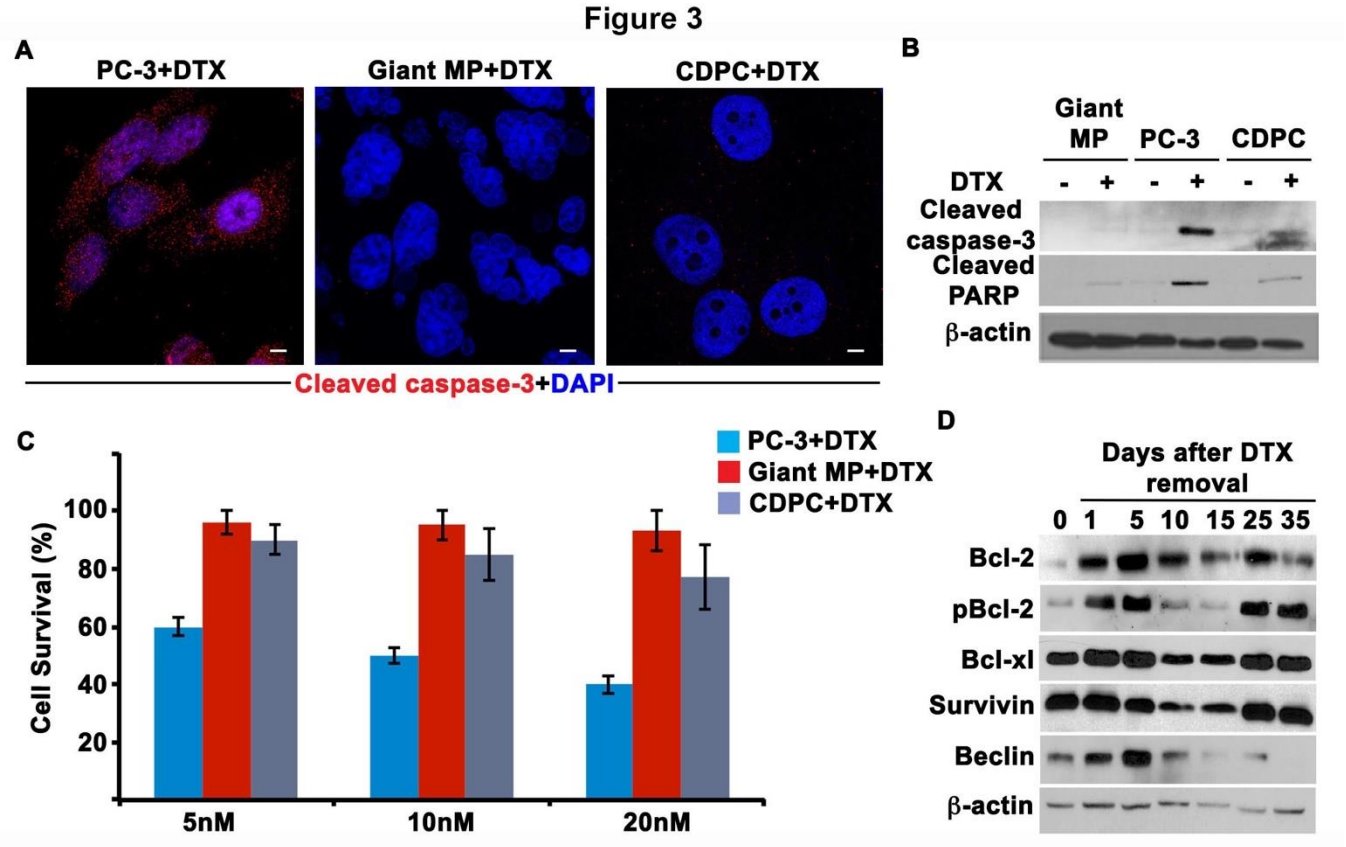

Figure 7.4.3Giant MP cells and CDPC are chemoresistant.
A) Confocal images of cleaved caspase-3 staining (red) on docetaxel treated PC-3 cells. **B)** Representative Immunoblot images of cleaved caspase-3 and cleaved-PARP for docetaxel treated cells. Actin was used as the loading control. **C)** Graphical representation of cell survival using MTT assay. Cells were treated with 3 different concentrations of docetaxel and MTT assay was done 48h after docetaxel treatment. **D)** Western blots of anti-apoptotic and survival proteins in at different days after docetaxel removal. D0 are control PC-3 cells while cells on D35 are CDPCs.

7.4.4 Giant MP cells and CDPC show differential ability to migrate and proliferate as compared to parent PC-3 cells

We next examined the ability of the giant MP cells and CDPC to migrate and proliferate and compared it to the parent PC-3 cells. Transwell migration assay was used to compare the migratory ability of CDPC and giant MP cells with that of the parent PC-3 cells. At 48 hours, the mean number of parent PC-3 cells that had migrated across the membrane was 9-fold higher than the giant MP cells and 2-fold higher than the CDPC cells (Figure 7.4.4A and B). The MTT assay showed the giant MP cells showed no signs of proliferation over a six-day period. On the other hand, the proliferation rate of CDPC was similar to that of the parent PC-3 cells over the six-day period (Figure.7.4.4C). Surprisingly, the mesenchymal marker vimentin was much higher in CDPC and giant MP as compared to the parent PC-3 cells (Figure.7.4.4D and Supplementary Table 7.7.3). We speculate that the giant MP cells use this mesenchymal phenotype to transport DNA through the branches in order to produce small mononucleated cells via neosis (Figure.7.4.2D). These results suggest that giant MP cells have slow proliferation and low rates of invasion and tumor formation compared to the parent PC-3 cells, suggesting that giant MP cells are less aggressive or malignant than that of parental cells.

We next wanted to see if the CDPCs have a different genetic profile as compared to the parent PC-3 cells. We measured the degree of aneuploidy in the CDPC and parent PC-3 cells using fluorescent in situ hybridization (FISH) (Figure.7.4.4E). The average number chromosomes in the parent PC-3 cells were 83 as compared to 82 in the CDPC (Figure.7.4.4F). We next calculated the percent aneuploidy in parent PC-3 and CDPCs by counting the number of cells that had either < 80 or > 86 chromosomes. Using this method, the percent aneuploidy in parent PC-3 cells was 12% compared to 18% in CDPC. Taken together the degree of aneuploidy in CDPC

was comparable to that of the parent PC-3 cells (eg: chromosomal translocation). Since there was a high number of translocations/duplications/etc. in the parent PC-3 cells, making many of the chromosomes unidentifiable, we were not able to measure the degree of structural chromosomal abnormalities in the PC-3 and CDPC cells. These results suggested that the degree of aneuploidy in the parent PC-3 and CDPC was not very different.

Figure 4

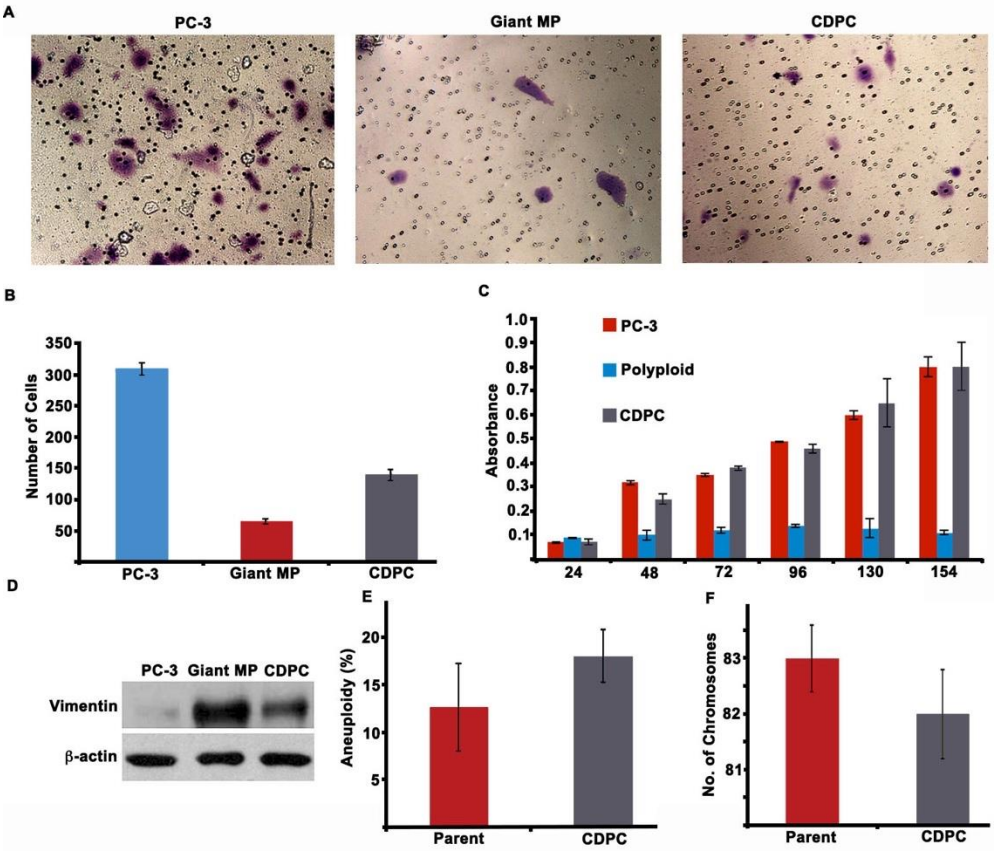

Figure 7.4 .4 Phenotypic changes in CDPC and giant MP cells.
A) Bright-field microscopic images of cells stained with crystal violet showing invasion capacity of PC-3, CDPC and giant MP cells. B) Bar graph representing the number of migrated cells in a Boyden chamber. C) Cell proliferation assay over a 7-day period using MTT assay. D) Representative immunoblots of Vimentin in PC-3, giant MP and CDPC's. E, F) Graphical representation of the percent aneuploidy and number chromosomes respectively using FISH analysis. A total of 50 cells were counted.

7.4.5 Giant MP cells have tumorigenic potential

To test the tumorigenicity of giant MP cells, we collected the giant MP cells 3 days after docetaxel treatment. A total of 50,000 PC-3 or giant MP cells were injected into the right flank of the nude mice (n=6). As shown in Figure.7.4.5A, 6/6 mice (100%) injected with PC-3 cells formed tumors while only 2/6 mice (33%) injected with giant MP cells formed tumors in the nude mice. We also measured the kinetics of the tumor growth over a period of 60 days. Measurable tumors started to form as early as 15 days post inoculation in mice injected with parent PC-3 cells. On the other hand, measurable tumors were started to form only after 28 days' post inoculation in mice injected with giant MP cells. The rate of tumor growth was also much higher in mice injected with PC-3 cells compared to mice that were injected with giant MP cells (Figure.7.4.5C). At the end of 60 days, the tumor weight of mice injected with PC-3 cells was 3 times higher than the tumors formed by giant MP cells (Figure.7.4.5B, C)). These results suggested that even though the giant MP cells have tumorigenic capacity the rate of tumor formation is much slower than the parent PC-3 cells.

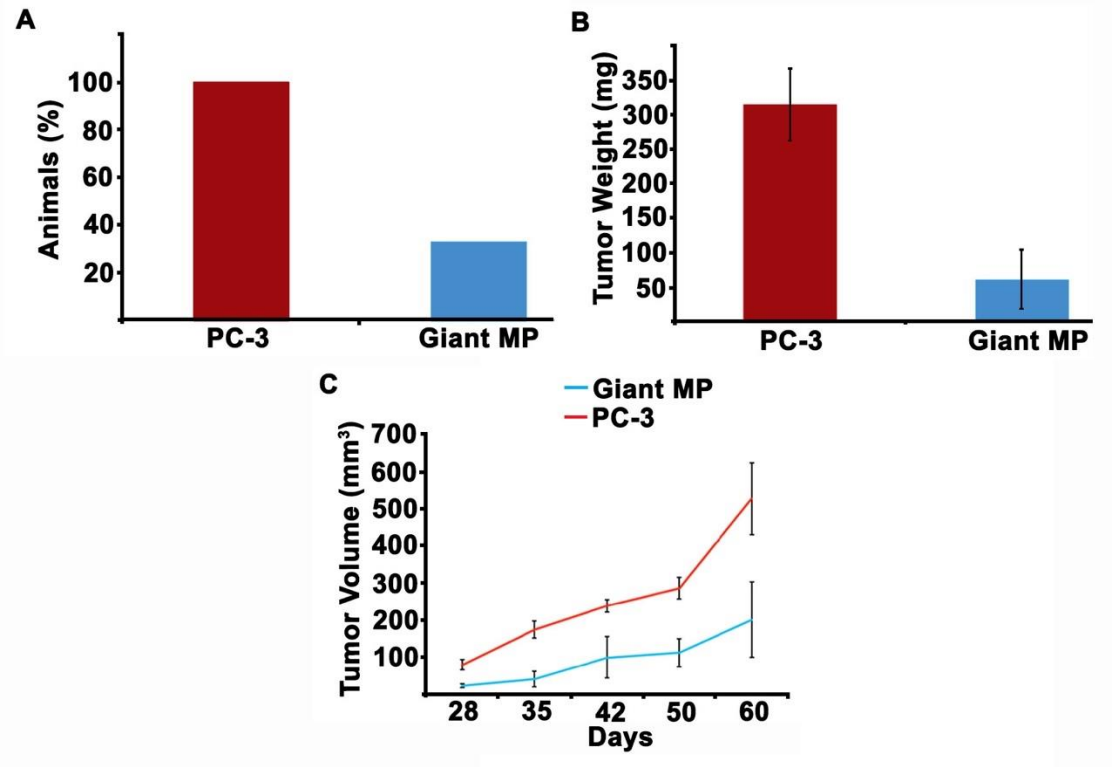

Figure 7.4.5Giant MP cells have tumorigenic potential.
A) Bar graph representing the number of animals forming tumors after injecting either PC-3 or giant MP cells. B) Bar graph representing the tumor weight. C) Tumor growth monitored (by Vernier calipers) and presented as tumor volume in cubic millimeter over a period of 60 days.

7.5 Discussion

Docetaxel, a member of the taxane class of antimicrotubule agents is the only FDA-approved chemotherapeutic agent for CRPC. In many clinical situations, tumors will initially respond successfully to docetaxel but subsequently relapse and become progressively more malignant. This is mainly because of the intermittent dosing schedule followed for docetaxel administration. This intermittent dosing regimen allows tumor regrowth between treatment schedules resulting in only a partial regression of the prostate tumor mass. Our current study very elegantly demonstrates that the formation of giant MP cells due to docetaxel treatment is the culprit cell population responsible for cancer relapse. We describe here that the formation of giant MP cells

is mainly a result of mitotic slippage. It is well known that the mitotically slipped cells can undergo a second round of DNA replication without undergoing mitosis leading to formation of giant MP cells [18] . This phenomenon is known as endoduplication [19, 20]. Several reports suggest that p53 is an important component of ploidy checkpoint and its overexpression can lead to endoduplication of cell [21]. Also, generation of resistant giant multinucleated cells has been reported in p53 mutated tumor cells [22]. Since PC-3 cells lack p53 [23], endoduplication and subsequent formation of giant MP cells may be attributed to the loss of p53 gene.

These giant MP cells can not only survive for a long period of time but could give rise to small mononucleated, actively proliferating cells that can later cause the tumor to relapse. Here, the giant MP cells undergo a novel type of cell division that involves nuclear budding followed by intracellular cytokinesis to produce mononucleated daughter cells that "bud off" from the giant MP cell, a phenomenon known as neosis or reductive cell division. Previous studies have also shown that giant MP cells can form small daughter cells through this process of neosis [10, 12, 16, 17, 24, 25]. These mononucleated daughter cells have previously been reported to be highly error -prone which increases the rates of genomic instability and contributes to tumor regrowth [26].

We further show that giant MP cells and cells generated from them (CDPC) are chemoresistant. The fact the giant MP cells are chemoresistant was not surprising. It is well known that tumor cells in patients' bodies are present in different phases of the cell cycle (G1, S, G2 and M) and conventional chemotherapy kills only the most vulnerable phase of the cell cycle but spares the others [27]. In other words, the cell death upon administration of the chemotherapeutic agent depends upon the "cytotoxicity window" of the drug [27]. In

particular, extensive literature reports that the high "cytotoxicity window" of docetaxel corresponds to late S and G2 phase of the cell cycle [28, 29]. Studies have convincingly demonstrated that cells are variably sensitive to docetaxel when treatment is applied to cells synchronized in different phases of the cell cycle It is now well established that docetaxel is almost totally lethal against S-phase cells but is only partially toxic against cells in G1 phase of the cell cycle. Since these giant MP cells are pseudo-G1 like cells, these cells are very unlikely to die upon docetaxel treatment. We also speculate that the chemoresistance of CDPC cells could be attributed in part to high expression of antiapoptotic (cIAP-1, cIAP-2, XIAP and survivin, clusterin) [30] proteins and survival proteins (Bcl-2, Bcl-XL) [31, 32]. It is also likely that CDPCs have altered expression of drug transporter proteins thus making them less susceptible to docetaxel toxicity.[33-36]

These cells also express cancer stem cell (CSC) marker CD44. This CSC marker plays a critical role in regulating the properties of CSCs like, tumor initiation, self-renewal and chemoradioresistance [37]. Our findings are in line with a previous study which reported that docetaxel resistant prostate cancer cells exhibit increased stemness compared to their parental counterpart [38]. Thus, targeting CSCs seems to be potential mechanism to combat the resistance and relapse developed after docetaxel treatment. In line with this a recent study showed that Napabucasin (BBI608) a cancer cell stemness inhibitor suppresses the prostate cancer growth and makes the prostate cancer cells sensitive to docetaxel by killing the prostate cancer stem cells that were resistant to docetaxel [39]. Thus, we speculate that the docetaxel treatment leads to clonal selection of highly aggressive phenotype with stem cell like phenotype and this in part is responsible for the chemotherapy failure.

Finally, we show evidence that giant MP cells have tumorigenic potential in nude mice. The giant MP cells take a significantly longer time to form the tumor as compared to the parent PC-3 cells. This is because the giant MP cells first need to produce the mononucleated daughter cells which then subsequently proliferate to form the tumor. This result is in concordance to the fact that tumor relapse always occurs after a significant delay usually ranging from a couple of months to sometimes years.

Taken together, our studies show that generation of giant MP cells that were once presumed to be either destined for terminal growth arrest or cell death may actually represent a "transition state" for generation of viable clones. These cells may play an integral part in tumor relapse and generation of chemoresistance. Strategies preventing the formation of giant MP cells and understanding the molecular mechanism of neosis will help us identify key targets to prevent tumor relapse.

7.6 References

1. Attard, G., J. Richards, and J.S. de Bono, *New strategies in metastatic prostate cancer: targeting the androgen receptor signaling pathway.* Clin Cancer Res, 2011. **17**(7): p. 1649-57.
2. Tong, D., et al., *The HIF/PHF8/AR axis promotes prostate cancer progression.* Oncogenesis, 2016. **5**(12): p. e283.
3. Tannock, I.F., et al., *Docetaxel plus prednisone or mitoxantrone plus prednisone for advanced prostate cancer.* N Engl J Med, 2004. **351**(15): p. 1502-12.
4. Hussain, M., et al., *Docetaxel (Taxotere) and estramustine versus mitoxantrone and prednisone for hormone-refractory prostate cancer: scientific basis and design of Southwest Oncology Group Study 9916.* Semin Oncol, 1999. **26**(5 Suppl 17): p. 55-60.
5. Lopez-Sanchez, L.M., et al., *CoCl2, a mimic of hypoxia, induces formation of polyploid giant cells with stem characteristics in colon cancer.* PLoS One, 2014. **9**(6): p. e99143.
6. Zhang, S., et al., *Generation of cancer stem-like cells through the formation of polyploid giant cancer cells.* Oncogene, 2014. **33**(1): p. 116-28.
7. Nakayama, Y., et al., *Bleomycin-induced over-replication involves sustained inhibition of mitotic entry through the ATM/ATR pathway.* Exp Cell Res, 2009. **315**(15): p. 2515-28.
8. Erenpreisa, J., et al., *Endopolyploidy in irradiated p53-deficient tumour cell lines: persistence of cell division activity in giant cells expressing Aurora-B kinase.* Cell Biol Int, 2008. **32**(9): p. 1044-56.
9. Sagona, A.P. and H. Stenmark, *Cytokinesis and cancer.* FEBS Lett, 2010. **584**(12): p. 2652-61.

10. Coward, J. and A. Harding, *Size Does Matter: Why Polyploid Tumor Cells are Critical Drug Targets in the War on Cancer.* Front Oncol, 2014. **4**: p. 123.
11. Erenpreisa, J. and M.S. Cragg, *Cancer: a matter of life cycle?* Cell Biol Int, 2007. **31**(12): p. 1507-10.
12. Puig, P.E., et al., *Tumor cells can escape DNA-damaging cisplatin through DNA endoreduplication and reversible polyploidy.* Cell Biol Int, 2008. **32**(9): p. 1031-43.
13. Makarovskiy, A.N., et al., *Survival of docetaxel-resistant prostate cancer cells in vitro depends on phenotype alterations and continuity of drug exposure.* Cell Mol Life Sci, 2002. **59**(7): p. 1198-211.
14. Martin, S.K., et al., *Multinucleation and Mesenchymal-to-Epithelial Transition Alleviate Resistance to Combined Cabazitaxel and Antiandrogen Therapy in Advanced Prostate Cancer.* Cancer Res, 2016. **76**(4): p. 912-26.
15. Mittal, K., et al., *Amplified centrosomes may underlie aggressive disease course in pancreatic ductal adenocarcinoma.* Cell Cycle, 2015. **14**(17): p. 2798-809.
16. Mittal, K., et al., *A centrosome clustering protein, KIFC1, predicts aggressive disease course in serous ovarian adenocarcinomas.* J Ovarian Res, 2016. **9**: p. 17.
17. Navolanic, P.M., S.M. Akula, and J.A. McCubrey, *Neosis and its potential role in cancer development and chemoresistance.* Cancer Biol Ther, 2004. **3**(2): p. 219-20.
18. Sundaram, M., et al., *Neosis: a novel type of cell division in cancer.* Cancer Biol Ther, 2004. **3**(2): p. 207-18.
19. Rajaraman, R., et al., *Neosis--a paradigm of self-renewal in cancer.* Cell Biol Int, 2005. **29**(12): p. 1084-97.
20. Galan-Malo, P., et al., *Cell fate after mitotic arrest in different tumor cells is determined by the balance between slippage and apoptotic threshold.* Toxicol Appl Pharmacol, 2012. **258**(3): p. 384-93.
21. Edgar, B.A. and T.L. Orr-Weaver, *Endoreplication cell cycles: more for less.* Cell, 2001. **105**(3): p. 297-306.
22. Lee, H.O., J.M. Davidson, and R.J. Duronio, *Endoreplication: polyploidy with purpose.* Genes Dev, 2009. **23**(21): p. 2461-77.
23. Aylon, Y. and M. Oren, *p53: guardian of ploidy.* Mol Oncol, 2011. **5**(4): p. 315-23.
24. Illidge, T.M., et al., *Polyploid giant cells provide a survival mechanism for p53 mutant cells after DNA damage.* Cell Biol Int, 2000. **24**(9): p. 621-33.
25. Rubin, S.J., et al., *Two prostate carcinoma cell lines demonstrate abnormalities in tumor suppressor genes.* J Surg Oncol, 1991. **46**(1): p. 31-6.
26. Zhang, Y.B., et al., *The effects of CoCl2 on HIF-1alpha protein under experimental conditions of autoprogressive hypoxia using mouse models.* Int J Mol Sci, 2014. **15**(6): p. 10999-1012.
27. Rajaraman, R., et al., *Stem cells, senescence, neosis and self-renewal in cancer.* Cancer Cell Int, 2006. **6**: p. 25.
28. Chen, S., et al., *Transient endoreplication down-regulates the kinesin-14 HSET and contributes to genomic instability.* Mol Biol Cell, 2016. **27**(19): p. 2911-23.
29. Abal, M., J.M. Andreu, and I. Barasoain, *Taxanes: microtubule and centrosome targets, and cell cycle dependent mechanisms of action.* Curr Cancer Drug Targets, 2003. **3**(3): p. 193-203.
30. Hennequin, C., N. Giocanti, and V. Favaudon, *S-phase specificity of cell killing by docetaxel (Taxotere) in synchronised HeLa cells.* Br J Cancer, 1995. **71**(6): p. 1194-8.

31. Paoletti, A., et al., *Pulse treatment of interphasic HeLa cells with nanomolar doses of docetaxel affects centrosome organization and leads to catastrophic exit of mitosis.* J Cell Sci, 1997. **110 (Pt 19)**: p. 2403-15.
32. McEleny, K., et al., *An antisense oligonucleotide to cIAP-1 sensitizes prostate cancer cells to fas and TNFalpha mediated apoptosis.* Prostate, 2004. **59**(4): p. 419-25.
33. Feldman, B.J. and D. Feldman, *The development of androgen-independent prostate cancer.* Nat Rev Cancer, 2001. **1**(1): p. 34-45.
34. O'Neill, A.J., et al., *Characterisation and manipulation of docetaxel resistant prostate cancer cell lines.* Mol Cancer, 2011. **10**: p. 126.
35. Aberuyi, N., S. Rahgozar, and A. Moafi, *The role of ATP-binding cassette transporter A2 in childhood acute lymphoblastic leukemia multidrug resistance.* Iran J Ped Hematol Oncol, 2014. **4**(3): p. 118-26.
36. Rahgozar, S., et al., *mRNA expression profile of multidrug-resistant genes in acute lymphoblastic leukemia of children, a prognostic value for ABCA3 and ABCA2.* Cancer Biol Ther, 2014. **15**(1): p. 35-41.
37. Ma, Y., et al., *Identification of mutations, gene expression changes and fusion transcripts by whole transcriptome RNAseq in docetaxel resistant prostate cancer cells.* Springerplus, 2016. **5**(1): p. 1861.
38. de Morree, E.S., et al., *Loss of SLCO1B3 drives taxane resistance in prostate cancer.* Br J Cancer, 2016. **115**(6): p. 674-81.
39. Yan, Y., X. Zuo, and D. Wei, *Concise Review: Emerging Role of CD44 in Cancer Stem Cells: A Promising Biomarker and Therapeutic Target.* Stem Cells Transl Med, 2015. **4**(9): p. 1033-43.
40. Puhr, M., et al., *Epithelial-to-mesenchymal transition leads to docetaxel resistance in prostate cancer and is mediated by reduced expression of miR-200c and miR-205.* Am J Pathol, 2012. **181**(6): p. 2188-201.
41. Zhang, Y., et al., *Suppression of prostate cancer progression by cancer cell stemness inhibitor napabucasin.* Cancer Med, 2016. **5**(6): p. 1251-8.

8 CONCLUSIONS

In the collection of the studies described in this dissertation we have presented centrosome amplification and clustering as important risk predictors of tumor aggressiveness and progression that can serve as a surrogate of intra tumor heterogeneity (ITH). Since there are no cost-effective readily quantifiable markers available for ITH these studies presented here highlight the role of CA as a more comprehensive biomarker which can work as a clinically adaptable readout of ITH.

High CA is associated with increased tumor grade and has been shown to impart aggressive phenotypes, such as invasive behavior and enhanced cell migration in pancreatic ductal adenocarcinoma (PDAC) and the genes that drive CA are associated with worse overall survival in this cancer type. Thus it is reasonable to suspect that CA is associated with worse clinicopathology and survival rates in PDAC and can serve as an independent prognostic marker for which there are no prognostic and predictive biomarkers available. In addition we also observed that the African American (AA) PDACs exhibited higher CA when compared to the European Americans (EA), AA PDACs have ~30% higher incidence and more aggressive disease course than EA PDAC patients[1], perhaps in part because their tumors display elevated mutations in genes whose dysregulation is known to drive CA that are common in PDAC (e.g., *TP53* [2, 3], *SMAD4* [4], *CDKN2A* [5], *CHEK2* [6],). The relationship between ethnicity and mutations in these genes needs to be further investigated.

Moreover, in DCIS where high levels of ITH is present and in order to predict the recurrence, there is a pressing clinical need for prognostic indices that can take into account the heterogeneous nature of DCIS lesions. Current recurrence predictors based on commonly used histopathological parameters such as histologic grade, tumor margins, and age lack consistency, reproducibility fails to integrate the molecular predictors, underestimating the heterogeneity of

DCIS lesions[7]. Deregulation of numerous pathways have been shown to result in CA; this phenotypes thus integratively captures information about deregulation of multiple pathways and the ITH-generating potential inherent in a tumor thus, the extent of CA can be used a predictor in recurrence in DCIS. The major challenge of using CA as a biomarker is that there are no clinically-facile methods to quantify CA in tumor cells. In order to quantify CA and investigate its utility as a predictive biomarker for recurrence in DCIS, we have pioneered a novel semi-automated platform that integrates immunofluorescent confocal microscopy with digital image analysis algorithms and yields a quantitative centrosomal amplification score (CAS) by evaluating the severity and extent of numerical and structural centrosomal aberrations in a clinical sample. We observed that the clinical samples with the higher risk of recurrence exhibited high CAS values thus indicating a great extent of CA and consequently higher degree of ITH compared to samples with a lower CAS value. Also, CAS was able to stratify the DCIS patients in high risk and low risk of recurrence in a multivariable model. Not only this when the performance of CAS was compared to another known predictor tool Van Nuys index, the performance of CAS was significantly better in prediction than the other model. Thus, CAS offers a comprehensive and a quantitatively precise measure of aberrant centrosomal status in DCIS lesions and with its ability to predict recurrence in these lesions provides us a new tool to help tailor the treatment according to individuals risk of recurrence in DCIS patients and avoid the over and under treatment of these patients. Furthermore, we observed that mixed DCIS cases which have the invasive component in them exhibited higher CAS compared to pure DCIS thus indicating that CA is associated with the greater risk of malignant transformation and thus its quantitation may help to determine which tumor will metastasize or become chemoresistant. Further studies are required to gain more insights into these intriguing issues.

Since centrosome amplification and clustering are cancer cell-specific phenomena, centrosome-clustering proteins may also serve as attractive prognostic markers and theranostic targets. The presence of higher KIFC1 in HGSOC and its association with poor overall survival and aggressive phenotype predict that the patients with high KIFC1 levels experience high mortality. In this study, we observed that primary tumors exhibited higher expression of KIFC1 gene expression and was associated with poor overall survival by contrast, while samples collected from the metastatic sites showed similar expression levels of KIFC1 as in primary sites, high KIFC1 expression in metastatic sites was not significantly correlated to poor survival. This differential effect of high KIFC1 expression strongly suggests that elevated KIFC1 in primary sites perhaps helps tumor cells present in the primary sites to acquire karyotypic diversity (through CIN), which is more likely to lead to successful metastasis and poor survival. It is possible that once metastasis commences, high KIFC1 levels in the metastatic clones provides little further survival advantage for the cancer cells; alternatively, once metastasis occurs, the survival difference between KIFC1-high and KIFC1-low patients is no longer so marked, an interesting question for future studies. Another intriguing avenue for future research would be to test whether HGSOC patients would benefit from the centrosome declustering drugs.

The non essential role of the KIFC1 in normal somatic cells and its crucial requirement for the viability of cancer cells, together makes KIFC1 an ideal cancer selective drug target. This proposition is bolstered by the observation that KIFC1 expression was significantly higher in the mutant p53 CRCs and that the depletion by pharmacological and genetic methods in CRC cells induced robust spindle multipolarity and subsequent apoptosis specifically in p53 null colorectal cancer cells without minimal toxicity to the WT cells, a mechanistic insight that can guide rational drug design as resistance to chemotherapy represents the major obstacle for the improvement of

survival of nearly 50% of CRC patients. Since, the current therapies to target mutant p53 are not effective as different mutations affect p53 function differently and different agents may be required to target different mutations.[8] The identification of molecules or pathways that can be targeted in p53 mutant CRC might help in improving the patient outcome. A major challenge faced in development of the targeted therapies for cancer is the fundamental disconnect between preclinical data and clinical results. Although the number of drugs entering in clinical trials is very high when compared to other diseases as in a span of 10 years ~30% (~3000)drugs which entered in clinical trials are for cancer but only 13.8% (~200) made it from the phase I to the testing approval [9]. This high rates of failure of therapies in the clinics is due to the lack of appropriate preclinical models which can recapitulate all the features of individuals tumor and show accurate efficacy rates. The preclinical models (both established tumor cell lines and tumor cell line xenografts) are far from ideal, they have been widely used given that the rapid doubling times in such models permit a fast-tracked drug-development timeline. Nonetheless, this perceived advantage rather puts us at a loss when the doubling time itself is in the spotlight and the drug's activity relies on the preponderance of the mitotic population, which hinges on doubling rate. The brisk doubling times of the preclinical models explain why drugs targeting mitosis proved active in these models but were ineffective against patient tumors.[10-12] Our study highlights the importance of low-passage patient-derived cell line systems as being most representative of the clinical scenario and thus constituting an invaluable experimental model that could better guide drug development and clinical trial design . We performed a rigorous, systematic analysis of the relationship between a universal prognostic factor (mitotic index) and a well-known cancer-cell-specific trait and a potential prognosticator (CA) in a spectrum of model systems ranging from cultured cells, preclinical tumor xenografts, patient-derived primary cultures and patient tumors. Our data

reconfirm that rapid cell division is not as predominant a trait of human tumors as it is of immortalized cell lines and tumor cell line xenografts which explains the lack of response of patient tumors to antimitotic drugs. Thus, to discern meaningful activity of drugs before they are tested in clinical trials, it is imperative that we consider the shortcomings of our existent cell line models and rather develop robust and relevant preclinical models that mimic cellular traits observed in patient tumors. As highlighted by our study the role of centrosome declustering drugs in tumor suppression and progression the study of these drugs in the early-passage patient-derived tumor cell lines, which exhibit similar CA to patient tumors remains a uncharted territory and thus can be an intriguing question for future studies.

A new era of precision medicine has dawned in oncology with the recent advances in cancer genomics—an era in which a patient's tumor can be characterized extensively for mutations and other molecular abnormalities, and treatment can be based mainly on the identified molecular changes (not just the type of cancer)[13, 14]. As defined by the National Cancer Institute precision or personalized medicine is "A form of medicine that uses information about a person's genes, proteins, and environment to prevent, diagnose, and treat disease"[15]. It further elaborates that "In cancer, personalized medicine uses specific information about a person's tumor to help diagnose, plan treatment, find out how well treatment is working, or make a prognosis." Thus, the biomarkers described herein constitute precision medicine because they can assist oncologists in prognostication and planning treatment. Collectively all the findings presented in this dissertation highlight the role of CA as a surrogate of ITH. Where it was presented that majority of the tumors exhibit CA and centrosome clustering and that clustering of supernumerary centrosomes during mitosis causes chromosome missegregation; thus, CA and centrosome clustering collectively fuel karyotypic diversification and, thus, ITH. Therefore, I envision that CA and centrosome clustering

these two factors may yield a reliable and comprehensive "ITH index" which can identify patients which are likely to exhibit heterogeneity and associated aggressive disease features with the increased need for aggressive treatment. Furthermore, the inclusion of the histopathological features and features associated with tumor microenvironment in the developed CAS score might help to develop models which can predict metastasis, which is the next question I intend to address in my post-doctoral research. I am also interested in investigating the process by which CA leads to the malignant transformation as the disease progresses which may help in limiting the extent of ITH at an early stage, thus rendering it relatively manageable.

References:

1. Yeo, T.P., *Demographics, epidemiology, and inheritance of pancreatic ductal adenocarcinoma.* Semin Oncol, 2015. **42**(1): p. 8-18.
2. Tarapore, P. and K. Fukasawa, *Loss of p53 and centrosome hyperamplification.* Oncogene, 2002. **21**(40): p. 6234-40.
3. Fukasawa, K., *P53, cyclin-dependent kinase and abnormal amplification of centrosomes.* Biochim Biophys Acta, 2008. **1786**(1): p. 15-23.
4. Bornstein, S., et al., *Smad4 loss in mice causes spontaneous head and neck cancer with increased genomic instability and inflammation.* J Clin Invest, 2009. **119**(11): p. 3408-19.
5. McDermott, K.M., et al., *p16(INK4a) Prevents Centrosome Dysfunction and Genomic Instability in Primary Cells.* PLoS Biology, 2006. **4**(3): p. e51.
6. Yang, H.W., et al., *Alternative Splicing of CHEK2 and Codeletion with NF2 Promote Chromosomal Instability in Meningioma.* Neoplasia (New York, N.Y.), 2012. **14**(1): p. 20-28.
7. Martinez-Perez, C., et al., *Current treatment trends and the need for better predictive tools in the management of ductal carcinoma in situ of the breast.* Cancer Treat Rev, 2017. **55**: p. 163-172.
8. Li, X.L., et al., *P53 mutations in colorectal cancer - molecular pathogenesis and pharmacological reactivation.* World J Gastroenterol, 2015. **21**(1): p. 84-93.
9. Mullard, A., *Parsing clinical success rates.* Nat Rev Drug Discov, 2016. **15**(7): p. 447.
10. Komlodi-Pasztor, E., et al., *Mitosis is not a key target of microtubule agents in patient tumors.* Nat Rev Clin Oncol, 2011. **8**(4): p. 244-50.
11. Komlodi-Pasztor, E., D.L. Sackett, and A.T. Fojo, *Inhibitors targeting mitosis: tales of how great drugs against a promising target were brought down by a flawed rationale.* Clin Cancer Res, 2012. **18**(1): p. 51-63.
12. Ogden, A., et al., *Interphase microtubules: chief casualties in the war on cancer?* Drug Discov Today, 2014. **19**(7): p. 824-9.
13. Verma, M., *Personalized medicine and cancer.* J Pers Med, 2012. **2**(1): p. 1-14.

14. Verma, M., *Molecular profiling and companion diagnostics: where is personalized medicine in cancer heading?* Per Med, 2014. **11**(8): p. 761-771.
15. Offit, K., *Personalized medicine: new genomics, old lessons.* Hum Genet, 2011. **130**(1): p. 3-14.

APPENDICES

Appendix A: Supplementary Data for chapter 2

Detailed Description of Centrosome Amplification Quantitation

To evaluate the number of centrosomes in tumor samples per cell, we immunostained centrosomes in tissues (normal and tumor for respective cancer types) with anti-γ-tubulin antibody and counterstained nuclei with DAPI. We imaged these tissue slides at low magnification (20x) employing LSM 700 confocal microscope to capture images of 10 fields of view that encompass several nuclei and centrosomes (Supplementary Figure. 2.7.1). For each field we selected a region with 30-35 clearly distinguishable nuclei and defined it as region of interest (ROI) by drawing a boundary around the outer edges of outermost nuclei in the ROI. Next, we quantified the number and volume of γ-tubulin foci in each ROI at higher magnification (63X objective). In our study, nuclei associated with more than two centrosomes were deemed to have "numerically" amplified centrosomes and nuclei associated with structurally abnormal centrosomes were accounted to have "structurally" amplified centrosomes. Centrosome amplification (CA) was calculated as a percentage by adding percent cells harboring more than two γ-tubulin foci and percent cells harboring γ-tubulin foci with volume greater than upper range of mean centrosomal volumes found in respective normal tissues (Supplementary Figure. 2.7.1). Since centrosomes pass through a duplication cycle that involves large volume changes, we needed to define a "normal range" for centrosomal volumes using both adjacent uninvolved tissue from cancer patients and normal tissue for disease-free individuals for each cancer type. To determine the normal range, we analyzed volumes of centrosomes (500 centrosomes for each sample) in adjacent uninvolved tissue from cancer patients (20 samples for each cancer type) and in normal tissues (20 normal tissue samples for breast, pancreas and bladder). Normal tissue samples were obtained from Biomax Inc. in the

form of commercial tissue microarrays. We evaluated the volume of centrosomes by using the three-dimensional measurement module in the Zeiss imaging software. Mean volumes of centrosomes in normal breast, pancreatic and bladder epithelial cells ranged between 0.22-0.76 μm^3, 0.20-0.56 μm^3, and 0.20-0.74 μm^3, respectively. The various centrosomal phenotypes observed in hypoxic conditions are represented in Supplementary Figure. 2.7.2 and 2.7.3. The presence of CA was confirmed via immunoblotting for CA-associated proteins as shown in Supplementary Figure.2.7. 4.

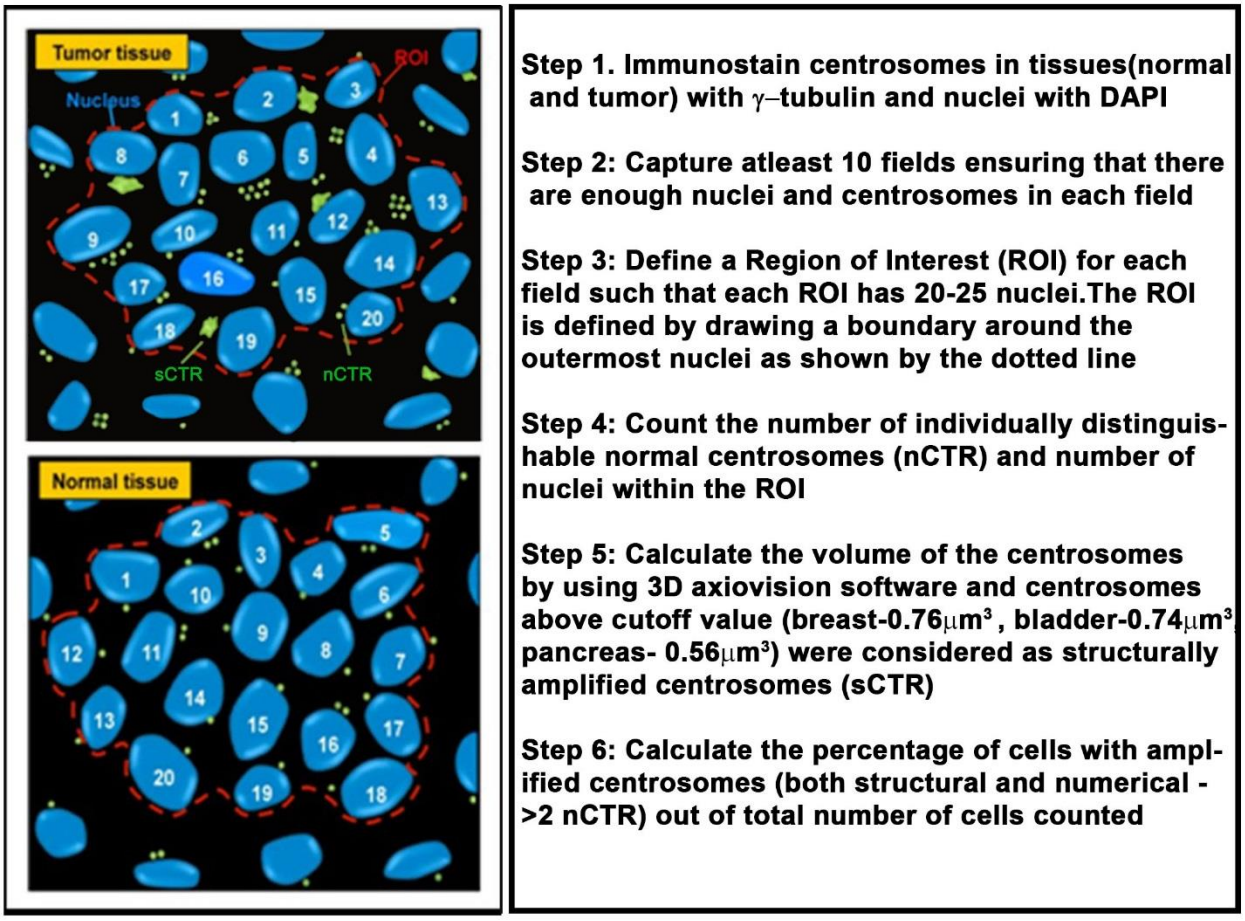

Figure 2.7.1 Schematic showing the steps followed for quantitation of CA in the cancer tissues, normal tissues and their corresponding cultured cell lines.

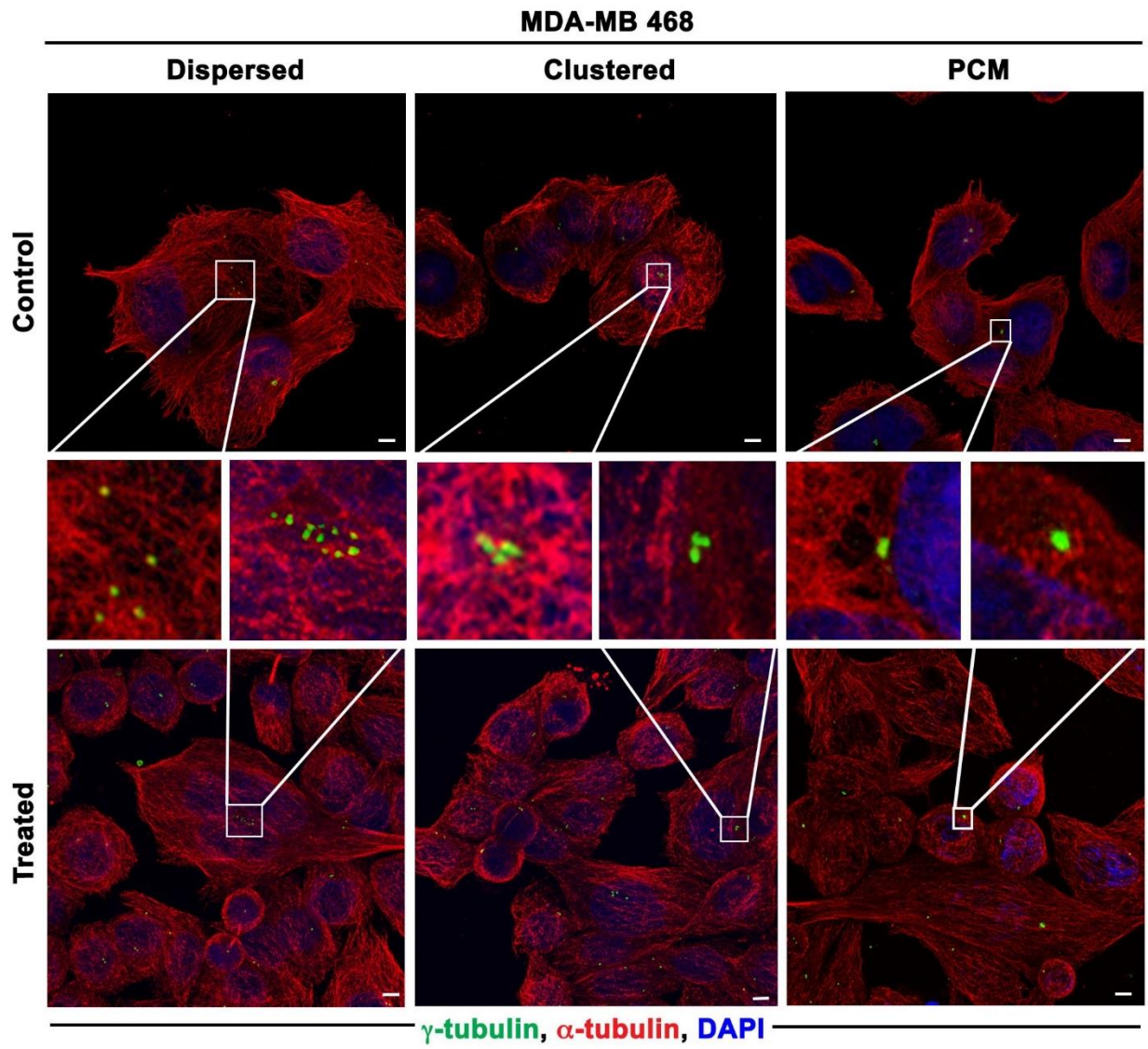

Figure 2.7.2 Different configurations of Centrosome amplification observed in MDA-MB 468 after hypoxia induction by treating them with $CoCl_2$.
Representative confocal micrographs of cells with centrosome amplification (dispersed represents cells with widely distributed centrosomes in the interphase, clustered represents cells with supernumerary centrosomes assembled together in the interphase but distinguishable, and PCM represents abnormally large centrosomes due to PCM accumulation).

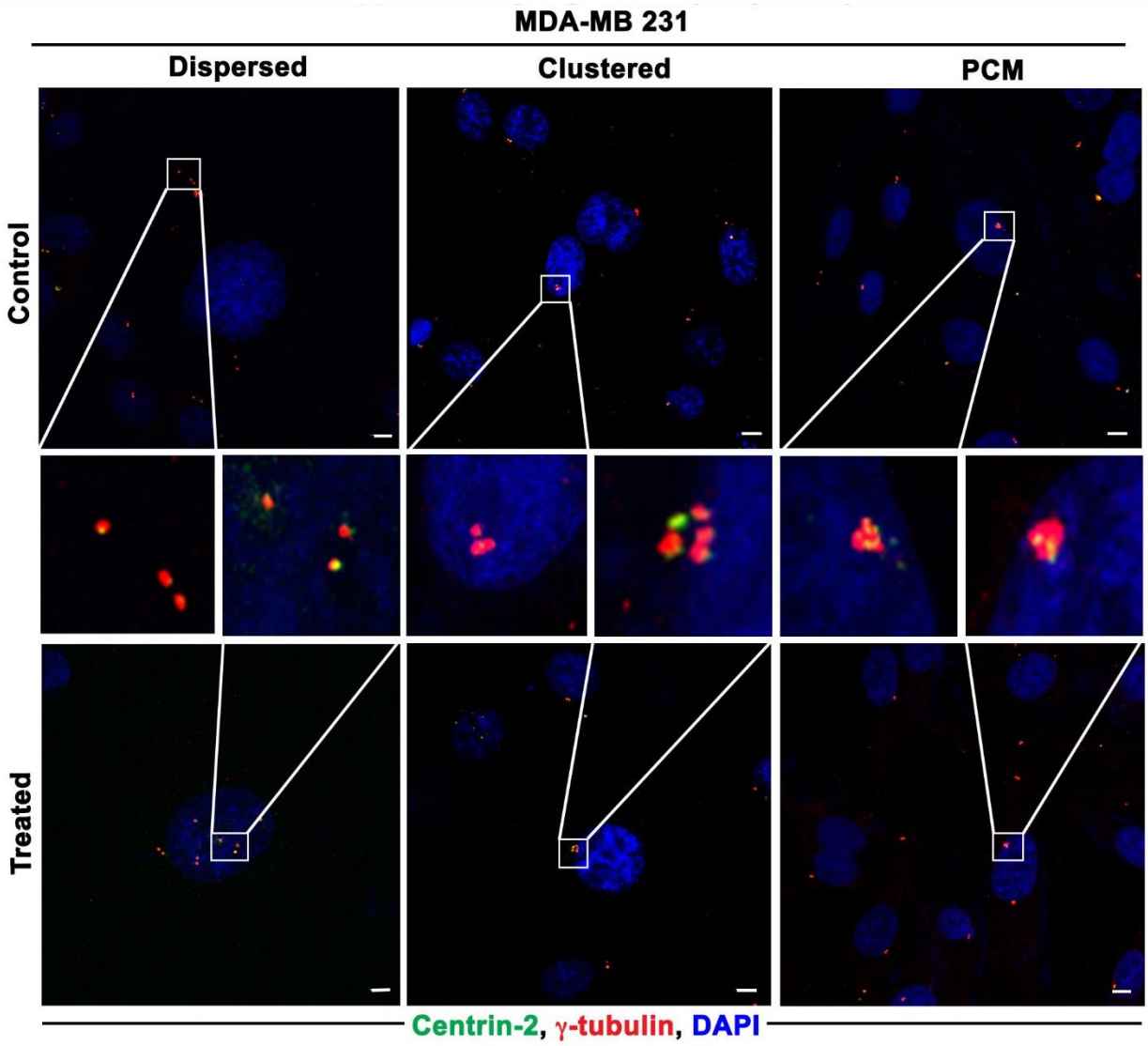

Figure 2.7.3 Different configurations of centrosome amplification observed in MDA-MB 231 cells immunolabeled for centrin-2 (green) and γ-tubulin (red) after treatment with $CoCl_2$.

Representative confocal micrographs of cells with centrosome amplification (dispersed represents cells with widely distributed centrosomes in the interphase, clustered represents cells with supernumerary centrosomes assembled together in the interphase but distinguishable, and PCM represents abnormally large centrosomes due to PCM accumulation). 200 cells were counted in each condition.

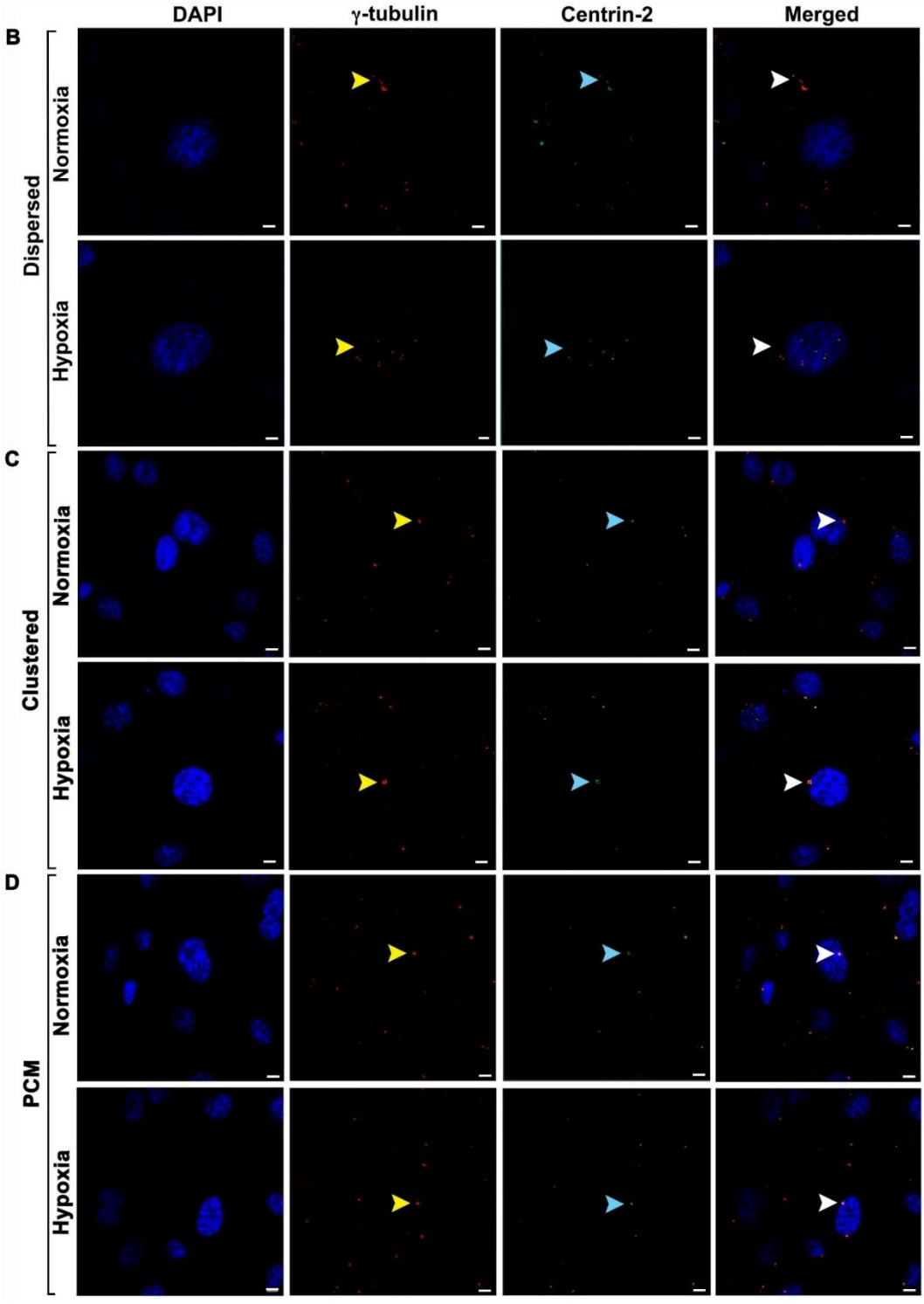

Figure 2.7.4 Representative immunographs of MDA-MB 231 immunolabeled for centrin-2 (green) and γ-tubulin (red) after treatment with $CoCl_2$ in split form.
B: Split confocal images of dispersed centrosome amplification. C: Split confocal images of the clustered CA. D: Split confocal images of structural amplification with PCM accumulation.

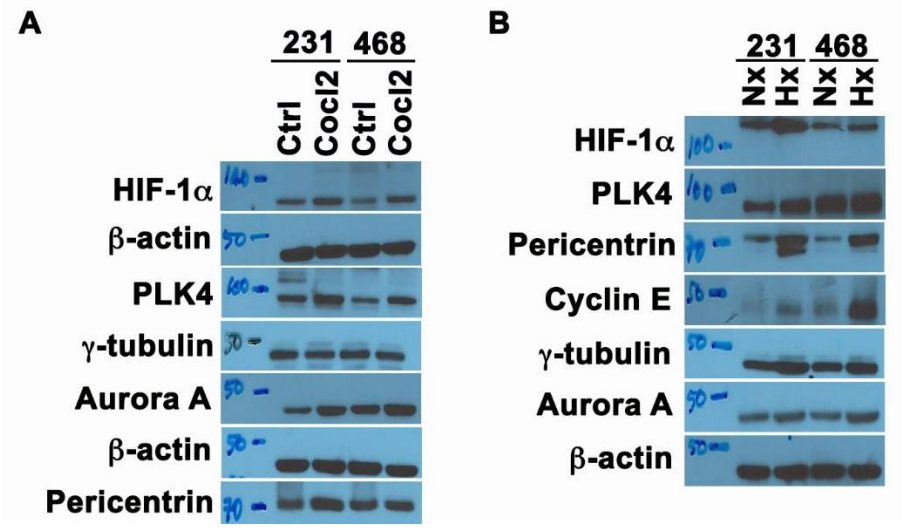

Figure 2.7.5 Immunoblots showing the levels of hypoxia and centrosomal markers in cells treated with $CoCl_2$ and cultured under hypoxia.
A : Immunoblots showing the levels of hypoxia and centrosomal markers in MDA-MB-231 and MDA-MB-468 cells treated with 100µM of $CoCl_2$ for 24 h. B. Immunoblots showing the levels of hypoxia and centrosomal markers in MDA-MB-231 and MDA-MB-468 cells exposed to hypoxia for 48 h.

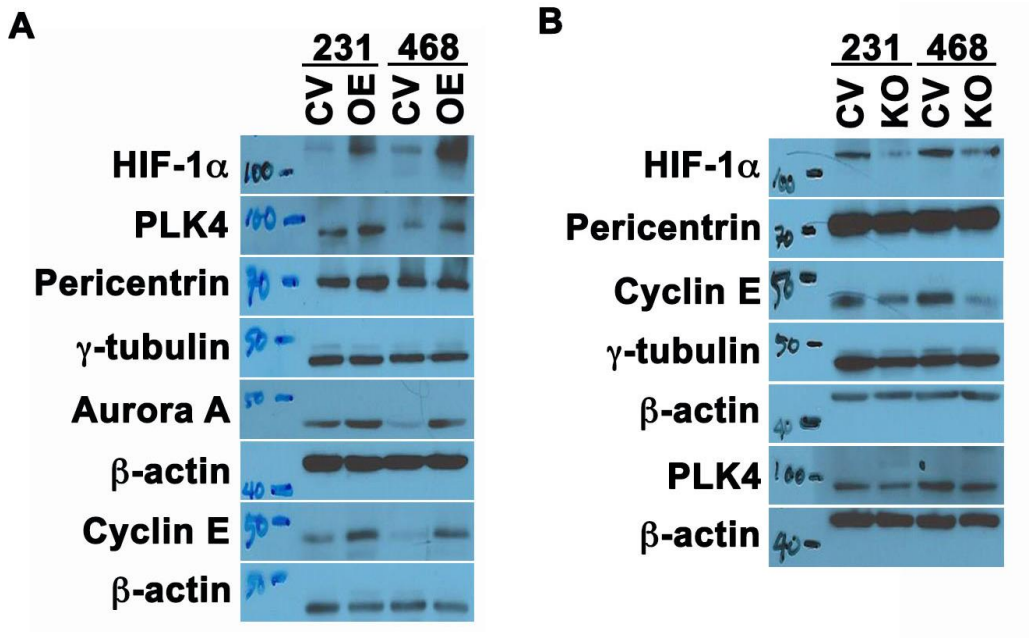

Figure 2.7.6 Immunoblots showing the levels of hypoxia and centrosomal markers in HIF-1α KO and OE cells.
A. Immunoblots of HIF-1α and centrosomal proteins in MDA-MB-231 and MDA-MB-468 transfected with empty vector or degradation-resistant HIF-1α. B. Immunoblots of HIF-1α and

centrosomal proteins in MDA-MB-231 and MDA-MB-468 transfected with Cas9-sgRNA (HIF-1α) construct or control vector (pSpCas9-2A-GFP).

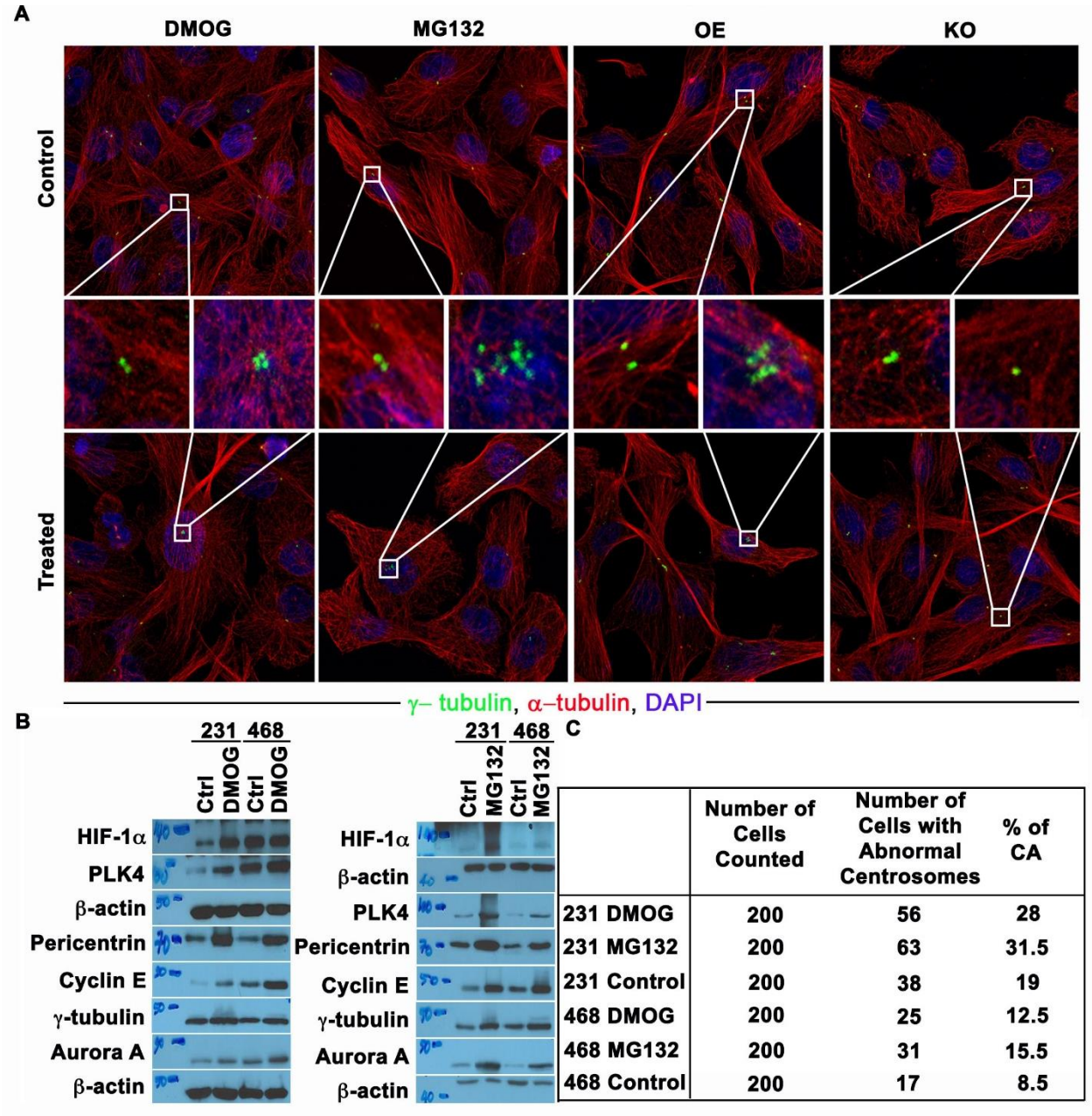

	Number of Cells Counted	Number of Cells with Abnormal Centrosomes	% of CA
231 DMOG	200	56	28
231 MG132	200	63	31.5
231 Control	200	38	19
468 DMOG	200	25	12.5
468 MG132	200	31	15.5
468 Control	200	17	8.5

Figure 2.7.7 Quantitation of CA in cells treated with DMOG and MG132
A. Representative confocal micrographs of centrosome amplification in MDA-MB-231 cells treated with DMOG and MG132. Representative confocal micrographs of centrosome amplification in MDA-MB-231 transfected with empty vector or degradation-resistant HIF-1α and with HIF-1α gene KO**. B.** Immunoblots showing the levels of hypoxia and centrosomal markers in cells treated with 1mM DMOG for 24 h. Immunoblots showing the levels of hypoxia and centrosomal markers in cells treated with 5μM of MG132 for 5 h**. C**. Quantitation of

centrosome amplification per microscopic examination for DMOG and MG132 treated and untreated MDA-MB-231 and MDA-MB-468 cells.

Enrichment of centrosomal gene expression in tumors with a hypoxia-high gene expression signature

We validated our in vitro findings of a correlation between CA and hypoxia in silico by probing the publicly-available Kao[1] and Jonsdottir[2] microarray datasets using Gene Set Enrichment Analysis (GSEA).[3] Essentially, our goal was to determine whether breast tumors that are enriched in hypoxia-associated transcripts also show a correlational enrichment in centrosomal transcripts. Publicly available pre-processed gene expression profiles of primary breast tumors (n=327 for the Kao dataset, GSE20685; n=94 for the Jonsdottir dataset, GSE46563) were used for GSEA. Within each dataset, patients were stratified into two groups by a hypoxia score, the reduced hypoxia metagene previously shown to have prognostic ability in multiple cancers.[4, 5] As previously defined, hypoxia scores were calculated as the median expression of 26 genes that are upregulated in response to hypoxia. Scores ≤ median were categorized as "hypoxia low" and scores > median were categorized as "hypoxia high." For the Kao dataset, Affymetrix probes with the "x_at" extension was removed unless no other probe was available (e.g., as with *ALDOA*). For the Jonsdottir dataset, Illumina probes with the "A" designator were preferentially used. When multiple probes were present, their median expression was used in score calculation. GSEA was performed with 1000 permutations, and false discovery rate q-values<0.05 were considered statistically significant.

Using the kao dataset, we collapsed features into gene symbols, resulting in 20,606 genes being available for gsea using curated gene sets from molecular signatures database[6] v5.0, including those from the gene ontology (go) consortium (for analysis of cellular components and

biological processes) and reactome [7] v53 (for pathway analysis), along with gene sets that we defined based on empirical evidence from the literature. We validated that the hypoxia-high group was differentially enriched in hypoxia-associated genes by performing gsea with the full hypoxia metagene as shown in supplementary Figure. 2.7.7 (also see supplementary table 2.7.1 for study details and supplementary table 2.7.2 for the ranked gene list; n=44 after filtering). We then performed GSEA to identify gene ontologies associated with the hypoxia-high group, which we found was significantly enriched in microtubule-organizing center and centrosome components, which were among the top-20 enriched cellular components (see supplementary table 1 for these and all other enriched gene ontologies). The hypoxia-high group was also enriched in cell cycle-related processes, which constituted the top-ranked gene ontology among biological processes. Cellular pathway analysis using reactome terms identified mitosis as the third-most enriched pathway, with various other cell cycle-related pathways also significantly enriched. Cellular pathway analysis revealed an enrichment in genes associated with the recruitment of centrosome proteins and complexes. Intriguingly, the hypoxia-high group was also enriched in genes involved in the cellular pathway associated with loss of ninein-like protein (nlp), a γ-tubulin-binding protein, from mitotic centrosomes. It is known that plk1 and nek2 phosphorylate nlp at the onset of mitosis, resulting displacement of nlp from the centrosome, which is associated with centrosome maturation (involving the recruitment of γ-tubulin ring complexes and other pericentriolar material components) and a concomitant increase in microtubule-nucleating capacity. Plk1 or nek2 overexpression results in premature nlp dissociation from centrosomes and also induces ca.[8]

Although hypoxia-high breast tumors were clearly found to be enriched in centrosomal components and pathways, we wanted to more specifically test the hypothesis that they are enriched in gene ontologies related to CA per se. No high-throughput screen of CA-associated

genes has been performed to inform construction of a CA gene set; nevertheless, the literature reports that CA is associated with hormone receptor-negative and node-positive breast cancer.[9] Thus, we analyzed enrichment of centrosome-associated genes (namely, experimentally identified human centrosomal proteins in the MiCroKiTS[10] database; n=540 genes) in hormone receptor-positive node-negative patients, rationalizing that this gene set has a high likelihood of representing CA. We found that 77 of these genes were enriched in hormone receptor-negative node-positive breast carcinomas. Next, we performed GSEA using these 77 genes as a gene set, which we found was significantly enriched in the hypoxia-high group, as shown in Supplementary Figure. 2.7.7B (also see Supplementary Table 2.7.3 for the ranked gene list). Many genes implicated in CA (such as *AURKA, CCNA2, CCNE2, CEP152, NEK2, PLK4, and STIL*) or amplified centrosome clustering (such as *KIFC1*, the top-ranked hit, along with *BIRC5* and *TACC3*) from the literature are among the enriched genes from this set. Because CA drives chromosomal instability (CIN), we wondered whether hypoxia-high cases were also enriched in CIN-associated genes. To this end, we performed GSEA with genes from the CIN25 signature, net overexpression of which has prognostic significance in various types of cancer.[11] We found this set was highly enriched in the hypoxia-high group (Supplementary Table 2.7.1). Collectively, these results suggest that hypoxic breast tumors are enriched in CA- and CIN-associated genes.

Enrichment of centrosomal gene expression in tumors with a hypoxia-high gene expression signature regardless of mitotic activity

Many CA-associated proteins do not exclusively localize to the centrosome; some also localize to the mitotic spindle. Thus, it could be argued that, rather than having a greater extent of CA, the hypoxia-high group merely has more mitotic cells than the hypoxia-low group. To test this hypothesis, we analyzed the Jonsdottir dataset, which contains gene expression profiles and

mitotic activity indices for 94 breast tumor specimens from lymph node-negative patients. To begin, we validated that the hypoxia-high group was enriched in hypoxia-associated genes. We performed GSEA with the full hypoxia metagene and found significant enrichment (Supplementary Table 2.7.1), which also underscores the robustness of this 26-gene hypoxia signature across platforms and breast cancer datasets. We then performed GSEA using the 77 potentially CA-associated genes (that is, those that were enriched in the hormone receptor-negative node-positive breast carcinomas from the Kao dataset) and found significant enrichment in the Jonsdottir dataset as well (Supplementary Table 2.7.4). This is especially interesting because the Jonsdottir patients are also all node-negative, indicating this gene set captures a phenotype that is not wholly dependent on nodal status. There was substantial overlap in the potentially CA-associated genes enriched in the Jonsdottir and Kao hypoxia-high groups. Next, we did find that the hypoxia-high group was associated with a high mitotic activity index (MAI; >10 mitotic figures per 10 fields of vision) based on the Mann-Whitney test ($p=0.01$). Nonetheless, when we performed GSEA on the MAI-low group ($n=60$) using hypoxia scores as the phenotype, we still found that the hypoxia-high group was enriched in potentially CA-associated genes (Supplementary Table 2.7.5). Thus, even among tumors with relatively low mitotic activity, hypoxia-high tumors show enrichment in potentially CA-associated genes, minimizing the probability that we are merely capturing proliferation-associated genes with our gene set. Combined with our in vitro data, these in silico data substantiate the hypothesis that hypoxia is associated with CA in patient breast tumors.

Finally, we were interested to determine whether hypoxia-associated CA, as determined by gene expression levels, predicts worse outcomes and, if so, whether its predictive ability depends on mitotic activity. To this end, we created a score based on the top ten CA-associated

genes enriched in the hypoxia-high samples of the Jonsdottir dataset (from Supplementary Table 2.7.4). Specifically, we defined the hypoxia-associated CA score as the median expression of those top 10 genes. Kaplan-Meier analysis and Cox regression were performed using SPSS Statistics version 21 (IBM). For multivariate Cox regression analysis, all potential predictors were entered into the full model and then eliminated stepwise based on an α=0.10 elimination criterion. Optimal cut points based on distant-metastasis-free survival (DMFS) were found using X-tile[12] per the highest X^2 value following dichotomization. We found that stratifying patients based on a cutpoint of 317 resulted in the CA score having the best predictive ability using the 94 node-negative breast cancer patients of the Jonsdottir dataset (p=0.020; Supplementary Figure. 2.7.6C). Univariate Cox regression revealed that a high hypoxia-associated CA score (i.e., >317) was associated with worse DMFS (HR=2.87; p=0.026), which was upheld in multivariate regression adjusting for all available potentially confounding covariates (including tumor size, Nottingham grade, estrogen and human epidermal growth factor receptor 2 statuses, and mitotic activity index). In fact, only this score remained in the final model. When hypoxia score was added to the Cox regression analysis, the effect of CA score on DMFS was more pronounced (HR=3.39, p=0.011). Only the CA score and hypoxia score remained in the final model, though the hypoxia score was no longer significant (HR=2.22, p=0.066). When the analysis was repeated without the CA score in the full model, however, the hypoxia score was a significant predictor of DMFS (HR=2.45, p=0.047), as was mitotic activity (HR=2.88, p=0.0.17), with no other variables in the final model. These results raise the tantalizing possibility that the ability of the hypoxia score to predict DMFS results from its association with CA. Even more intriguing is the idea that hypoxia might upregulate CA to drive metastatic dissemination, an exciting avenue of future research.

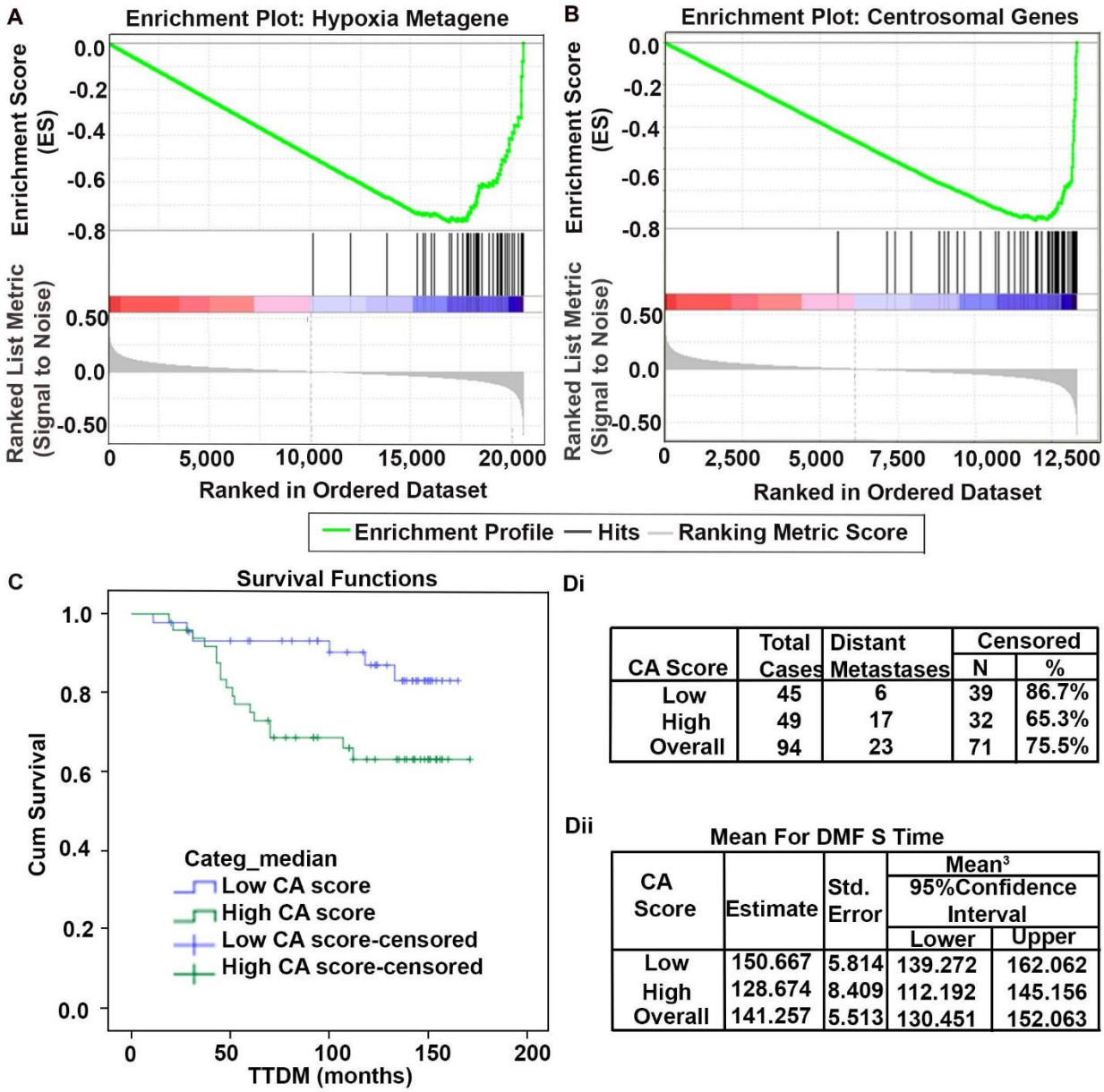

CA Score	Total Cases	Distant Metastases	Censored N	Censored %
Low	45	6	39	86.7%
High	49	17	32	65.3%
Overall	94	23	71	75.5%

CA Score	Estimate	Std. Error	Mean[3] 95%Confidence Interval Lower	Mean[3] 95%Confidence Interval Upper
Low	150.667	5.814	139.272	162.062
High	128.674	8.409	112.192	145.156
Overall	141.257	5.513	130.451	152.063

Figure 2.7.8 Gene-set enrichment and Kaplan-Meier analyses based on hypoxia- and centrosome amplification-associated genes.

A. Enrichment plots of hypoxia metagene components available in the Kao dataset and B. genes potentially associated with centrosome amplification (CA), with red indicating correlation with the hypoxia-low group and blue the hypoxia-high group. C. Plots of Kaplan-Meier product limit estimates of distant metastasis-free survival of patients in the Jonsdottir dataset stratified by hypoxia-associated CA score (low vs. high), p=0.020 by the log-rank tesst. TTDM=time to distant metastasis. Di. Number of distant metastases and censored cases by centrosome amplification score. Dii. Mean distant metastasis-free survival time by centrosome amplification score.

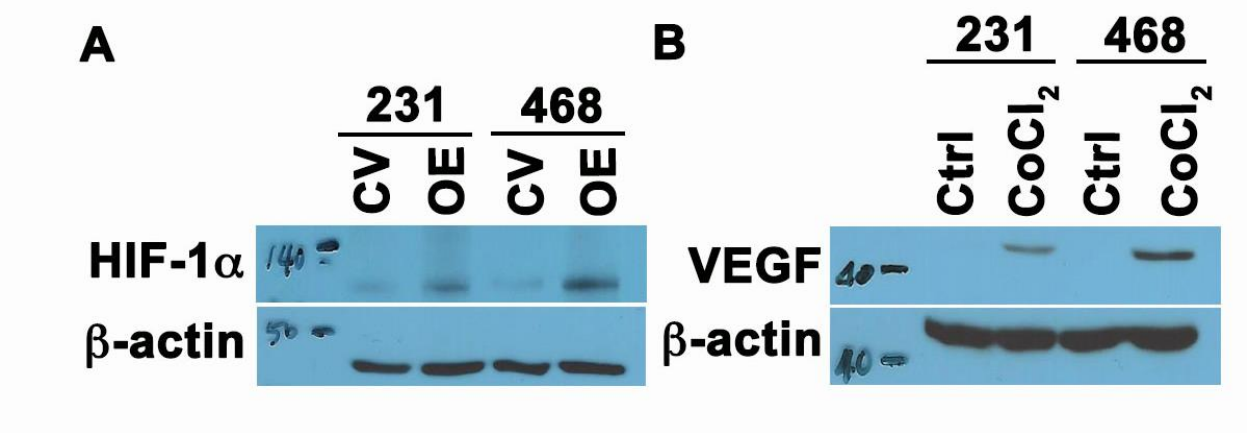

Figure 2.7.9 Representative immunoblots
A. Immunoblots of HIF-1α in MDA-MB-231 and MDA-MB-468 transfected with empty vector or degradation-resistant HIF-1α. B. Immunoblots of VEGF in MDA-MB-231 and MDA-MB-468 cells treated with 100μM of $CoCl_2$ for 24 hrs.

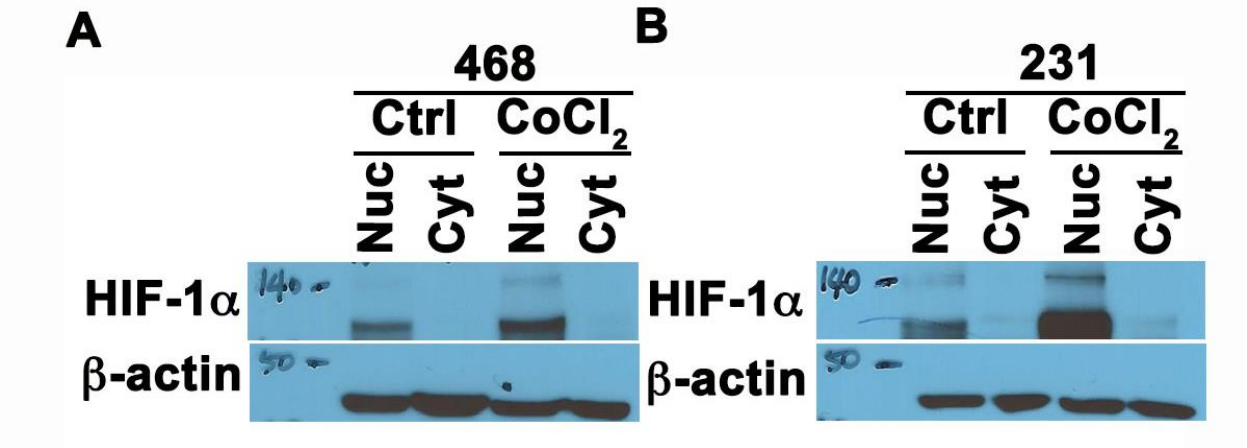

Figure 2.7.10 Representative immunoblots showing the levels of HIF-1α in nuclear and cytoplasmic lysates of MDA-MB-231 and MDA-MB-468 cells treated with 100μM of $CoCl_2$ for 24 hrs.

Table 2.6.1 Gene Set Enrichment Analyses for specified Gene Ontologies.
Reactome pathways, literature-based gene sets, and self-defined gene sets. GO and Reactome IDs (for curated gene sets) and publication details (for literature-based gene sets) are given in parentheses. ES=Enrichment Score; NES=Normalized Enrichment Score; NOM=nominal; FDR=False Discovery Rate; FWER=Family-Wise Error Rate

Gene Set	Size after Filtering	ES	ES	NOM p-value	FDR q-value	FWER p-value	Rank at Max
Kao- Entire Dataset							
Hypoxia Metagene (Buffa et al., 2010)	44	-0.77	-2.04	<0.001	<0.001	<0.001	3686
Microtubule Organizing Center (GO:0005815)	57	-0.54	-2.06	<0.001	4.5E-03	0.03	1531
Centrosome (GO:0005813)	49	-0.54	-2.01	<0.001	0.01	0.05	1531
Cell cycle (GO:0007049)	285	-0.61	-2.33	<0.001	3.1E-03	0.02	2632
Cell Cycle - Mitotic (Pathway:6927)	271	-0.67	-2.29	<0.001	4.2E-03	0.01	2316
Recruitment of Mitotic Centrosome Proteins and Complexes (Pathway:380270)	54	-0.46	-1.89	0.02	0.02	0.01	2313
Loss of NLP from Mitotic Centrosomes (Pathway:380259)	47	-0.46	-1.85	0.02	0.02	0.40	2313
Centrosomal Genes Upregulated in ER/PR+ Node-Tumors	77	-0.82	-1.88	<0.001	<0.001	<0.001	2630
CIN25 Genes (Carter et al., 2006)	23	-0.89	1.69	<0.001	<0.001	<0.001	1297
Jonsdottir - Entire Dataset							

Hypoxia Metagene (Buffa et al., 2010)	47	-0.81	-1.55	0.01	0.01	0.003	5057
Centrosomal Genes Upregulated in ER/PR+ Node-Tumors	77	-0.81	-1.56	4.0E-03	4.0E-03	2.0E-03	4008
Jonsdottir - MAI-Low Only							
Hypoxia Metagene (Buffa et al., 2010)	47	-0.75	-1.49	0.04	0.04	0.02	5163
Centrosomal Genes Upregulated in ER/PR+ Node-Tumors	77	-0.85	-1.72	<0.001	<0.001	<0.001	1813

Table 2.6.2 Rank-ordered list of filtered hypoxia metagene components with associated rank metric scores, enrichment scores (ES), and whether each gene is part of the core enriched genes (i.e., the leading-edge subset) in the hypoxia-high group of the Kao dataset

GENE SYMBOL	RANK IN GENE LIST	RANK METRIC SCORE	RUNNING ES	CORE ENRICHMENT
ALDOA	10185	-0.001037822	-0.4951352	No
ANKRD37	12004	-0.013171702	-0.5810628	No
LRRC42	13846	-0.026962586	-0.6655041	No
MCTS1	15337	-0.04007807	-0.73039776	No
MIF	15612	-0.042822175	-0.7356349	No
CHCHD2	15748	-0.044233657	-0.7338455	No
LDHA	16016	-0.047092326	-0.7379356	No
GAPDH	16182	-0.049089462	-0.73668796	No
GPI	16921	-0.058381788	-0.76155204	Yes
SEC61G	17016	-0.059670471	-0.75485283	Yes
UTP11L	17344	-0.064875908	-0.75850195	Yes
HK2	17604	-0.069081984	-0.75804955	Yes
TUBB6	17812	-0.072616458	-0.7544006	Yes
PSMA7	17838	-0.073151112	-0.7417994	Yes
SLC25A32	17903	-0.074541941	-0.7308322	Yes
PGK1	18012	-0.076205611	-0.72169065	Yes
BNIP3	18017	-0.076291725	-0.70747495	Yes
P4HA1	18145	-0.07900098	-0.69872946	Yes

MAD2L2	18230	-0.080925092	-0.68752927	Yes
CORO1C	18285	-0.082037203	-0.67465997	Yes
ENO1	18319	-0.082770482	-0.6606309	Yes
TPI1	18340	-0.083269544	-0.64587533	Yes
SLC16A1	18401	-0.084655896	-0.63280326	Yes
YKT6	18405	-0.084711224	-0.6169486	Yes
DDIT4	18565	-0.088841394	-0.6079007	Yes
MRPL15	18878	-0.098103359	-0.60454416	Yes
MRPL13	19107	-0.106322989	-0.59554994	Yes
AK3L1	19315	-0.114598989	-0.5839712	Yes
NDRG1	19351	-0.11648801	-0.56367075	Yes
NP	19458	-0.121711895	-0.5458365	Yes
SLC2A1	19484	-0.12285845	-0.52384645	Yes
MRPS17	19534	-0.126033917	-0.50242376	Yes
ACOT7	19727	-0.138207912	-0.48565617	Yes
PFKP	19803	-0.144859448	-0.46194214	Yes
HIG2	19898	-0.152798504	-0.4376526	Yes
PSRC1	19910	-0.154252052	-0.4090519	Yes
ADM	20066	-0.17373921	-0.38377362	Yes
CA9	20175	-0.192664087	-0.35263497	Yes
CTSL2	20338	-0.228577107	-0.31733918	Yes
SHCBP1	20490	-0.299957722	-0.2680258	Yes
CDKN3	20524	-0.333389521	-0.20665893	Yes
KIF20A	20528	-0.337646633	-0.14302899	Yes
KIF4A	20545	-0.356419325	-0.07648543	Yes
ANLN	20585	-0.420125276	9.73E-04	Yes

Table 2.6.4 Rank-ordered list of potential centrosome amplification-associated genes with associated rank metric scores, enrichment scores (ES), and whether each gene is part of the core enriched genes (i.e., the leading-edge subset) in the hypoxia-high group of the Kao dataset.

GENE SYMBOL	RANK IN GENE LIST	RANK METRIC SCORE	RUNNING ES	CORE ENRICHMENT
TRIM22	9257	0.005535	-0.45051	No
PRKAA1	10390	-0.0025	-0.50547	No
MAP1B	11819	-0.01194	-0.57415	No
GIMAP5	12039	-0.01341	-0.58383	No
FYN	12842	-0.01913	-0.62148	No
ODF2L	13067	-0.02089	-0.63085	No
RASSF5	14099	-0.02883	-0.67894	No

PRKD3	14243	-0.02992	-0.6837	No
MARCKS	14472	-0.03196	-0.69244	No
LIMK1	14658	-0.03361	-0.69897	No
SYK	14810	-0.0351	-0.70373	No
HAP1	15154	-0.03818	-0.71762	No
PIM1	16282	-0.05017	-0.76881	No
FIGN	16589	-0.05401	-0.77973	No
LIMK2	16953	-0.05886	-0.79306	No
BRSK1	17048	-0.06002	-0.79321	No
PRKCQ	17094	-0.06075	-0.79091	No
SMURF2	17543	-0.06803	-0.80771	No
SOCS1	17796	-0.07242	-0.81464	No
NEK6	17977	-0.07552	-0.81783	Yes
CRYAB	18091	-0.07784	-0.81758	Yes
RUNX3	18196	-0.08005	-0.81673	Yes
SPHK1	18224	-0.0808	-0.81208	Yes
SASS6	18240	-0.08116	-0.80682	Yes
SLC16A1	18401	-0.08466	-0.80836	Yes
GNAI1	18457	-0.08613	-0.80467	Yes
TSKS	18806	-0.09576	-0.81455	Yes
WASF1	18833	-0.0967	-0.80867	Yes
PLEKHG6	19038	-0.10343	-0.81097	Yes
PDE7A	19279	-0.11301	-0.81431	Yes
LCK	19344	-0.11619	-0.80885	Yes
NDRG1	19351	-0.11649	-0.80054	Yes
CCNA1	19406	-0.1191	-0.79437	Yes
CENPJ	19444	-0.12114	-0.78722	Yes
LMO4	19518	-0.12512	-0.78154	Yes
PSMD3	19615	-0.13063	-0.77656	Yes
VAC14	19642	-0.13237	-0.76805	Yes
CDC25B	19705	-0.13691	-0.76096	Yes
CHEK2	19769	-0.14153	-0.75357	Yes
RANBP1	19788	-0.14291	-0.74389	Yes
GPSM2	19923	-0.15544	-0.73894	Yes
CKAP2	19951	-0.15892	-0.72852	Yes
CEP152	19990	-0.16318	-0.71831	Yes
MCM5	19996	-0.16407	-0.70644	Yes
GMNN	20040	-0.16928	-0.69603	Yes
EIF4EBP1	20052	-0.17204	-0.68385	Yes
TACC3	20230	-0.20252	-0.67752	Yes
FANCA	20250	-0.20734	-0.66313	Yes

BRCA2	20291	-0.21723	-0.64903	Yes
SGOL1	20325	-0.22475	-0.63403	Yes
STIL	20384	-0.24633	-0.61866	Yes
ESPL1	20406	-0.25368	-0.60095	Yes
CHEK1	20417	-0.2561	-0.58252	Yes
TROAP	20421	-0.25745	-0.56365	Yes
CCNB1	20430	-0.26098	-0.54476	Yes
PTTG1	20441	-0.26845	-0.52542	Yes
CRABP1	20449	-0.27154	-0.5057	Yes
CCNA2	20464	-0.28031	-0.48567	Yes
KIF15	20467	-0.28398	-0.4648	Yes
MAD2L1	20468	-0.28479	-0.44376	Yes
CENPF	20471	-0.28903	-0.42251	Yes
AURKA	20480	-0.29411	-0.40117	Yes
KIF11	20487	-0.29864	-0.3794	Yes
HMMR	20503	-0.31248	-0.35705	Yes
CDC25C	20510	-0.32075	-0.33365	Yes
CCNE2	20511	-0.32077	-0.30996	Yes
NEK2	20517	-0.32682	-0.28606	Yes
CDKN3	20524	-0.33339	-0.26172	Yes
KIF14	20548	-0.35903	-0.23632	Yes
PLK1	20550	-0.35933	-0.20983	Yes
KIF18A	20556	-0.37178	-0.18261	Yes
ASPM	20557	-0.37248	-0.1551	Yes
TTK	20560	-0.37723	-0.12733	Yes
CEP55	20561	-0.37875	-0.09935	Yes
BIRC5	20577	-0.40346	-0.07028	Yes
CDC20	20586	-0.42014	-0.03964	Yes
KIFC1	20603	-0.54844	9.75E-05	Yes

Table 2.6.5 Rank-ordered list of potential centrosome amplification-associated genes with associated rank metric scores, enrichment scores (ES), and whether each gene is part of the core enriched genes (i.e., the leading-edge subset) in the hypoxia-high group of the entire Jonsdottir dataset.

GENE SYMBOL	**RANK IN GENE LIST**	**RANK METRIC SCORE**	**RUNNING ES**	**CORE ENRICHMENT**
MAP1B	9927	0.027879	-0.2694731	No
GIMAP5	11620	0.018845	-0.3146127	No
NEK6	14304	0.006694	-0.3874912	No
TSKS	20675	-0.02045	-0.5602645	No

LCK	21643	-0.0252	-0.585253	No
GNAI1	21692	-0.02545	-0.5851359	No
MARCKS	25609	-0.04594	-0.6894773	No
SYK	25673	-0.04634	-0.6885981	No
WASF1	25818	-0.04722	-0.689881	No
FIGN	26288	-0.05058	-0.6998489	No
SMURF2	26579	-0.05269	-0.704811	No
CCNB1	26876	-0.05483	-0.7098172	No
TRIM22	28230	-0.06621	-0.7430442	No
SLC16A1	28325	-0.06714	-0.7418446	No
BRCA2	29320	-0.07824	-0.764595	No
RASSF5	29744	-0.08353	-0.7714585	No
PRKAA1	30331	-0.0924	-0.7822752	No
HAP1	30451	-0.09399	-0.780252	No
ODF2L	30904	-0.10177	-0.7868843	No
FYN	31621	-0.1156	-0.7999487	No
PRKD3	31760	-0.11896	-0.7970437	No
PSMD3	32154	-0.12857	-0.8005617	Yes
SOCS1	32256	-0.13107	-0.7959673	Yes
CRABP1	32696	-0.14402	-0.7998746	Yes
CCNA1	32921	-0.15105	-0.7975177	Yes
SASS6	33107	-0.15692	-0.7937663	Yes
BRSK1	33320	-0.16365	-0.7903748	Yes
CHEK2	33524	-0.17026	-0.7863668	Yes
RUNX3	34028	-0.19051	-0.7894138	Yes
LIMK1	34450	-0.20953	-0.789155	Yes
KIF14	34790	-0.22531	-0.7857721	Yes
SPHK1	34813	-0.22655	-0.7736645	Yes
TACC3	34830	-0.22751	-0.7613397	Yes
PRKCQ	34832	-0.22752	-0.7486046	Yes
ESPL1	34847	-0.22799	-0.7361981	Yes
FANCA	34935	-0.23268	-0.7255213	Yes
CDC25C	34988	-0.23525	-0.7137451	Yes
VAC14	35284	-0.25222	-0.7076517	Yes
HMMR	35293	-0.25279	-0.6936903	Yes
PLEKHG6	35543	-0.27288	-0.6851819	Yes
CDC25B	35587	-0.27725	-0.6708041	Yes
PLK1	35601	-0.27839	-0.655543	Yes
EIF4EBP1	35641	-0.28117	-0.6408358	Yes
CRYAB	35712	-0.28594	-0.6267073	Yes
MCM5	35760	-0.29006	-0.61172	Yes

CKAP2	35792	-0.29443	-0.5960506	Yes
ASPM	35799	-0.29504	-0.5796646	Yes
KIF11	35823	-0.29804	-0.5635741	Yes
CCNE2	35873	-0.30251	-0.5479429	Yes
GMNN	35987	-0.31268	-0.5334887	Yes
CENPJ	35995	-0.31324	-0.5161092	Yes
NEK2	36018	-0.31532	-0.4990226	Yes
CEP55	36028	-0.31635	-0.4815231	Yes
CDKN3	36053	-0.31868	-0.4643022	Yes
PIM1	36092	-0.32313	-0.4472143	Yes
BIRC5	36106	-0.32495	-0.4293416	Yes
KIF18A	36150	-0.3296	-0.4120271	Yes
MAD2L1	36155	-0.33	-0.3936251	Yes
CENPF	36214	-0.33744	-0.3762802	Yes
PTTG1	36249	-0.34282	-0.3579785	Yes
TROAP	36260	-0.3446	-0.3389218	Yes
KIF15	36303	-0.35197	-0.3203251	Yes
CEP152	36317	-0.35415	-0.3008146	Yes
SGOL1	36319	-0.35452	-0.2809555	Yes
TTK	36354	-0.3624	-0.2615553	Yes
CDC20	36396	-0.36887	-0.2419837	Yes
CCNA2	36406	-0.37126	-0.221404	Yes
KIFC1	36418	-0.37251	-0.2008091	Yes
LIMK2	36451	-0.37996	-0.1803693	Yes
AURKA	36460	-0.38249	-0.1591323	Yes
PDE7A	36488	-0.38882	-0.1380591	Yes
GPSM2	36559	-0.4058	-0.1172072	Yes
NDRG1	36567	-0.40833	-0.0944937	Yes
RANBP1	36571	-0.40905	-0.0716305	Yes
LMO4	36595	-0.41683	-0.0488768	Yes
STIL	36597	-0.41794	-0.02546	Yes
CHEK1	36684	-0.50451	4.92E-04	Yes

Table 2.6.6 Rank-ordered list of potential centrosome amplification-associated genes with associated rank metric scores, enrichment scores (ES), and whether each gene is part of the core enriched genes (i.e., the leading-edge subset) in the hypoxia-high group of the mitosis-activity-index-low cases of the Jonsdottir dataset

GENE SYMBOL	**RANK IN GENE LIST**	**RANK METRIC SCORE**	**RUNNING ES**	**CORE ENRICHMENT**
CRABP1	1247	0.196209	-0.022491	No

SYK	4586	0.083097	-0.108734	No
MAP1B	4941	0.077617	-0.113828	No
GNAI1	6693	0.05668	-0.158298	No
PRKCQ	7260	0.051505	-0.170718	No
CCNA1	11454	0.025851	-0.283677	No
GIMAP5	12204	0.022238	-0.302817	No
LIMK1	13681	0.015818	-0.342184	No
TSKS	14283	0.013139	-0.35782	No
HAP1	14837	0.010819	-0.372281	No
NEK6	15431	0.008267	-0.387985	No
LCK	16809	0.002983	-0.425406	No
RUNX3	18761	-0.004223	-0.478425	No
WASF1	19448	-0.006835	-0.496752	No
SMURF2	20802	-0.012268	-0.532971	No
SOCS1	21207	-0.014023	-0.543175	No
CRYAB	23902	-0.025877	-0.615206	No
PRKD3	24183	-0.027193	-0.621249	No
SLC16A1	24424	-0.028282	-0.626136	No
FANCA	24474	-0.028508	-0.625795	No
TRIM22	26151	-0.036923	-0.66938	No
ODF2L	26970	-0.041393	-0.689276	No
LMO4	27255	-0.042918	-0.694502	No
VAC14	28281	-0.049818	-0.719554	No
FIGN	28767	-0.053333	-0.729655	No
MARCKS	28812	-0.053722	-0.727692	No
EIF4EBP1	30948	-0.074622	-0.781589	No
CHEK2	31454	-0.081308	-0.790588	No
RASSF5	32122	-0.091782	-0.803394	No
FYN	32229	-0.093444	-0.800785	No
PRKAA1	33495	-0.122161	-0.828128	No
SPHK1	33904	-0.13265	-0.831455	No
BRCA2	34464	-0.152763	-0.837721	No
PIM1	34891	-0.169697	-0.839357	Yes
BRSK1	35120	-0.181113	-0.834915	Yes
LIMK2	35200	-0.184675	-0.826196	Yes
PDE7A	35419	-0.198272	-0.82047	Yes
PLEKHG6	35542	-0.20546	-0.811701	Yes
PSMD3	35718	-0.219175	-0.80357	Yes
GMNN	35762	-0.222346	-0.791649	Yes
NDRG1	35901	-0.235135	-0.781568	Yes
RANBP1	35918	-0.236222	-0.768093	Yes

MCM5	35984	-0.242655	-0.755576	Yes
PLK1	36105	-0.258397	-0.743634	Yes
SASS6	36241	-0.277588	-0.730971	Yes
CEP152	36386	-0.312943	-0.716472	Yes
CENPF	36392	-0.313983	-0.698116	Yes
CDC25B	36411	-0.319583	-0.679785	Yes
STIL	36430	-0.324553	-0.661162	Yes
ASPM	36438	-0.326208	-0.642141	Yes
AURKA	36476	-0.341741	-0.623024	Yes
KIF14	36482	-0.342514	-0.602988	Yes
BIRC5	36494	-0.345894	-0.582916	Yes
CCNB1	36500	-0.348213	-0.562544	Yes
KIF18A	36520	-0.356315	-0.542078	Yes
TACC3	36528	-0.35818	-0.521174	Yes
HMMR	36541	-0.363636	-0.500085	Yes
CKAP2	36568	-0.374923	-0.478713	Yes
MAD2L1	36570	-0.37601	-0.456595	Yes
SGOL1	36580	-0.38294	-0.434287	Yes
CCNE2	36581	-0.383755	-0.411685	Yes
KIFC1	36583	-0.383929	-0.389101	Yes
CCNA2	36587	-0.38714	-0.366382	Yes
GPSM2	36588	-0.388246	-0.343516	Yes
CDKN3	36616	-0.40076	-0.32065	Yes
CDC20	36621	-0.406762	-0.296802	Yes
ESPL1	36626	-0.410511	-0.272734	Yes
CHEK1	36627	-0.412625	-0.248432	Yes
TTK	36633	-0.414843	-0.224136	Yes
CEP55	36647	-0.434241	-0.198916	Yes
TROAP	36665	-0.460532	-0.172257	Yes
KIF11	36671	-0.467194	-0.144878	Yes
CDC25C	36678	-0.47623	-0.116993	Yes
KIF15	36679	-0.477443	-0.088874	Yes
NEK2	36683	-0.486579	-0.060298	Yes
PTTG1	36691	-0.501135	-0.030975	Yes
CENPJ	36699	-0.530558	8.18E-05	Yes

References

1.Kao, K.-J., et al., *Correlation of microarray-based breast cancer molecular subtypes and clinical outcomes: implications for treatment optimization.* BMC Cancer, 2011. **11**: p. 143-143.

2.Jonsdottir, K., et al., *Prognostic value of gene signatures and proliferation in lymph-node-negative breast cancer.* PLoS One, 2014. **9**(3): p. e90642.

3.Subramanian, A., et al., *Gene set enrichment analysis: a knowledge-based approach for interpreting genome-wide expression profiles.* Proc Natl Acad Sci U S A, 2005. **102**(43): p. 15545-50.

4.Eustace, A., et al., *A 26-gene hypoxia signature predicts benefit from hypoxia-modifying therapy in laryngeal cancer but not bladder cancer.* Clin Cancer Res, 2013. **19**(17): p. 4879-88.

5.Buffa, F.M., et al., *Large meta-analysis of multiple cancers reveals a common, compact and highly prognostic hypoxia metagene.* Br J Cancer, 2010. **102**(2): p. 428-35.

6.Liberzon, A., et al., *Molecular signatures database (MSigDB) 3.0.* Bioinformatics, 2011. **27**(12): p. 1739-40.

7.Matthews, L., et al., *Reactome knowledgebase of human biological pathways and processes.* Nucleic Acids Research, 2009. **37**(Database issue): p. D619-D622.

8.Rapley , J., et al., *Coordinate Regulation of the Mother Centriole Component Nlp by Nek2 and Plk1 Protein Kinases.* Molecular and Cellular Biology, 2005. **25**(4): p. 1309-1324.

9.Schneeweiss, A., et al., *Centrosomal aberrations in primary invasive breast cancer are associated with nodal status and hormone receptor expression.* Int J Cancer, 2003. **107**(3): p. 346-52.

10.Huang, Z., et al., *MiCroKiTS 4.0: a database of midbody, centrosome, kinetochore, telomere and spindle.* Nucleic Acids Research, 2015. **43**(D1): p. D328-D334.

11.Carter, S.L., et al., *A signature of chromosomal instability inferred from gene expression profiles predicts clinical outcome in multiple human cancers.* Nat Genet, 2006. **38**(9): p. 1043-1048.

12.Camp, R.L., M. Dolled-Filhart, and D.L. Rimm, *X-Tile: A New Bio-Informatics Tool for Biomarker Assessment and Outcome-Based Cut-Point Optimization.* Clinical Cancer Research, 2004. **10**(21): p. 7252-7259.

Appendix B: Supplementary Data for Chapter 3

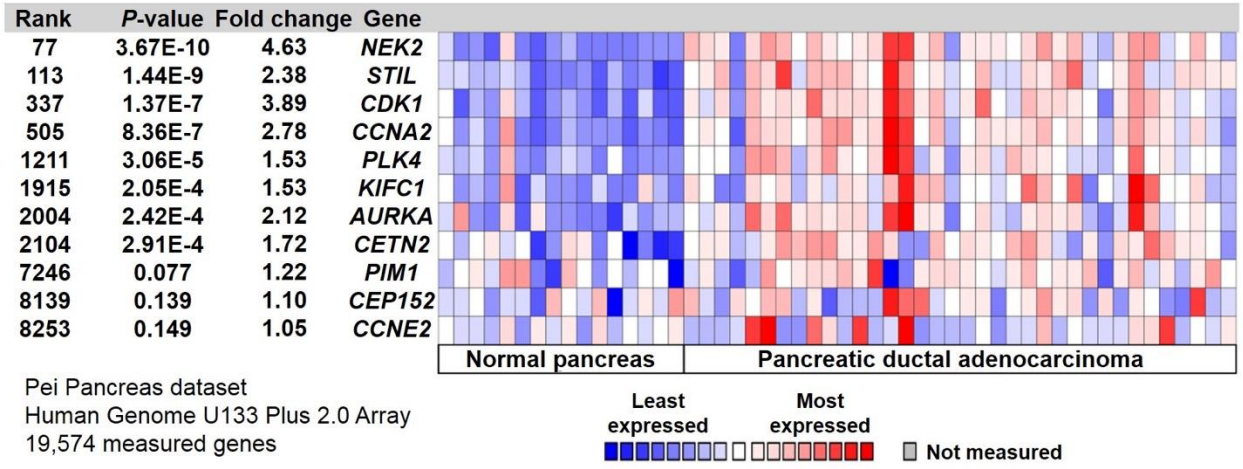

Supplementary Figure 3.7.1 Heat maps of genes whose dysregulation drives centrosome amplification and clustering.
Heat maps of genes whose dysregulation drives centrosome amplification and clustering are upregulated in pancreastic ductal adenocarcinoma (N=36) relative to normal pancreas (N=16). Heat map generated with Oncomine Gene Browser.

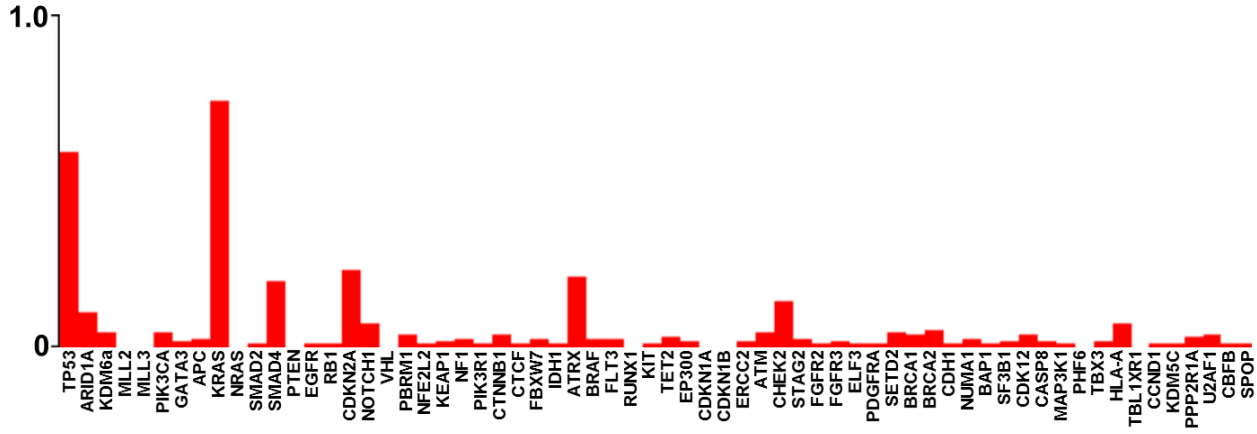

Supplementary Figure 3.7.2 The proportion of gene-level non-silent somatic mutations in The Cancer Genome Atlas pancreatic adenocarcinoma dataset (N=144).

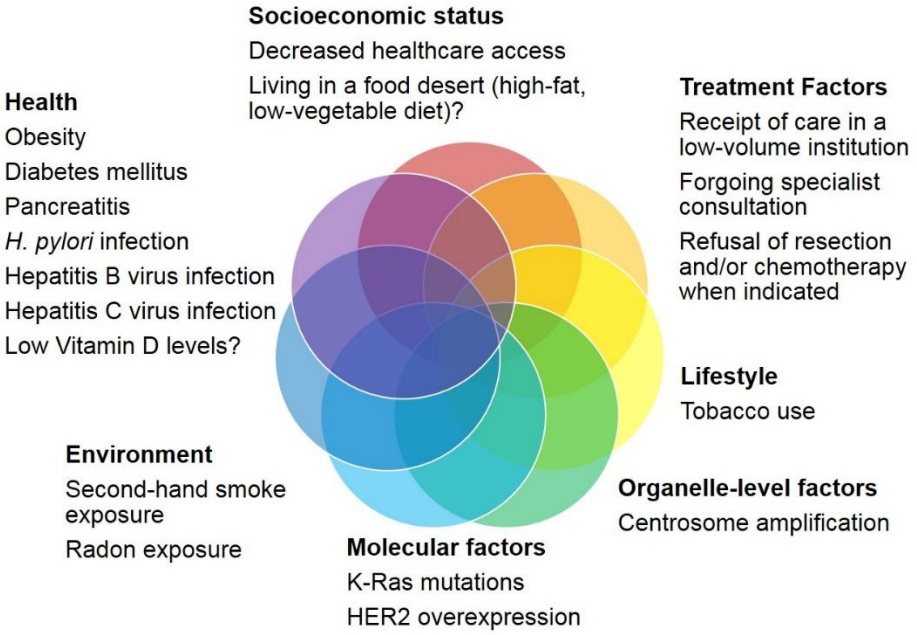

Supplementary Figure 3.7.3 Risk factors for the development of PDAC that are associated with African American ethnicity

Appendix C: Supplementary Data for Chapter 5

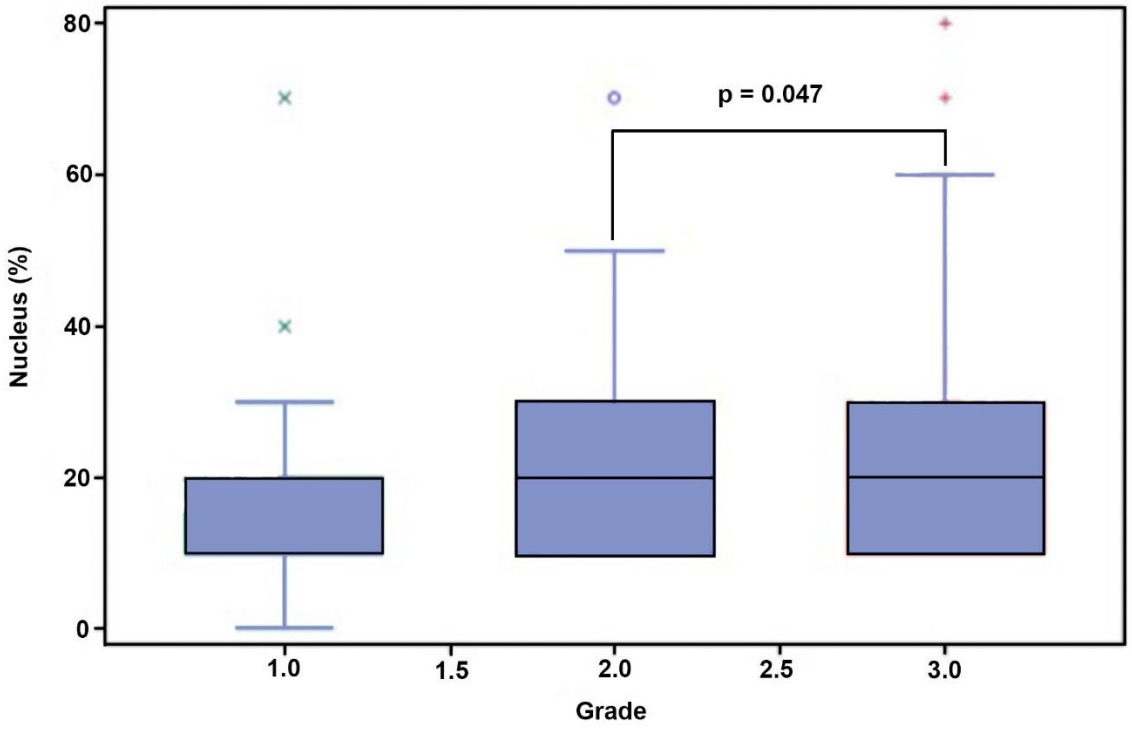

Supplementary Figure 5.7.1 High grade serous ovarian carcinomas exhibit higher expression of KIFC1. A. Box-whisker plot representing the weighted index for KIFC1 expression in low and high-grade SOC tissues.

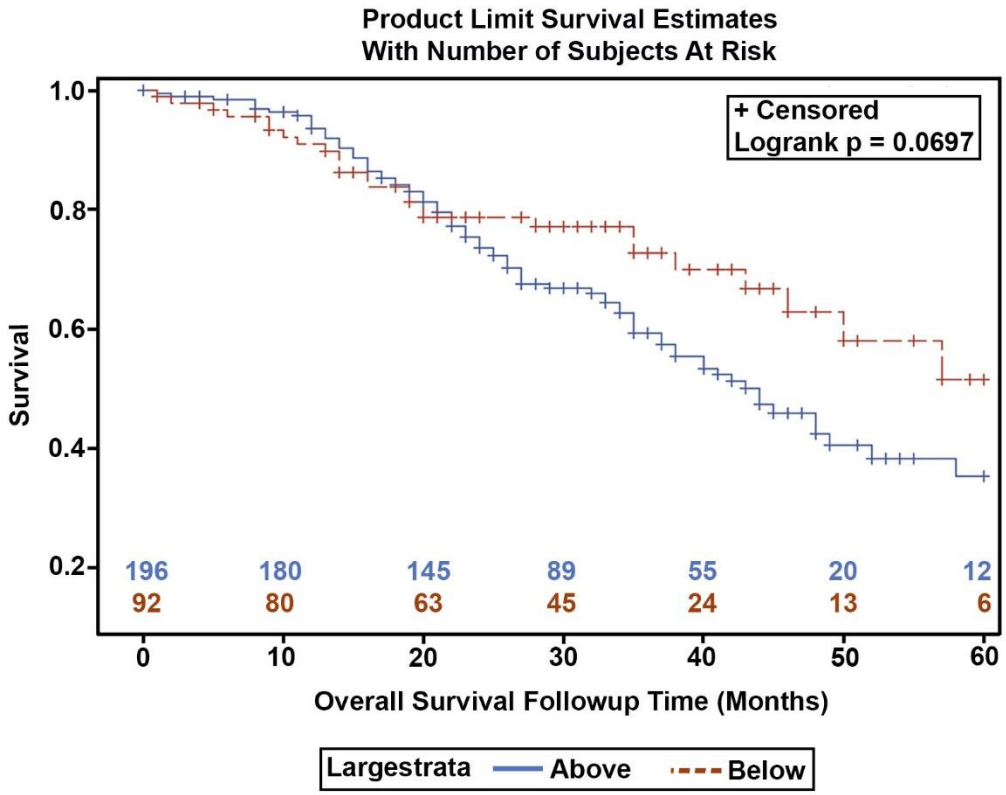

Supplementary Figure 5.7.2 Kaplan-Meier plots of overall survival based on low or high expression of KIFC1 gene in ovarian cancer patients regardless of histotypes.

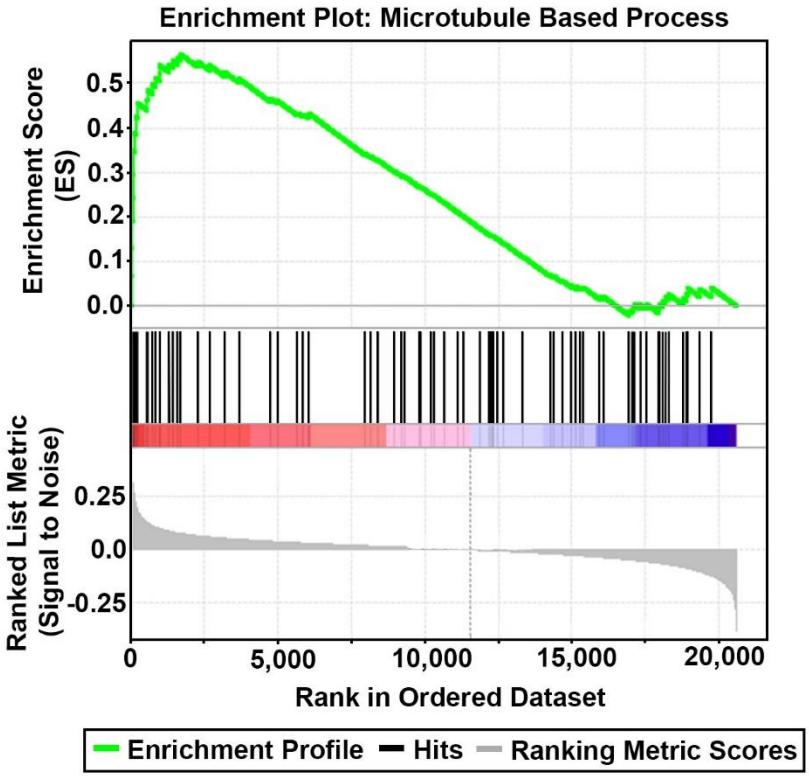

Supplementary Figure 5.7.3 Gene set enrichment analyses for biological processes associated to KIFC1 high group. A. Enrichment plot of genes associated to microtubule-based processes, with red indicating correlation with the KIFC1-high group and blue the KIFC1-low group.

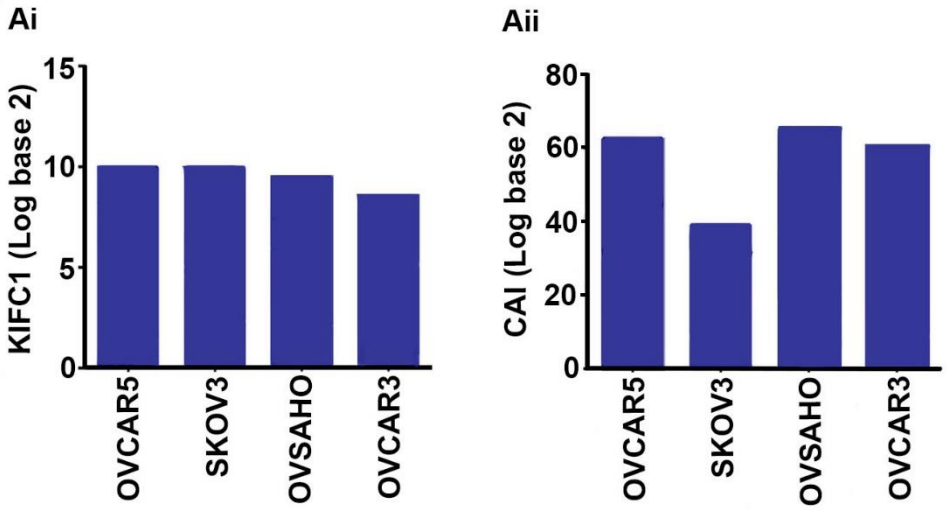

Supplementary Figure 5.7.4 HGSOC cell lines show higher expression of genes, driving Centrosome amplification, and KIFC1 in silico. Ai. Bar graph representing Log Base 2

KIFC1expression in ovarian cell lines (Ovcar5, OVCAR3, OVSAHO, and SKOV3). Aii Bar graph representing Log Base 2 Centrosome amplification index expression in ovarian cell lines (OVCAR5, OVCAR3, OVSAHO, and SKOV3).

Table 5.7.1 Descriptive table for univariate and multivariate analysis.

Univariate analysis

Analysis of Maximum Likelihood Estimates										
Parameter		DF	Parameter Estimate	Standard Error	Chi-Square	Pr > ChiSq	Hazard Ratio	95% Hazard Ratio Confidence Limits		Label
KIFC1 Threshold	Above	1	0.76065	0.33921	5.0284	0.0249	2.14	1.101	4.16	KIFC1 Threshold Above

Multivariate analysis

Analysis of Maximum Likelihood Estimates										
Parameter		DF	Parameter Estimate	Standard Error	Chi-Square	Pr > ChiSq	Hazard Ratio	95% Hazard Ratio Confidence Limits		Label
KIFC1 Threshold	Above	1	0.96403	0.35609	7.3294	0.0068	2.622	1.305	5.27	HSET Threshold Above
Stage	I	1	-2.94842	1.07247	7.5579	0.006	0.052	0.006	0.429	Figo Stage I Ovarian Serous Ade-nocarcinoma
Stage	II	1	-2.79558	1.07091	6.8145	0.009	0.061	0.007	0.498	Figo Stage II Ovarian Serous Ade-nocarcinoma
Stage	III	1	-1.60511	0.38692	17.2097	<0.0001	0.201	0.094	0.429	Figo Stage III Ovarian Serous Ade-nocarcinoma
Grade	Grade1	1	-13.20833	1037	0.0002	0.9898	0	0		Grade Grade1
Grade	Grade2	1	0.24076	0.30536	0.6216	0.4304	1.272	0.699	2.315	Grade Grade2

Table 5.7.2 Rank-ordered list of filtered genes comprising centrosome components with associated rank metric scores, enrichment scores (ES), and whether each gene is part of the core enriched genes (i.e., the leading-edge subset) in the KIFC1-high group.

GENE SYMBOL	RANK IN GENE LIST	RANK METRIC SCORE	RUNNING ES	CORE ENRICHMENT
TOP2A	25	0.334119827	0.0778286	Yes
KIF15	31	0.329936087	0.15564038	Yes
BIRC5	33	0.328538954	0.23331621	Yes
NEK2	49	0.306233615	0.30503407	Yes
PLK1	69	0.277375519	0.3697302	Yes
CTAG2	133	0.232606009	0.42169446	Yes
ESPL1	163	0.211262807	0.47026342	Yes
SAC3D1	317	0.161001891	0.50090957	Yes
NDE1	394	0.147750571	0.5321666	Yes
BRCA2	470	0.137022048	0.5609342	Yes
CROCC	841	0.106630601	0.56816083	Yes
AZI1	1055	0.095914356	0.58048993	Yes
CKAP5	1293	0.087143637	0.58957654	Yes

Table 5.7.3 Rank-ordered list of filtered genes associated to mitotic cycle components with associated rank metric scores, enrichment scores (ES), and whether each gene is part of the core enriched genes (i.e., the leading-edge subset) in the KIFC1-high group.

GENE SYMBOL	RANK IN GENE LIST	RANK METRIC SCORE	RUNNING ES	CORE ENRICHMENT
KIF23	7	0.380206674	0.026178278	Yes
KIF2C	16	0.34368071	0.04975993	Yes
NCAPH	19	0.341490924	0.07348197	Yes
KIF15	31	0.329936087	0.095958345	Yes

BIRC5	33	0.328538954	0.118825816	Yes
TPX2	43	0.312425733	0.14017852	Yes
BUB1	45	0.311746061	0.16187464	Yes
ANLN	47	0.309315741	0.18340124	Yes
PRC1	48	0.307584703	0.20485595	Yes
NEK2	49	0.306233615	0.22621644	Yes
CDKN3	52	0.303843647	0.24731249	Yes
CDC6	54	0.301827401	0.26831678	Yes
UBE2C	58	0.294732958	0.28872848	Yes
TTK	59	0.294727236	0.30928636	Yes
NUSAP1	65	0.281409442	0.328671	Yes
CENPF	68	0.277548671	0.34793293	Yes
PLK1	69	0.277375519	0.3672805	Yes
CDC7	72	0.27584514	0.3864236	Yes
CENPE	76	0.275140435	0.4054687	Yes
AURKA	77	0.274723768	0.4246313	Yes
FBXO5	86	0.270314395	0.44309548	Yes
CDC25C	93	0.264975429	0.46128497	Yes
BUB1B	106	0.255380183	0.47851205	Yes
KIF11	126	0.236126006	0.49405414	Yes
CCNA2	128	0.235330373	0.5104201	Yes
CDCA5	131	0.234785706	0.5266992	Yes
RCC1	157	0.2154641	0.54050696	Yes
ESPL1	163	0.211262807	0.55499876	Yes
ZWINT	185	0.202192873	0.5680762	Yes
CDK2	201	0.19581379	0.5810018	Yes
CDKN2A	207	0.191838071	0.5941387	Yes
STMN1	238	0.180245936	0.6052456	Yes
CIT	255	0.175560325	0.61670965	Yes

KNTC1	264	0.173231944	0.6284021	Yes
MAD2L1	305	0.16407761	0.6378927	Yes
CDKN2D	327	0.159156412	0.6479683	Yes
KIF22	343	0.157049492	0.65819	Yes
E2F1	390	0.147849038	0.66625553	Yes
SKP2	420	0.144821107	0.67494035	Yes
MAD2L2	450	0.140390754	0.6833162	Yes
DBF4	488	0.135220751	0.6909405	Yes
CDKN2C	553	0.128658727	0.696788	Yes
POLD1	564	0.127196997	0.70517176	Yes
POLE	710	0.11385873	0.7060298	Yes
DDX11	726	0.113228329	0.7131949	Yes
PKMYT1	774	0.109883375	0.7185633	Yes
SMC4	852	0.105742373	0.7221773	Yes
PIN1	1119	0.093436472	0.71569943	Yes
TBRG4	1304	0.086835429	0.71276724	Yes
ASNS	1397	0.084191032	0.7141451	Yes
SMC1A	1575	0.079489306	0.71104246	Yes
PPP5C	1741	0.076085858	0.70828867	Yes
CDC25B	1758	0.075692296	0.7127867	Yes
CDC27	1859	0.073668718	0.7130398	Yes
POLA1	1913	0.072428539	0.71550256	Yes
BTG3	1918	0.072311886	0.72035104	Yes
GSPT1	1927	0.072142698	0.72499233	Yes

Table 5.7.4 Rank-ordered list of filtered genes associated microtubule-based processes with associated rank metric scores, enrichment scores (ES), and whether each gene is part of the core enriched genes (i.e., the leading-edge subset) in the KIFC1-high group.

GENE SYMBOL	RANK IN GENE LIST	RANK METRIC SCORE	RUNNING ES	CORE ENRICHMENT
KIF23	7	0.380206674	0.068447836	Yes
KIF2C	16	0.34368071	0.13023852	Yes
KIF4A	32	0.329859108	0.18918754	Yes
PRC1	48	0.307584703	0.24410658	Yes
TTK	59	0.294727236	0.29694292	Yes
NUSAP1	65	0.281409442	0.34761333	Yes
KIF11	126	0.236126006	0.38741168	Yes
RCC1	157	0.2154641	0.42493314	Yes
STMN1	238	0.180245936	0.45364717	Yes
TUBG1	542	0.129438803	0.46230626	Yes
KIF1A	577	0.125762284	0.4834036	Yes
KIF1B	729	0.112902582	0.496475	Yes
NLGN1	846	0.106165938	0.51003253	Yes
YKT6	972	0.098996036	0.5218544	Yes
MAP1S	976	0.098900363	0.5396018	Yes
CKAP5	1293	0.087143637	0.5399754	Yes
SNAP29	1408	0.083875522	0.54959744	Yes
SMC1A	1575	0.079489306	0.5558929	Yes
CENPJ	1691	0.076832272	0.56419194	Yes

Appendix D: Supplementary Data for Chapter 7

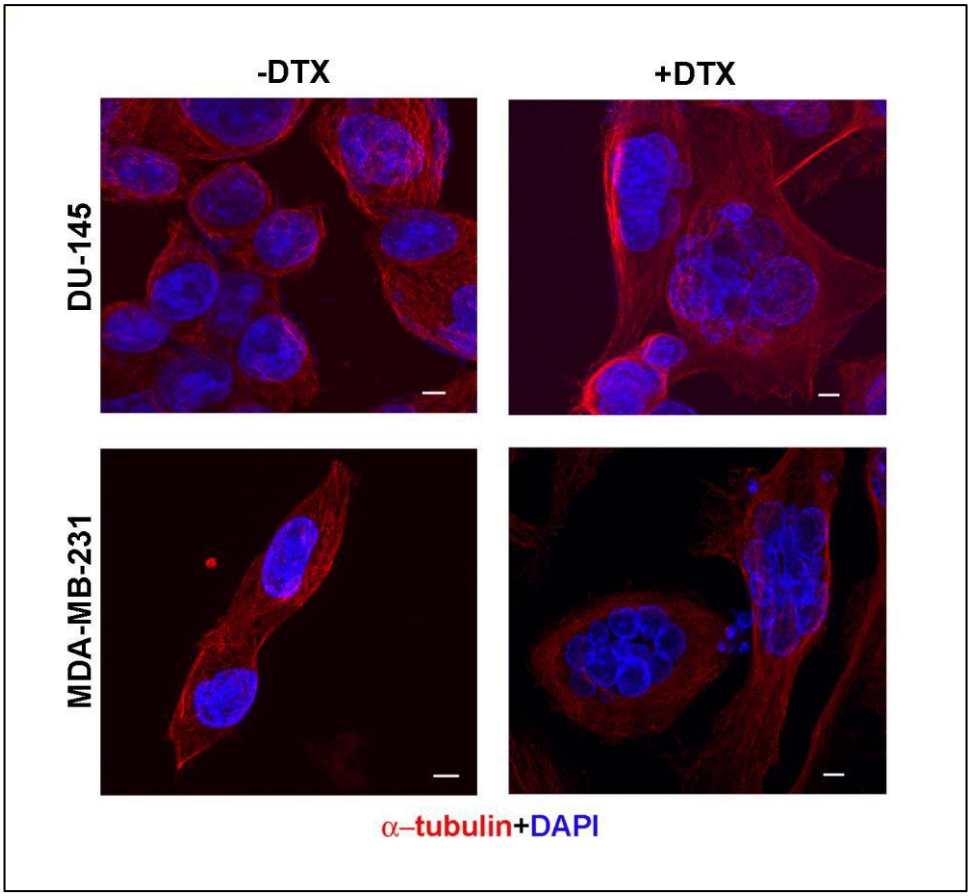

Supplementary Figure 7.7.1: MDA-MB-231 and DU-145 cells showing formation of giant MP cells 72 h after treatment with 5nM docetaxel (DTX).

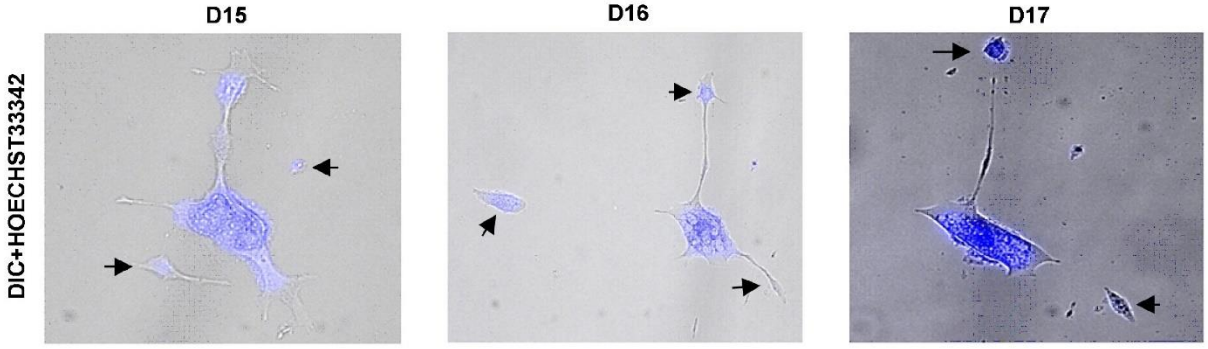

Supplementary Figure 7.7.2: DIC and Hoechst 33342 images showing presence of DNA (black arrows) in cells budding from the giant MP cells.

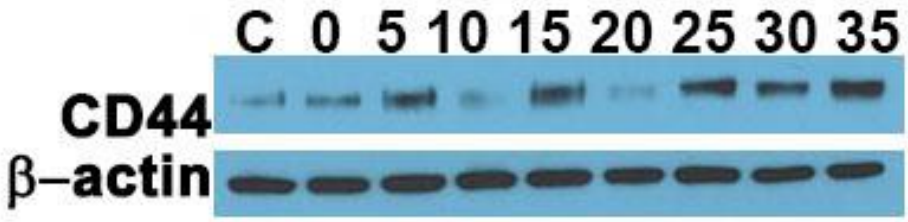

Supplementary Figure 7.7.3: Immunoblots of CD44 at different days after docetaxel removal. C are control PC-3 cells while cells on D0 are cells collected 72 h post docetaxel treatment.

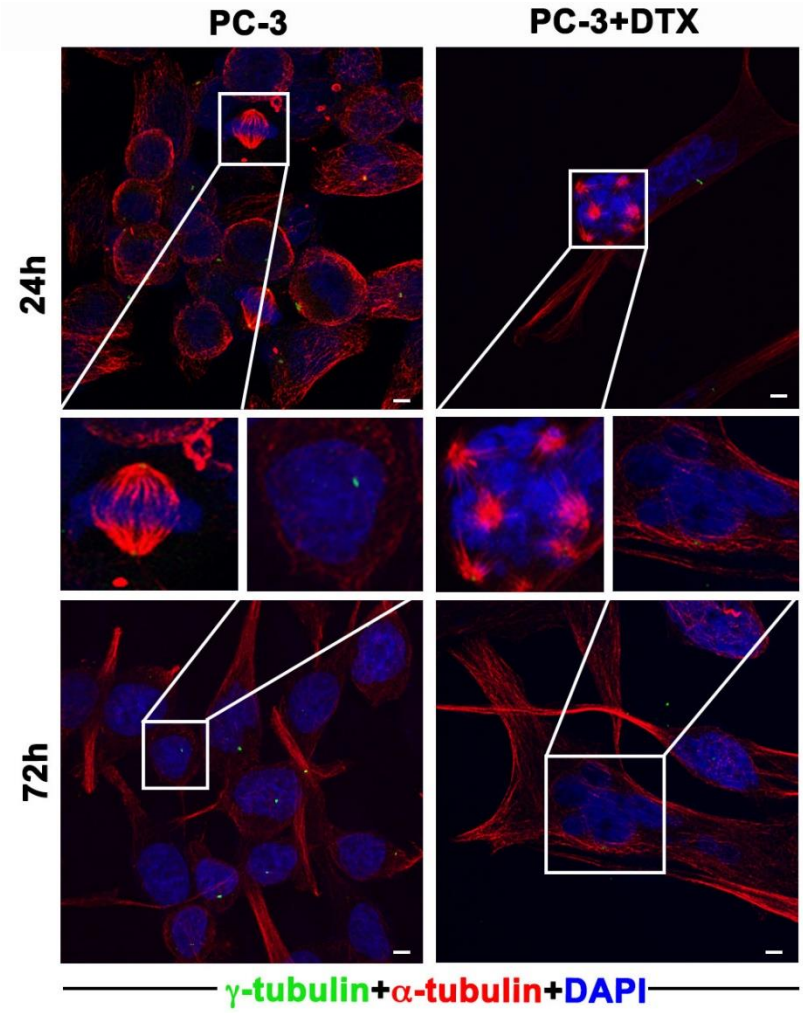

Supplementary Figure 7.7.4: Representative immunofluorescent confocal micrographs of PC-3 cells treated with docetaxel (5nM) for 24 h and 72 h indicating mitotic arrest and emergence of giant multinucleated polyploid cells respectively.

Centrosomes and microtubules were immunolabeled for γ-tubulin (green) and α-tubulin (red), respectively, and DNA was counterstained with DAPI (blue). Scale bar (white) 5 μm

Supplementary Table 1: The quantification of Western Blot densitometry values in relation to loading control β-actin for Fig 3B (calculated using Image-J software).

Cell type	Cleaved PARP	Cleaved Caspase
Giant MP -	0.027111272	0.02259534
Giant MP +	0.440467057	0.57760081
PC-3 -	0.070632216	0.054661554
PC-3 +	1.035792334	1.586356511
CDPC -	0.027747402	0.049495095
CDPC +	0.746083581	0.827335698

Supplementary Table 2: The quantification of Western Blot densitometry values in relation to loading control β-actin for Fig 3D (calculated using Image-J software).

Days after drug removal	Beclin-2	Survivin	Bcl-XL	P-Bcl2	Bcl2
0	0.941251727	0.803824128	0.941123482	0.065360381	0.055159161
1	2.822945541	0.981694271	0.803645446	1.195198385	0.804328047
5	3.713716836	0.781451901	0.972501709	1.130220819	1.209606137
10	0.433636748	1.074286244	0.434295141	0.461309892	0.34912065
15	0.138397195	0.697108731	1.073126657	0.585133676	0.916490447
25	0.074917074	1.469521135	1.339419773	1.17057988	0.517625674
35	0.072369018	1.383199964	1.237650405	1.10612344	0.26394166

Supplementary Table 3: The quantification of Western Blot densitometry values in relation to loading control β-actin for Fig 4D (calculated using Image-J software).

	Vimentin
PC-3	0.194946108
Giant MP	1.683074943

CDPC	1.480074389

Supplementary Table 4: The quantification of Western Blot densitometry values in relation to loading control β-actin for Supplementary Fig 3 (calculated using Image-J software).

Days after Drug Removal	CD44
C	0.209981839
0	0.895492234
5	0.804897313
10	0.260869891
15	0.601404075
20	0.149114788
25	1.697150291
30	0.682945733
35	0.696615458